



Welding High Strength Modern Line Pipe Steel

by

Graeme Robertson Goodall

Department of Mining and Materials Engineering

McGill University

Montreal, Quebec, Canada

2011

A thesis submitted to McGill University in partial fulfilment of the Degree of:

Doctor of Philosophy

©Copyright 2011 All rights reserved.



Welding High Strength Modern Line Pipe Steel



Abstract

The effect of modern mechanized girth welding on high strength line pipe has been investigated. The single cycle grain coarsened heat affected zone in three grade 690 line pipe steels and a grade 550 steel has been simulated using a Gleeble thermo-mechanical simulator. The continuous cooling transformation diagrams applicable to the grain coarsened heat affected zone resulting from a range of heat inputs applicable to modern mechanized welding have been established by dilatometry and metallography. The coarse grained heat affected zone was found to transform to lath martensite, bainite, and granular bainite depending on the cooling rate. The impact toughness of the steels was measured using Charpy impact toughness and compared to the toughness of the grain coarsened heat affected zone corresponding to a welding thermal cycle. The ductile to brittle transition temperature was found to be lowest for the steel with the highest hardenability. The toughness resulting from three different thermal cycles including a novel interrupted intercritically reheated grain coarsened (NTR ICR GC HAZ) that can result from dual torch welding at fast travel speed and close torch spacing have been investigated. All of the thermally HAZ regions showed reduced toughness that was attributed to bainitic microstructure and large effective grain sizes.

Continuous cooling transformation diagrams for five weld metal chemistries applicable to mechanized pulsed gas metal arc welding of modern high strength pipe steel (SMYS > 550 MPa) have been constructed. Welds at heat inputs of 1.5 kJmm^{-1} and 0.5 kJmm^{-1} have been created for simulation and analysis. Dilatometric analysis was performed on weld metal specimens cut from single pass 1.5 kJmm^{-1} as deposited beads. The resulting microstructures were found to range from martensite to polygonal ferrite. There is excellent agreement between the simulated and as deposited weld metal regions. Toughness testing indicates improved energy absorption at $-20 \text{ }^\circ\text{C}$ with increased cooling time.



Résumé

L'effet des méthodes modernes de soudage circonférentiel mécanisé sur des aciers à forte résistance utilisés pour les tubes de canalisation a été investigué. La zone affectée thermiquement ayant subi une croissance de grain lors d'un cycle thermique simple de soudage a été simulée pour trois grades d'acier à tubes de canalisation 690 et un grade d'acier 550 à l'aide d'un appareil de simulation thermomécanique Gleeble. Les diagrammes de transformation en refroidissement continu pour la zone affectée thermiquement ayant subi une croissance de grains ont été établis pour un spectre de chaleur induite représentatif du procédé de soudage mécanisé en utilisant la dilatométrie ainsi que des analyses métallographiques. Il résulte que la zone affectée thermiquement ayant subi une croissance de grain connaît un changement de phase vers une martensite massive, une bainite ou une bainite granulaire selon le taux de refroidissement rencontré. La résistance des aciers étudiés a été mesurée par essais Charpy et comparée à la résistance obtenue pour la zone affectée thermiquement ayant subi une croissance de grains correspondant à un cycle thermique de soudage. Le plus bas température de transition ductile-fragile a été obtenue pour les grades d'acier ayant la plus grande aptitude à la trempe. La résistance résultante des structures obtenues pour trois différents cycles thermique, notamment un nouveau cycle thermique interrompu par recuit intercritique similaire à l'effet que peut avoir un soudage à double torche à déplacement rapide et espacement réduit, a été étudié. Toutes les zones affectée thermiquement montrent une baisse de résistance causée par l'apparition d'une structure bainitique et la croissance des grains.

Les diagrammes de transformations en refroidissement continu ont été établis pour 5 alliages de soudage applicable pour le soudage pulsé à l'arc sous gas des aciers à tube modernes à haute résistance. Des soudures avec un apport de chaleur de $1,5 \text{ kJmm}^{-1}$ et $0,5 \text{ kJmm}^{-1}$ ont été utilisées pour les simulations et les analyses. Des essais de



Welding High Strength Modern Line Pipe Steel

dilatométrie ont été faits sur des échantillons prélevés des cordons de soudure déposés en une passe à $1,5 \text{ kJmm}^{-1}$. L'observation métallographique des échantillons présente une structure allant de la martensite à la ferrite polygonale. Une excellente concordance a été établie entre la structure du métal obtenu par simulation et telle que déposé. Les tests de résistance indiquent une amélioration de l'énergie absorbée à -20°C lorsque le temps de refroidissement est plus long



Dedication

This is for my Family

Those alive and those to come



Acknowledgments

I would like to thank Mathieu Brochu for his support, encouragement and friendship. The path of my success has been illuminated by his light of understanding. I would like to thank John Bowker and Jim Gianetto for granting me access to their laboratory, equipment and knowledge. This project would have been impossible without their support. Barbara Hanley has saved me from missing more deadlines than I care to mention and has contributed laughter and wit every day. The NAIN research group at McGill is a tremendous collective who certainly have made learning exciting and I thank them for freely sharing their energetic problem-solving skills with me. Pei Liu and Renata Zavadil will always have my gratitude for opening the doors of metallography and friendship to me and for being willing to help with any problem.

My parents have been my ardent supporters and have given me the courage to tackle every obstacle in my path. I can only hope to be as good a parent to my own children because no better exists. My siblings Emma, Susie, Gord, Bill and Anne have always encouraged and inspired me by setting high bars with their own accomplished lives. Thank you to Laurie and Allan for welcoming me into your family and considering me one of your own. I feel privileged to be a member of the Cruess clan and there is definitely some Eagle Lake in here.

To my kind, beautiful, supportive and patient wife Stephanie, I love you. Let's have adventures for the rest of our lives.



Table of Contents

1	INTRODUCTION	1
1.1	CONTRIBUTIONS OF CO-AUTHORS	4
2	LITERATURE SURVEY	5
2.1	LINE PIPE STEEL	5
2.1.1	<i>Iron Metallurgy</i>	<i>5</i>
2.1.1.1	Iron	5
2.1.1.2	Iron + Carbon= Steel.....	6
2.1.1.3	Alloying and weldability	7
2.1.2	<i>The beginning of HSLA Steel.....</i>	<i>10</i>
2.1.3	<i>Alloy Design and development.....</i>	<i>12</i>
2.1.3.1	Niobium.....	13
2.1.3.2	Titanium	14
2.1.3.3	Vanadium	14
2.1.4	<i>Processing Parameters for HSLA.....</i>	<i>15</i>
2.1.4.1	Reheating	15
2.1.4.2	Roughing	17
2.1.4.3	Finishing	18
2.1.5	<i>Modern Line Pipe Steel.....</i>	<i>19</i>
2.1.5.1	Processing	19
2.1.5.1.1	Direct Quench and Temper.....	19
2.1.5.1.2	Accelerated Cooling	20
2.1.5.2	Steel grades.....	22
2.1.5.2.1	X80	22
2.1.5.2.2	X100	23
2.1.5.3	Toughness	24
2.1.5.4	Pipe Manufacture.....	26



2.2	WELDING	27
2.2.1	<i>Fusion welding</i>	27
2.2.1.1	Gas Metal Arc Welding (GMAW).....	29
2.2.1.2	Pulsed Gas Metal Arc Welding (P-GMAW).....	31
2.2.1.3	Tandem	32
2.2.1.4	Dual Torch	33
2.2.2	<i>Weld Metal</i>	34
2.2.2.1	Alloying Strategies for High Strength Line Pipe Weld Metal.....	34
2.2.3	<i>Solidification in P-GMAW girth welds</i>	36
2.2.3.1	Weld Transformations.....	37
2.2.3.1.1	Transformations from Austenite	39
2.2.4	<i>HAZ</i>	41
2.2.4.1	Thermal Cycles	43
2.2.4.2	Grain Coarsened Heat Affected Zone	44
2.2.4.3	Fine Grain Heat Affected Zone	45
2.2.4.4	Intercritical and subcritical heat affected zones	45
2.2.4.5	Multi cycle heat affected zones	46
2.2.5	<i>Simulation</i>	47
2.2.5.1	Physical.....	48
2.2.5.2	Continuous Cooling Transformation Diagrams	49
3	OBJECTIVES.....	53
4	COMPARISON OF BASE METAL AND HAZ CCT DIAGRAMS FOR X100 PIPE	
	STEEL	54
4.1	PREFACE.....	54
4.2	ABSTRACT:.....	55
4.3	INTRODUCTION:.....	56
4.4	EXPERIMENTAL	58
4.4.1	<i>Gleeble 3800</i>	59



4.4.2	<i>BÄHR DIL 805A/D</i>	59
4.4.3	<i>Metallography</i>	60
4.5	RESULTS AND DISCUSSION.....	60
4.5.1	<i>Microstructure</i>	63
4.5.1.1	1350 °C Peak Cycles.....	63
4.5.1.2	900 °C Peak Cycles.....	66
4.5.2	<i>CCT Diagrams</i>	68
4.6	CONCLUSIONS	74
4.7	ACKNOWLEDGEMENTS	74
5	CCT DIAGRAMS AND IMPACT TOUGHNESS APPLICABLE TO THE GC HAZ REGION GENERATED IN X100 LINE PIPE	75
5.1	PREFACE.....	75
5.2	ABSTRACT:.....	76
5.3	INTRODUCTION	77
5.4	EXPERIMENTAL	79
5.4.1	<i>Materials</i>	79
5.4.2	<i>Thermal Cycles and Testing Procedures</i>	82
5.4.3	<i>Metallography & Micro hardness</i>	84
5.5	RESULTS AND DISCUSSION	85
5.5.1	<i>Single Torch Rolled Weld Macrostructure and hardness</i>	85
5.5.2	<i>Microstructure and CCT Diagrams</i>	87
5.5.3	<i>Simulated Properties</i>	95
5.5.4	<i>Mechanical Properties</i>	98
5.6	CONCLUSIONS	104
5.7	ACKNOWLEDGEMENTS	105
6	CCT DIAGRAMS OF WELD METAL APPLICABLE FOR GIRTH WELDING OF X100 LINE PIPE.....	106



6.1	PREFACE.....	106
6.2	ABSTRACT.....	107
6.3	INTRODUCTION	108
6.4	EXPERIMENTAL PROCEDURE	111
6.4.1	<i>Weld and Specimen Preparation.....</i>	<i>111</i>
6.4.2	<i>Simulation</i>	<i>113</i>
6.4.3	<i>Microstructural Analysis</i>	<i>115</i>
6.4.4	<i>Dilatometric Analysis</i>	<i>115</i>
6.4.5	<i>Mechanical Properties</i>	<i>117</i>
6.5	RESULTS AND DISCUSSION.....	117
6.5.1	<i>Thermal Simulation and CCT.....</i>	<i>117</i>
6.5.2	<i>Weld analysis</i>	<i>125</i>
6.5.3	<i>Simulation of as-deposited weld metal.....</i>	<i>130</i>
6.5.4	<i>Mechanical Properties</i>	<i>132</i>
6.6	CONCLUSIONS	133
6.7	ACKNOWLEDGMENTS.....	134
7	THERMAL SIMULATION OF HAZ REGIONS IN A MODERN HIGH STRENGTH STEEL.....	136
7.1	SELECTED DISCUSSION FROM CHAPTER 4, 5 AND 6.....	136
7.2	PREFACE.....	138
7.3	ABSTRACT.....	139
7.4	INTRODUCTION	140
7.5	EXPERIMENTAL PROCEDURE	142
7.5.1	<i>Materials.....</i>	<i>142</i>
7.5.2	<i>Simulation and testing</i>	<i>143</i>
7.5.3	<i>Microscopy.....</i>	<i>145</i>
7.6	RESULTS.....	146



7.6.1	<i>CCT and Microstructure</i>	146
7.6.2	<i>Prior austenite grain size</i>	148
7.6.3	<i>Thermal Simulation</i>	151
7.6.4	<i>Toughness</i>	153
7.7	DISCUSSION	157
7.8	CONCLUSIONS	160
7.9	ACKNOWLEDGEMENTS	160
8	COMPREHENSIVE CONCLUSIONS	162
9	CONTRIBUTIONS TO ORIGINAL KNOWLEDGE	166
	APPENDIX A – EXPERIMENTAL TECHNIQUES	168
	THERMAL CYCLES	168
	<i>Measurement</i>	168
	<i>Analysis & Correlation</i>	169
	<i>Simulation Setup</i>	169
	ANALYSIS	170
	<i>Microscopy</i>	170
	<i>Charpy & Hardness</i>	171
	<i>Dilatometry</i>	172
10	REFERENCES	174



Table of Figures

FIGURE 2-1 - THE IRON CARBON PHASE DIAGRAM, FROM [21].....	6
FIGURE 2-2 - THE CHANGE IN THE HAZ HARDNESS AS A FUNCTION OF COOLING RATE, FROM [22].....	9
FIGURE 2-3- TENDENCY OF MAE TO FORM OXIDES, SULPHIDES AND NITRIDES ALONG WITH PRECIPITATION STRENGTHENING POTENTIAL. FROM [8] AFTER [9].....	12
FIGURE 2-4- EFFECT OF MICROALLOY CONTENT ON RECRYSTALLIZATION STOP TEMPERATURE (T_R), FROM [3]	15
FIGURE 2-5- SOLUBILITIES OF NbC, TiC AND TiC IN FERRITE AND AUSTENITE, FROM [6].....	16
FIGURE 2-6- THE GRAIN COARSENING TEMPERATURE AS A FUNCTION OF CONCENTRATION FOR 4 DIFFERENT MAE, FROM [5].....	17
FIGURE 2-7- VARIOUS TMCP SCHEDULES. RECR.: RECRYSTALLIZED, MLE: MAXIMUM LIKELIHOOD ESTIMATION, TM: THERMOMECHANICAL TREATMENT, ACC: ACCELERATED COOLING, DQ: DIRECT QUENCH, QST: QUENCH AND SELF TEMPER, IC: INTERMEDIATE COOLING, FROM [60]	21
FIGURE 2-8 - HISTORICAL CHANGES IN THE REQUIREMENTS OF LINE PIPE STEEL WITH TIME, FROM [59]	22
FIGURE 2-9 - PROCESSING PARAMETER WINDOW FOR X100 STEEL, FROM [74].....	23
FIGURE 2-10 - SCHEMATIC REPRESENTATION OF THE UOE PIPE FORMING PROCESS [2].....	27
FIGURE 2-11 - A) GMAW WELD SCHEMATIC [98] AND B) CROSS-SECTIONAL IMAGE OF AN X100 DUAL TORCH GMAW WELD.....	28
FIGURE 2-13 - SCHEMATIC OF P-GMAW WAVEFORM WITH CORRESPONDING DROPLET, FROM [107]	31
FIGURE 2-12- NARROW GAP P-GMAW GIRTH WELD JOINT GEOMETRY, FROM [4].....	31
FIGURE 2-14 TANDEM TORCH SCHEMATIC, FROM [1].....	33
FIGURE 2-15 - THE EFFECT OF SOLUTE AND G/R ON SOLIDIFICATION, FROM [7].....	37
FIGURE 2-16 - GROWTH OF FERRITE. (A) GRAIN BOUNDARY (B) WIDMANSTÄTTEN, FROM [117].....	39
FIGURE 2-17 - HEAT AFFECTED ZONE (HAZ) AND CORRESPONDING PHASE DIAGRAM, FROM [153].....	42
FIGURE 2-18- DIFFERENT THERMAL PROFILES FROM THE SAME HEAT INPUT PARAMETERS, FROM [156]	44
FIGURE 2-19- SCHEMATIC OF VARIOUS HAZ ZONES DEVELOPED IN MULTIPASS WELDING, FROM [129]	47
FIGURE 2-20 - FACTORS THAT INFLUENCE THE AUSTENITE TRANSFORMATION, FROM [182].....	49
FIGURE 2-21- CCT DIAGRAMS. (A) FG HAZ (B) GC HAZ (C) WM, FROM [182].....	50



Welding High Strength Modern Line Pipe Steel

FIGURE 2-22 – ILLUSTRATION OF THE LEVER RULE USED TO MEASURE FRACTION OF AUSTENITE TRANSFORMED, FROM [190]	51
FIGURE 4-1– THERMAL CYCLES FOR ΔT_{8-5} COOLING TIMES OF 30 SECONDS FOR 1350 °C AND 900 °C PEAKS	62
FIGURE 4-2- MICROGRAPHS FOR THE 1350 °C PEAK TEMPERATURE THERMAL CYCLES. ΔT_{8-5} = (A) 1.3s (B) 10s (C) 25s (D) 50s.....	63
FIGURE 4-3– SEM IMAGES OF 1350 °C PEAK TRANSFORMATION PRODUCTS. (A) MARTENSITE, ΔT_{8-5} =1.3s (B) BAINITE, ΔT_{8-5} = 10s (C) GRANULAR BAINITE, ΔT_{8-5} = 50s.....	65
FIGURE 4-4– TEM IMAGES OF 1350 °C TRANSFORMATION PRODUCTS. (A) BAINITE, ΔT_{8-5} =10s (B) LATH MARTENSITE ΔT_{8-5} = 1.3s.....	66
FIGURE 4-5– MICROGRAPHS FOR THE 900 °C PEAK TEMPERATURE THERMAL CYCLES ETCHED WITH NITAL UNLESS SPECIFIED. ΔT_{8-5} =: (A) 1 s (B) 6.1 s (C) 17 s (D) 100 s (E) 3000 s (F) 3000 s ETCHED WITH LE PERA’S.....	67
FIGURE 4-6– CCT DIAGRAM FROM 900 °C SHOWING MARTENSITE (M), BAINITE (B), POLYGONAL FERRITE (F), PEARLITE (P) AND MA FROM BÄHR DIL 805A/D DILATOMETER DATA.....	69
FIGURE 4-7– DILATOMETRIC RESPONSE DURING SLOW AND FAST COOLING FROM 900 °C SHOWING THE START AND FINISH TEMPERATURES OF FERRITE- PEARLITE (F-P), MA AND MARTENSITE (M)	70
FIGURE 4-8– CCT DIAGRAM FROM 1350 °C PEAK SHOWING MARTENSITE (M), BAINITE (B) AND GRANULAR BAINITE (GB) FROM GLEEBLE 3800 DATA	71
FIGURE 4-9– COMPARISON OF START AND FINISH TEMPERATURES FOR 900 °C AND 1350 °C PEAK TEMPERATURES AS A FUNCTION OF COOLING TIME FROM 800 °C TO 500 °C	73
FIGURE 5-1- MICROSTRUCTURE OF THE PIPE MATERIALS. (A) X100-2 (B) X100-5 (C) X100-4.....	81
FIGURE 5-2–THE HAZ REGION DEVELOPED FROM P-GMAW IN THE X100-5 STEEL (A) MACROGRAPH (B) DETAIL SHOWING WIDTH OF THE GC-HAZ.....	86
FIGURE 5-3– CCT DIAGRAM FOR X100-2 FROM 1350 °C SHOWING THE FORMATION OF MARTENSITE (M), BAINITE (B) AND GRANULAR BAINITE (GB).....	87
FIGURE 5-4– SEM OF (A) MARTENSITE, ΔT_{8-5} =1.2s (B) BAINITE AND MARTENSITE, ΔT_{8-5} = 3s (C) BAINITE AND GRANULAR BAINITE, ΔT_{8-5} =50s, IN X100-2.....	88
FIGURE 5-5- CCT DIAGRAM FOR X100-5 FROM 1350 °C SHOWING THE FORMATION OF MARTENSITE (M), BAINITE (B) AND GRANULAR BAINITE (GB).....	89
FIGURE 5-6– SEM OF (A) MARTENSITE, ΔT_{8-5} = 1.2s (B) BAINITE AND MARTENSITE, ΔT_{8-5} = 3s (C) BAINITE AND GRANULAR BAINITE, ΔT_{8-5} = 50s, IN X100-5	91
FIGURE 5-7– GC-HAZ IN X100-5 (A) REAL WELD (B) SIMULATED AT ΔT_{8-5} = 6 s, 1.9 kJmm ⁻¹	92
FIGURE 5-8- CCT DIAGRAM FOR X100-4 FROM 1350 °C SHOWING THE FORMATION OF MARTENSITE (M), BAINITE (B) AND GRANULAR BAINITE (GB).....	92



Welding High Strength Modern Line Pipe Steel

FIGURE 5-9- SEM OF X100-4 (A) MARTENSITE, $\Delta T_{8-5} = 1.2s$ (B) BAINITE AND MARTENSITE, $\Delta T_{8-5} = 3s$ (C) BAINITE AND GRANULAR BAINITE, $\Delta T_{8-5} = 50s$ (D) TEM OF LATH MARTENSITE	93
FIGURE 5-10- PEAK TEMPERATURE DISTRIBUTION FOR A 10 X 10 MM BAR AS A FUNCTION OF FREE SPAN	95
FIGURE 5-11- X100-4 SPECIMEN AFTER A $\Delta T_{8-5} = 6s$ THERMAL CYCLE AT A 15 MM FREE SPAN SHOWING THE HARDNESS DISTRIBUTION ACROSS THE THERMAL ZONE.	96
FIGURE 5-12 – HARDNESS PROFILES DEVELOPED IN X100-4 WITH $\Delta T_{8-5} = 10s$ AT GRIP SPACING OF 10, 15 AND 20 MM FROM TOP TO BOTTOM	97
FIGURE 5-13 – IMPACT ENERGY RESULTS (A) BASE METAL (B) X100-2 (C) X100-5 (D) X100-4.....	98
FIGURE 5-14 – ETCHED FRACTURE SURFACE OF X100-5 BM BROKEN AT $-120\text{ }^\circ\text{C}$	99
FIGURE 5-15– (A) FRACTURE SURFACE OF X100-2 GC HAZ $\Delta T_{8-5} = 6s$ (B) CLEAVAGE FACET.....	100
FIGURE 5-16 – X100-5 GC HAZ (A) LARGE FACETS (B) MA (ARROW)	101
FIGURE 5-17 – MOUNTED FRACTURE SURFACE FOR X100-4 (A) GC HAZ $\Delta T_{8-5} = 6s$ (B) GC HAZ $\Delta T_{8-5} = 10s$	102
FIGURE 6-1 – MICROGRAPH OF THE NiMo80 WELD. (A) THE COMPLETE WELD SHOWING THE LOWER 0.5 KJ NOMINAL ENERGY INPUT MULTI- PASS REGION AND UPPER 1.5 KJ SINGLE PASS REGION WITH SCHEMATIC OF WELD METAL SPECIMEN ORIENTATION. (B) NiMo80 SPECIMEN AFTER THERMAL CYCLING.	112
FIGURE 6-2– ILLUSTRATION OF THE LEVER RULE TECHNIQUE EMPLOYED FOR CALCULATING CCT TRANSFORMATION TEMPERATURES AS THE LENGTH OF THE BC LINE SEGMENT DIVIDED BY AC. START AND FINISH TEMPERATURES ARE THEN CALCULATED AS 2% AND 98% OF THE FRACTION TRANSFORMED.	116
FIGURE 6-3 – CCT DIAGRAM FOR WM 1 FROM $1300\text{ }^\circ\text{C}$	118
FIGURE 6-4 – CCT DIAGRAM FOR WM 2 FROM $1300\text{ }^\circ\text{C}$	118
FIGURE 6-5 - CCT DIAGRAM FOR NiMo80 FROM $1300\text{ }^\circ\text{C}$	119
FIGURE 6-6 – CCT DIAGRAM FOR WM 3 FROM $1300\text{ }^\circ\text{C}$	119
FIGURE 6-7 – CCT DIAGRAM FOR WM 4 FROM $1300\text{ }^\circ\text{C}$	120
FIGURE 6-8 – NiMo80 MICROSTRUCTURES CORRESPONDING TO $\Delta T_{8/5}$ COOLING TIMES OF 2, 3.5, 5, 7.5, 10, 20 AND 50 SECONDS. (A) MARTENSITE AND BAINITE. (B) BAINITE AND ACICULAR FERRITE. (C) BAINITE AND ACICULAR FERRITE. (D) BAINITE AND ACICULAR FERRITE. (E) BAINITE AND ACICULAR FERRITE. (F) BAINITE AND ACICULAR FERRITE WITH SOME GRAIN BOUNDARY FERRITE. (G) ACICULAR FERRITE AND GRAIN BOUNDARY FERRITE	123
FIGURE 6-9- MICROSTRUCTURES FORMED AFTER COOLING AT $\Delta T_{8/5} = 50s$. (A) WM1, $CE_{IIW} = 0.46$ (B) WM4, $CE_{IIW} = 0.65$	124



Welding High Strength Modern Line Pipe Steel

FIGURE 6-10 – HARDNESS MAP (IN HV AT 300 GF) FOR THE NiMo80 SPECIMEN POST THERMAL CYCLE SHOWING A RELATIVELY HOMOGENEOUS HARDNESS PROFILE THROUGH THE CENTER OF THE SPECIMEN.....	125
FIGURE 6-11 – MICROHARDNESS SURVEYS PERFORMED ON THE NiMo80 WELD SECTION. (A) SCALE IMAGE SHOWING THE PLACEMENT OF THE TRAVERSES THROUGH THE 1.5 KJMM ⁻¹ DEPOSIT, THE 0.5 KJMM ⁻¹ DEPOSIT AND FROM THE CAP TO THE ROOT. (B) RESULTS OF THE CROSS WELD TRAVERSES THROUGH THE 1.5 KJMM ⁻¹ AND 0.5 KJMM ⁻¹ DEPOSITS.	127
FIGURE 6-12 – WELD HARDNESS AS A FUNCTION OF CARBON EQUIVALENT IN THE 1.5KJMM ⁻¹ AND 0.5 KJMM ⁻¹ REGIONS.....	129
FIGURE 6-13 – HARDNESS SURVEY FOR NiMo80 WELD FROM THE CAP TO THE ROOT SECTION THROUGH BOTH THE 1.5 KJMM ⁻¹ AND 0.5 KJMM ⁻¹ REGIONS OF THE WELD. THE CYCLIC RISE AND FALL OF THE HARDNESS IN THE 0.5 KJMM ⁻¹ REGION CORRESPONDS TO THE MULTIPLE DEPOSITS OF WELD METAL.....	130
FIGURE 6-14 – MICROSTRUCTURES DEVELOPED FOR WM3 (A) AFTER A $\Delta T_{8/5} = 5s$ GLEEBLE THERMAL CYCLE (B) IN THE 0.5 KJMM ⁻¹ REGION OF THE WELD	131
FIGURE 6-15 – CHARPY V NOTCH RESULTS FOR WM2, NiMo80 AND WM3 TESTED AT -20 °C FOR THE AS WELDED AND AT $\Delta T_{8/5}$ COOLING TIMES OF 5, 10 AND 20 SECONDS	132
FIGURE 6-16 – FRACTOGRAPHY OF WM3 SAMPLES (A) UNETCHED (B) ETCHED.....	133
FIGURE 7-1 – SCHEMATIC OF AN INTERRUPTED THERMAL CYCLE FROM DUAL TORCH WELDING	141
FIGURE 7-2 - MICROSTRUCTURE OF X80 PIPE	143
FIGURE 7-3 – CCT DIAGRAM FOR X80 FROM 1350 °C	147
FIGURE 7-4 – MICROSTRUCTURES DEVELOPED IN X80 COOLING FROM 1350 (A) BAINITE AND MARTENSITE (B) BAINITE (C) GRANULAR BAINITE.....	148
FIGURE 7-5 – THERMAL CYCLES USED TO MEASURE THE PRIOR AUSTENITE GRAIN SIZE AND RESULTS (INSET GRAPH).....	149
FIGURE 7-6 – MICROSTRUCTURE DEVELOPED FROM (A) 1450 °C (B) 1100 °C.....	150
FIGURE 7-7– CORRELATION OF PRIOR AUSTENITE GRAIN SIZE (PAG) AND TRANSFORMATION START TEMPERATURE TO PEAK TEMPERATURE (MOVING AVERAGE LINES).....	150
FIGURE 7-8 – THERMAL CYCLE AND DILATATION RESPONSE FOR NTR- ICR GC HAZ.....	151
FIGURE 7-9 – THERMAL SIMULATION MICROSTRUCTURES (A) ICR GC HAZ (ARROW INDICATES DECORATED PAG BOUNDARY) (B) NTR- ICR GC HAZ	152
FIGURE 7-10 – CHARPY IMPACT ENERGY VERSUS TEST TEMPERATURE FOR SIMULATED X80 SPECIMENS (A) BASE METAL (B) SINGLE CYCLE GC HAZ (C) ICR GC HAZ (D) NTR ICR GC HAZ.....	153
FIGURE 7-11 – BRITTLE FRACTURE SURFACES. (A) BASE METAL (B) GC-HAZ $\Delta T_{8-5} = 6s$ (C) ICR GC HAZ (D) NTR- ICR GC HAZ.....	155



FIGURE 7-12 – DIFFERENT TYPES OF CLEAVAGE TRIGGERING SITES IN A GC HAZ SPECIMEN (A) MA ISLAND (B) MULTIPLE FACETS WITH LOW MISORIENTATION 156

FIGURE 7-13 – SEM FRACTOGRAPHY (A) ETCHED CLEAVAGE FACET (B) DETAIL OF MICRO-CRACK (C) CRACK FRONT IN THE MOUNTED GC HAZ SAMPLE (D) MICROCRACKING IN THE MOUNTED SAMPLE 157



List of Abbreviations

- A₁ Lower Boundary of α -Ferrite + Austenite Region
- A₃ Upper Boundary of α -Ferrite + Austenite Region
- ACC Accelerated Cooling
- ASTM American Society for Testing and Materials
- AW As Welded
- BCC Body Centered Cubic
- BTU British Thermal Unit
- CCT Continuous Cooling Transformation
- CE Carbon Equivalent
- CTOD Crack Tip Opening Displacement
- CVN Charpy V Notch
- DBTT Ductile to Brittle Transition Temperature
- DWTT Drop Weight Tear Test
- ETT Energy Transition Temperature
- FCC Face Centered Cubic
- FEG Field Emission Gun
- FGHAZ Fine Grain Heat Affected Zone
- GC Grain Coarsened
- GHAZ Grain Coarsened Heat Affected Zone
- GMAW Gas Metal Arc Welding
- GTAW Gas Tungsten Arc Welding
- HAZ Heat Affect(ed) Zone
- HSLA High Strength Low Alloy
- HV Vicker's Hardness
- ICHAZ Intercritical Heat Affected Zone



- ICR Intercritically Reheated
- IIW International Institute of Welding
- JWS Japanese Welding Society
- kJ Kilo Joule
- km Kilometer
- ksi Thousand pound per inch
- LOM Light Optical Microscope
- LVDT Linear Variable Differential Transformer
- MA Martensite/ Austenite
- mm millimeter
- MPa Mega Pascal
- Nb (C,N) Niobium Carbo-Nitride(s)
- NRT Interrupted
- NSERC National Research Council of Canada
- PAG Prior Austenite Grain Size
- P-GMAW Pulsed Gas Metal Arc Welding
- SCHAZ Sub-critical Heat Affected Zone
- SEM Scanning Electron Microscope
- SMAW Submerged Metal Arc Welding
- SMYS Specified Mean Yield Strength
- TEM Transmission Electron Microscope
- TMCP Thermo Mechanical Controlled Processing
- TPA Transverse to the Pipe Axis
- UHS Ultra High Strength
- VN Vanadium Nitride
- WM Weld Metal
- X100 Grade 690 Steel



Welding High Strength Modern Line Pipe Steel

- X80 Grade 550 Steel
- α Low Temperature Ferrite
- α' Martensite
- γ Austenite
- δ High Temperature Ferrite
- μm Micron



1 Introduction

There is a huge demand for energy to meet the needs of modern society. The Department of Energy for the United States of America estimated consumption for 2008 (the most recent value available at the time of publication) at 99 quadrillion BTU, of which 24 quadrillion BTU was supplied by natural gas and 37 quadrillion BTU by petroleum [10]. Efficient transportation of such vast amounts of petroleum products can be achieved through the use of pipelines. In North America, the natural gas reserves that are being investigated for future exploitation are located in the far north on the shores of the Arctic Ocean. The northern extent of the current gas distribution network throughout Canada and the United States is located in central Alberta. Two projects are, at the time of publication, under consideration for approval to expand the network north to the Arctic. The Mackenzie Gas Project is proposed as an entirely Canadian pipeline to join onshore natural gas extraction fields located in the Arctic region of the North West Territories to central Alberta along an 1196 km route [11]. The second proposed project is the Alaska Pipeline Project which is planned to connect the natural gas fields of Prudhoe Bay, Alaska to Alberta. The Alberta option for the proposed route comprises 2736 km of pipeline, of which 1554 km would be built in Alberta with the remainder in Alaska[12].

The challenges associated with projects of the scale proposed by either the Mackenzie or the Alaska pipeline projects can be assessed under economic or material paradigms. The economic considerations require that the investment in line pipe material, transportation costs to the installation site, field girth welding, corrosion and maintenance costs can be offset by the capacity of the pipeline and the rate at which the invested capital can be recouped. The associated material challenges must surmount



geological factors of discontinuous permafrost with seasonal heave and thaw, operating pressures, field weldability and repair potential. The use of high strength line pipe steel for the proposed pipeline projects can address both the economic and material challenges.

Line pipe steel with specified minimum yield strengths in excess of 550 MPa are deemed to be high strength [13]. There are three grades, 550 MPa (80 ksi), 690 MPa (100 ksi) and 830 MPa (120 ksi) of high strength steel now covered in the American Petroleum Institute's standard for line pipe (API 5L) [14]. Of these grades, 690 and 830 are ultra high strength and only grade 550 has had any significant application in North America [13, 15]. The high strength afforded by these steels increases economic viability by allowing larger diameter pipelines to be built from thinner walled line pipe. This thinner walled line pipe reduces the required tonnage of steel, the transportation costs to the installation site and the construction costs, which combined, can provide cost savings of 30% over lower strength grade 483 MPa steel [16]. These cost savings are further augmented by increased pressure tolerances to cope with the operational design pressures that have been rising at an exponential rate over the last 30 years [13]. The geographic and geologic forces that develop in sub-arctic regions of discontinuous permafrost require very strong materials with dependable strain behavior. These requirements can be met by high and ultra high strength steels [15].

The construction of the pipeline involves joining sections of line pipe with circumferential welds known as girth welds. The girth welding procedure becomes a rate limiting step in pipeline construction. New, high efficiency welding procedures have been developed in the past 8 years to address this issue with regards to long pipeline construction projects. The application of Tandem, Dual Torch and Dual Tandem welding procedures have been advanced for evaluation as welding methods for both the Mackenzie and Alaska pipeline projects.



The response of high strength steel to new high efficiency welding procedures requires study to assess the impact of the joining procedure on the resulting weldment. The objective of this study is to assess the influence of novel high efficiency welding procedures on the heat affected zone that develops in high strength steel and on the weld metal deposited.

This thesis describes the transformations that occur in high strength steel as a result of novel, high efficiency welding procedures. Specifically, the effect of low heat input welding parameters on the transformation of austenite to ferrite in the grain coarsened region adjacent to the fusion zone has been characterized for three different commercially produced grade 690 and one grade 550 line pipes. The microstructural evolution that occurs as a function of welding parameters applicable to novel welding procedures has been presented in the form of continuous cooling transformation diagrams. The mechanical properties that develop as a function of welding parameters have been correlated to the microstructural evolution. The effect of novel welding procedures on the reheating of weld metal applicable to high strength steel has been studied and continuous transformation diagrams have been produced for five different consumable chemistries. The properties of selected weld metal chemistries have been evaluated and correlated to the microstructural evolution.

The format of this dissertation is four distinct manuscripts introduced by a comprehensive literature review. The first manuscript introduced the differences in the continuous cooling transformation diagrams for the same line pipe steel from different peak temperatures and will be submitted to *ISIJ International*. The second manuscript presents three CCT diagrams and compares the grain coarsened heat affected zone and mechanical properties of three different grade 690 line pipe steels and will be submitted to *Materials Science and Technology*. The third manuscript compares the CCT diagrams for five different weld metals applicable to P-GMAW with mechanical properties and will



be submitted to the *Science and Technology of Welding and Joining*. The fourth manuscript presents a novel thermal simulation for dual torch welding with the CCT diagram, microstructure and mechanical properties of 3 different HAZ regions for a grade 550 MPa steel and will be submitted to *Metallurgical and Materials Transactions A*. The results of the four manuscripts are summarized with a comprehensive conclusion with suggestions for further study.

1.1 Contributions of Co-authors

I am the lead author on all of the manuscripts included in this dissertation and have performed the experimental work and have analyzed the resulting data. The one exception is in the first manuscript where Benoit Voyzelle operated the BÄHR DIL 805A/D dilatometer and reported transformation temperatures that I correlated with metallographic results and plotted. Jim Gianetto contributed by acquiring the raw materials, liaising with the machine shop and helping with direction. John Bowker supervised my progress at Canmet and provided insight into the techniques relevant to the microstructural analysis I used. Professor Mathieu Brochu was in charge of the overall project supervision.



2 Literature Survey

2.1 Line Pipe Steel

2.1.1 Iron Metallurgy

Steel is a versatile alloy based on a mixture of iron and carbon that can, and has, been classified into literally hundreds of categories based on alloy composition, strength, application, forming process, etc. [17]. As the current work discusses the many transformations that result from the application of different heating, cooling and deformation schedules in steel, it is necessary to introduce the reader briefly to the fundamental principles that govern the resulting reactions.

2.1.1.1 Iron

The most basic form of steel is a mixture of iron and carbon where the carbon content is less than 2.14 wt% [18]. The dominant constituent, iron, is an allotropic metal with four distinct crystal structures depending on temperature and pressure. The three phases that form at atmospheric pressure are, in order of decreasing temperature, delta ferrite (δ), gamma austenite (γ), and alpha iron (α). The fourth allotrope, epsilon (ϵ) occurs only at extreme pressures (>13 GPa at room temperature) and thus will not be discussed further in this work [19]. Of the phases that form readily at atmospheric pressure, both of the ferrite phases take body centered cubic (BCC) crystal structures, while austenite occurs in a face centered cubic (FCC) structure. While the number of atoms per unit cell is greater for austenite than ferrite at 4 to 2, the FCC lattice arrangement allows a higher atomic density, known as the atomic packing factor of 0.74 versus 0.68 for ferrite. This implies that for a fixed mass of iron, there must be a volumetric expansion or contraction that accompanies any phase change between the



two. The difference for pure iron is 2.64 % between the FCC and BCC phases[20]. This factor, combined with changes in the ability to accommodate alloying elements, forms the basis for all steel transformations.

2.1.1.2 Iron + Carbon= Steel

The addition of carbon to iron has a dramatic effect. The first noticeable change is that the melting point of carbon saturated iron (4.3 wt% C) decreases from 1539 °C to 1130 °C. The second remarkable outcome is that a second phase, cementite (Fe_3C) must co-exist with iron. The region of the phase diagram shown in Figure 2-1 that interests producers of line pipe steel is the hypo-eutectoid region at carbon levels of less than 0.5 %.

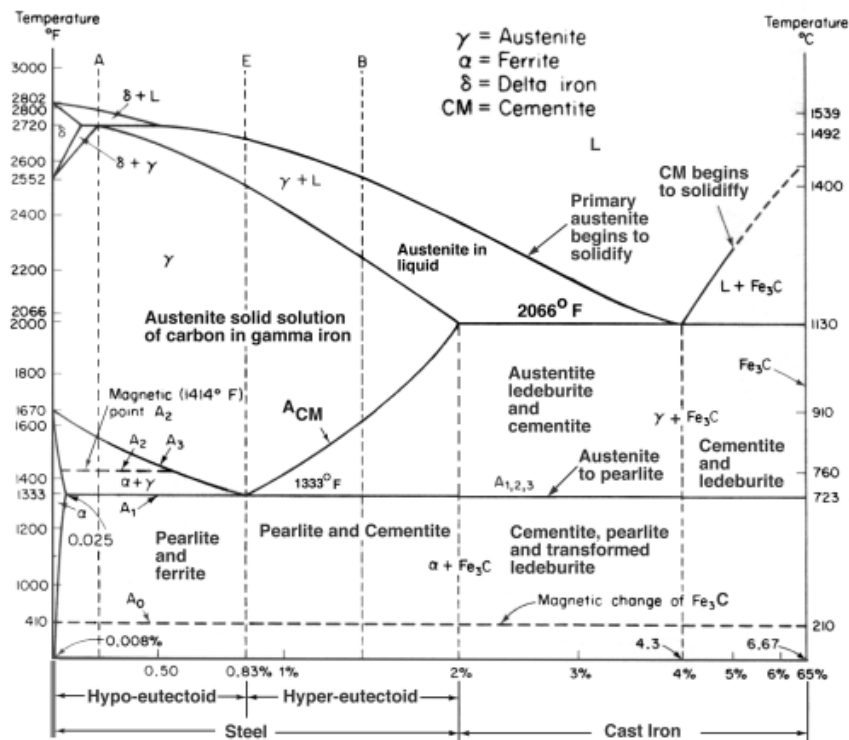


Figure 2-1 - The iron carbon phase diagram, from [21]



The feature of the phase diagram that is most important to modern steels is that ~2 % carbon is soluble in austenite, while the ferrite solubility decreases from a maximum of 0.025% at 723°C to 0.008 % at room temperature. Understanding the coexisting phases of ferrite, cementite and austenite in all their variants, with the ability to manipulate said variants to achieve a desired set of properties, constitutes the foundation of modern line pipe metallurgy. Some of the common terminology used in describing steel transformations can also be most easily explained using the phase diagram. The A_1 and A_3 lines shown in Figure 2-1 correspond to the lower and upper limits of the $\alpha + \gamma$ region at equilibrium. These critical lines are denoted as Ar_3 and Ar_1 during continuous cooling and Ac_3 and Ac_1 during continuous heating.

2.1.1.3 Alloying and weldability

The addition of metallic and non metallic alloying elements to steel can produce a huge array of properties and microstructures. Strengthening of steel was classically achieved by increasing the carbon content and by adding elements like chromium, copper, manganese, molybdenum, nickel or vanadium. The consequence of this approach was a reduction in the utility of the steel resulting from deleterious over hardening of heat affected zones (HAZ) when the steel was welded. The correlation of the propensity to form martensite as a function of carbon content was termed 'hardenability'. In addition to carbon, it was found that many of the alloying elements used to strengthen the steel also increased hardenability, as did an increase in the cooling rate. The high hardenability in the HAZ lead to cracking and poor toughness, but these issues could be mitigated during fabrication by heating the steel prior to welding to decrease the cooling rate, or by post-weld heating to achieve the same resulting decrease in cooling rate. Because of the variety of elements in addition to carbon that could influence the formation of martensite, a series of equations to calculate carbon equivalents have been developed.



The International Institute of Welding (IIW) was an early adopter of carbon equivalents to help explain how the hardness of a weld HAZ will vary with composition. The formula derived below has excellent agreement when the carbon is greater than 0.18%[22].

$$CE_{IIW} = C + \frac{Mn}{6} + \frac{(Ni + Cu)}{15} + \frac{(Cr + Mo + V)}{5}$$

Equation 2-1

The amounts of the elements listed are in weight percent. Carbon equivalents are important for many aspects of alloy design including the prediction of hardness. For a given composition, represented by the carbon equivalent, there is an increase of the HAZ hardness as the cooling rate increases. In welding, the cooling rate is often described as the time to cool from 800 °C to 500 °C (Δt_{8-5}) as this is the region where the Ar_3 and Ar_1 temperatures are commonly found. In all fusion welding processes, there is a region of the ferritic microstructure that will be heated into the upper austenite phase. The cooling rate, along with the composition, determines if that austenite transforms into ferrite/pearlite, acicular ferrite, bainite or martensite. The effect of increased cooling rate, and thus decreased Δt_{8-5} , is shown in Figure 2-2.

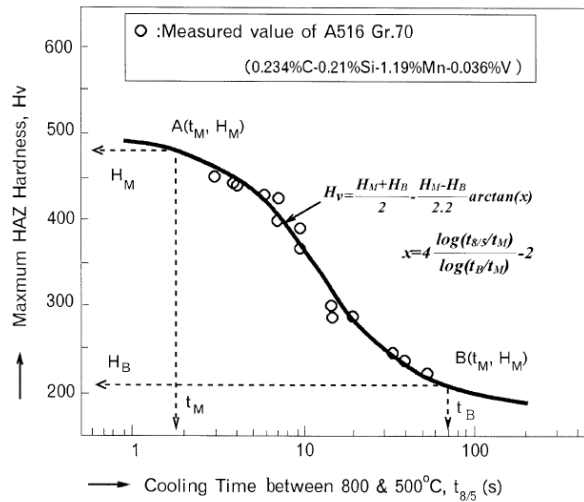


Figure 2-2 - The change in the HAZ hardness as a function of cooling rate, from [22].

There are compositional boundaries established for all carbon equivalent equations. Thus the CE_{IIW} , which works very well for carbon levels exceeding 0.18% and Δt_{8-5} times of 12 seconds or more, does not describe the formation of phases below the bounding limits. A number of equations have been calculated to describe lower carbon steels and the faster cooling rates that can be achieved with modern welding techniques. The Parameter crack measurement, P_{cm} , is frequently used to describe the hardenability of line pipe steels[22, 23].

$$P_{cm} = C + \frac{Si}{30} + \frac{(Mn + Cu + Cr)}{20} + \frac{Ni}{60} + \frac{Mo}{15} + \frac{V}{10} + 5B$$

Equation 2-2

Again the elements are described by weight %, however this relation is valid for carbon less than 0.22% and Δt_{8-5} times under 6 seconds. There are two further equivalents that have relevance to modern line pipe steel and are:

$$CE_{PLS} = C + \frac{Si}{25} + \frac{Mn}{20} + \frac{Cu}{16} + \frac{Ni}{60} + \frac{Cr}{20} + \frac{Mo}{40} + \frac{V}{15}$$

Equation 2-3



and

$$CE_{HSLA} = C + \frac{Mn}{16} + \frac{Ni}{50} + \frac{Cr}{23} + \frac{Mo}{7} + \frac{Nb}{5} + \frac{V}{9}$$

Equation 2-4

These equations represent relationships for the pipeline steel (CE_{PLS}) and high strength low alloy (CE_{HSLA}) equivalents respectively [22]. The primary difference between the CE_{IIV} and the more modern equivalents is the emphasis placed on carbon. Because the CE_{IIV} is derived from higher carbon steels, the effect of the alloying elements is more profound than small fluctuations in the carbon content. For the Pcm, CE_{PLS} and CE_{HSLA} , the effect of small variations in carbon has a much more profound effect. Yurioka *et al.* developed the CE_N equivalent to bridge the higher and lower carbon equivalents [24]:

$$CE_N = C + A(C) \cdot \left\{ \frac{Si}{24} + \frac{Mn}{C} + \frac{Cu}{15} + \frac{Ni}{20} + \frac{Cr + Mo + Nb + V}{5} + 5B \right\}$$
$$A(C) = 0.75 + 0.25 \cdot \tanh[20(C - 0.12)]$$

Equation 2-5

where all elements are in weight percent. The advantage of the CE_N calculation is that the effect of carbon concentration is accounted for. Thus the weldability of a greater range of steels can be evaluated using one formula.

2.1.2 The beginning of HSLA Steel

The steels used in modern line pipe applications belong to a family known as Ultra High Strength (UHS) which have evolved from the High Strength Low Alloy (HSLA) family of steel [13] in the last decade. However, the evolution of HSLA steels began in the early 1900's with the first additions of 0.12 % to 0.20% vanadium to mild steel which resulted



in a refined grain structure and improved strength [25]. This initial period of work resulted in empirical relationships relating the effects of additions of alloying elements to the strength and toughness of the resulting alloy. These alloy additions violated the definition for mild steel summarized in 1969 by Duckworth and Baird [26] as an iron and carbon alloy without further deliberate alloying with the exception of manganese for oxygen control and sulphur stabilization. However, the early alloy additions were of insufficient quantity to qualify the resulting steel as an 'alloy steel' as this category required derivation of properties from the primary alloying element added [27]. The improvement in strength and toughness was correctly attributed to refinement of the ferrite grains, but according to Woodhead [28], as empirical relationships only. The discovery in 1951 by Hall [29] that the lower yield point, σ_{LYP} , for a very low carbon steel was proportional to the grain size, d , by the relation:

$$\sigma_{LYP} = \sigma' \propto d^{-1/2}$$

Equation 2-6

where σ' is the yield stress for a single crystal was supplemented in 1953 by a similar discovery by Petch [30]. Petch found that the fracture stress of mild steel could also be related to the grain size and formulated the equation:

$$\sigma_{LYP} = \sigma_0 + k^* d^{-1/2}$$

Equation 2-7

where σ_0 and k^* are constants. Heslop, working with Petch, made another impressive contribution in 1958 [31] where the ductile to brittle transition temperature (DBTT), T_c , was related to the ferrite grain size via:

$$T_c = A - B \ln d^{-1/2}$$

Equation 2-8



where A and B are constants. These three discoveries formed the fundamental science that explained the empirical effects of improved strength and toughness as a function of refining ferrite grains from small alloy additions. Thus in the early 1960's the stage was set for an impressive growth in metallurgical knowledge and a systematic correlation of alloy contribution to mechanical performance via metallurgical control.

2.1.3 Alloy Design and development

With the stage set by pioneers like Hall and Petch, early HSLA adopters could begin

to systematically study the effects of alloy additions, often referred to as microalloying elements (MAE), on grain refinement and the resulting properties. Common characteristics of the MAE were that their interactions and additions were not designed to change the chemical composition of the iron matrix, but to interact with harmful tramp elements [32].

The characteristic features of MAE for HSLA steels are contents of 10^{-3} to 10^{-1} % that interact with tramp elements like C, N and S to precipitate second phase particles that strongly affect the structure. What was found to be interesting was that the dissolution of and re-precipitation of these particles could be controlled through processing parameters[33].

It was thus established that the MAE could control the structural parameters of grain size and shape, ferrite structure, dislocation density and

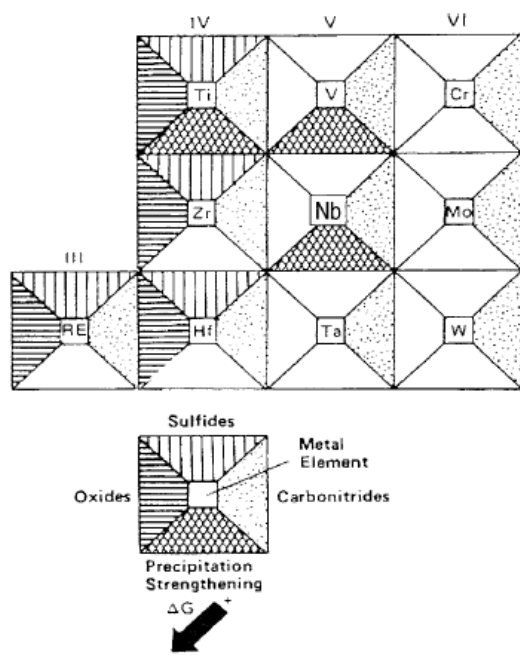


Figure 2-3– Tendency of MAE to form oxides, sulphides and nitrides along with precipitation strengthening potential. From [8] after [9].



texture to name a few. The precipitation strengthening potential of MAE and their tendency to form oxides, sulphides and nitrides is represented in Figure 2-3 as a function of their position in the periodic table. However, not all of the MAE listed in Figure 2-3 are effective as structure modifying agents. The critical factor was found to be solubility in austenite and the ability to re-precipitate during cooling and deformation [32]. Only three of the MAE form precipitates that are effective for dissolution or precipitation in the hot working range of steel. Niobium carbonitrides (Nb(C,N)), titanium nitride (TiN), and vanadium nitride (VN) are capable of both dissolving and precipitating during processing.

2.1.3.1 Niobium

Niobium has received a great amount of attention as a critically important MAE [34-46] for the formation of high strength steel. It was found that very small additions of niobium, often in the range of 0.01% to 0.05%, had a dramatic grain refining effect. The fine dispersion of the niobium carbonitride makes it an effective agent for grain refinement. At normal slab re-heating temperatures of 1250 °C, the austenite is capable of dissolving substantial amounts of niobium. When the slab is deformed in the lower austenite phase field, there is a strain induced precipitation of finely dispersed niobium carbonitrides [46]. The carbonitrides prevent recrystallization of the austenite grains through solute pinning drag at the grain boundaries. The retardation effect of strain precipitated carbonitride on the austenite recrystallization increases with decreased processing temperature as the thermal contribution to grain boundary motion is reduced. The consequence is an elongated, or pancaked, austenite grain which subsequently transforms to very fine ferrite. Once the ferrite transformation has occurred, niobium carbonitrides continue to increase hardness. The formation of semi-coherent carbonitrides precipitated in the ferrite act as precipitation hardening phases



which impede the motion of dislocations and serve to increase hardness with further deformation of the finish rolling passes and pipe forming process [35, 37, 46].

2.1.3.2 Titanium

Titanium is a versatile MAE addition to HSLA steels and can perform a variety of functions within the steel. The high affinity of titanium for nitrogen reduces the free nitrogen of the steel and consequently the susceptibility to ageing. Ageing is the term given to the diffusion of nitrogen to dislocations within the steel matrix, which reduces their mobility and causes discontinuous yielding [47]. The ability of titanium to reduce the ageing characteristic of the steel by binding the nitrogen is valuable in its own right, yet there are more advantages. Like niobium, there is a strain induced precipitation of titanium carbides which function much the same as niobium carbonitrides to refine the austenite during deformation. The amount of titanium required to raise the no-recrystallization temperature is significantly more than that for niobium, but it can achieve or surpass the effectiveness of niobium as the effect increases linearly with concentration much farther than that of niobium[32, 48]. The affinity of titanium for sulphur is also advantageous in the control of manganese sulphide stringers which are known to be detrimental to the steel properties.

2.1.3.3 Vanadium

The solubility of vanadium in austenite is significantly greater than either niobium or titanium, which leads to a reduced grain refining effect through precipitation and pancaking of the austenite at comparable temperatures and concentrations[32, 49]. As presented Figure 2-4, recrystallization can be stopped at 950 °C with 0.04% Nb, while 0.24% V is required to achieve the same result. The higher solubility of V in austenite can be advantageous given tight control of tramp elements as the vanadium remains in solution up to the ferrite transformation temperature where it precipitates as either

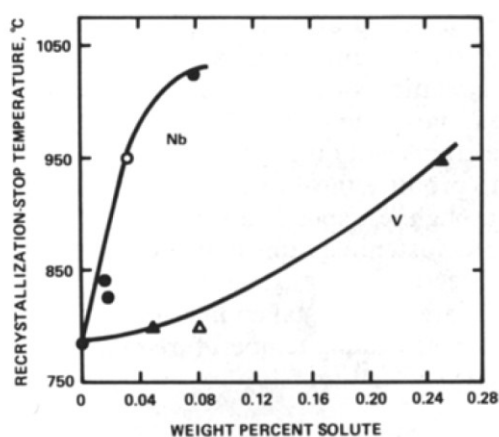


Figure 2-4- Effect of microalloy content on recrystallization stop temperature (T_R), from[3]

carbide or nitride depending on the steel composition, and hardens the ferrite by impeding dislocation motion. This then allows a reduced load to be placed on the rolls of a mill in the roughing stages with more hardening occurring during the finish passes.

2.1.4 Processing Parameters for HSLA

Many of the advances made in the alloying practices used in HSLA steels were developed to enhance various facets of deformation. The production of a steel plate some 20 mm thick, 3-4 m wide and 30 m long from a slab some 150 mm to 200 mm thick is no simple feat [50]. There are three distinct phases of deformation used in the processing of HSLA steels which together form a process known as thermomechanical controlled processing (TMCP). TMCP methods are under perpetual revision and the current practice is significantly changed from the state of the art 20 or 30 years ago. The three traditional stages will each be discussed, along with the changes effected in modern integrated steel mills.

2.1.4.1 Reheating

The solubility of various alloying elements in austenite is critical to the development of the steel. Clearly, strain induced precipitation of Nb(C,N) cannot occur unless those elements are in solution. The solubility is also a function of composition. At 1250 °C,



approximately 0.02% Nb is soluble in steel with a carbon content of 0.4 %. At the same temperature, the solubility of Nb increases to 0.07% if the carbon content is reduced to 0.1% [50]. The desire to maximize dissolution of the MAE must be balanced against the

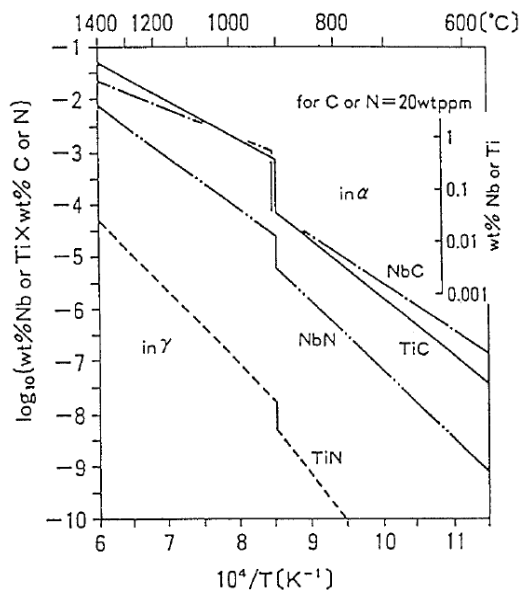


Figure 2-5– Solubilities of NbC, TiC and TiN in ferrite and austenite, from [6]

increase in austenite grain size that results once the precipitates that formerly pinned the boundaries have dissolved. As the entire effort of MAE addition is to control and reduce the austenite grain size, allowing massive grains to form during the reheat stage only increases the work required later to reduce them. The austenite can of course be stabilized by particles that show little to no solubility in austenite [51]. However these particles will usually decrease the toughness of the steel as they exhibit no coherency with the matrix [52]. The reduced solubility of titanium compared to niobium shown in Figure 2-5 means that less is taken into solution. The titanium nitride particles that remain undissolved in the austenite serve to pin the grain boundaries and retard the austenite growth. The effect of this pinning is illustrated in Figure 2-6 where the grain coarsening temperature is plotted as a function of MAE concentration for four different elements[5].

increase in austenite grain size that results once the precipitates that formerly pinned the boundaries have dissolved. As the entire effort of MAE addition is to control and reduce the austenite grain size, allowing massive grains to form during the reheat stage only increases the work required later to reduce them. The austenite can of course be stabilized by particles that show little to no solubility in austenite [51]. However these particles will usually decrease the toughness of the steel as they exhibit no coherency with the matrix [52]. The reduced solubility of titanium compared to niobium shown in Figure 2-5 means that less is taken into solution. The titanium nitride particles that remain undissolved in the austenite serve to pin the grain boundaries and retard the austenite growth. The effect of this pinning is illustrated in Figure 2-6 where the grain coarsening temperature is plotted as a function of MAE concentration for four different elements[5].

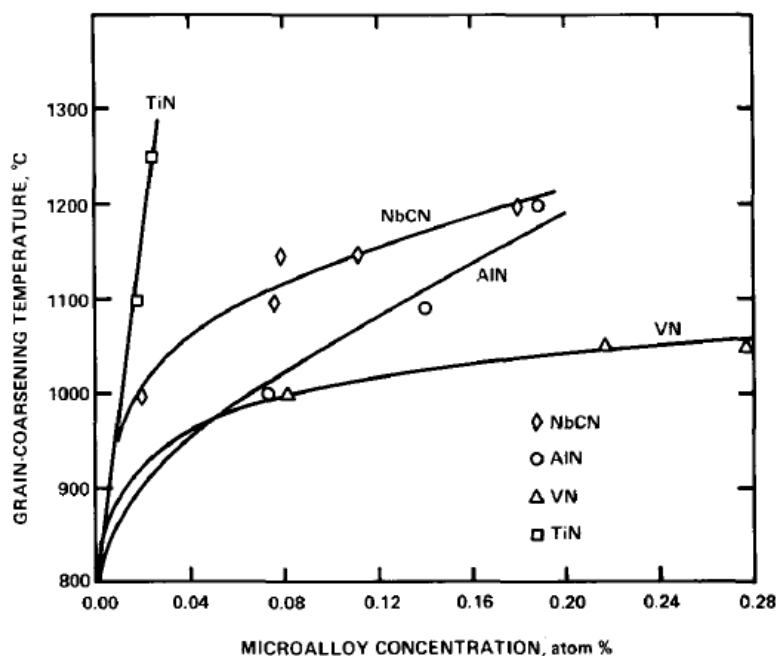


Figure 2-6— The grain coarsening temperature as a function of concentration for 4 different MAE, from [5]

2.1.4.2 Roughing

The initial stage of rolling conducted in the austenite field is termed roughing. The goal of deforming austenite with strain-precipitating elements is to retain the strain and increase the aspect ratio of the austenite grains. The roughing stage must strike a balance between the amount of deformation and the amount of recrystallization. If the recrystallization stop temperature, T_R , is too high, significant precipitation during the early passes of the roughing can increase strain within the austenite grains beyond the capacity of the rolling mill. At the same time, the accumulation of sufficient strain to increase the aspect ratio of the austenite and yield a pancaked structure with high strain energy must be observed. The reduction of the austenite is critical as the austenite thickness is what controls the final ferrite grain size[3]. The goal of the roughing is to reduce the slab sufficiently above the T_R so that there is sufficient MAE left in solution during the final roughing passes below the T_R to pin the austenite substructure and



increase the austenite aspect ratio [53]. Care must be taken to prevent dynamic coarsening of the precipitates as the most effective particles are <6nm [46].

2.1.4.3 Finishing

The final deformation passes of the plate production are typically carried out near the Ar_3 temperature to increase the density of fine precipitates in the austenite substructure as much as possible. The limits of the strength increase by ferrite size reduction alone are reached for a ferrite size of approximately $3\mu\text{m}$ with a corresponding yield strength of ~ 450 MPa [50]. Further strengthening is possible if the precipitation of phases like vanadium carbonitride in the ferrite matrix along with a small amount of 'warm' deformation below the Ar_3 temperature is employed to strain harden the steel. The microstructure is most usually ferrite and pearlite. Pickering found that the strength of the steel could be increased without adjusting the carbon content by increasing the transformation temperature [54]. He found that as the cooling rate increased, the microstructure changed from ferrite/pearlite to acicular ferrite, upper bainite, lower bainite and martensite in that order. The strength of the steel increased correspondingly with the proportion of lower temperature transformation products (bainite, martensite). The first HSLA steels with an acicular ferrite microstructure were produced in the mid 1970's [55-57]. A composition of an early acicular ferrite steel produced at the Steel Company of Canada is given by Krishnadev as 0.05 % C, 1.93 % Mn, 0.26 % Ni, 0.43 % Mo and 0.065 % Nb[56]. While this composition was capable of producing good strength and improved low temperature toughness, the weldability of the steel was reduced by the Mn and Mo content. The desire for higher strength while limiting the alloy content to maintain toughness and weldability required use of accelerated cooling. The accelerated cooling is achieved most often by direct water spray and is a key component in manufacturing modern high strength line pipe steel.



2.1.5 Modern Line Pipe Steel

2.1.5.1 Processing

The current era of high strength line pipe steel began with the coupling of controlled rolling with accelerated cooling (ACC) to produce steel with yield strengths in excess of the 450 MPa achievable by ferrite grain size reduction alone. The discoveries of the 1950s, 1960s, 1970s and the early 1980s could now be combined and integrated into the metallurgy of a steel melt and the metallurgical manipulation of a rolling mill. The advances in precipitate hardening by microalloying could now be used to predict accurately the T_R (recrystallization stop temperature) for steels with mixtures of microalloying elements. It was now understood that rolling below the T_R would increase the austenite aspect ratio, while precipitating new second phase particles to pin the substructure, and that the high retained strain energy, in conjunction with the highly dislocated austenite grains, caused ferrite refining. The additional strengthening achieved by warm rolling below the A_{r3} was being used to strain harden ferrite and increase the yield strength of the plate. The effect of accelerated cooling to modify the microstructure by suppressing the A_{r3} was also understood, and two methods, direct quench and tempering, and accelerated cooling, were implemented to achieve this result.

2.1.5.1.1 Direct Quench and Temper

In the direct quenching and tempering of steel plate, the temperature of the plate is reduced to ambient as quickly as possible. This can be achieved by quenching in oil, but water is more often employed for ease of use [58]. The development of martensite in the microstructure increases the yield strength to maximum levels. However, the toughness of a martensitic structure is limited as the lattice is already at, or near, maximum strain. Therefore a second stage of processing is used to re-heat the plate and



allow carbides to precipitate within the martensite, releasing some lattice strain while maintaining good yield strength from the fine microstructure. Quenching and tempering has advantages in that it is a robust method that could be added to most steel mills without a complete overhaul. The downside is that the cooling process is divided into two steps, each taking time and thus reducing productivity.

2.1.5.1.2 Accelerated Cooling

Accelerated cooling requires more sophisticated online control than direct quench and temper. The steel is cooled with direct water spray in the ferrite transformation range (between A_{r3} and A_{r1}), then air cooled to allow self tempering. This has the advantage of a one-step cooling process that increases productivity. Additionally, there is a greater degree of control afforded to the mill operators in the ability to select and achieve microstructures by manipulating cooling rates to different levels [59]. A selection of different TMCP schedules is shown in Figure 2-7.

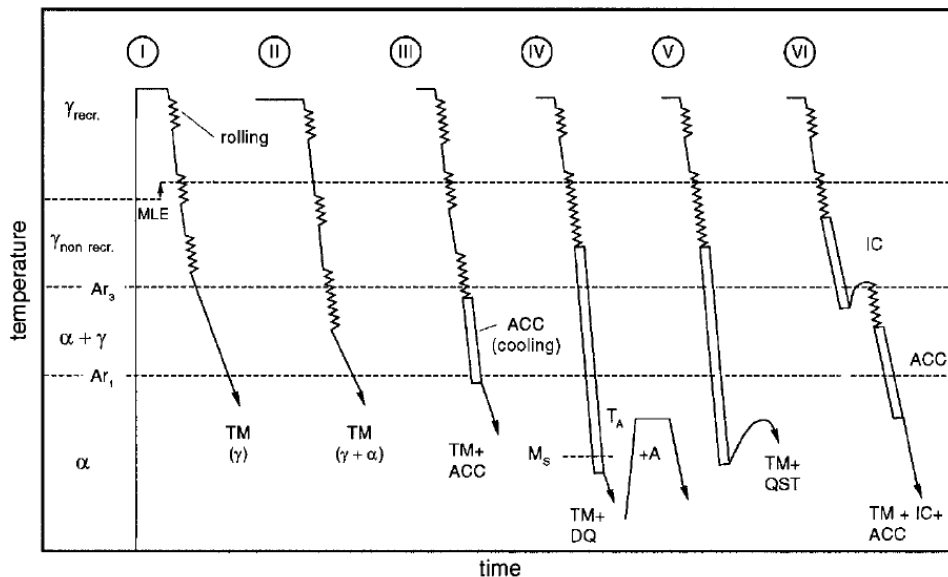


Figure 2-7– Various TMCP schedules. Recr.: Recrystallized, MLE: Maximum likelihood estimation, TM: thermomechanical treatment, ACC: Accelerated cooling, DQ: Direct Quench, QST: quench and self temper, IC: intermediate cooling, from [60]

A major obstacle encountered in the application of ACC is plate thickness. An underlying principle for steel design is the accurate prediction of properties. While this does not necessarily require a homogeneous microstructure, the evolved microstructure should be uniform throughout the product. Accelerated cooling must be achieved by a thermal gradient on the surface. This gradient limits the capacity to cool the entire thickness of the plate at a uniform rate and results in microstructural inhomogeneity from the surface to the center. For this reason, the ACC has proven to be most effective on thinner plate (15 mm to 20 mm) while direct quench and temper remains the processing route of choice for high strength thick plate[59, 61-63].



2.1.5.2 Steel grades

Line pipe steel is frequently referred to and classified by yield strength more than any other property [64]. The yield strength is usually referenced in thousands of pounds per square inch (KSi), giving rise to classifications of X65, X70, X80, X90, X100, and X120. The nominal yield strength for these steels expressed in SI units is 450, 480, 550, 620, 690, 830 MPa. As the literature frequently refers to line pipe steel by the X designation, that format will be used here as well [65-73].

2.1.5.2.1 X80

The X80 line pipe steels with minimum specified mean yield stress (SMYS) of 550 MPa (X80) were the first produced by TMCP with ACC specifically to achieve a bainitic microstructure [59]. As shown in Figure 2-8, the progress since the 1970's in line pipe has produced increased yield strength, increased low temperature toughness and increased weldability through reduced carbon equivalents. The microstructure designed for X80 is ferrite and bainite or granular bainite [71, 74]. This combination gives the required resistance to fracture at the specified yield strength.

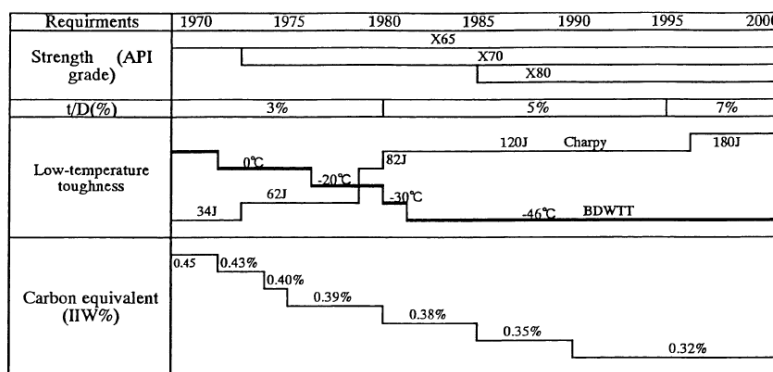


Figure 2-8 – Historical changes in the requirements of line pipe steel with time, from [59]



2.1.5.2.2 X100

Interest in X100 grades of steel started in the 1990s for long distance applications through hostile terrain where frost heaving, seismic loading and cold operation are a reality [66]. The increased strength required to cope with these challenges moved interest away from the X80. The X100 microstructure is designed to be very strong, and the increased strength comes as a function of the TMCP processing. There are multiple processing routes to achieve the strength needed for X100 steel, as shown in Figure 2-9, that allow variations between the carbon content, carbon equivalent, the cooling rate and the cooling stop temperature.

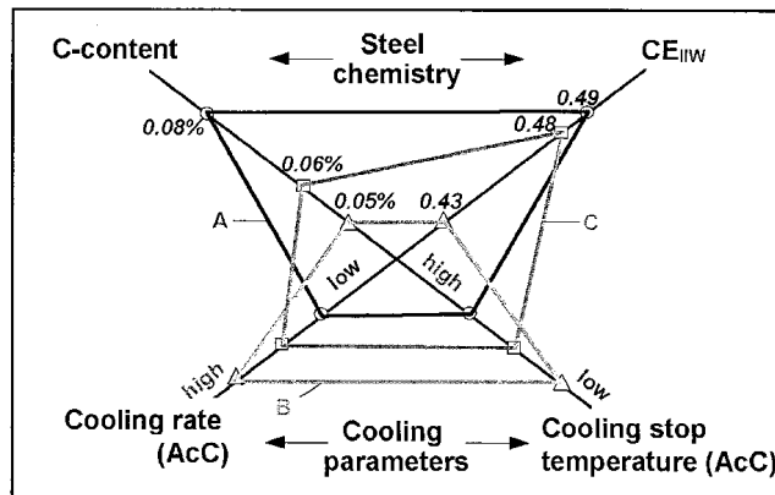


Figure 2-9 – Processing parameter window for X100 Steel, from [74]

One of the modifications to the TMCP process required to achieve X80 and X100 grades of steel is the addition of a cooling stop temperature [74]. This stage was found to be necessary to limit the formation of martensite and martensite-austenite phases. Overcooling the steel deteriorates the toughness as the proportion of hard phases increases. The inability to increase alloy content to favor the formation of lower temperature transformation products has forced research into grain refinement with



Nb, Ti, Al, Mg, B, V with aggressive TMCP. The P_{cm} is targeted to remain below 0.20 in X100 steel [75]. This is a restricting alloying limit and some approaches to increase strength by TMCP have used titanium oxide (Ti_2O_3) particles to help in nucleating fine ferrite intragranularly during the austenite transformation. In Figure 2-9 the relationship between the effect of increasing strength by alloy additions and increasing the carbon can be compared to the increase in aggressive TMCP processing [76]. An increase in one necessarily leads to a decrease in the other to maintain the properties of the steel [77-84]. The variations in chemistry between X80, X100 and even X120 can be quite minor [77], and yet there is a difference in yield strength that can be up to 280 MPa. Different yield strengths can in fact be achieved with the exact same composition [60]. The difference between the grades is that increased cooling rates are used to favor shear dominated transformation products including lath martensite [85]. There are very specific alloying compositions that have been developed by individual mills, but much of the current data has not been published for proprietary reasons. Generalized X100 grades will give values of 0.06 % C, 1.9 % Mn, 0.04 % Nb, 0.02 % Ti, 0.004 % N, and sufficient V, Cu, Ni, Mo and Si to achieve a P_{cm} of 0.20 and a CE_{IIW} of 0.47-0.49 without giving specifics [23, 74, 81, 83, 86].

2.1.5.3 Toughness

The ability of high strength steel to avoid and arrest crack propagation is a critical design parameter in the event that the integrity of the pipeline is compromised, be it by corrosion, impact, or explosive rupture. The move to higher strength line pipe steel stems from the harsh climates that the pipelines will need to traverse to reach production fields. Many of the predicted harsh climates are in arctic or sub-arctic locations where the cold operating temperatures can lead to brittle failure. Nevertheless, the toughness requirements are not constrained solely by concerns of brittle fracture as unstable ductile failure can be just as catastrophic. The ability of steel



to arrest brittle fracture can be measured by the drop weight tear test (DWTT) developed by Battelle [75, 81, 87-89]. The empirical results derived from this test can be correlated to the ability of the steel to arrest brittle fracture by measuring the percentage shear of the fractured surface.

In the failure of a gas transmission pipeline, the initial crack allows decompression of the gas. The decompression wave caused by the escaping gas propagates down the pipe and is chased by the crack [87]. Because the crack chases the decompression wave, a fast crack produces high pressure at the crack front, while a slow crack produces low pressure at the crack front. The interaction between the crack speed and the pressure developed at the crack front with the resistance of the steel determines the extent to which the crack will propagate. The DWTT is conducted at the design temperature and the percentage shear in the fracture surface is measured. If there is more than 85% shear area the test usually indicates that the brittle crack will be arrested because the rate of fracture, 300-400 m/sec, is less than the decompression rate [76, 87, 90, 91]. The harsh climates predicted for high strength line pipe applications has forced a reduction in the DWTT testing temperature to frigid extremes of -60 °C or even -80 °C.

Toughness data can be generated through tests other than the DWTT. The Charpy impact test or Charpy V notch (CVN) test uses a 10 mm x 10 mm x 55 mm specimen bar with a 2 mm notch. The bar is cooled to the desired temperature and fracture initiated by a pendulum of fixed potential energy (gravity). The difference in the potential energy on the swing-through is what was absorbed by the specimen during failure[92]. The Battelle equation correlates the amount of absorbed energy for a 2/3 Charpy specimen to the hoop stress and geometry for fracture arrest as:

$$Cv_{2/3} = 2.382 \times 10^{-5} \sigma_H^2 (Rt)^{1/3}$$

Equation 2-9



where $C_{V2/3}$ is a 2/3 sized Charpy impact specimen energy (J), σ_H is the hoop stress (MPa), R is the pipe radius (mm) and t is the wall thickness (mm)[91]. The strong dependence of impact energy on hoop stress indicates that the toughness must increase with increased strength[91]. The fatigue notch crack tip opening displacement (CTOD), or J integral, can give excellent data during the failure as it progresses much more slowly than the rapid Charpy and DWTT. In the CTOD test a specimen with a notch is fatigue pre-cracked and then set into a three point bending jig. The specimen is then loaded and the displacement as a function of load is recorded. Even if brittle failure occurs, there is the possibility of the crack arresting and the test continuing [93]. The use of full scale burst testing is a dramatic test where catastrophic failure of a pipeline loaded to design pressure and temperature is initiated by explosive charge detonated within the pipe. Usually in the test setup, the various properties of the pipe sections to be burst will be assessed and those indicating higher toughness will be added to either end of the initiating pipe in order of increasing toughness. In this way the self arrest of the crack has a much better probability of occurring [90, 91, 94]. The instrumentation in the pipe allows measurement of decompression rate, and both the speed and the arrest of the crack can be calculated and correlated to the mechanical properties.

2.1.5.4 Pipe Manufacture

One method of forming ultra high strength steels pipes from TMCP processed plates is the UOE process as shown in Figure 2-10. In the UOE forming, steel plates are formed into a U-shape, followed by an O-shape and subsequently joined with submerged metal arc welds (SMAW) before being hydrostatically expanded to final dimensions [68]. A major portion of the pipe strength is derived from the microstructure created during the TMCP processing, and this is enhanced further by strain hardening during UOE forming. A single steel chemistry can be used for either X80 or X100 with only minor element additions [68, 95]. This makes the consistent production of uniform pipe challenging for



mills, as there is a very real danger of over strengthening the pipe beyond specification. From a mill and forming perspective, the higher strength of the steel impacts the

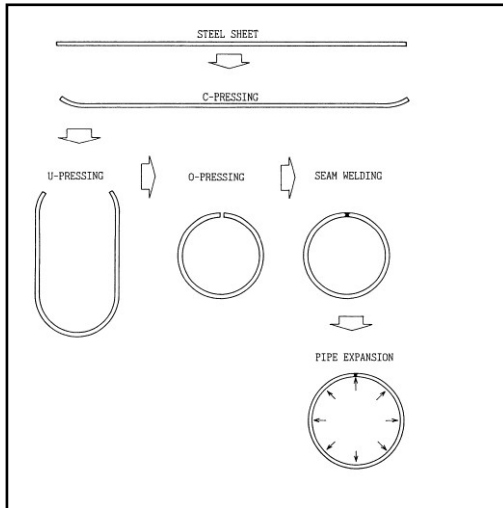


Figure 2-10 - Schematic representation of the UOE pipe forming process [2]

strength of the forming press. The nature of the steel itself, with a high propensity for spring back, causes challenges that need to be solved carefully and with an eye on the ultimate properties of the pipe [68].

The other, less common, production route for UHS pipe is spiral welding. In this process the plate is twisted into a tube and a continuous SMAW seam is applied. There is slightly more waste in this process as the irregular ends of the pipe must be trimmed square and to length. On the other hand, the same plate dimensions can be formed into a much wider selection of pipe diameters due to the flexibility of the forming process[96]. The location of the seam weld at 40 to 50 degrees to the pipe axis offers benefits in strain based engineering with a reduction of exposure to the full transverse pipe stress [97].

2.2 Welding

2.2.1 Fusion welding

Fusion welding is the most common method used to join steel because it produces joints with the best combination of properties. Fusion welding on the most basic scale involves a heat source producing a molten metal pool within the joint which solidifies and forms a continuous metallic bridge[7]. The differences in the heat sources, (flame, arc, laser etc) and nature of the metal melted to form the pool (solid wire, metal cored,



shielded), along with the method of atmospheric shielding (gas, flux) comprise the various systems of welding. Most high productivity welding techniques use an electric current to strike an arc between the base metal and an electrode. Aside from Gas Tungsten Arc Welding (GTAW) where the electrode is tungsten, the electrode used to strike the arc melts and, with some melted base metal, forms the weld metal. This type of welding is Gas Metal Arc Welding (GMAW) and the gas is a shielding mixture designed to protect the molten weld pool, Figure 2-11. There are many variants of GMAW which will be discussed in later sections. In line pipe steel there are two fusion welds, the seam weld that is used to join the edges of the plate together to form the pipe and the girth weld that joins the sections of pipe together. The technology, application and science applicable to girth welds will be reviewed.

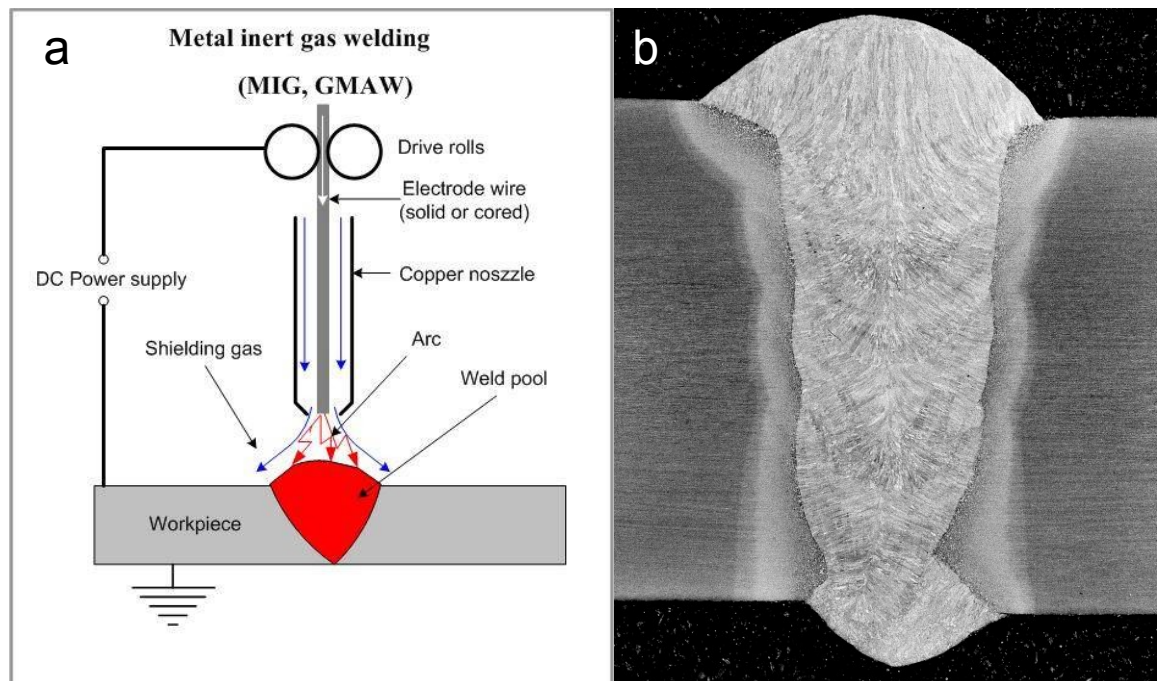


Figure 2-11 - a) GMAW weld schematic [98] and b) cross-sectional image of an X100 Dual torch GMAW weld



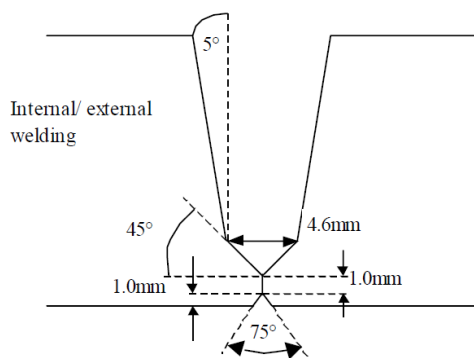
2.2.1.1 Gas Metal Arc Welding (GMAW)

The GMAW setup shown in Figure 2-11 employs an electrode fed through the welding gun towards the workpiece. The gun and the workpiece are connected electrically to a power supply which in modern workshops is a highly sophisticated device with complex electronic controls. The most basic function of the power source is to convert high voltage, low current power supplied in most electrical mains in to a low voltage high current output. Contact between the work-piece and the tip of the electrode creates a short and completes the electrical circuit. Withdrawing the electrode from the surface breaks the physical contact, but the electrical circuit is maintained by a stream of electrons passing from one to the other via though the gas in the gap between the two. The ionization of the gas in the gap by the electrons is what allows the circuit to function, and what forms the visible arc. In the most basic of GMAW designs, a constant voltage is maintained in the circuit. The electrode wire is characteristically less than 1.6mm in diameter, and is fed though the gun by a set of mechanized wheels. The wire exposed to the high current density of the arc melts, thus lengthening the arc, which increases the resistance of the circuit and the inversely the amperage. The feed wheels of the wire are controlled in this scenario so that the decreasing amperage draw increases the feed rate to self-adjust the arc length and return the system to a steady state. While self-adjustment facilitates manual welding, it is hugely beneficial to mechanization [7, 99, 100]. Ferrous GMAW is almost always achieved with a DC power supply with the consumable electrode wire as the positive pole. The gas used to form the arc can vary in composition, but is always supplied from the nozzle of the welding gun. The shielding gas is designed to protect the weld from atmospheric contamination (O_2 , N_2) and various combinations of inert (Ar) and active (CO_2) gasses are used to maintain the stability of the arc. Mechanized gas metal arc has been used for pipeline welding for almost 40 years[4].



Variations in voltage and current applied between the electrode and the work-piece change the metal transfer characteristics [101-104]. There are three primary variants for metal transfer in GMAW, short circuit, globular and spray. Short circuit transfer occurs under low voltage conditions where the wire is fed faster than it can melt. The short circuit formed causes a spike in the current, which heats the wire through resistance heating and causes fusion. Surface tension in the melt pool draws the liquid section of the wire away from the remaining solid, the arc is re-established and the cycle restarted. Short circuit transfer, while subject to splatter from cyclical amperage spikes, allows welding in all positions. Globular transfer occurs at moderate to low amperage and high voltage. The electrode wire melts, forming a drop that detaches under gravitational forces. The droplets are controlled only by the surface tension and gravitational forces and constitute a random size distribution. As gravity is the detaching force, globular transfer can only be achieved in the flat position. An increase in the current will cause the globular transfer to transition to that of spray transfer. The increased current causes the electromagnetic forces generated in the arc to pull droplets off of the electrode wire before the droplet diameter exceeds that of the wire. There are two spray transfer modes, projected and streaming with streaming occurring at the upper amperage range. The higher electromagnetic forces generated by the increased power detach smaller droplets from the electrode and results in an electrode with a tapered end [102]. The high power required to detach droplets in spray transfer creates a large weld pool from the high wire feed rate. This limits the positional application as the gravitational forces causes the weld pool to flow out of the joint before solidification can occur.

The joint geometry used for girth welding of high strength line pipe is a narrow gap. An example of this is given in Figure 2-12. This geometry has been developed to allow good penetration of the base metal on both sides of the joint by a single electrode[105].



Additionally, the thermal gradient in the resulting weld pool is very steep as both edges of the liquid are in contact with the base metal.

Figure 2-12- Narrow gap P-GMAW girth weld joint geometry, from [4]

2.2.1.2 Pulsed Gas Metal Arc Welding (P-GMAW)

A solution to the positional limitation of spray transfer is to limit the absolute current delivered by the power supply by pulsing a peak current over a background current as shown in Figure 2-13 [106-109].

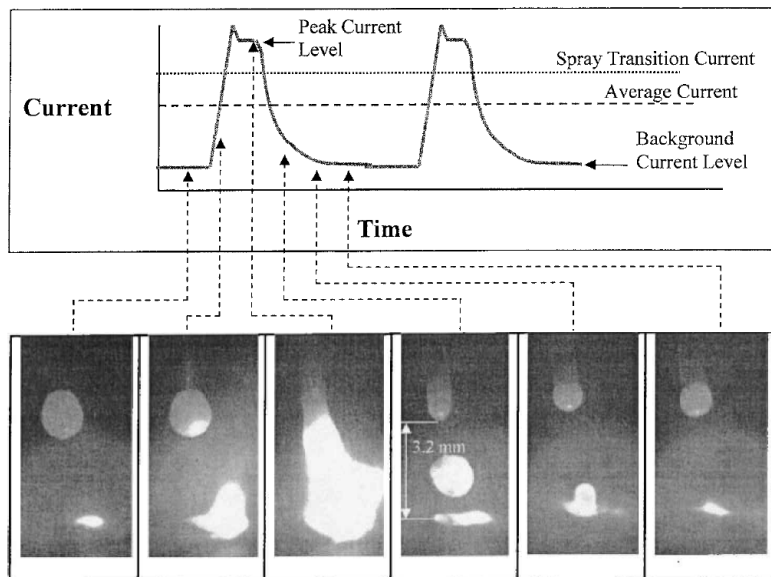


Figure 2-13 – Schematic of P-GMAW waveform with corresponding droplet, from [107]



The ability to control and produce pulses of differing amplitude and waveform at variable rise and fall rates through transistor electronics made the application of P-GMAW much more relevant. A mean current of 100 A can be achieved by pulsing 370 A over a base current of 64 A with a peak time of 5.5 ms at 25 Hz, or by pulsing 440 A over a base current of 35 A with 3.5 ms peaks at 100Hz[110]. The number of dependent variables that must all be adjusted to maintain stable welding parameters that P-GMAW systems be electronically controlled. In this way operator manipulation of one variable is accounted for in the parameters of the entire system. The short high current pulse provides the electromagnetic force to spray the droplet while maintaining a lower average current and power, and consequently a reduced heat input [111]. This reduced power permits P-GMAW to be used in more positions [110]. The heat input to the workpiece (H) from P-GMAW can be expressed as

$$H = \frac{VI}{S}\eta$$

Equation 2-10

where V is voltage, I is current , S is weld speed and η is the arc efficiency factor [111].

2.2.1.3 Tandem

In GMAW welding, the desire for higher productivity has spurred research to develop methods of depositing more weld metal in less time. This can be accomplished by modifying the welding heads so that two wires are fed simultaneously in to the same weld pool as depicted in Figure 2-14.

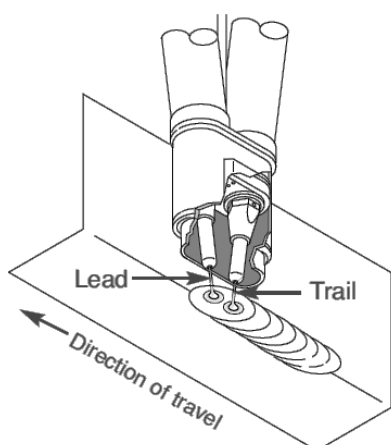


Figure 2-14 Tandem torch schematic, from [1]

The contact tips are electrically insulated from each other and current is switched between the two. Much faster travel speeds can be achieved with tandem welding while maintaining acceptable heat inputs[112]. The weld pool is fed by two wires which increase the total current, but the weld pool is elongated and the travel speed increased. The result is longer contact with the sidewall for improved defect prevention with minimal increases to the heat input [113]. Yapp and Blackman show that the thermal profile for a thermocouple plunged in a tandem weld pool is identical to that of a single wire

GMAW system [4]. The tandem technology is currently being used by TransCanada PipeLines Limited for girth welding X100 line pipe [66, 93, 112, 114, 115].

2.2.1.4 Dual Torch

The term dual torch is relatively new to GMAW welding and data on the results is limited [4, 115, 116]. The dual torch welding system consists of two independent welding heads mounted on the same carriage and spaced 50 – 100 mm apart. The goal of dual torch is improved productivity by filling more of the weld gap per pass. To this end, a dual tandem torch configuration has been developed by Cranfield University as the Cranfield Automated Pipewelding System (CAPS)[4].



2.2.2 Weld Metal

The molten metal used to form a metallic bridge and fuse two components together constitutes the weld metal of a weldment. In most cases metal must be added to a joint to fill it up during the welding process. The composition of the weld metal is derived from the filler metal, the amount of the base metal of the components being joined that is melted into the weld pool and the high temperature chemical reactions occurring in, and between, the molten metal and atmospheric gases. The goal of any welding procedure is to create a joint with sound mechanical properties. The primary variables that affect the transformation behavior, and resulting mechanical properties of weld metal, are the total alloy content, the solidification microstructure, prior austenite grain size, weld thermal cycle and the concentration and variety of non-metallic inclusions[117]. The transformations that occur in the weld metal are fundamentally the same as those that occur during rolling and forming of steel but with significant differences stemming from the highly dynamic nature of welding. The solidification of the liquid phase results in segregation of alloying elements to the interdendritic regions and can result in a chemical inhomogeneity that further influences the transformation kinetics. The high concentration of secondary oxide particles in the weld metal increased the number of ferrite nucleation sites compared to steels, both as heterogeneous sites and by refining the austenite grain size. The combination of these factors causes weld metal to behave in a significantly different manner from steel [118, 119].

2.2.2.1 Alloying Strategies for High Strength Line Pipe Weld Metal

The selection of alloying elements for weld metal must be judicious to maintain weld properties over the greatest possible variation of operational parameters. The division of elements can be categorized based on various roles with some elements added to strengthen the ferrite matrix through interstitial or substitutional strengthening and others added for their tendencies to react with other elements in the alloy. Interstitial



alloying elements are usually C, N and B due to their size while Mn, Si, Ni, Cu, Mo, Cr, Al, V, Ti, Nb can substitute for Fe in the lattice. Many alloying elements perform multiple roles and can form carbide, nitride, oxide or sulphide non-metallic particles depending on thermodynamic and kinetic considerations. The primary particle formers are Mo, Cr, V, Ti, Nb, Al, Mn, Si, Mg and Zr. In general the elements Mn, Si, Ni, Mo and Cr are added in larger quantities where the amounts are measured in whole weight percents while B, Al, V, Ti and Nb are added in fractional amounts that are often expressed in parts per million[120-123].

In addition to forming non-metallic inclusions, the presence of different elements in the iron matrix can stabilize either the austenite or ferrite phase. The austenite stabilizers are C, Ni, Mn, N, Co and Cu to a minor degree. The common ferrite stabilizers are Cr, Al, Mo, Si, Nb, T, and V. Different alloying strategies have been developed to balance the stabilization or promotion of phases with strength for different processes and cooling rates [123].

In pipeline applications, it is desirable to form weld metal that is stronger than the steel of the pipeline. The longitudinal forces generated by thermal expansion and contraction combined with geological loading from frost heave and thaw strain the pipeline. If the weld metal has higher yield strength than the line pipe steel, any strain imposed on the pipeline will be accommodated by the weaker line pipe which constitutes the vast majority of the pipeline, rather than becoming concentrated in the relatively small regions of weld metal [114, 124]. The high strength of the line pipe has made the creation of weld metals that are both sufficiently strong and tough challenging. Nakano *et al.* tested a solid GMAW wire for grade 690 girth welding with the composition of 0.06% C – 0.5% % Si – 1.4 % Mn – 2.7 % Ni – 0.2 % Cr – 0.5 % Mo and found that it produced a weld with good strength and reasonable toughness [125]. Over a range of heat inputs from 0.5kJmm^{-1} to 2kJmm^{-2} , the strength decreased while the



CVN toughness increased. Gianetto *et al.* conducted a series of strength and toughness evaluations on X100 weld metal with compositions of 0.075 – 0.082 % C, 1.6 % Mn, 0.78 – 0.82 % Ni, 0.03 % Cr, 0.28 % Mo, 0.008 % Nb, 0.004 % V and 0.037% Ti [93]. The low heat input used with these chemistries again produced acceptable strength and toughness. For GMAW processes, the alloy composition of the welding wire is slightly higher in carbon than the base metal, and the overall there is more alloy with typical $CE_{I\!W}$ values of 0.35 – 0.55 and P_{cm} values of 0.18 to 0.29 which are higher than the P_{cm} of 0.2 for ultra high strength steel [4, 76, 90, 101, 114-116]. Many of the chemistries under development for X100 line pipe steel have been based on the work produced by Mark Hudson in his PhD thesis at Cranfield University [69].

2.2.3 Solidification in P-GMAW girth welds

When the heat source that forms a molten weld pool is removed there is a thermal gradient from the center of the pool to the base metal. The liquid metal at the fusion boundary is in intimate contact with the solid steel of the base metal from which delta ferrite grows epitaxially along the thermal gradient to form a columnar structure. There are different solidification structures that can form depending on the solute concentration of the weld metal and the rate of solidification. The rate of solidification is normally expressed as the thermal gradient (G) divided by the velocity of the solidification front (R). As seen in Figure 2-15, the different combinations of solute and G/R can achieve planar, cellular, cellular dendritic or columnar dendritic microstructures.

The solidification of weld metal is highly dynamic as both the thermal gradient and the solute concentration vary. Because the thermal gradient is created by a moving heat source, as the arc travels away, the thermal gradient decreases. At the same time there is a rejection of solute from the solidifying delta ferrite into the remaining liquid. Thus the microstructure of a weld at the fusion boundary can be entirely different from that at the center of the weld [7, 99, 100, 123, 126]. This effect is minimized in P-GMAW girth

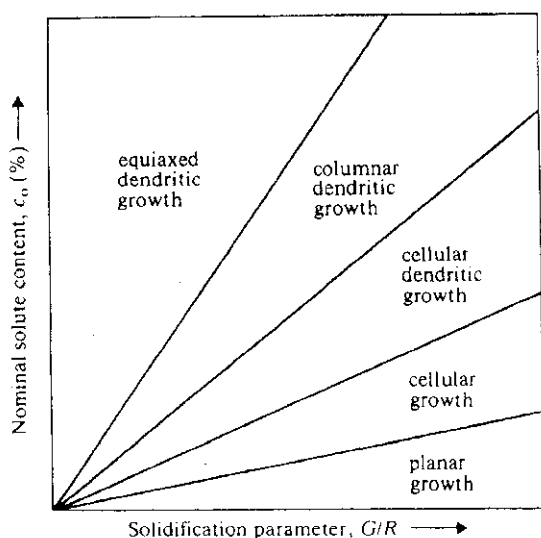


Figure 2-15 – The effect of solute and G/R on solidification, from [7]

welds by the low energy input and the narrow groove design which gives a short distance for solidification with a high thermal gradient. The transition from a columnar to an equiaxed morphology that is common in higher energy welding [127, 128] is less pronounced in mechanized line pipe P-GMAW girth welding [93].

2.2.3.1 Weld Transformations

The delta ferrite solidified out of the liquid weld metal forms with a BCC structure which transforms to FCC austenite upon cooling. The austenite phase is not the stable at room temperature and the austenite transforms to alpha ferrite upon cooling below the Ar_3 temperature. In Table 2-1 the terminology developed by the International Institute for Welding is compared to that of the Japanese Welding Society (JWS). The JWS terminology was developed in an attempt to unify terminology that developed separately for steel and weld metal.



Table 2-1 – Comparison between the International Institute of Welding and the Japan Welding Society microstructure terminology, after [129] with modification.

JWS System	IIW System
Ferrite	Primary Ferrite
-Grain boundary ferrite	-Grain boundary ferrite
-Intragranular polygonal ferrite	-Intragranular polygonal ferrite
-Ferrite side plate	
Pearlite	Ferrite Carbide Aggregate
-Pearlite	-Pearlite
Acicular ferrite	Acicular ferrite
-Acicular Ferrite	-Acicular ferrite
Bainite	Ferrite with Second Phase
-Upper bainite	-Ferrite with aligned second
-Lower bainite	phase
	-Ferrite with non-aligned
	second phase
Martensite	Martensite
-Lath martensite	-Lath marteniste
-M-A constituent	-Twin martensite

There are many different terminologies of steel microstructure and different attempts have been made towards a singular unified system. Unification to date has not been achieved [117, 129-132].



2.2.3.1.1 Transformations from Austenite

The first phase to transform from austenite is allotriomorphic ferrite which can nucleate either at the austenite grain boundary or intragranularly within the austenite grain. The formation of allotriomorphic ferrite is favored at high temperatures, $\sim 700\text{ }^\circ\text{C}$, and slow cooling rates and the ferrite growth follows parabolic rate kinetics with a planar incoherent front [133]. This blocky or polygonal ferrite can form ferrite veins that delineate the austenite boundaries. As the temperature decreases, the diffusion rate of carbon becomes insufficient to maintain the planar growth front into the austenite. Continued ferrite growth into the austenite occurs laterally by ledges along low energy interfaces between the ferrite and the austenite. This leads to a Kurdjumov-Sachs relationship between the ferrite and the austenite with $(110)_\alpha$ parallel to $(111)_\gamma$ and $[111]_\alpha$ parallel to $[011]_\gamma$. Ferrite with this orientation relationship is referred to as Widmanstätten ferrite, or ferrite side plate. The reduced diffusion distance required for carbon in the advancing ferrite front increases the transformation speed. The carbon rejected to the austenite between the plates may be retained to room temperature, or may transform to cementite, pearlite or martensite in small amounts termed microphases. This transition is illustrated in Figure 2-16.

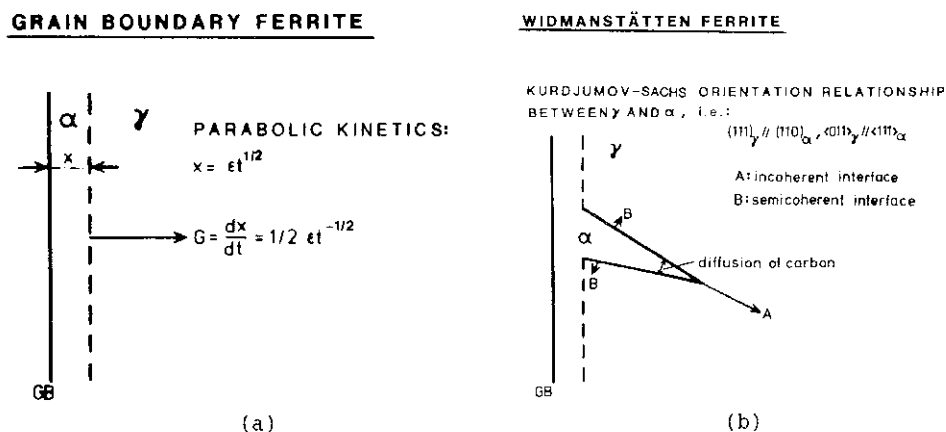


Figure 2-16 – Growth of ferrite. (a) grain boundary (b) Widmanstätten, from [117]



At higher undercooling the nucleation of ferrite on non-metallic inclusions becomes energetically favorable. Due to the high driving force from increased undercooling, idiomorphic acicular ferrite nucleates heterogeneously on non-metallic inclusions and grows as randomly oriented plates into the austenite. Growth is continuous until hard impingement occurs. The random orientation and nucleation from many sources with fast growth gives acicular ferrite plates an aspect ratio between 3:1 and 10:1 and overall chaotic and interwoven appearance. Acicular ferrite is known to nucleate preferentially on titanium oxide inclusions, but not exclusively [134-136]. Yamada *et al.* found that acicular ferrite can nucleate on a variety of different inclusions such as $MnAl_2O_4$, but that in TEM analysis, there was a layer of titanium oxide present between the mixed manganese oxide and the ferrite [137]. Acicular ferrite can also form sympathetically at the austenite interface of acicular ferrite heterogeneously nucleated and by this mechanism there need not be a 1:1 ratio of inclusions to nucleation events [138, 139].

When the austenite has been undercooled to the point that diffusion is no longer possible, bainite can form at the austenite boundaries. Bainite is formed of sub-units of laths or plates of ferrite that are separated by cementite, martensite or retained austenite. The sub-units form sheaves which nucleate at the austenite grain surface and growth occurs by the deformation of the austenite matrix through an invariant plain strain. Bainitic growth occurs in two stages, ferrite growth followed by cementite precipitation. In the higher transformation temperature range for bainite, the cementite precipitates parallel to the habit planes of the bainitic ferrite. In the lower temperature region of the bainite transformation, the cementite precipitates both between the ferrite plates and within them. The carbide that precipitates within the ferrite maintains a single crystallographic variant [140, 141]. In HSLA steels, there is a morphology of bainite formed at prolonged cooling times and higher temperatures referred to in the literature as granular bainite [72, 142-149]. The formation mechanism for granular bainite is the same as that of normal bainite, causing no discernable difference under



TEM observation. At the optical scale, granular bainite appears much more coarse than normal bainite and may have a dispersion of small islands of retained austenite or martensite [141].

At the most extreme cooling rates austenite transforms directly to ferrite via shear of the face centered cubic structure to accommodate the interstitial carbon atoms. The resultant crystal structure is face centered tetragonal supersaturated with carbon and with massive internal dislocation density. Martensite in low carbon steels forms as laths of very high aspect ratios separated by thin regions of retained austenite [150]. Regions of higher solute in the austenite matrix resulting from segregation during delta ferrite solidification or partitioning during the austenite transformation may result in localized regions that remain as austenite or transform to small regions of martensite forming the martensite-austenite phase, MA [151, 152].

2.2.4 HAZ

A weldment consists of the entire region created or altered by the fusion of two metals [7]. In the instance of pipeline steel this includes the deposited weld metal, the weld metal reheated by subsequent thermal cycles, and the heat affected zone (HAZ).

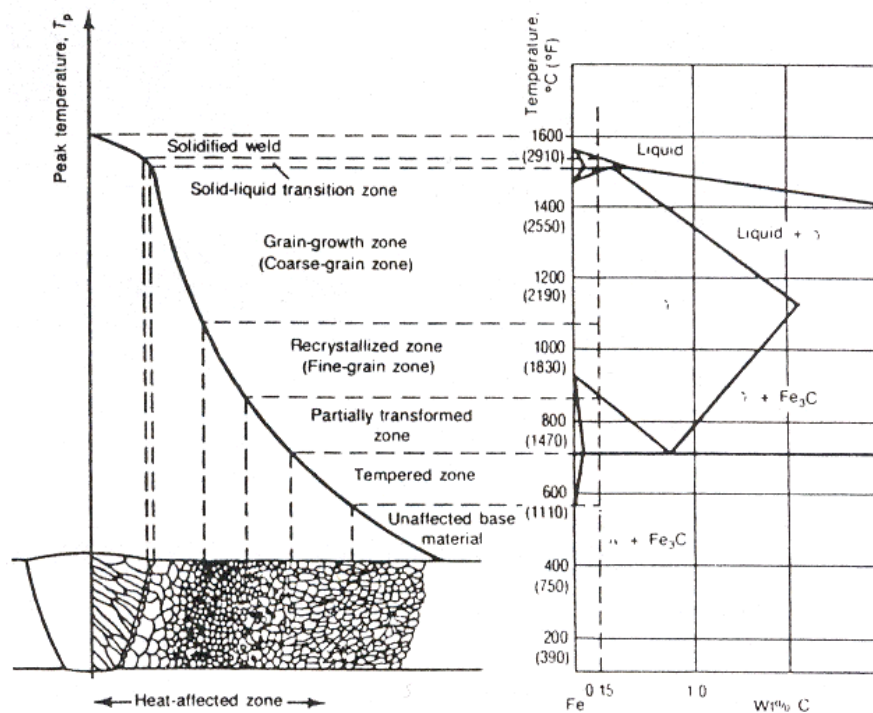


Figure 2-17 - Heat affected zone (HAZ) and corresponding phase diagram, from [153]

The dissipation of the heat from the molten weld pool used to fuse the metals together results in the formation of a heat affected zone in the base metal adjacent to the weld metal. As seen in Figure 2-17 the HAZ can be broken into four regions depending on the temperature achieved. In the grain coarsened (GCHAZ) region adjacent to the fusion line, the base metal is fully heated into the austenite region and some intermetallic particles are dissolved. This allows grain growth so coarsening of the microstructure is expected. In the fine grain zone (FGHAZ) the metal is heated into the austenite region, but to a lower temperature. Intermetallic particles present in the steel may not be dissolved and thus the austenite grain growth is retarded resulting in a fine grained region. The intercritical zone (ICHAZ) has some austenite transformation, but only to a limited degree. Finally the subcritical zone (SCHAZ) experiences no transformations, but tempering of the microstructure may occur [129]. It should be noted that Figure 2-17 is a schematic diagram only and uses an equilibrium phase



diagram to illustrate the transformation temperatures within the steel. In reality, the transformation temperatures exhibited by the steel would not match the equilibrium conditions presented due to rapid thermal cycles and the alloy elements present in the steel.

2.2.4.1 Thermal Cycles

The dissipation of the heat energy generated in fusion welding has an effect on the HAZ of the base metal that can be measured in both space and time. The former relates to the variation in peak temperature as a function of distance from the heat source (fusion line) as shown in Figure 2-17 while the latter is the rate at which the heat energy can be extracted from any region of the HAZ. The derivation of the thermal cycles is based on the heat source being represented by a point, line or plane source which will yield solutions in three, two or one dimensions respectively [7, 123]. The equations developed by Rosenthal and Rykalin are commonly used to describe the thermal profile in the HAZ [153-156]. The Rykalin three dimensional cooling equation is [157]:

$$T - T_0 = \frac{q}{2\pi\lambda t} \exp\left(-\frac{r^2}{4kt}\right)$$

Equation 2-11

where T is the temperature, t is time, q is the heat input, λ is thermal conductivity, κ is thermal diffusivity, r is the radial distance from the weld center and T_0 is the initial temperature. The following relation was used to substitute for the radial distance r:

$$r = \sqrt{\frac{2q}{T_p c \rho \pi}}$$

Equation 2-12



where T_p is the peak temperature, c is the specific heat capacity, ρ is the density of the steel. A comparison of the different cooling curves generated by Rykalin 2D, Rykalin 3D and Rosenthal equations is presented in Figure 2-18.

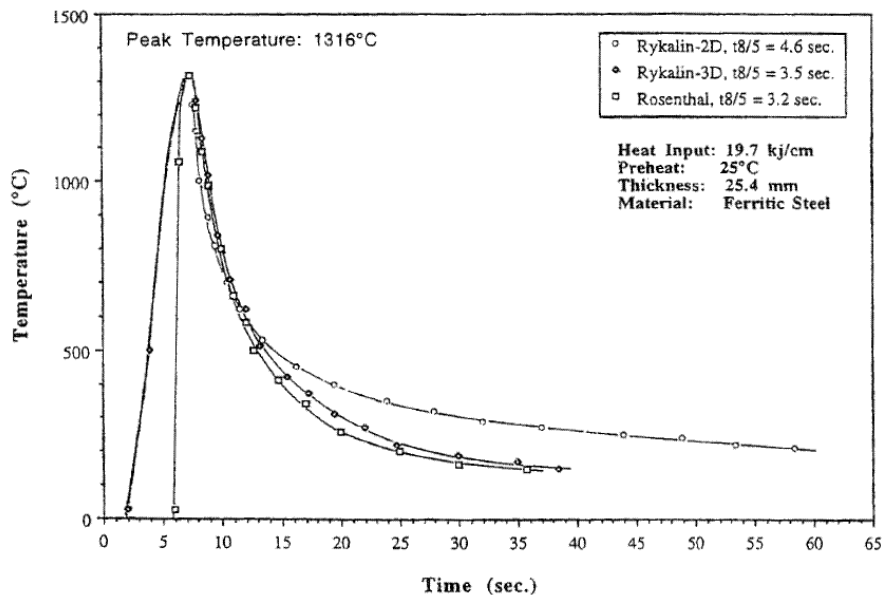


Figure 2-18- Different thermal profiles from the same heat input parameters, from [156]

The correlation of the simulated thermal cycle to that of the real HAZ is a challenge because of the inherent difficulties associated in obtaining reliable thermal data. The work of Poorhaydari *et al.* found that the HAZ was best described by a weighted solution of the Rosenthal thick and thin plate solutions developed by Ashby and Easterling [153, 158].

2.2.4.2 Grain Coarsened Heat Affected Zone

The grain coarsened heat affected zone is usually classified as the region subjected to a peak temperature between 1100 °C and the melting point of the steel [123, 153, 159]. It should be noted that this is the same temperature range that is used in the reheating stage of TMCP. There is a complete transformation of the ferrite to austenite



and the precipitated microalloying phases can dissolve into the austenite. The degree of austenite coarsening is dependent upon the alloy composition and the energy input from the weld which gives a kinetic strength to dissolve the various carbide and nitride precipitates that pin the austenite boundaries [160-163] .

In P-GMAW with heat inputs in the order of 1 kJmm^{-1} , the cooling rates experienced by the GC HAZ are very fast resulting in the formation of martensite and bainite [67, 93, 115, 116, 164, 165]. The large prior austenite grains dominated by bainitic microstructures can become critical zones for reduced toughness [93, 149, 165, 166]. The high heat experienced in the GC HAZ can also lead to the formation of coarse M-A phase in bainite referred to as granular bainite. The hard MA phase can have a deleterious effect on the toughness[152].

2.2.4.3 Fine Grain Heat Affected Zone

The fine grain heat affected zone is created by heating steel above the Ac_3 temperature but below $\sim 1100 \text{ }^\circ\text{C}$. In this temperature range the carbonitride precipitates do not dissolve and continue to retard grain boundary motion. The austenite that forms from the ferrite is frequently very fine as the dislocated ferrite substructure formed during the TMCP and pipe forming process provide a large number of nucleation sites. This results in a very fine austenite structure with increased grain boundary area. The transformation of the fine austenite upon cooling results in very fine ferrite as nucleation from multiple sites within already small austenite grains is supported [129].

2.2.4.4 Intercritical and subcritical heat affected zones

The intercritical region comprises a section that was heated above the critical Ac_1 but below the critical Ac_3 temperature. The microstructure that results is dependent upon the phases that were present upon heating. Applying the lever rule to the $\alpha+\gamma$ region of



the phase diagram at the intercritical temperature will indicate the volumes of austenite and ferrite that satisfy equilibrium. If austenite was retained in the ferrite matrix, then nucleation need not occur and carbon diffusion into the austenite can occur assuming the free energy is negative. If during solidification no austenite was retained, nucleation of the austenite must precede the growth. The carbon enrichment of the austenite may result in carbide formation upon cooling, or may stabilize the austenite to room temperature[167].

In the subcritical heat affected zone no austenite is formed as the temperature never exceeds A_{c1} . There is no visible change in the microstructure at optical resolution, but the precipitation of carbides in martensite and minor coarsening of cementite at grain boundaries can occur. Dislocations present in the ferrite have increased mobility and can sweep up nitrogen and other interstitial impurities. The dislocations become locked in position when the temperature decreases and the immobile dislocations can result in a brittle region[168].

2.2.4.5 Multi cycle heat affected zones

In a mechanized P-GMAW weld there can be anywhere from 6-8 welding passes used to fill the joint. Each one imposes a thermal cycle on a region of previously unaltered base metal and on a region already subjected to at least one thermal cycle. This leads to regions of the weld that can be named in combinations of thermal cycles like the intercritically reheated coarse grain heat affected zone (ICR GC HAZ). The joint is filled linearly and assuming that the heat input remains constant, all subsequent HAZ cycles at the same position will be to a lower peak temperature than the original. The effect of the additive thermal cycles is illustrated in Figure 2-19.

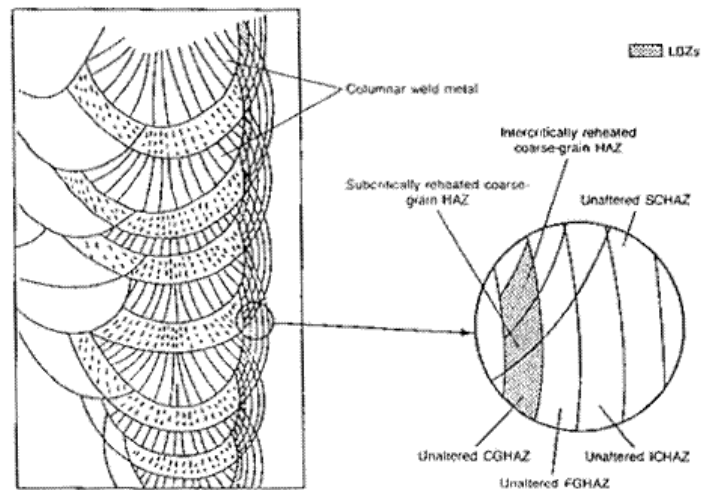


Figure 2-19- Schematic of various HAZ zones developed in multipass welding, from [129]

The ICR GC HAZ in particular is a region of interest as it has been associated with local brittle zones [167, 169, 170]. The intercritical reheating of the initial GC HAZ structure with large prior austenite grains results in austenite formation at the prior austenite grains. The carbon enrichment of the austenite and subsequent transformation to hard carbide or MA phase can initiate brittle cracks.

With the introduction of dual torch welding, the possibility arises for interrupted cooling cycles stemming from different torch spacing and travel speeds. These potential interrupted cooling cycles may result in a second thermal cycle, which would interrupt the austenite transformation of the first cycle at various stages of completion. No data exists in the literature regarding this phenomenon.

2.2.5 Simulation

Confidence in the properties of a pipeline requires a significant investment in testing and data analysis to ensure that in service behavior is predictable and conforms to standard. The need to quantify the response of the steel to various welding thermal cycles is challenging using material from weldments due to geometric and parametric



variability of the welding process. Some of the regions, such as the ICR GC HAZ, that are known to be harmful to the overall properties may occur in regions that are irregularly shaped and too small to use as a test sample. Simulating the effect of a weld by heating a sample using a representative thermal cycle allows a regular and standard size sample to be generated.

2.2.5.1 Physical

The most common and best known physical welding simulator used in research is the Gleeble system manufactured by Dynamic Systems Inc and has been used by many researchers [151, 171-175]. The Gleeble consists of a computer controlled electrically conductive set of jaws coupled to a hydraulic ram. Various different specimen holders can be used in the jaws with a variety of specimen shapes and dimensions. The system relies on direct feedback from a thermocouple welded to the specimen for thermal control. Alternately, a pyrometer may be used for control at suitably elevated temperatures or for high deformation experiments where the thermocouple junction may be compromised. The specimen holders are water cooled and an external spray system is available for external cooling. Heating is achieved by electrical resistance and can reach rates of $10000\text{ }^{\circ}\text{Cs}^{-1}$ under ideal conditions[171]. The hydraulic arm can be used to strain the specimen using tension or compression, or can be used in a zero force setting to eliminate all strain, including thermal. The direct feedback from the thermocouple allows computer generated cooling curves to be applied directly to the specimen. Common specimen geometries are cylinders with diameters of 4 to 10 mm. Cuboid bars with a square cross section of 10-11mm and lengths of 60-80 mm are also used as the standard Charpy specimen of 10 x 10 x55 mm can be machined from the thermally cycled specimen [116, 176]. Cooling is achieved by thermal conduction into the water cooled jaws. Walsh *et al.* found that the separation of the jaws had a direct effect on the width of homogeneous thermal zone [177]. The research found that



judicious selection of simulation parameters was required to achieve certain results, but that the data was entirely reliable. Knorovsky *et al.* found that errors in thermal measurement can be created by improper welding of the control thermocouple, but that a good weld produced accurate measurements [178]. Different commercial weld thermal simulators exist and are used in laboratories throughout the world but are less common [179, 180]. No literature was found citing a simulation technique capable of exactly reproducing a weld.

2.2.5.2 Continuous Cooling Transformation Diagrams

One of the uses for thermal simulation is the mapping of the austenite transformation as a function of the cooling rate. These diagrams are called continuous cooling transformation diagrams and have been produced since the 1940s to help rationalize the different microstructures found in steel [181]. The transformations that occur in steel are dependent upon the composition, temperature, austenite microstructure, cooling rate and strain present during transformation [182, 183]. These factors are illustrated in Figure 2-20.

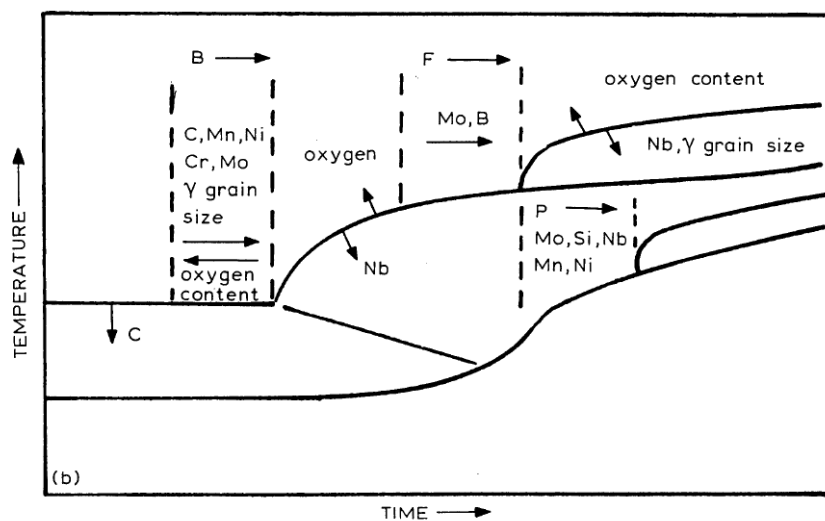


Figure 2-20 – Factors that influence the austenite transformation, from [182]



There are two variants of CCT diagrams, one is for thermal processing, and the other is for welding. In TMCP of steel precise control of the microstructure necessitates accurate application of accelerated cooling [184]. In welding, understanding the relationship between the cooling rate and the microstructure in both the HAZ and the weld metal is critical to maintaining high integrity joints [185]. In both cases, the CCT diagram is a reflection of the shift from equilibrium transformation predicted by the phase diagram under non-equilibrium cooling conditions. The different types of CCT diagrams and their application to the GC HAZ, FG HAZ and the weld metal are illustrated in Figure 2-21.

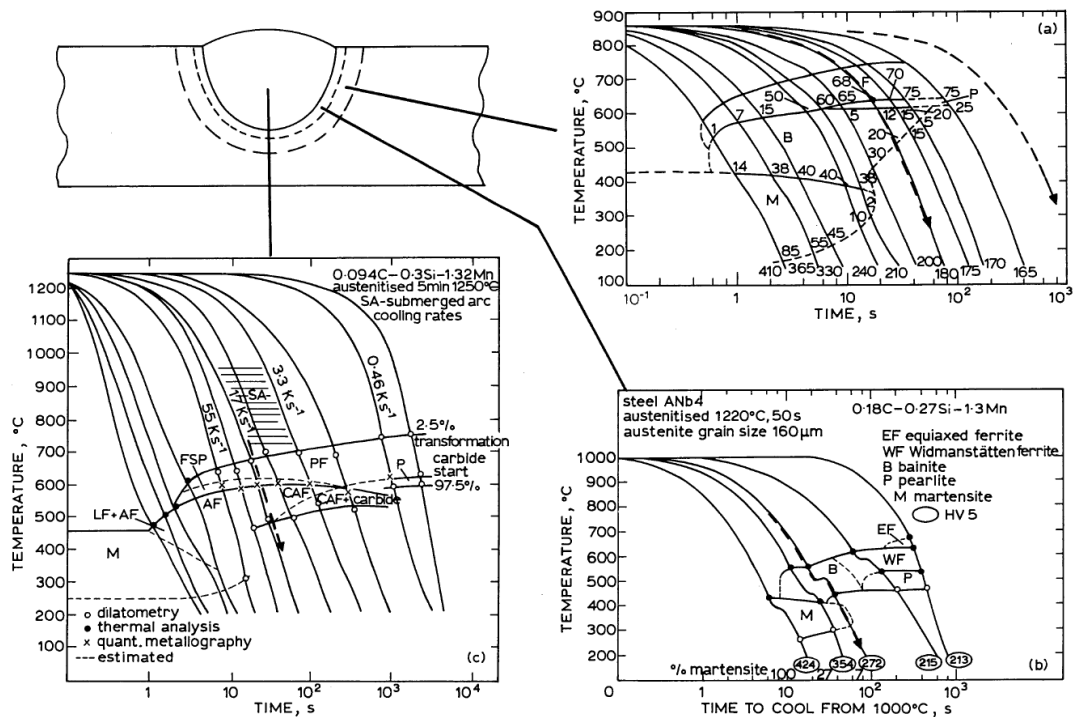


Figure 2-21- CCT diagrams. (a) FG HAZ (b) GC HAZ (c) WM, from [182]

The transformation of FCC austenite to BCC ferrite can be detected in a number of ways. Differential thermal analysis measures the evolution of latent heat that accompanies the solid state transformation as a function of time or temperature.



Acoustic emission can be used to detect the elastic waves initiated by shear transformations (martensite, bainite). The most common transformation detection method is dilatometry whereby the different densities of the FCC and BCC phases are detected volumetrically [186, 187]. Dilatometer specimens are cylindrical rods and the volume expansion can be measured radially or linearly. The expansion is normally detected by a linear variable differential transformer (LVDT) attached to quartz rods [186, 188]. The contraction of the FCC austenite phase varies linearly with temperature (thermal strain) and the A_{r3} temperature can be detected as a volumetric expansion and deviation from linearity on a plot of strain versus temperature. The A_{r1} temperature is the point at which the lattice expansion ceases and the plot of strain versus temperature returns to linearity [188, 189]. The volume of austenite transformed can be calculated for any temperature between the A_{r3} and A_{r1} by the lever rule as illustrated in Figure 2-22.

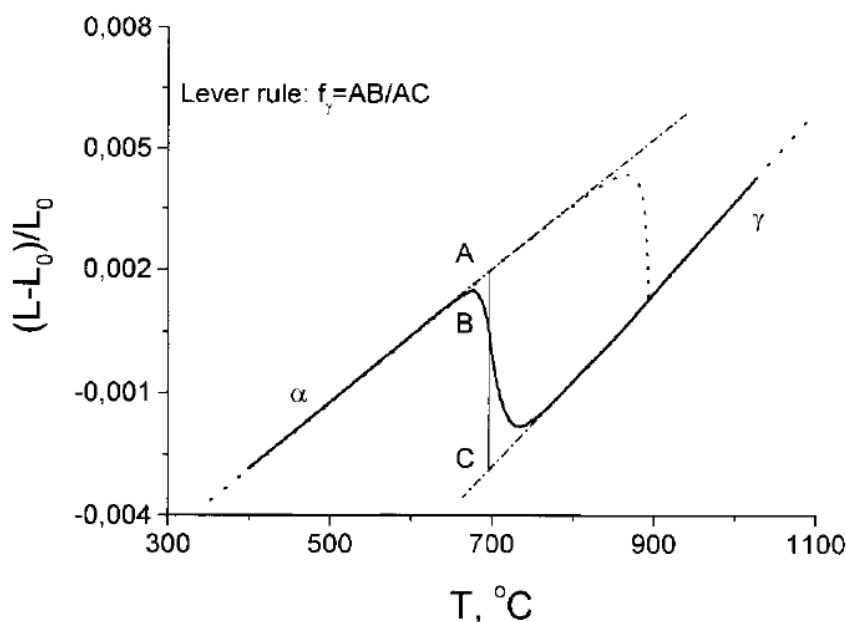


Figure 2-22 – Illustration of the lever rule used to measure fraction of austenite transformed, from [190]



The limits of the detectable volume are a function of the LVDT resolution and the sample size. Yang and Bhadeshia have achieved sensitivities of 1.1×10^{-3} percent martensite in austenite [191], but due to noise in the data, the exact point of expansion can be difficult to detect, particularly at very fast cooling rates. An offset technique can be employed to improve the reproducibility of the data. Yang *et al.* propose a method for determining the offset as a 1% martensite strain within the austenite [191]. The Ar_3 , Ar_1 and % austenite transformed temperatures are then plotted as a function time. Metallography and micro hardness are used to confirm the microstructures formed at each cooling rate.



3 Objectives

The objectives of the work presented in this thesis are to provide a detailed understanding of the effect that low heat input modern welding procedures have on weldments in high strength line pipe. This understanding is essential to qualifying welding procedures for Canadian pipeline applications. This understanding is advanced through thermal simulation and detailed microstructural analysis of the grain coarsened heat affected zone and the reheated weld metal of commercially produced line pipe steels and consumables.

The effect of novel welding procedures and previously unattainable thermal cycles on TMCP line pipe is also reported. The correlation of these microstructures with mechanical properties will allow conclusions to be drawn regarding the result of welding high strength line pipe with novel procedures. This understanding will be published in part through continuous cooling transformation diagrams applicable to the heat affected zone of high strength and ultra high strength line pipe steels showing the microstructural evolution that occurs from various thermal cycles.



4 Comparison of Base Metal and HAZ CCT diagrams for X100 pipe steel

Graeme Goodall^{*}, Benoit Voyzelle^{**}, John Bowker^{**}, Mathieu Brochu^{*}

* Department of Mining and Materials Engineering, McGill University, 3610 University Street, Montreal, Quebec, H3A 2B2

** NRCan CANMET-MTL, 568 Booth St, Ottawa, Ontario, K1A 0G1

4.1 Preface

The various factors that contribute to the temperature at which austenite transforms to ferrite are discussed in paragraph 2.2.3.1.1. This manuscript explores the explicit differences exhibited by a high strength steel during transformation resulting from two different series of thermal cycles. One series was comprised of a low peak temperature with moderate heating rate and is applicable to the processing of the steel that would occur during TMCP. The second series of thermal cycles had much higher peak temperatures and more severe heating rates that are representative of welding.



4.2 Abstract:

Continuous cooling transformation (CCT) diagrams were constructed for an X100 pipe steel. Two peak temperatures were used, 1350 °C to simulate the grain coarsened heat affected zone (GC HAZ) resulting from welding, and 900 °C to characterize the transformation behaviour of the steel. A separate instrument was used for each peak temperature, a BÄHR DIL 805A/D dilatometer was used for the 900 °C experiments and a Gleeble 3800 was used for the 1350 °C series. It was found that both peak temperatures produced lath martensite at the fastest cooling and that bainite formed at intermediate cooling times. The 1350 °C peak produced both bainite and granular bainite over the cooling times tested while the 900 °C peak produced only bainite at intermediate cooling times and polygonal ferrite, pearlite and martensite – austenite (MA) at slower cooling times. The hardness of the samples varied in the case of the 1350 °C samples from 357 to 256 HV over a cooling time from 800 °C to 500 °C (Δt_{8-5}) of 1.3 to 50 seconds. The 900 °C peak samples had hardness's from 332 to 185 HV over a Δt_{8-5} range of 1 to 9987 seconds.

Keywords:

CCT, GC-HAZ, X100, pipe steel, welding, bainite,



4.3 Introduction:

The design of gas pipelines in North America is currently experiencing a challenging new set of conditions imposed by terrain and climate along the length of the transmission route, from arctic to temperate regions [192]. The remote nature of North American gas fields, often thousands of kilometres from existing infrastructure, requires very cost efficient transportation to make extraction viable. At the same time the construction costs associated with laying the pipe must be minimized. Large diameter pipe made from high strength steel addresses both cost considerations by providing a high capacity conduit while minimizing the tonnage and transportation costs of the pipe material [65, 66, 68]. A new grade of steel has been classified by the American Pipe Institute (API) with a specified mean yield strength (SMYS) in excess of 690 MPa (100 ksi) as X100 and is under investigation for applicability in North American gas transmission pipelines.

Developments in steel mill production technology over the past twenty years and more have culminated in the ability to precisely control microstructure during dimensional reduction through thermo-mechanical-controlled-processing (TMCP)[63, 193]. Significant improvements to the strength and toughness of steel can be achieved by reducing the grain size of the microstructure through TMCP [194]. Knowledge of these process parameters has drastically changed the steel industry as new microstructure and strength combinations are devised and the requirement for alloy and solute strengthening are reduced, leading to the high strength low alloy (HSLA) family of steels. Problems can arise when TCMP steels are joined using techniques like gas metal arc welding due to the coarsening of grains adjacent to the fusion line [165].

Welding TCMP steel causes changes in the microstructure adjacent to the fusion zone that are characteristic of peak temperature and thermal energy and are described as the heat affected zone (HAZ). Four distinct regions are apparent in the HAZ and are,



from highest peak temperature to lowest: grain coarsened (GC-HAZ), grain refined (GR-HAZ), inter-critical (IC-HAZ), and sub critical (SC-HAZ) [7]. Traditionally, the region of the HAZ with the most detrimentally affected properties is the GC-HAZ where the peak temperature is the highest and the fully re-austenitized grains have sufficient thermal energy to grow and coalesce. Combination of coarse grains and longer cooling times resulting from the high thermal energy generally result in softer transformation products with poor crack arresting properties. The GR-HAZ reaches a temperature above the A_{c3} , but does not have sufficient thermal energy for grain growth and coalescence, resulting in a fine substructure. The IC-HAZ exists where the steel has exceeded the A_{c1} temperature, but not the critical A_{c3} , resulting in re-austenitization at the prior austenite grain boundaries. The SC-HAZ is sometimes difficult to distinguish optically as there is no re-austenitization, only tempering of the microstructure. Investigating the properties of the GC-HAZ is critical to understanding the transformation behaviour and products that will form as a result of various joining procedures. One method of measuring the transformation of steel during a thermal treatment is the use of a dilatometer to monitor the volume of the lattice as a function of thermal expansion and phase transformation. The two allotrophic forms of iron are ferrite (α & δ) which has a body centered cubic (BCC) structure and austenite (γ) which is a face centered cubic (FCC) structure. Ferrite and austenite have different densities, which are detectable during heating and cooling as deviations from normally induced thermal strain.

Continuous cooling transformation (CCT) diagrams are useful tools for understanding the microstructures that develop as steel cools. There are numerous methods to construct and report CCT diagrams and the recent standard (ASTM A1033-10) released by the ASTM attempts to impose a uniform procedure. However, the ASTM standard does not contain a procedure for standardizing CCT diagrams for weld HAZ regions. The peak temperature of the GC-HAZ exceeds the $A_{c3} + 50$ °C stipulation of ASTM A1033-10 by 300-400 °C for most steels. Additionally, the linear cooling prescribed in the



procedure does not reflect the cooling profile for a moving point heat source. In this paper, a low temperature CCT diagram constructed to near ASTM standards is compared to a high peak temperature GC-HAZ CCT diagram in an X100 pipe steel. The goal is to see what can be learned from studying both aspects of the transformation behaviour concurrently.

4.4 Experimental

Samples for thermal cycling were cut from a 19 mm thick pipe produced by TMCP. The chemistry of the steel is given in Table 4-1 along with the carbon equivalents calculated using the following equations [22]:

$$CE_{IIV} = C + \frac{Mn}{6} + \frac{Cu + Ni}{15} + \frac{Cr + Mo + V}{5}$$

Equation 4-1

$$P_{cm} = C + \frac{Si}{30} + \frac{Mn}{20} + \frac{Cu}{20} + \frac{Ni}{60} + \frac{Cr}{20} + \frac{Mo}{15} + \frac{V}{10} + 5B$$

Equation 4-2

where the fractions of elements are in weight percent. The bainite and martensite start temperatures calculated by the classic Steven and Haynes equations [195] are also given in Table 4-1.

Table 4-1 – Chemical composition of the steel (wt%)

C	Mn	Si	Nb	Ti	N	Ni+Mo+Cr	S	CE _{IIV}	P _{cm}	B _s	M _s
0.050	1.87	0.19	0.030	0.010	0.0025	1.09	0.001	0.55	0.21	585	457

Two different experimental apparatuses were used for the dilatometric experiments, a BÄHR DIL 805A/D dilatometer and a Gleeble 3800, and will be described separately.



4.4.1 Gleeble 3800

The Gleeble specimens were cut as 75 mm long bars with a 10 mm square cross section. This geometry was selected to be consistent with concurrent research outside the scope of this paper. The square bars were reduced at mid length to produce a round 6 mm diameter over a 6 mm length with a 45° chamfer. The temperature of the samples was monitored directly by a thermocouple welded to the specimen surface at mid length using a welding jig supplied by the manufacturer. The samples were held in water cooled copper grips with a chiller temperature of 19 °C. The samples were Joule heated at 300 °C s⁻¹ to 1350 °C and held for one second before being subjected to three dimensional Rykalin cooling curves with 800 °C -500 °C cooling times (Δt_{8-5}) from 3 to 100 seconds. Selected cooling curves were repeated to ascertain scatter.

4.4.2 BÄHR DIL 805A/D

Hollow cylindrical specimens 10 mm long with an outside diameter of 4 mm and a wall thickness of 1 mm were cut 5 mm from the pipe OD surface. The temperature was monitored via a Type S thermocouple welded directly to the specimen surface at mid length using a welding jig supplied by the manufacturer. Experiments were conducted under vacuum where applicable and cooling was achieved using He gas on both the outer and inner surfaces. Samples were heated using a high frequency radio induction coil at a rate of 5 °C s⁻¹ to 950 °C where they were held for 5 minutes before being cooled at rates ranging from 300 °C s⁻¹ to 0.01 °C s⁻¹. Hollow quartz push rods connected to an LVDT were used to hold the specimen and conduct the He gas through the center of the specimen



4.4.3 Metallography

Representative samples were cut from specimens using a low speed diamond blade and prepared for both light optical microscopy (LOM) and transmission electron microscopy (TEM). The LOM samples were mounted in phenolic resin then ground and polished using diamond suspensions to a final 1 μm finish. The samples were then etched with 3% nital for 15 seconds and micrographed. Selected samples were re-polished from 3 μm and etched with Le Pera's reagent for 20 seconds, dried and re-etched for 5 seconds where it was desirable to reveal martensite-austenite (MA).

The specimens for TEM analysis were cut with a precision saw using a general purpose diamond wafering blade. A slice of 500 μ thick was made. Discs were punched with a Gatan 3.0 mm diameter punch. The samples were reduced using silicon carbide 240, 320, 400, 600 and 1200 grit papers to reduce thickness of pieces equally on both sides. Approximately 40-50 μm thick samples were obtained. Samples were dimpled using 3 μ diamond paste and 4-6 μ CBN to a depth of approximately 30 μm and then fine dimpled using 1/4 diamond for about 1 min. Ion milling was carried out using Gatan Duo-Mill with Liquid nitrogen cold stage to prevent heating of sample.

TEM examination was carried out using a Philips CM20 FEG TEM equipped with a Schottky field emission gun that was operated at a voltage of 200 kV.

Hardness measurements were made using a Clemex Vicker's micro-indenter at a 300 gram force load on re-polished LOM specimens.

4.5 Results and Discussion

The cooling rates at 700 $^{\circ}\text{C}$ along with the Δt_{8-5} are given for the 1350 $^{\circ}\text{C}$ and 900 $^{\circ}\text{C}$ peak temperature thermal cycles in Table 4-2 and Table 4-3 respectively.



Comparison of Base Metal and HAZ CCT diagrams for X100 pipe steel

Table 4-2 – Cooling data for CGHAZ simulation from 1350 °C peak

	$\Delta t_{8.5}$ for 1350 °C peak (s)									
	1.3	2	3	5	6	10	17	25	30	50
Rate at 700 °C (°Cs⁻¹)	261.5	189.3	118.6	71	59.5	37.2	23.0	14.7	12.2	7.6
$\Delta t_{T>1000^\circ\text{C}}$	3.05	3.16	3.92	4.1	4.3	6	10.6	14.5	15.2	23.1

Table 4-3 – Cooling data for CCT diagram from 900 °C peak

	$\Delta t_{8.5}$ for 900 °C peak (s)											
	1.0	1.3	2.1	3.0	6.1	17	30	100	300	1000	3000	9987
Rate 800-500 °C (°Cs⁻¹)	300	250	200	111	50	20	10	3	1	0.3	0.1	0.03
Rate at 700 °C (°Cs⁻¹)	315.9	282.7	218.6	131.6	54.7	23.2	11.1	3.3	1.1	0.33	0.1	0.03

The total time above 1000 °C is given for the 1350 °C thermal cycles in Table 4-2 due to the growth of austenite in that temperature range [196-199]. The niobium carbide solvus temperature for the steel was calculated to be 1206 °C [200] which is well below the peak temperature of the thermal cycle, however the time above the solvus is less than 2 seconds for all thermal cycles. The two sets of thermal cycles are fundamentally different as seen in Figure 4-1 where the full thermal cycles corresponding to a $\Delta t_{8.5}$ cooling time of 30 seconds are shown for both peak temperatures.

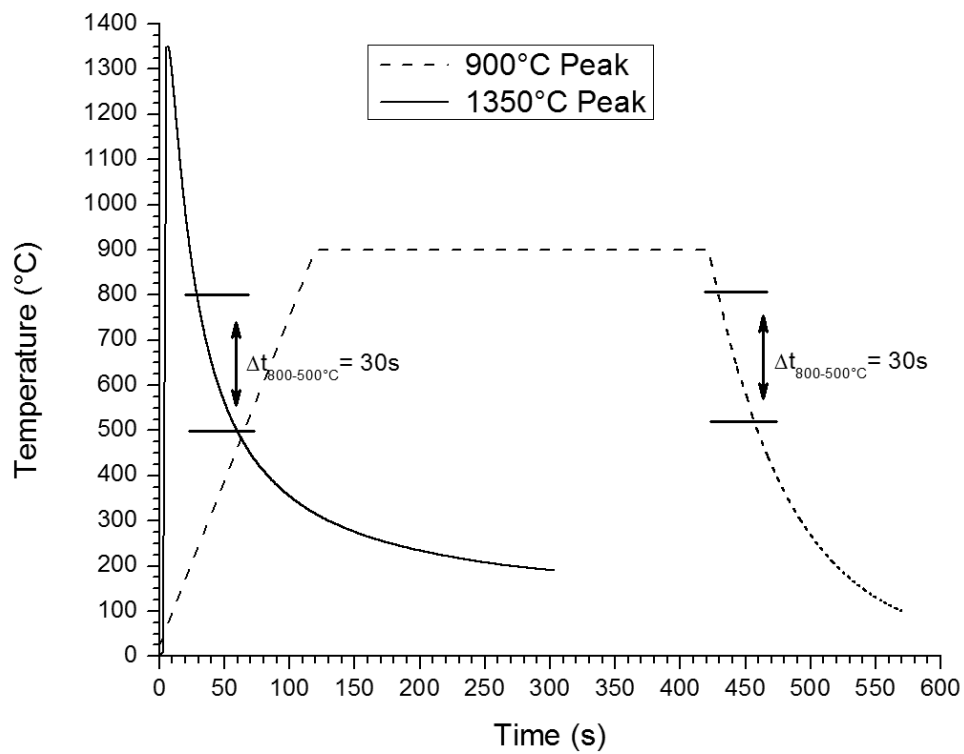


Figure 4-1– Thermal cycles for $\Delta t_{8.5}$ cooling times of 30 seconds for 1350 °C and 900 °C peaks

It is evident that the 1350 °C peak profile more closely resembles the rapid thermal flux associated with the GC HAZ region of a GMAW weldment. The 5 min hold used in the 900 °C cycles was used to homogenize the steel while minimizing grain growth.



4.5.1 Microstructure

4.5.1.1 1350 °C Peak Cycles

Three transformation products appeared in the steel cooled from 1350 °C, martensite, bainite and granular bainite. Figure 4-2 presents micrographs representative of the three microstructures.

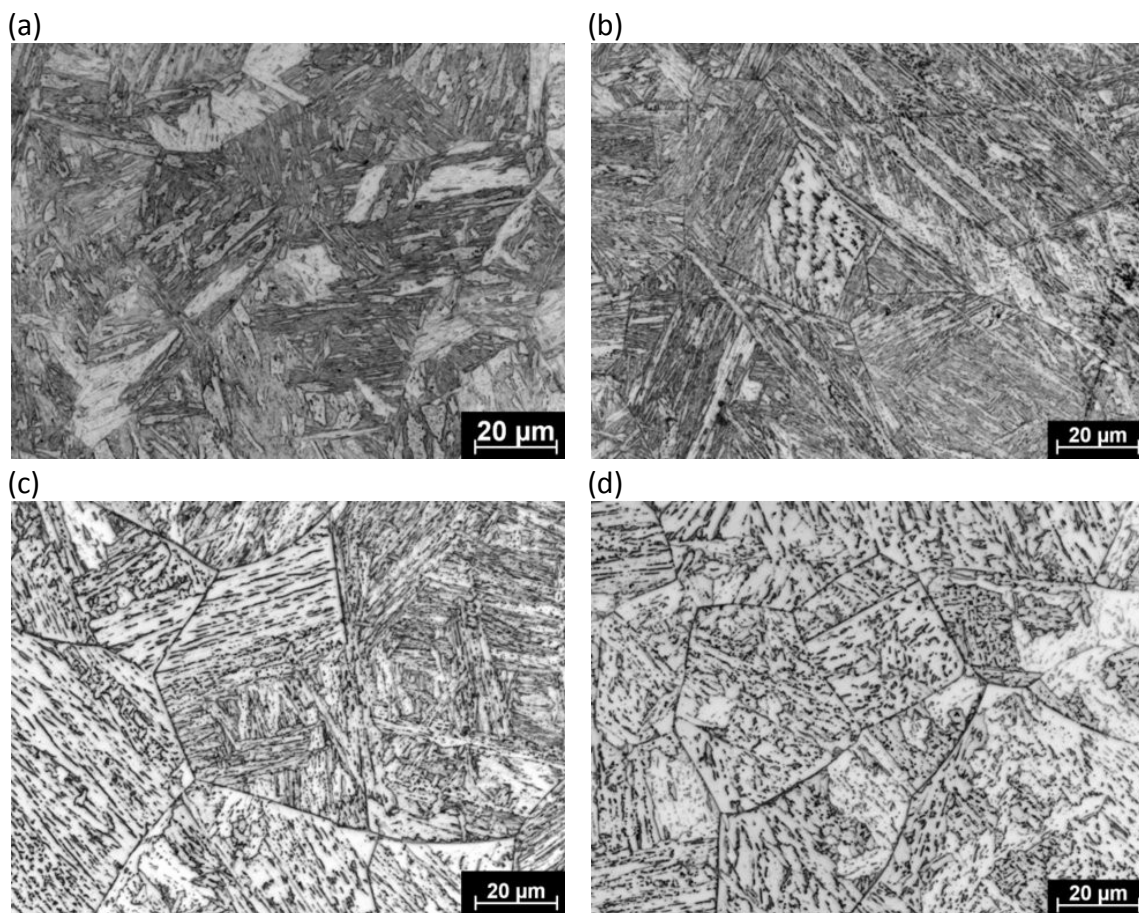


Figure 4-2- Micrographs for the 1350 °C peak temperature thermal cycles. Δt_{8-5} = (a) 1.3s (b) 10s (c) 25s (d) 50s



In Figure 4-2 (a) the microstructure consists of very fine and feathery lath martensite. The high peak temperature has clearly allowed the austenite grains to coarsen, however comparing Figure 4-2 (a) and (d) for the fastest and slowest cooling rates, there is not a significant increase in prior austenite grain size despite the much longer time the slow cooled specimen was held above 1000 °C as given in Table 4-2. This could be partially due to the incomplete dissolution of the boundary pinning particles, or because the Nb(C-N) particles re-precipitated during cooling between the solvus of 1206 °C and the limit of austenite growth at 1000 °C. The average prior austenite grain size for 1350 °C specimens was estimated by the lineal intercept method at $51 \pm 20 \mu\text{m}$. The microstructures presented in Figure 4-2 (b) and (c) show the bainite microstructure and the mixed bainite and granular bainite microstructure respectively. The SEM micrographs of martensite, bainite and granular bainite formed during cooling from 1350 °C in Figure 4-3 (a) through (c) show that both the martensite and bainite phases and are nucleated at prior austenite boundaries and that there is no growth across the austenite grain boundary [141].

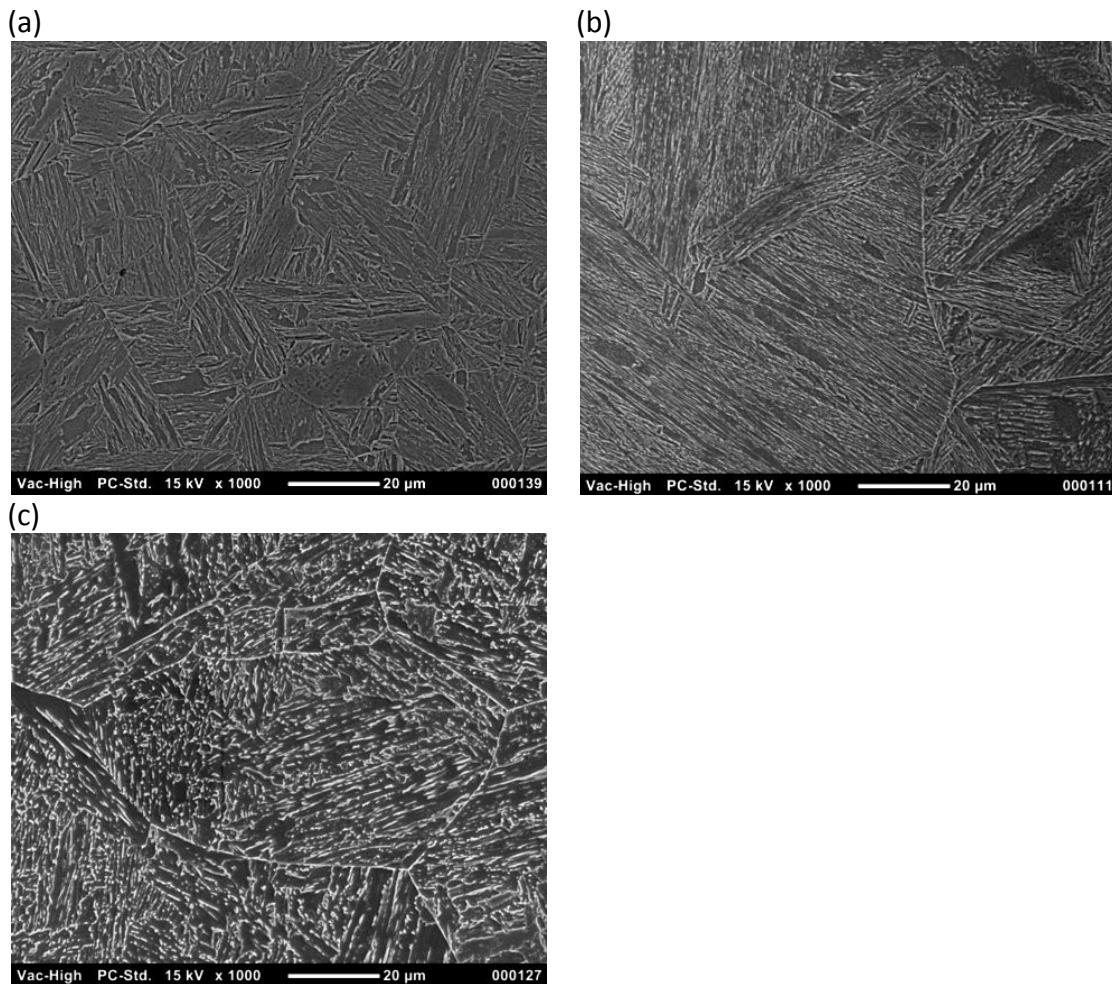


Figure 4-3– SEM images of 1350 °C peak transformation products. (a) martensite, $\Delta t_{8-5}=1.3s$ (b) bainite, $\Delta t_{8-5}= 10s$ (c) granular bainite, $\Delta t_{8-5}= 50s$

The fine laths of ferrite with aligned carbide second phase seen in Figure 4-3 (b) are typical of bainite. The coarser ferrite plates seen in Figure 4-3 (c) are consistent with granular bainite. The sheaves of bainite with ferrite plates and carbide phases can be seen in the TEM image in Figure 4-4 (a) and the very fine laths of martensite without a carbide phase can be seen in Figure 4-4 (b).

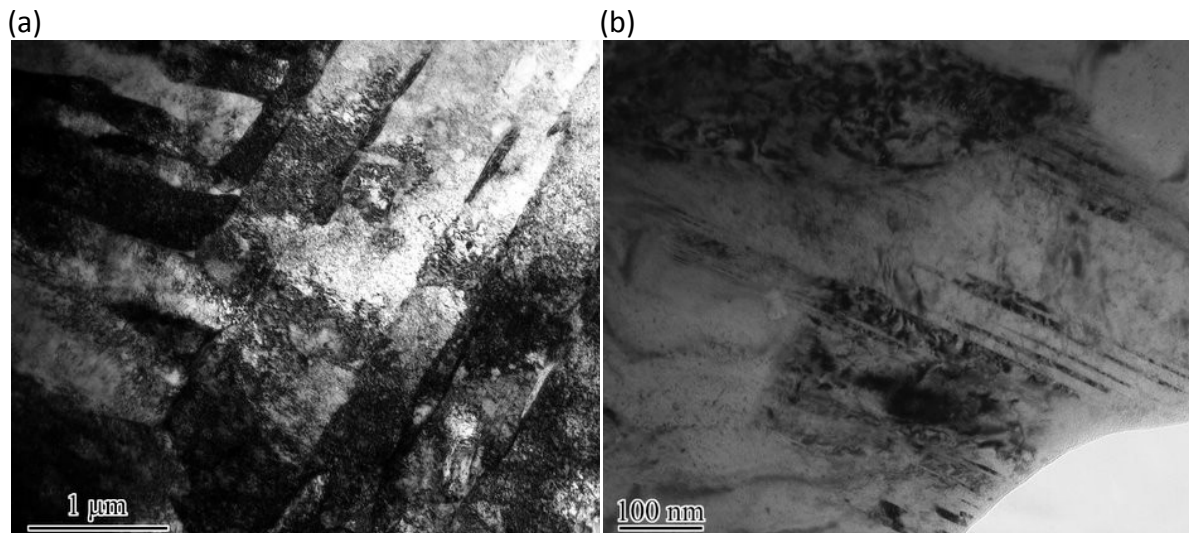


Figure 4-4– TEM images of 1350 °C transformation products. (a) Bainite, $\Delta t_{0.5}=10s$ (b) lath martensite $\Delta t_{0.5}= 1.3s$

The high dislocation density and lattice strain associated with martensite gives the average Vickers hardness values in this steel of 357 HV while the bainite phase averages 330 HV and the granular bainite averages 259 HV.

4.5.1.2 900 °C Peak Cycles

The microstructure of the steel heated to a 900 °C peak temperature is dominated by a very fine lath martensite at fast cooling rates which subsides to form bainite, grain boundary ferrite and pearlite with increased cooling time. The 900 °C peak temperature with a 5 minute hold time allows some chemical homogenization but is well below the solvus of the austenite grain boundary pinning precipitates leading to an average prior austenite grain size of $3.6 \pm 0.4 \mu m$. Figure 4-5 presents LOM images of the characteristic microstructures developed during cooling of the steel.



Comparison of Base Metal and HAZ CCT diagrams for X100 pipe steel

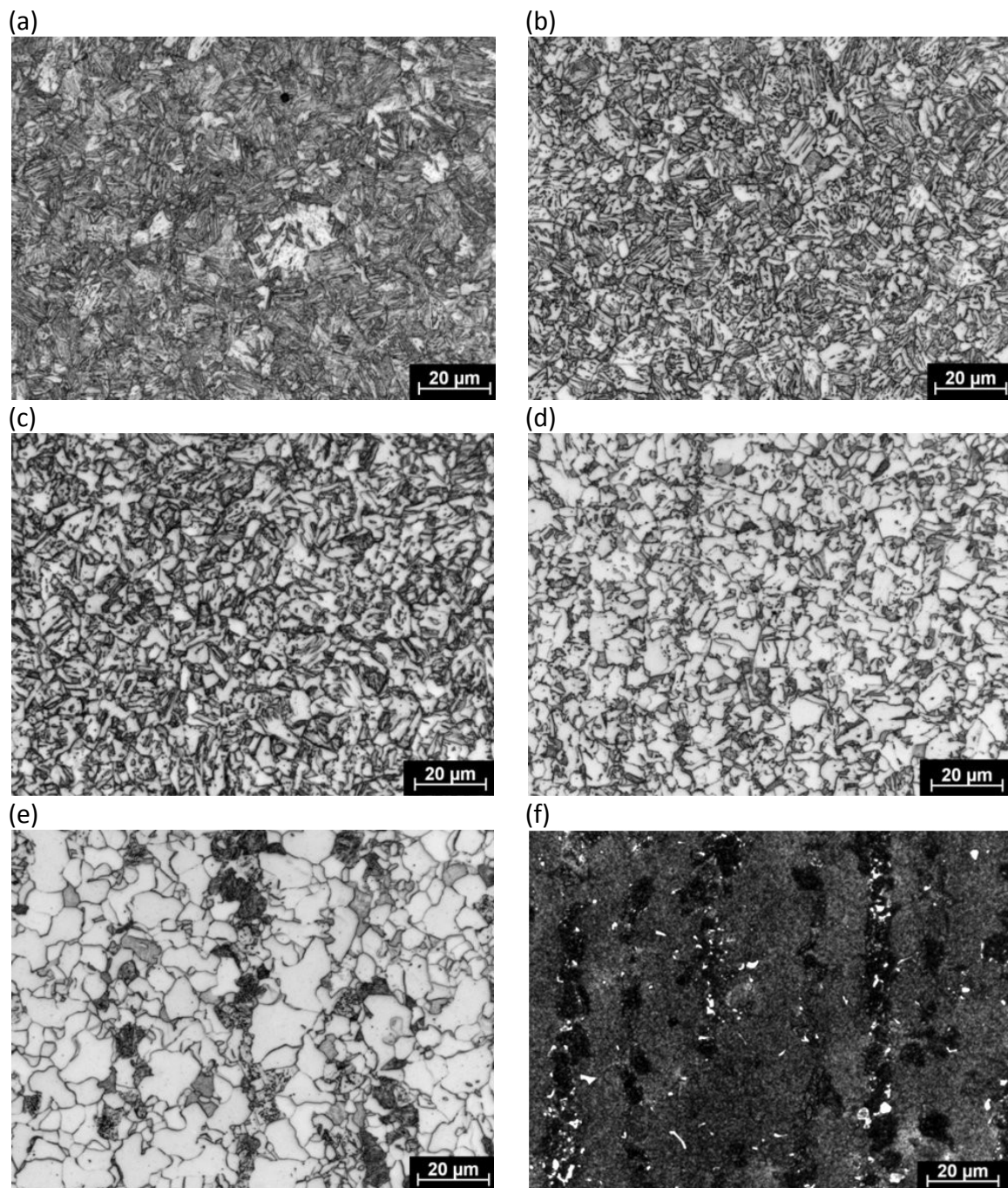


Figure 4-5– Micrographs for the 900 °C peak temperature thermal cycles etched with nital unless specified. Δt_{8-5} =: (a) 1 s (b) 6.1 s (c) 17 s (d) 100 s (e) 3000 s (f) 3000 s etched with Le Pera's

The displacive transformation products martensite and bainite are clearly visible in Figure 4-5 (a) and (b) respectively with a very fine lath structure emanating from the



prior austenite grain boundaries. Displacive reactions do not cross austenite grain boundaries leaving them visible post transformation. In Figure 4-5 (c) and (d) there is some bainite still forming, but reconstructive transformations are starting to dominate. Grain boundary and polygonal ferrite become the prominent transformation products in Figure 4-5 (d) and the delineation of the prior austenite grain boundaries diminishes. The final transformation products, at a $\Delta t_{8-5} = 3000$ s are polygonal ferrite, pearlite and MA. The MA phase was revealed by etching the $\Delta t_{8-5} = 3000$ s sample with Le Pera's solution where 3 phases appear in Figure 4-5 (f) showing a white MA phase, grey ferrite phase and black pearlite phase. The regular banding of the ferrite–pearlite microstructure formed at the slowest cooling rates is an artefact of the TMCP rolling during the manufacture of the steel [201].

4.5.2 CCT Diagrams

Continuous cooling transformation diagrams were constructed from both 1350 °C and 900 °C by monitoring the variation in lattice strain as a function of temperature. Due to the different starting temperatures the diagrams cannot be normalized to the same starting temperature and thus will be analyzed separately. The detection of transformation temperatures was accomplished using a linear best fit of the data for both start and finish transformation measurements.

The transformation start and finish temperatures corresponding to the Ar_3 and Ar_1 temperatures of the steel were determined as the point at which the linear contraction of the lattice owing to thermal strain deviated due to the strain associated with crystallographic transformation [191, 202, 203]. Figure 4-6 gives the CCT diagram from 900 °C where solid lines have been detected via dilatometry and the dashed lines have been added from microstructural analysis and hardness measurements.



Comparison of Base Metal and HAZ CCT diagrams for X100 pipe steel

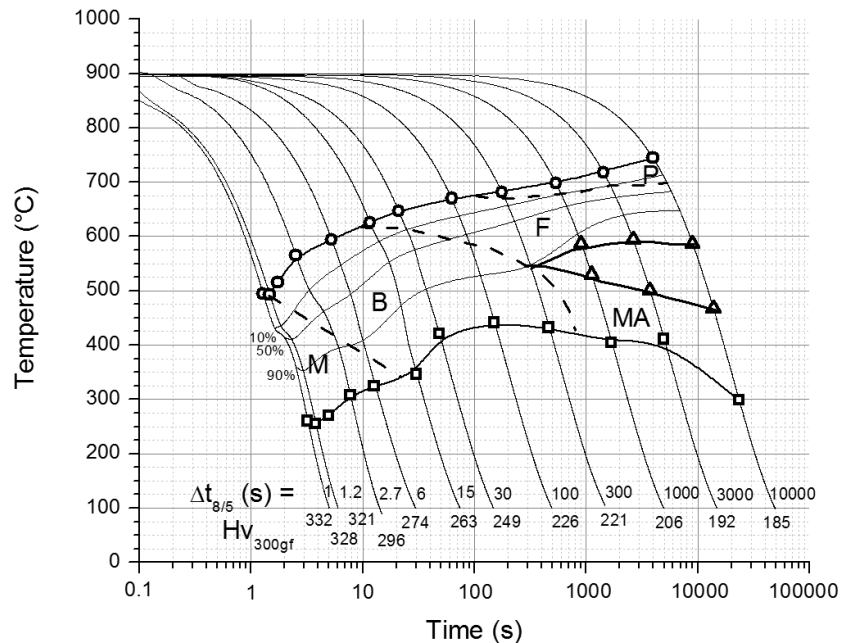


Figure 4-6– CCT diagram from 900 °C showing martensite (M), bainite (B), polygonal ferrite (F), pearlite (P) and MA from BÄHR DIL 805A/D Dilatometer data

The 10, 50 and 90% lines refer to the volume of austenite transformed at each temperature as calculated by the lever rule [204]. There is a martensite start temperature of 493 °C with a corresponding 332 HV hardness. The bainite field shows an increasing start temperature, which gives way to polygonal ferrite with decreased cooling rates. There is no discernable change in the dilatation from bainite to polygonal ferrite. At the slowest cooling there is a low temperature transformation corresponding to a very small transformation volume that can be seen in Figure 4-7.



Comparison of Base Metal and HAZ CCT diagrams for X100 pipe steel

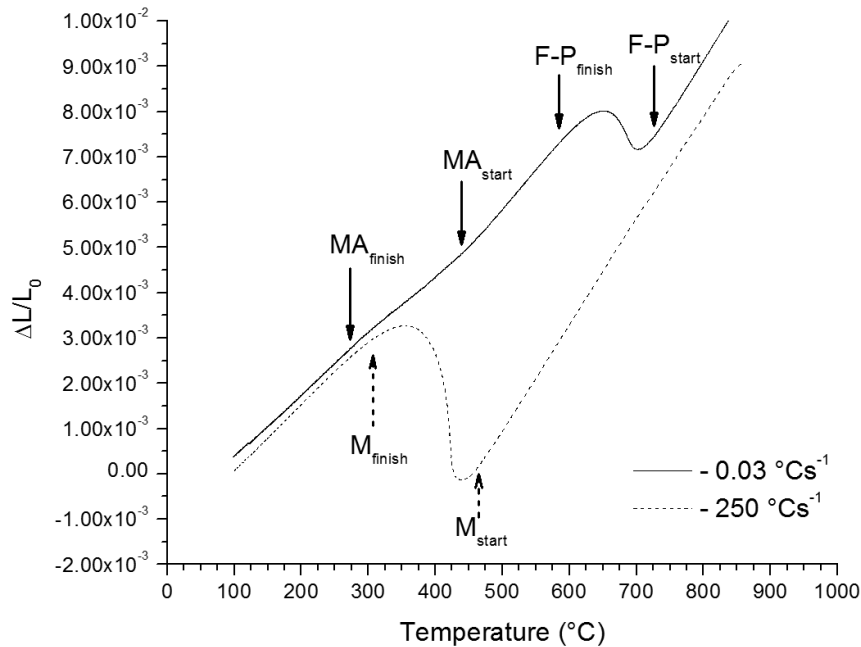


Figure 4-7– Dilatometric response during slow and fast cooling from 900 $^{\circ}\text{C}$ showing the start and finish temperatures of ferrite- pearlite (F-P), MA and martensite (M)

A single phase martensite transformation generated from a fast cooling rate is also included in Figure 4-7 where it is evident that only one strain event is detectable. Etching the slow cooled sample with Le Pera's reagent Figure 4-5 (f), reveals this to be MA and corresponds to a volume of less than 5%. The transformation region of the CCT diagram appears to be a significant volume, but is in reality only a significant thermal range over which the MA transforms with a very small volume.

The microstructural evolution of the steel as a function of the cooling rate from 1350 $^{\circ}\text{C}$ is presented as a CCT diagram in Figure 4-8.



Comparison of Base Metal and HAZ CCT diagrams for X100 pipe steel

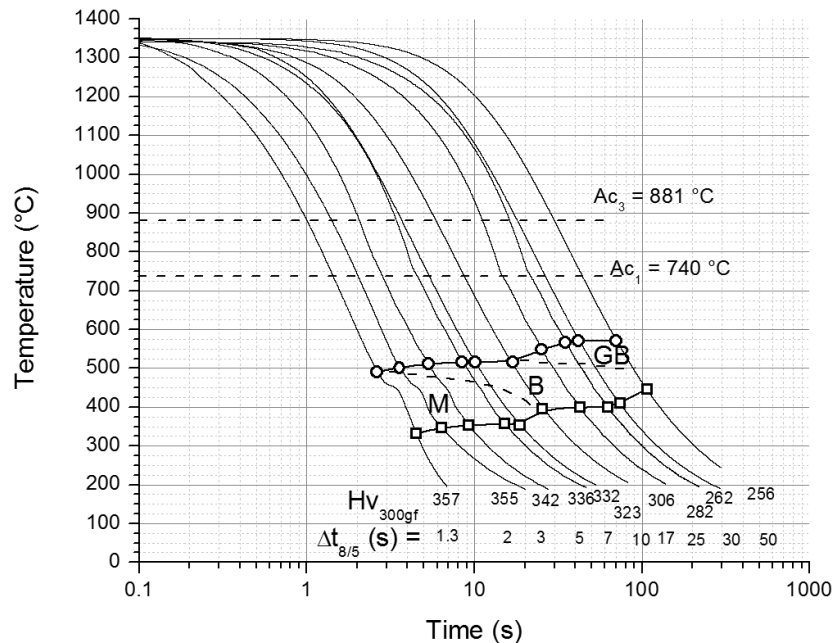


Figure 4-8– CCT Diagram from 1350 °C peak showing martensite (M), bainite (B) and granular bainite (GB) from Gleeble 3800 data

The martensite start is measured at 491 °C, which is very much in line with the start temperature detected from a 900 °C peak. However both values are approximately 50 °C above the predicted Ms given in Table 4-1. It is interesting to see that the size of the austenite grains has not affected the martensite start (Ms) temperature as should be the case [205]. There should be a suppression of martensite start temperature with a reduction in the grain size. The absence of this effect is most likely due to the relatively large austenite grains formed at both peak temperatures as the magnitude of the effect is much greater for austenite grains under 10 μm [205, 206]. The suppression of the bainite start to lower cooling rates is evident as are the two near plateaus associated with the bainite and granular bainite start temperatures. The predicted bainite start (Bs) of 585 °C given in Table 4-1 is very close to the measured upper limit for Bs of 570 °C



seen in Figure 4-8. The 1350 °C peak with $\Delta t_{8-5} = 10$ s transformation start temperature was measured as $514.9 \text{ °C} \pm 3.2 \text{ °C}$ and the finish as $395.8 \text{ °C} \pm 5.2 \text{ °C}$. The error of the measurement is approximately the size of the data markers used in Figure 4-6 and Figure 4-8. The excellent agreement of these tests allows high confidence in the measured transformation temperatures for all other cooling rates.

While the actual CCT diagrams for the two peak temperatures cannot be superimposed, and reflect very different thermal cycles, a direct comparison can be made by plotting the transformation start and finish temperatures as a function of the cooling times from 800 °C to 500 °C given in Table 4-2 and Table 4-3. The plot of comparative transformation start and finish temperatures is presented in Figure 4-9. It shows the increase of hardenability associated with the 1350 °C peak temperature with martensite of 357 HV compared to 332 HV for the 900 °C peak along with the suppression of reconstructive transformation products. The 1350 °C peak cycles were not extended to the same slow rates as the 900 °C as the purpose of the higher peak cycles is to simulate the GC HAZ region associated with welding. The slowest cooling is not representative of the heat inputs of P-GMAW welding investigated for this steel composition and application.

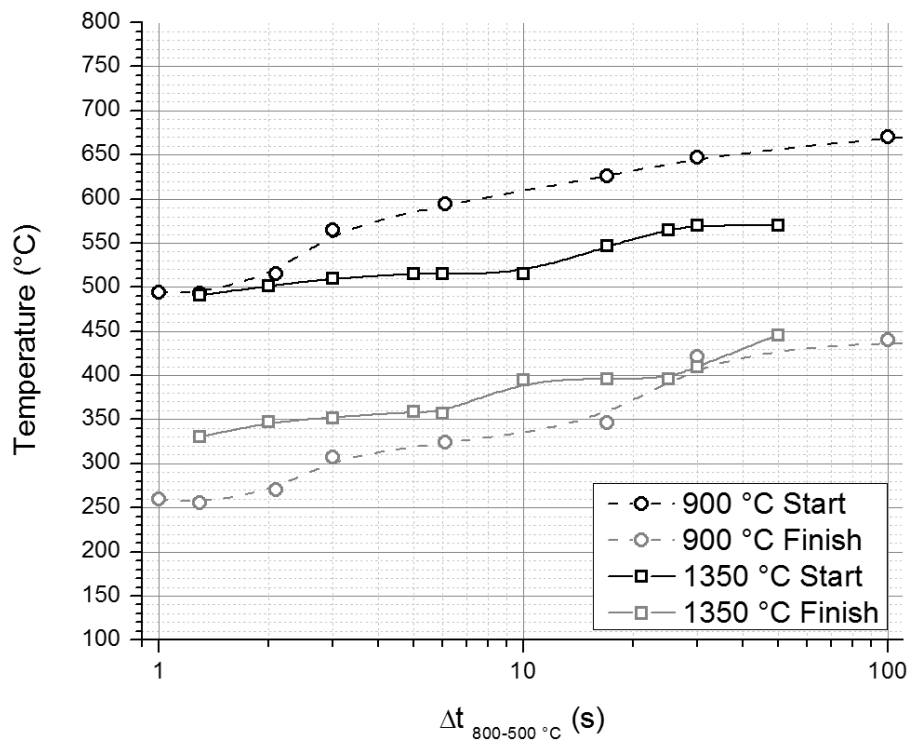


Figure 4-9– Comparison of start and finish temperatures for 900 °C and 1350 °C peak temperatures as a function of cooling time from 800 °C to 500 °C

It is interesting to see that in Figure 4-9 the transformation range for the 1350 °C peak cycles is considerably narrower than the 900 °C peak. The 1350 °C peak CCT diagram is representative of the GC HAZ region while the 900 °C gives a standard CCT diagram for the steel. The research of Shome and Mohanty [207] on HSLA steels found that a 1000 °C peak temperature, without hold, was representative of the FGHAZ region. Clearly the 5 minute hold used in the 900 °C thermal cycle is not representative of a welding thermal cycle and the fine grained structure presented should not be confused with the FG HAZ.



4.6 Conclusions

- The transformation behaviour of an X100 steel from 1350 °C and 900 °C has been analysed and is presented as separate CCT diagrams.
- The transformation products formed from a 1350 °C peak with Δt_{8-5} from 1.3 to 50 seconds are martensite, bainite and granular bainite.
- The transformation products formed from a 900 °C peak with Δt_{8-5} from 1 to 9987 seconds are martensite, bainite, polygonal ferrite, pearlite and MA.
- The hardenability (suppression of reconstructive transformation products) is enhanced when cooling from a 1350 °C peak temperature.
- The thermal range over which both displacive and reconstructive transformations occur is narrower when cooling from a 1350 °C peak temperature.

4.7 Acknowledgements

This research was funded by CANMET-MTL and the Federal Interdepartmental Program for Energy Research and Development. The authors would like to thank Mr. M. Kerry for his machining expertise and Mr. J. Gianetto for his help with materials acquisition and advice. The research is part of a larger consolidated program jointly funded by the Pipeline and Hazardous Materials Safety Administration of the U.S. Department of Transportation (DOT), and the Pipeline Research Council International, Inc. (PRCI). The views and conclusions in this paper are those of the authors and should not be interpreted as representing the official policies of any of these organizations.

The author (G.G.) also wishes to acknowledge CANMET-MTL management for providing the opportunity to work and have access to laboratory facilities during the course of this research and to NSERC and McGill University for funding grants.



5 CCT diagrams and impact toughness applicable to the GC HAZ region generated in X100 line pipe

Graeme Goodall*, James Gianetto**, John Bowker**, Mathieu Brochu*

* Department of Mining and Materials Engineering, McGill University, 3610 University Street, Montreal, Quebec, H3A 2B2

** NRCAN CANMET-MTL, 568 Booth St, Ottawa, Ontario, K1A 0G1

5.1 Preface

Using the dilatometer techniques developed in the previous section, the study of the GC HAZ was extended to encompass 3 different grade 690 linepipes with different chemical compositions. The simulation of the GC HAZ was validated by analysis of a rolled weld made in the linepipe by mechanized P-GMAW. The toughness developed in the GC HAZ at different cooling times was measured using full size Charpy impact bars subjected to thermal cycles simulated with a Gleeble thermo-mechanical simulator. The GC HAZ toughness measurements were then compared against each other and against the toughness of the linepipe. Fractography on both the freshly broken surface and the surface etched to reveal the microstructure allowed correlation of microstructure with toughness.



5.2 Abstract:

Three different commercially produced pipe steels with specified mean yield stresses of 690 MPa (100 KSi) were investigated. The grain coarsened heat affected zone (GC-HAZ) typical of pulsed gas metal arc welding (P-GMAW) used for pipeline field girth welding was simulated using a Gleeble thermo-mechanical simulator. Continuous cooling transformation (CCT) diagrams were constructed for all three steels through dilatometric analysis of the austenite transformation temperatures during cooling. It was found that in all three steels, martensite formed for short cooling times, bainite at intermediate cooling rates and granular bainite at prolonged cooling times. The impact toughness of the steels was measured using Charpy impact toughness tests conducted over a range of temperatures and compared to the toughness of single cycle simulated GC-HAZ regions corresponding to a P-GMAW thermal cycle used for pipeline girth welding. The ductile to brittle transition temperature (DBTT) was found to be best for the steel with the highest hardenability.

Keywords:

CCT, X100, Pipe Steel, P-GMAW, Welding, HAZ, Dilatometry, Charpy, Microstructure



5.3 Introduction

One of the current sources for natural gas development in North America is the arctic basin [15, 66, 68]. There are numerous challenges associated with the design and construction of long pipelines which must perform in both arctic and temperate climates. Additionally, the extreme distance from gas field to customer centers requires very efficient transportation. The return on investment for a pipeline is contingent upon the construction costs, which are directly proportional to material costs. Welding is an integral part of pipeline construction and with short construction seasons, companies are always seeking ways to reduce cost while meeting stringent property requirements. Application of modern high strength steel pipe requires implementation of welding processes and procedures that not only allow strength overmatching of welds but also reduce the detrimental effects on the pipe steel, especially in the weld heat-affect zone regions.

High strength low alloy steels have been investigated for use in pipelines since the 1970's [71] with continuous improvements to both strength and toughness through improved knowledge of microstructure and properties achievable with alloy selection and thermo mechanical controlled processing (TMCP) [208]. The use of high-strength steel allows significant cost savings to be realized by the pipeline industry via reduced tonnage of steel required for pipe production, reduced weight for transportation and in the reduction of welding time required for mainline girth and tie-in welding operations [16]. The mechanization of welding techniques to maximize productivity can realize significant cost savings on long transmission lines. However, the mechanization of pulsed – gas metal arc welding (P-GMAW) techniques has lead to the reduction of heat input with a corresponding increase in cooling rates (shorter cooling times) within the weld heat affected zone (HAZ) [66]. Microstructural evolution in steel as a function of distance from the fusion line is well understood [123] with the development of grain coarsened



(GC) fine grain (FG), inter-critical (IC) and sub-critical (SC) regions forming as a function of decreasing peak temperature. Mechanized P-GMAW heat affected zones are difficult to study because the full range of HAZ sub groups are produced over a limited area compared to higher heat input techniques [158]. The design microstructure for the steel can be entirely destroyed in the HAZ, understanding the implication of the HAZ on mechanical properties becomes critically important to overall design.

Part of the versatility that steel enjoys as a structural construction material is due to the allotropic nature of iron, the primary component of steel alloys. Many different morphologies can be realized from a single steel alloy by exploiting the solubility differences of carbon and alloying elements within the body centered cubic (BCC) ferrite phase (α) and the face centered cubic (FCC) austenite phase (γ) of iron. Steel is by definition an alloy of carbon and iron where the maximum solubility of carbon in ferrite decreases from 0.021% at 910°C to 0.005% at 0 °C while austenite has a maximum solubility of 2.04 % at 1146 °C [18]. Different morphologies of steel are created by manipulating the cooling rate and the thus the diffusion of carbon. When the cooling rate is slow, carbon and ferrite can form from the austenite matrix concurrently through reconstructive diffusion reactions [126]. Fast cooling rates limit diffusion and result in displacive transformation reactions. Quenching steel to prevent all carbon diffusion results in martensite (α'), a highly dislocated body centered tetragonal (BCT) structure. This versatility also provides engineering challenges when a controlled microstructure designed into the pipe through TMCP is subjected to high peak temperatures associated with the GC-HAZ. The GC-HAZ is notoriously the region of a weldment with the poorest mechanical properties owing to the large, coarse grains that do little to deflect the path of propagating cracks [209]. Understanding the welding procedures that generate enhanced GC-HAZ microstructures can help optimize the overall mechanical performance.



One technique to monitor the evolution of microstructures as a function of temperature is dilatometry which exploits the differences in density between γ , α and α' [183, 188, 191, 210]. Continuous cooling transformation (CCT) diagrams indicate the start and finish temperatures for the γ to α reaction for a range of cooling rates. The application of CCT diagrams to welding is important so that proper procedures can be selected to ensure adequate mechanical property compliance is achievable [182]. Correlating the transformation behaviour with mechanical properties is critical for the safe design of welded joints. In this study, CCT diagrams for the GC-HAZ of three modern X100 pipe steels are developed and are used to establish correlations between the resultant microstructures and notch toughness. The thermal simulation is achieved using physical specimens cut from line pipe and thermally cycled using a Gleeble 3800.

5.4 Experimental

Three different commercially produced X100 (grade 690) pipes were used for this study, labeled X100-2, X100-5 and X100-4. A series of monitored welds were made using a solid Union NiMo80 electrode wire and an automated single torch P-GMAW technique. The welding head was maintained at a constant 1 o'clock position while the pipe was rolled (1G position). The welds were then sectioned and studied for metallographic and material properties. The three X100 pipes were characterized by chemical analysis, Charpy impact, dilatometry, Vickers hardness, light optical and electron microscopy.

5.4.1 Materials

The large diameter pipes used were low alloy thermo-mechanical controlled processed (TMCP) with a minimum specified yield strength of 690 MPa (100 ksi). The composition and carbon equivalents calculated from the following equations are presented in Table 5-1 [22].



CCT diagrams and impact toughness applicable to the GC HAZ region generated in X100 line pipe

$$CE_{IW} = C + \frac{Mn}{6} + \frac{Cu + Ni}{15} + \frac{Cr + Mo + V}{5}$$

Equation 5-1

$$P_{cm} = C + \frac{Si}{30} + \frac{Mn}{20} + \frac{Cu}{20} + \frac{Ni}{60} + \frac{Cr}{20} + \frac{Mo}{15} + \frac{V}{10} + 5B$$

Equation 5-2

Table 5-1- X100 composition and calculated values

X	C	Mn	Si	Nb	Ti	V	N	Mo+Cr	Cu	Ni	CE _{IW}	P _{cm}	B _s	M _s
100-2	0.058	1.80	0.09	0.046	0.010	0.004	0.0060	0.295	0.25	0.14	0.43	0.18	628	467
100-5	0.061	1.76	0.10	0.029	0.012	0.004	0.0025	0.239	0.28	0.50	0.47	0.20	612	459
100-4	0.050	1.87	0.19	0.030	0.010	0.004	0.0030	0.65	0.45	0.44	0.55	0.21	585	457

In general X100-2 has a baseline chemistry to which nickel is added in X100-5 and nickel, molybdenum and chromium in X100-4. The martensite and bainite start temperatures as calculated from Steven and Haynes' equations are also presented in Table 5-1 [195]. The initial microstructures of the line pipe are presented in Figure 5-1.

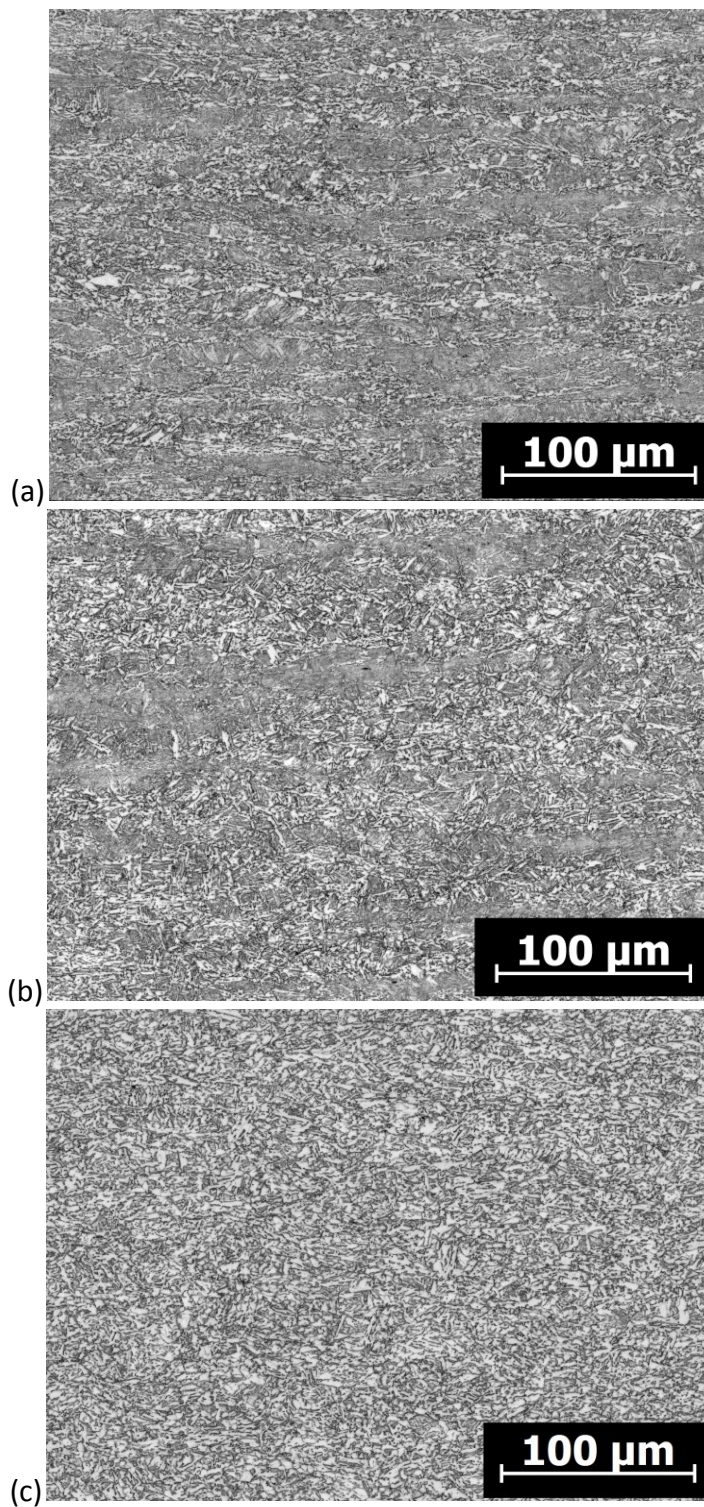


Figure 5-1- Microstructure of the pipe materials. (a) X100-2 (b) X100-5 (c) X100-4



The microstructure of X100-2 and X100-5 consist of fine bainite and martensite with occasional intercritical ferrite also observed. In this case significant banding is apparent in the microstructure owing to the steelmaking and thermo-mechanical processing used in steel production. The structure of X100-4 was predominately bainite with some polygonal ferrite. Specimens were cut from mid wall of the pipes as cuboid bars 76 mm long with a 10 mm square cross section. The long axis of the specimen was parallel to the pipe axis and the specimens were labeled to maintain the interior and exterior pipe diameter relation.

5.4.2 Thermal Cycles and Testing Procedures

The specimen bars were thermally cycled in a Gleeble 2000 and a Gleeble 3800 using parameters adopted from the data generated in the weld trials. A series of Rykalin 3D cooling curves were designed to simulated the thermal profile characteristic of the GC-HAZ region formed over a range of cooling times [157].

Specimens destined for Charpy impact testing were cycled as cuboids which were then reduced to specification (10 x 10 x 55 mm) and notched through thickness to asses transverse to the pipe axis (TPA) toughness properties. Testing was conducted in a TINIUS OLSEN Model #64 impact tester from 20 °C to -140 °C. The un-notched Charpy bar blanks will be referred to simply as Gleeble bars. The specimens for dilatometric analysis were reduced at mid length to a cylinder of 6 mm diameter over 6 mm length. To assist in the examination of phases formed at extreme cooling rates, a few specimens were reduced to a 4 mm diameter over the 6 mm length. The expansion and contraction of the steel was monitored with the supplied linear variable differential transformer (LVDT). The LVDT was placed at the exact mid length of the reduced section. Thermal control was maintained via a Type K thermocouple welded to the surface of the specimen. The radial expansion/contraction of the steel was then correlated to temperature.



All specimens, Charpy and dilatometric, were heated at $300\text{ }^{\circ}\text{C s}^{-1}$ to a peak temperature of $1350\text{ }^{\circ}\text{C}$ and held for 1 second. The specimens were then cooled at a variety of rates such that the time taken to cool from $800\text{ }^{\circ}\text{C}$ to $500\text{ }^{\circ}\text{C}$ (Δt_{8-5}) was 1.2, 2, 3, 5, 6, 7, 16, 30 and 50 seconds. The temperatures for the resulting transformations were obtained from the dilatation curves and subsequently plotted as a GC HAZ continuous cooling transformation (CCT) diagram. The majority of the thermal cycles were selected to reflect the P-GMAW parameters and focus on shorter cooling rates, while the longer times were used to establish the transformation behaviors of the steels over a wider range of simulation conditions.

The specimens were held in water cooled solid copper blocks with a pressure fit to ensure optimal heat conduction. The free-span between the grips was set and maintained at 15mm after the results of initial testing. Thermal simulation is always a balance between the desired outcome and what can be realistically achieved. Thermal cycles corresponding to a 1 kJmm^{-1} low heat input P-GMAW weld have a Δt_{8-5} between 3 and 5 seconds depending on intrinsic variables and factors like pre heat [158]. The cooling rates achievable with the Gleeble are dependent upon the sample geometry and mass, along with the rate of heat extraction. For standard size Charpy V notch impact bars, there is very little that can be done to minimize the geometry or mass, the only option is to reduce the free span between the copper cooled jaws. Due to the joule heating of the Gleeble system, there is a maximum resistance at the midpoint between the conductive grips. It is critical that the control thermocouple be positioned at this point to maintain a symmetrical thermal profile [177]. The width of the uniform thermal zone is a direct function of the free span, with a reduction of the free span resulting in a compression of the thermal profile.



5.4.3 Metallography & Micro hardness

Metallographic analysis of the Gleeble simulated specimens was achieved by removing the 6 mm reduced section of the specimen and cutting 2 mm away from the thermocouple. The section was then vacuum mounted in clear epoxy. The samples were ground flush to the thermocouple plane to guarantee correlation of the thermal cycle and the microstructure. Grinding and polishing were achieved using diamond suspensions to a size of 1 μm followed by a final colloidal silica polish of 0.05 μm . Samples were etched using a 3% Nital solution for 8-12 seconds. The microstructures were examined using an optical microscope at a range of magnifications. Micro hardness was measured using a Clemex micro hardness indenter at 300 gram force and the values reported in the CCT diagrams are the average of a minimum of 10 indents. Full hardness maps were made where applicable using a square grid spacing of 500 μm over the entire specimen. Scanning electron microscopy was performed on a JEOL JCM-500 NeoScope. Selected specimens were prepared for TEM analysis to confirm the interpretation and classification of the microstructures identified optically and with SEM. Samples were cut with a precision saw using a general purpose diamond wafering blade. A slice of 500 μm thick was made. Discs were punched with a Gatan 3.0 mm diameter punch. The samples were reduced using silicon carbide 240, 320, 400, 600 and 1200 grit papers to reduce thickness of pieces equally on both sides. Approximately 40-50 μm thick samples were obtained. Samples were dimpled using 3 μm diamond paste and 4-6 μm CBN to a depth of approximately 30 μm and then fine dimpled using $\frac{1}{4}$ μm diamond for about 1 min. Ion milling was carried out using Gatan Duo-Mill with liquid nitrogen cold stage to prevent heating of sample.

TEM examination was carried out using a Philips CM20 FEG TEM equipped with a Schottky field emission gun that was operated at a voltage of 200 kV.



5.5 Results and discussion

5.5.1 Single Torch Rolled Weld Macrostructure and hardness

The HAZ regions developed in X100-5 in Figure 5-2 have been evaluated with the series of microhardness indents visible along the fusion line and at the top, sub cap, and mid thickness positions in Figure 5-2 (a). The overall width of the HAZ is narrow and generally does not extend beyond approximately 2000 μm as seen in Figure 5-2 (a). The microhardness indents along the fusion line visible in Figure 5-2 were placed manually at a distance of 50 to 100 μm from the fusion line and an indent into the GC HAZ can be seen in Figure 5-2 (b). In this case the influence of reheating the GC HAZ by successive weld passes is evaluated. The GC-HAZ average hardness along the fusion line is $272 \text{ HV} \pm 22$ and the width of the GC-HAZ is approximately 100 to 200 μm . The first eight measurements beneath the cap pass provide an indication of the hardness of the GC-HAZ with an average of $309 \pm 14 \text{ HV}$, which corresponds to the GC-HAZ subjected to only one thermal cycle.

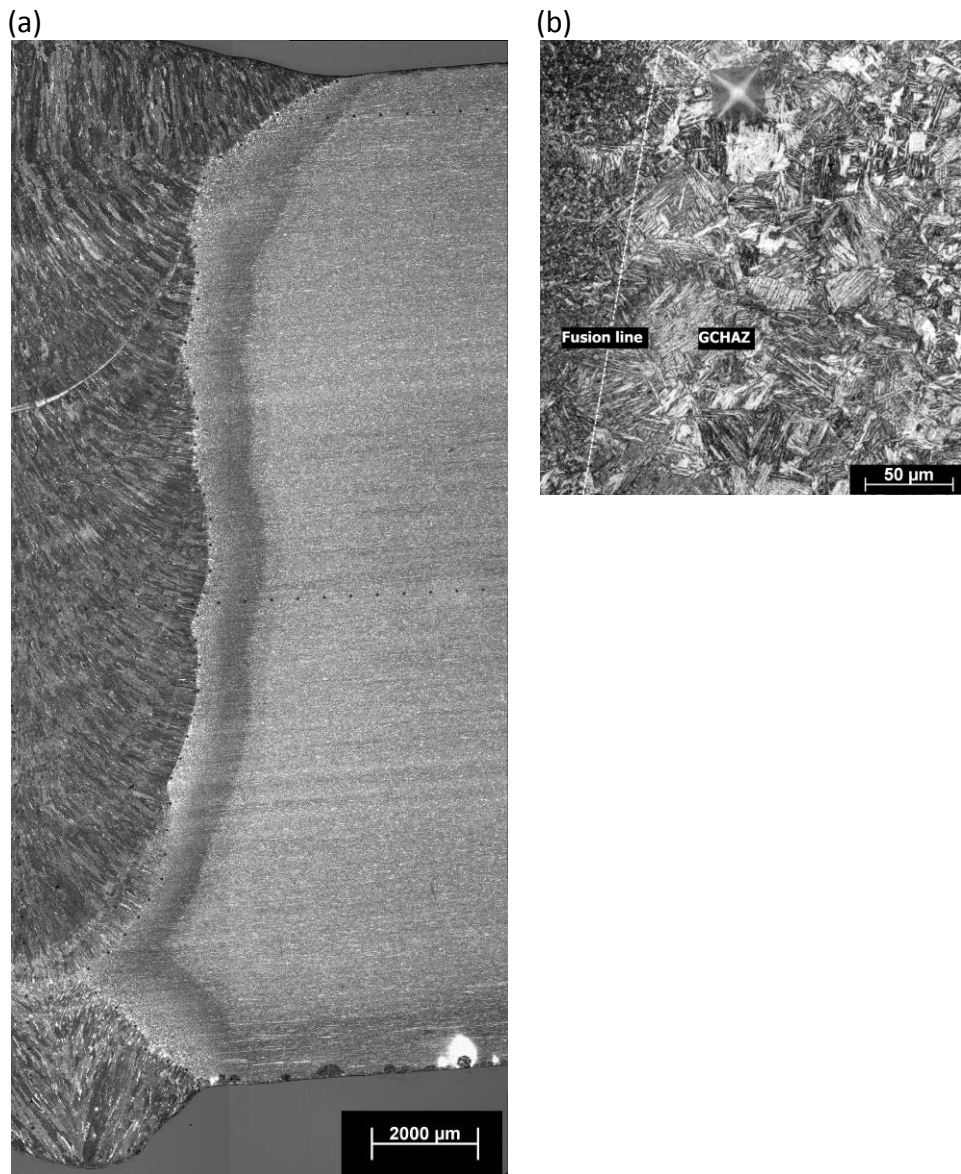


Figure 5-2–The HAZ region developed from P-GMAW in the X100-5 steel (a) Macrograph (b) detail showing width of the GC-HAZ



5.5.2 Microstructure and CCT Diagrams

The microstructure evolved as a function of cooling rate from a peak temperature of 1350 °C has been established for the three steels by dilatometry and direct observation. The dilatometric curves have been analyzed and correlated to produce CCT diagrams for the GC-HAZ simulated region from a 1350 °C peak temperature. The CCT diagram for X100-2 is given in Figure 5-3 and shows three phases forming, martensite(M), bainite (B) and granular bainite (GB)[130].

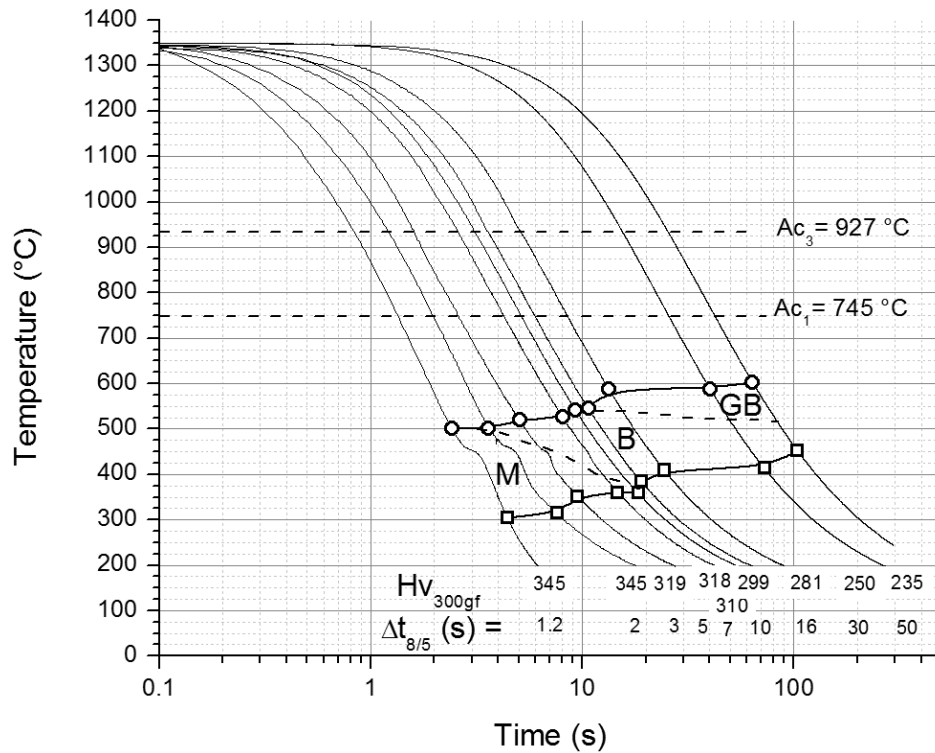


Figure 5-3– CCT diagram for X100-2 from 1350 °C showing the formation of martensite (M), bainite (B) and granular bainite (GB)

The martensite structure developed in X100-2 can be seen in Figure 5-4 (a) and corresponds to the measured start Hv temperature from Figure 5-3 of 501 °C. The Vickers



hardness is 345 HV at 300 gram force load. There is a plateau for the martensite start temperature over 2 cooling rates with identical hardness values measured for each. The formation of bainite begins at $\Delta t_{8-5} = 3s$ and is denoted by an 18 °C increase in the transformation start temperature to 519 °C with a corresponding decrease in the hardness to 319 HV. SEM micrographs of the martensitic, bainitic and granular bainite structures can be seen in Figure 5-4 (a) through (c) respectively.

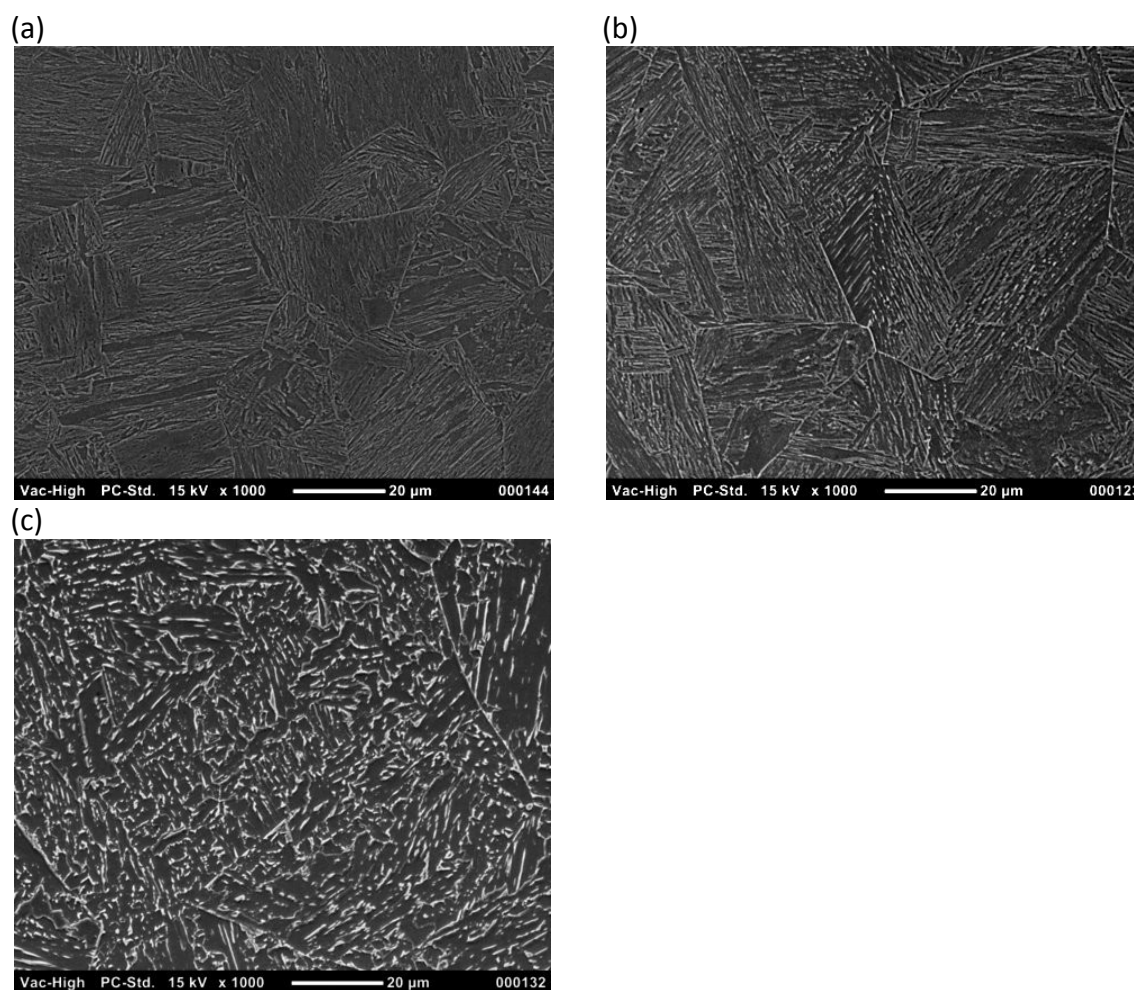


Figure 5-4– SEM of (a) martensite, $\Delta t_{8-5} = 1.2s$ (b) bainite and martensite, $\Delta t_{8-5} = 3s$ (c) bainite and granular bainite, $\Delta t_{8-5} = 50s$, in X100-2



The formation of granular bainite begins at a relatively fast cooling time of $\Delta t_{8-5} > 10s$ and the transformation start temperature rises from 546 °C to 588 °C. The appearance of coarse bainitic ferrite can be seen in Figure 5-4 (c) and is characteristic of granular bainite [130]. While the cooling rate found here for the formation of granular bainite is relatively fast, it is well within the limits proposed by Wilson [132]. At a heating rate of $300\text{ }^\circ\text{C s}^{-1}$, the Ac_1 and Ac_3 temperatures have been measured to be 745 °C and 927 °C respectively.

The evolution of the microstructure for the X100-05 steel is presented as a CCT diagram in Figure 5-5 and shows a similar formation of phases as the X100-2 steel.

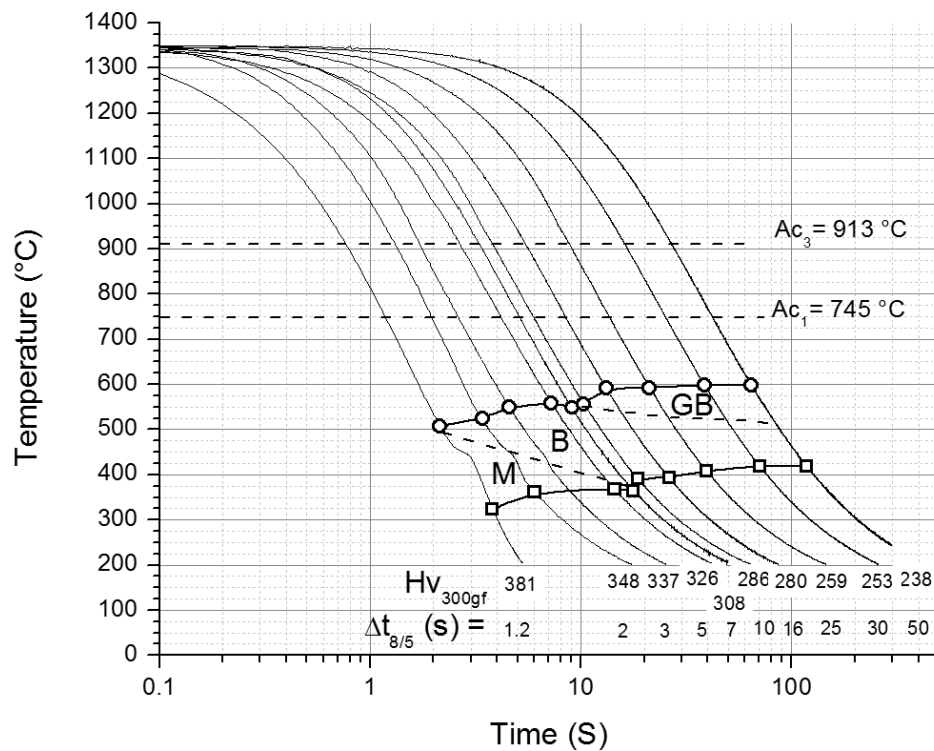


Figure 5-5- CCT diagram for X100-5 from 1350 °C showing the formation of martensite (M), bainite (B) and granular bainite (GB)



Micrographs characteristic of the austenite reaction products are presented in Figure 5-6 (a) through (c). Martensite forms at $\Delta t_{8-5} < 5s$ with the austenite decomposition forming bainite at $\Delta t_{8-5} > 2s$. At the fastest cooling achieved, $\Delta t_{8-5} = 1.2 s$, the hardness was measured as 381 HV. There is an increase in the transformation start temperature to 558 °C at $\Delta t_{8-5} = 5s$ with a decrease in the hardness to 308 HV. The bainite formed at this range is shown in Figure 5-6 (b). At $\Delta t_{8-5} > 7s$ granular bainite begins to form and an SEM of the microstructure is presented in Figure 5-6 (c). At $\Delta t_{8-5} = 50s$ the hardness is 238 HV with a mixed microstructure of bainite and granular bainite. The Ac_1 and Ac_3 temperatures for X100-05 were measured as 745 °C and 913 °C respectively at 300 °C s^{-1} . The hardness developed in the GC-HAZ of the real weld at 309 HV corresponds to a Δt_{8-5} of 6 s, which has a simulated energy of 1.9 kJ mm^{-1} .

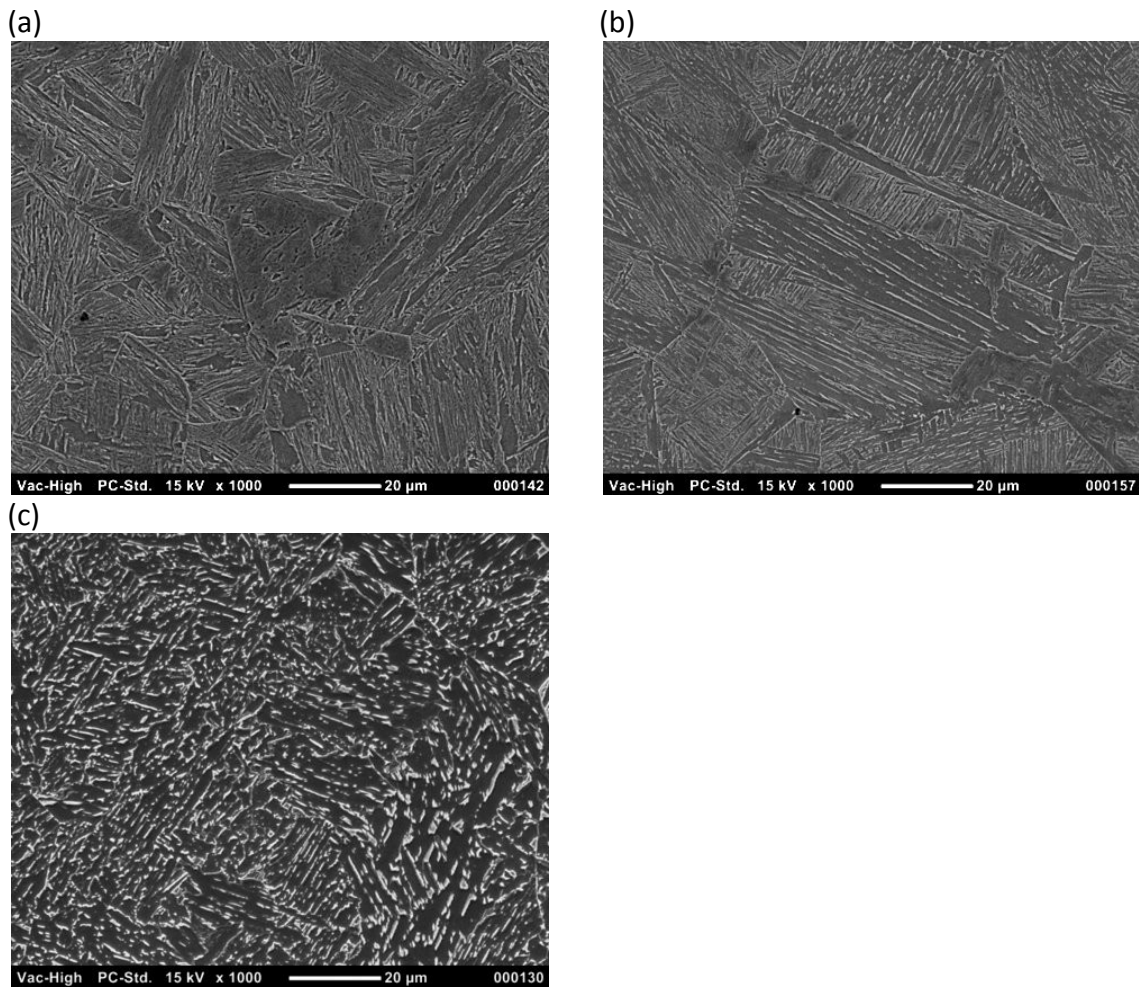


Figure 5-6– SEM of (a) martensite, $\Delta t_{8-5} = 1.2s$ (b) bainite and martensite, $\Delta t_{8-5} = 3s$ (c) bainite and granular bainite, $\Delta t_{8-5} = 50s$, in X100-5

The microstructure developed in the real weld GC-HAZ and the simulated GC-HAZ at $\Delta t_{8-5} = 6 s$ can be seen in Figure 5-7. There is excellent likeness in the bainite formed in both the real and simulated GC-HAZ.



CCT diagrams and impact toughness applicable to the GC HAZ region generated in X100 line pipe

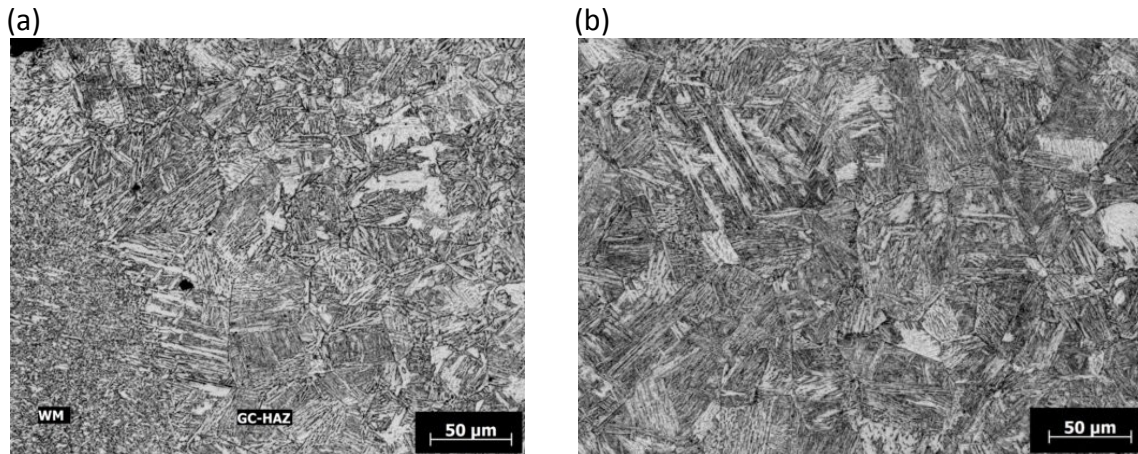


Figure 5-7– GC-HAZ in X100-5 (a) real weld (b) simulated at $\Delta t_{8-5} = 6 \text{ s}$, 1.9 kJmm^{-1}

Steel X100-4 shows a mild increase in the transformation start temperature from 501 °C to 515 °C over a Δt_{8-5} of 2 to 10 s as shown in the CCT diagram in Figure 5-8.

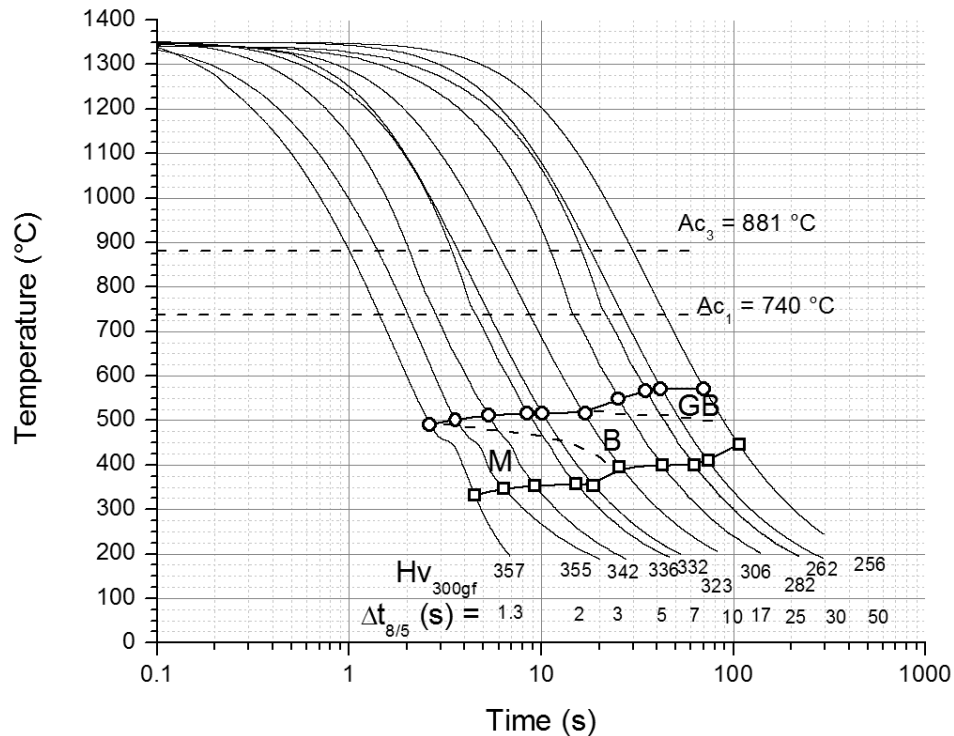


Figure 5-8- CCT diagram for X100-4 from 1350 °C showing the formation of martensite (M), bainite (B) and granular bainite (GB)



The measured martensite start temperature is 491 °C which is more than 30 degrees above that predicted in Table 5-1. The hardness of 357 HV for the $\Delta t_{8-5} = 1.3s$ combined with the developed microstructure shown in Figure 5-9 (a) indicate that the GC HAZ will be primarily martensitic at fast cooling over a much greater cooling range than the other steels. The mild decrease in hardness to 323 HV at $\Delta t_{8-5} = 10 s$ gives a good plateau for bainite formation which is easily achievable with P-GMAW welding techniques.

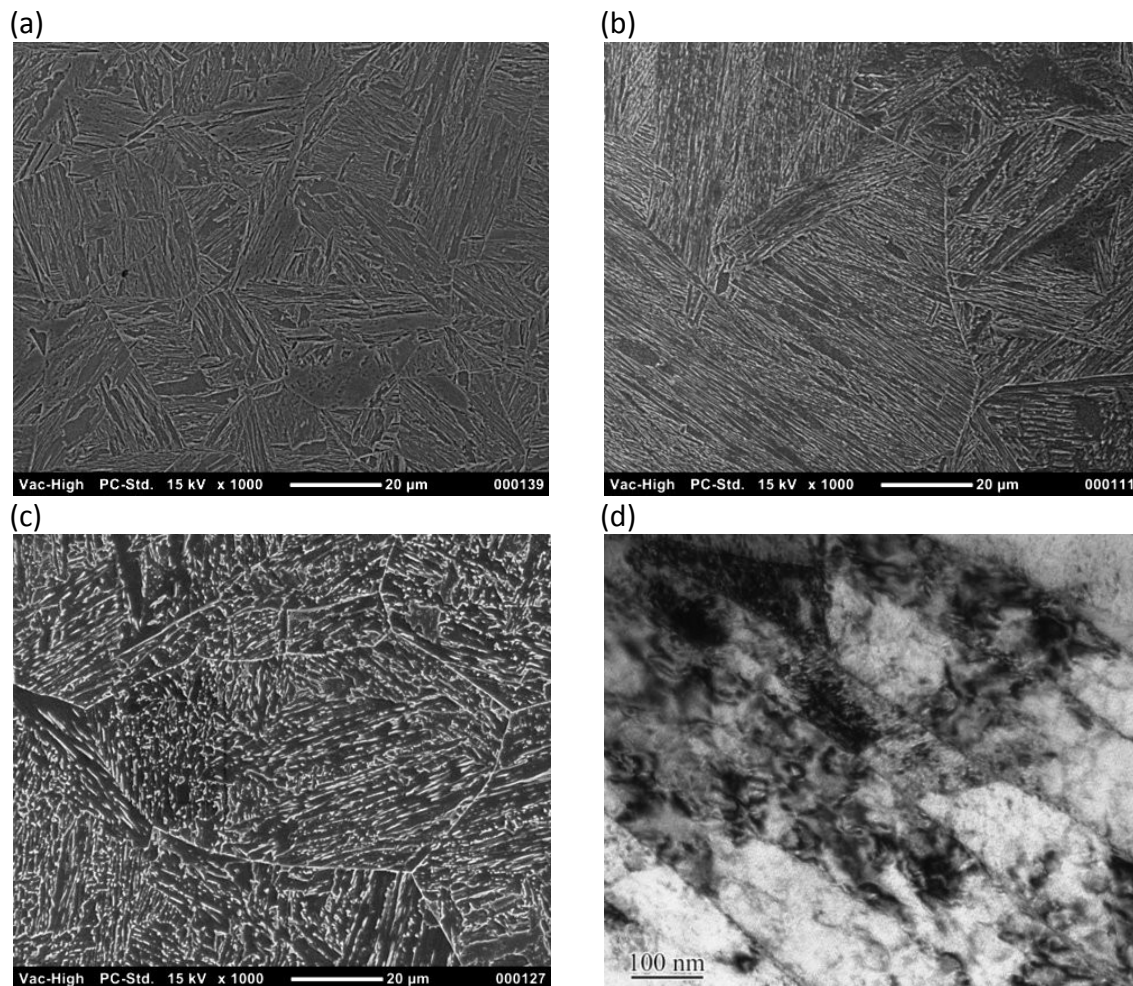


Figure 5-9- SEM of X100-4 (a) martensite, $\Delta t_{8-5} = 1.2s$ (b) bainite and martensite, $\Delta t_{8-5} = 3s$ (c) bainite and granular bainite, $\Delta t_{8-5} = 50s$ (d) TEM of lath martensite



The SEM image of MA in Figure 5-9 (c) formed at longer cooling times is indicative of granular bainite. The transformation start temperature plateaus over the last two cooling rates at 570 °C which is only 15 degrees shy of the predicted bainite start temperature. The Ac_1 and Ac_3 temperatures for X100-4 were measured to be 740 °C and 881 °C respectively. TEM of selected microstructures was conducted to aide in confirmation of optical and SEM microscopy. Figure 5-9 (d) shows lath martensite.

In all three cases it was found that the formation of granular bainite occurs at high temperatures and slower cooling rates than bainite. This is agreement with Sun *et al.* who report the formation of granular bainite in a 610 MPa HSLA steel [146]. The islands of martensite or martensite-austenite dispersed in equiaxed bainite grains form at the lower cooling rates as solute is rejected from the transforming bainitic ferrite into the remaining austenite. This solute enrichment increases constitutional undercooling of the austenite phase which either transforms to martensite once the M_s temperature for the new composition is reached or is sufficiently stabilized to remain as austenite at room temperature [141, 211].

The bainite sheaves can be seen to nucleate and grow from the prior austenite grain boundaries in Figure 5-4, Figure 5-6, and Figure 5-9 for each of the steels. Tang and Strumpf, along with others found that deformation is critical to nucleating acicular ferrite in Nb alloyed pipe steels of similar compositions [212, 213]. The same steels processed without deformation results in bainitic microstructures, similar to those found here, at rapid cooling rates where the energy to nucleate bainite at the prior austenite grain boundaries is high. The high peak temperature used in these thermal cycles allows complete re-austenitizing of the steel and eliminates the high density of dislocations that are reported to aide in nucleation of acicular ferrite. The effect of the Mo and Cr alloying elements added to X100-4 can be seen when the CCT diagrams of X100-4 and X100-5 are compared (Figure 5-8 and Figure 5-5) and the suppression of the austenite



transformation start temperature seen in X100-4 is readily noticeable. This is most probably more the effect of Mo than Cr as was found by Ha *et al* [214].

5.5.3 Simulated Properties

The results of trials conducted with Charpy bars to measure the width of the thermal zone as a function of the free span are shown in Figure 5-10 for the X100-4 steel, with identical results found for the remaining compositions.

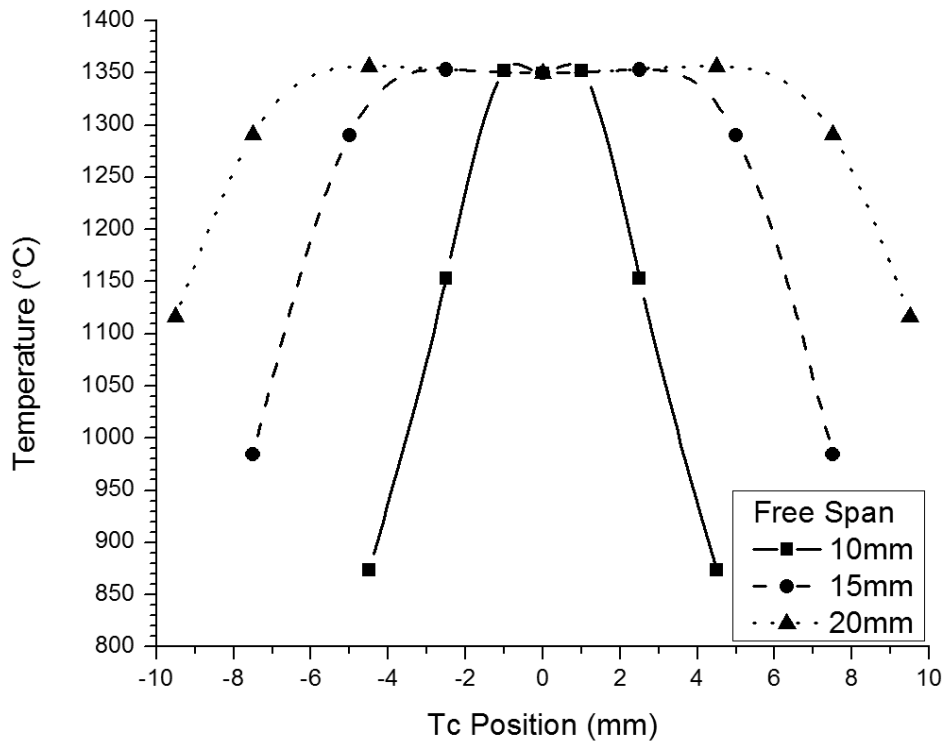


Figure 5-10- Peak pipe temperature distribution for a 10 x 10 mm bar as a function of free span

The advantage of narrow free spans is shorter cooling times which have a greater applicability to P-GMAW parameters, with the disadvantage of a reduced uniform thermal zone and potentially inhomogeneous properties. Due to the stochastic nature of



Charpy impact testing where cracks propagate along the path of least resistance, a 15 mm free span was chosen for thermal cycles to provide a wider thermally cycled zone with homogeneous properties. The fastest consistent Δt_{8-5} cooling time achievable for the 15 mm free span was found to be 6 seconds. A macrograph of an X100-4 Charpy specimen cycled at 6s is presented in Figure 5-11 along with a hardness map of the entire specimen bar.

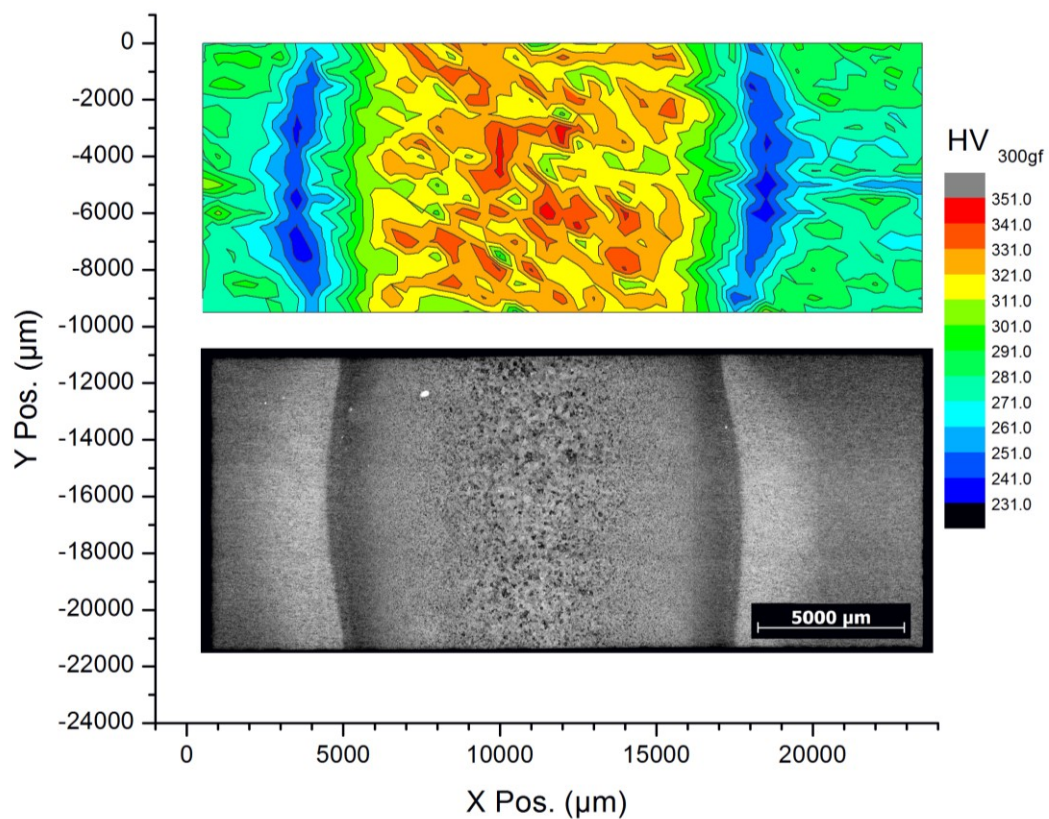


Figure 5-11- X100-4 specimen after a $\Delta t_{8-5} = 6s$ thermal cycle at a 15 mm free span showing the hardness distribution across the thermal zone.

Both the map and macrograph are presented at identical scales to facilitate direct comparison. The width of the zone of uniform hardness matches the width of uniform peak temperature predicted in Figure 5-10 of approximately 6000 μm (6 mm). However,



it can be clearly seen in Figure 5-11 that the uniform GC HAZ does not extend over 6000 μm and is in fact only ~ 3500 μm wide. The notching of Charpy impact bars was thus ensured to be as precise as achievable such that the induced crack would propagate through the GC HAZ region only. The results of free span trials conducted at 10, 15 and 20 mm spacings for $\Delta t_{8.5} = 10\text{s}$ are shown in Figure 5-12. It should be noted that the scaling used in Figure 5-12 is consistent, but the Y values have been offset to accommodate all three plots. The variation in hardness seen here has not been reported anywhere else to the best of the author's knowledge.

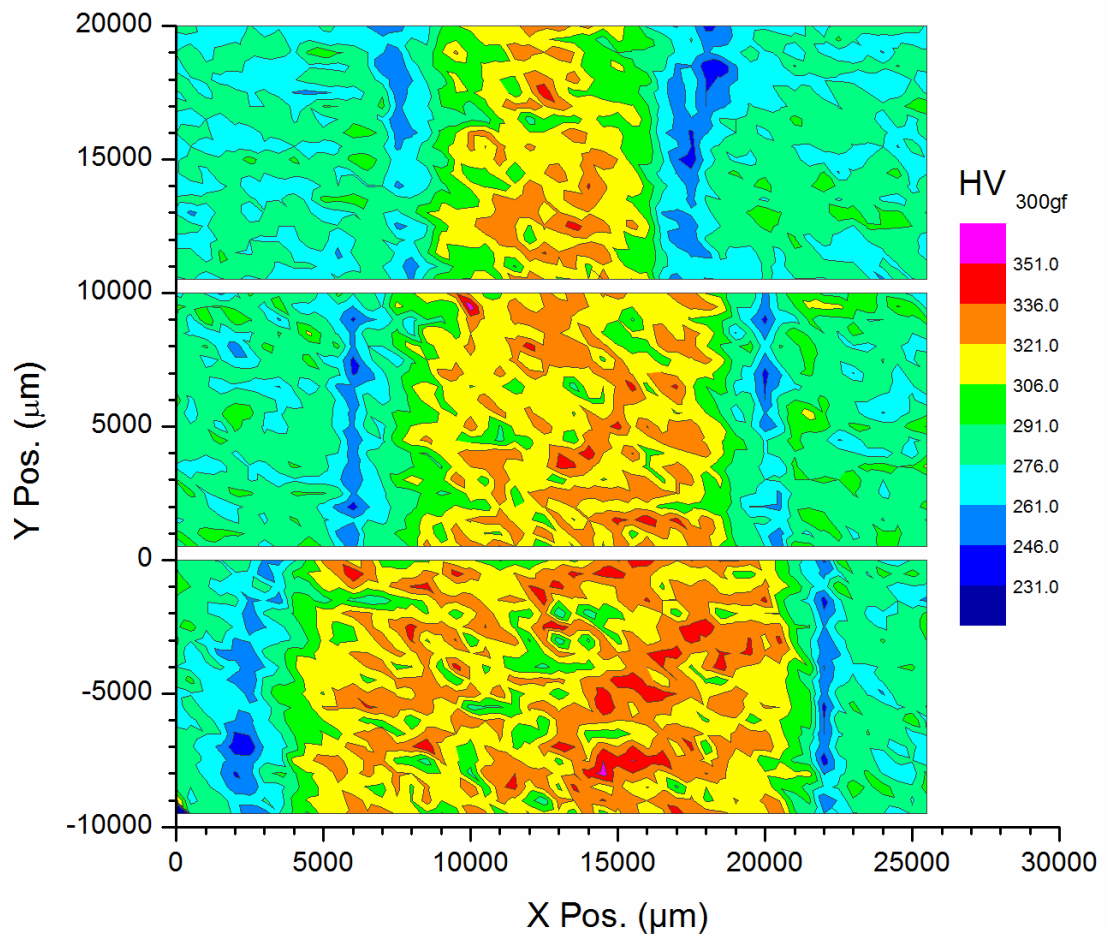


Figure 5-12 – Hardness profiles developed in X100-4 with $\Delta t_{8.5} = 10\text{s}$ at grip spacing of 10, 15 and 20 mm from top to bottom



5.5.4 Mechanical Properties

The absorbed impact energy for the base metal of each pipe was established as a baseline and to ensure that the ductile to brittle transition temperature (DBTT) was greater than the application specification of -20 °C. The plots of absorbed energy as a function of test temperature are given in Figure 5-13 (a) for X100-2, X100-5 and X100-4 base metals and the GC HAZ data are plotted against the base metal in Figure 5-13 (b) through (d) for X100-2, X100-5 and X100-4 respectively.

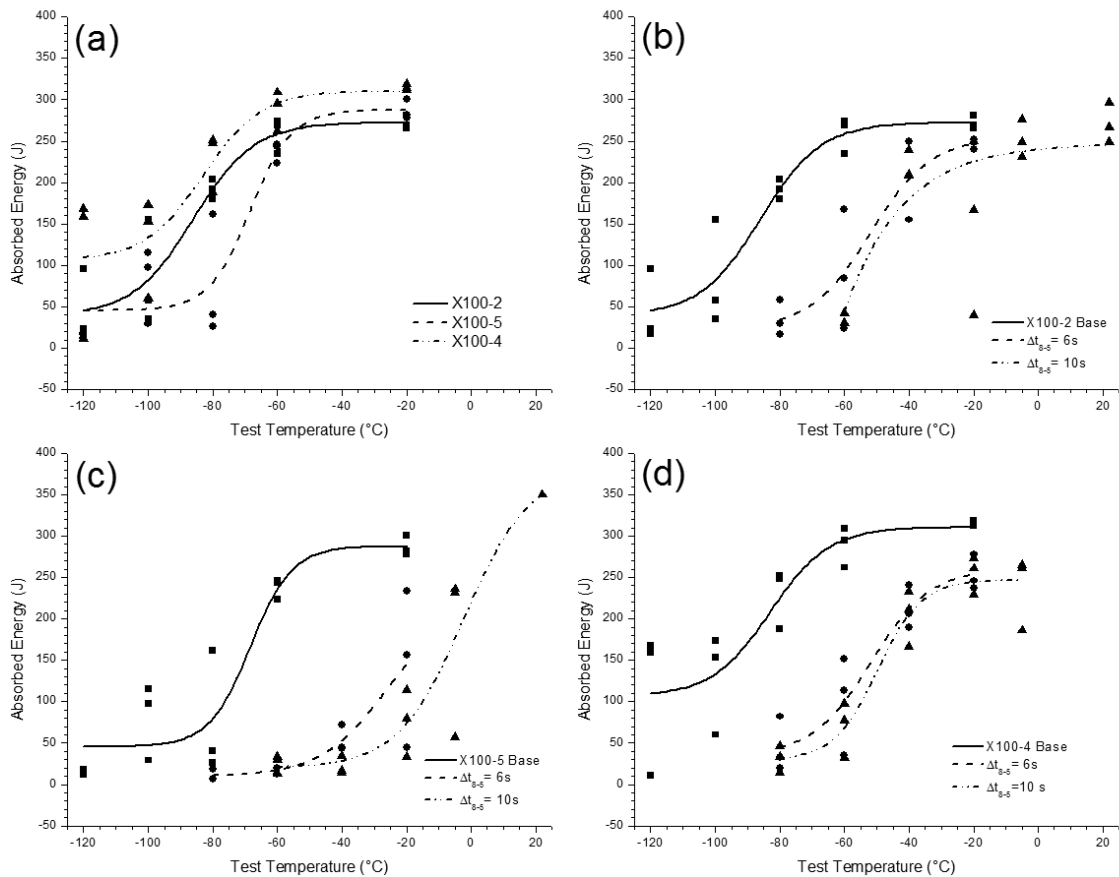


Figure 5-13 – Impact energy results (a) base metal (b) X100-2 (c) X100-5 (d) X100-4



The data was fit using a sigmoidal Boltzmann equation. The energy transition temperature (ETT), the temperature corresponding to the average of the upper and lower shelf energies, for the base metals is excellent at approximately $-85\text{ }^{\circ}\text{C}$ for both X100-2 and X100-4, and $-70\text{ }^{\circ}\text{C}$ for x100-5. From the fracture surfaces for X100-2 broken at $-20\text{ }^{\circ}\text{C}$ and $-100\text{ }^{\circ}\text{C}$ it is evident that the ductile tearing has occurred at $-20\text{ }^{\circ}\text{C}$ while brittle fracture takes place at $-100\text{ }^{\circ}\text{C}$. The same trend was observed for X100-5 with ductile tearing at higher temperatures and brittle fracture at the lower end. The upper and lower shelf impact energies were measured as $272 \pm 18\text{ J}$ and $39 \pm 28\text{ J}$ for X100-2 base metal and $46 \pm 19\text{ J}$ and $288 \pm 26\text{ J}$ for X100-5 base metal. X100-4 had the best shelf energies of the group at $106 \pm 36\text{ J}$ and $310 \pm 26\text{ J}$ for the lower and upper shelves respectively. The etched surface of an X100-5 base metal specimen broken at $-120\text{ }^{\circ}\text{C}$ is shown in Figure 5-14 where short secondary cracks can be seen to start and stop at ≈ 5 to $15\text{ }\mu\text{m}$ intervals. The small effective grain size produced by the TMCP of the pipe material affords excellent toughness.

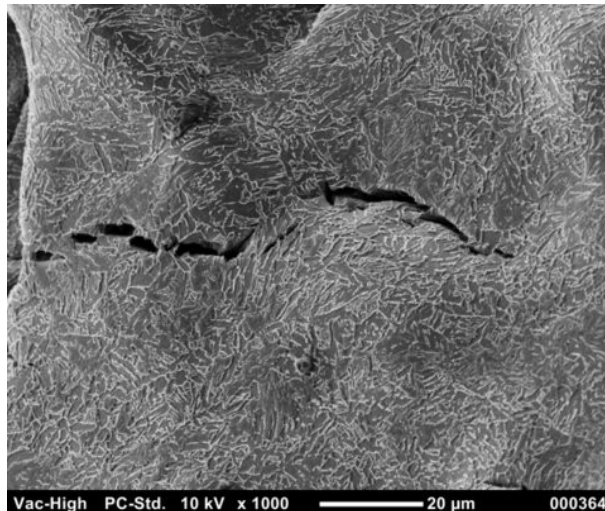


Figure 5-14 – Etched fracture surface of X100-5 BM broken at $-120\text{ }^{\circ}\text{C}$



The influence of the GC-HAZ microstructure on the impact toughness for X100-2 can be seen in Figure 5-13 (b) where the base metal DBTT curve is presented alongside the curves for X100-2 sample bars subjected to Δt_{8-5} cooling curves of 6 s and 10 s. The transition temperature is shifted to higher temperatures in both cases with an ETT of -50 °C for both with the start of transition at or above -20 °C. The upper shelf energies for X100-2 GC HAZ samples are slightly lower than the base metal at 254 ± 38 J for $\Delta t_{8-5} = 6$ s and 247 ± 56 J for $\Delta t_{8-5} = 10$ s. The fracture surface of the X100-2 specimen with a GC HAZ $\Delta t_{8-5} = 6$ s thermal cycle is shown in Figure 5-15 (a) with a detail of a cleavage facet shown in Figure 5-15 (b). The river pattern of fracture was traced to the initiation site, however multiple initiating cleavage facets were found suggesting that a number of large facets with low misorientations initiated failure rather than a second or hard phase particle [215-217].

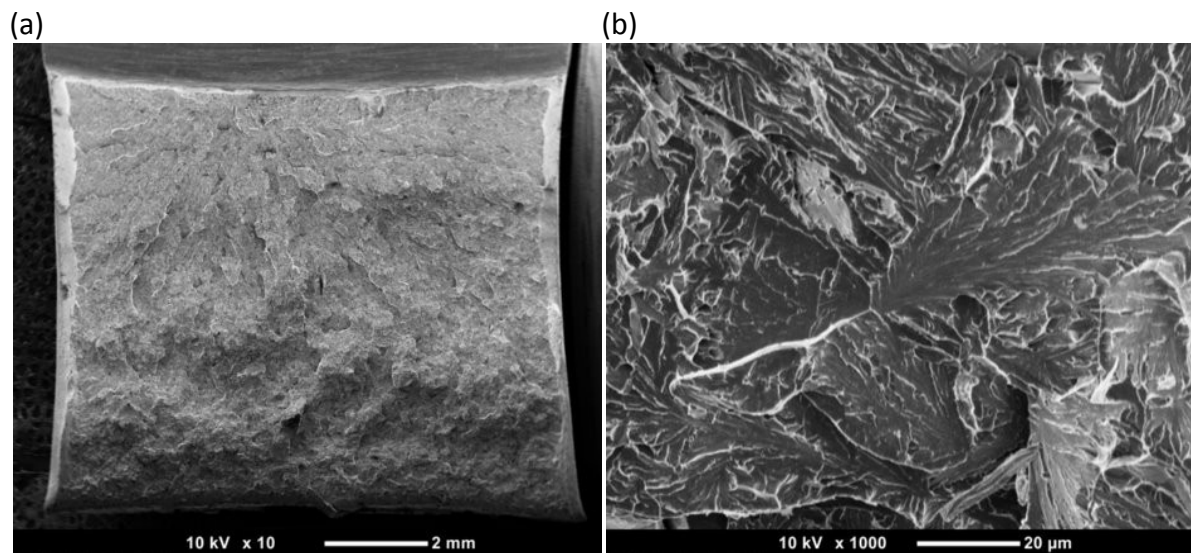


Figure 5-15– (a) Fracture surface of X100-2 GC HAZ $\Delta t_{8-5} = 6$ s (b) cleavage facet



The effect of GC-HAZ thermal cycle on the X100-5 steel is much more deleterious to the DBTT. The DBTT curves for X100-05 are given in Figure 5-13 (c) for the base metal, $\Delta t_{8-5} = 6$ s and $\Delta t_{8-5} = 10$ s thermally simulated samples. There is a drastic reduction in the DBTT temperature for X100-5 with both $\Delta t_{8-5} = 6$ and 10 s showing ETT's of -26 °C and -3 °C respectively. At -20 °C for $\Delta t_{8-5} = 6$ s the absorbed energy is 144 ± 95 J with a range of 45 J to 233 J. The drastic reduction in toughness is somewhat surprising as there is very little difference between the composition of X100-2 and X100-5 in either chemistry or starting microstructure. The fracture surface of a $\Delta t_{8-5} = 10$ s X100-5 sample tested at -120 °C is shown in Figure 5-16 (a).

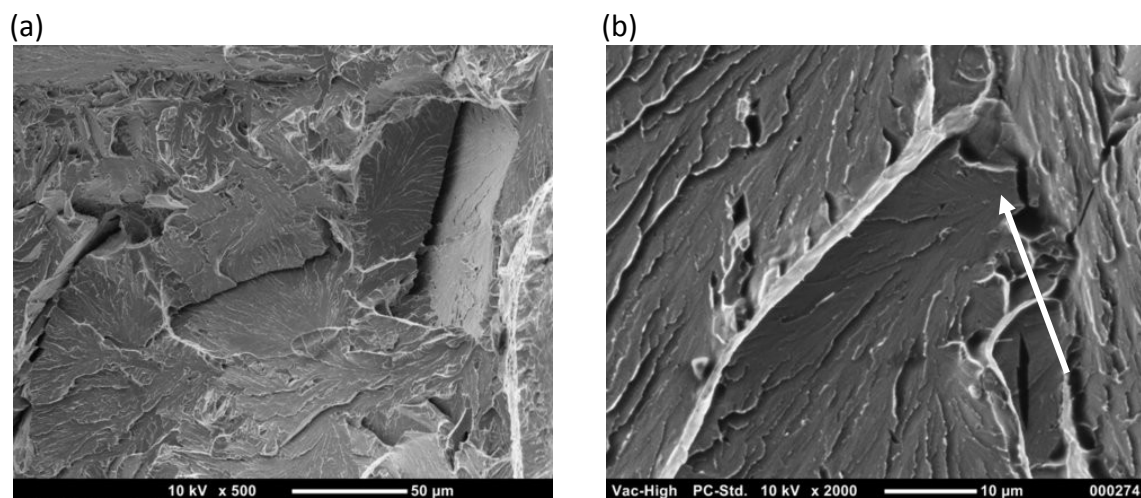


Figure 5-16 – X100-5 GC HAZ (a) large facets (b) MA (arrow)

Multiple large cleavage facets can be seen where the facet size is approximately that same as the PAG boundary. In Figure 5-16 (b) a cleavage facet originating at an MA particle can be seen. The fracture surface of the X100-5 specimens was very faceted suggesting transgranular fracture initiated by large facets with low misorientation and hard MA phase. The presence of hard second phases (MA) can strengthen steels if the correct size and distribution are maintained [214]. In these cases the cracks will pass around the second phase particles increasing the crack unit length [218]. However the opposite effect is true when the coarseness of the phases is too great and cracks are



both initiated at the second phase and propagate through them, rather than around. This is the type of fracture seen in Figure 5-16 (b) for X100-5 where cracks were initiated at the MA phase and then propagated through the coarse bainite without being deflected by other phases or high angle boundaries.

The best toughness performance can be seen in Figure 5-13 (d) for X100-4 material where the DBTT does not begin above -20 °C. The upper shelf energies for the GC HAZ simulated samples are lower than the base metal, but are still reasonable at 260 ± 32 J for $\Delta t_{8.5} = 6$ s and 246 ± 13 J for $\Delta t_{8.5} = 10$ s. More importantly, while the ETT increases from -85 °C to -50 °C between base metal and GC HAZ, there is only a 2 °C difference between the $\Delta t_{8.5} = 6$ and 10s GC HAZ samples. From the CCT diagrams and microstructural analysis, the X100-2 and X100-4 microstructures at $\Delta t_{8.5} = 6$ s are mixture of bainitic and martensite, while the X100-5 at the same rate is a mixture of bainite and granular bainite. From the mounted fracture surface for X100-4 $\Delta t_{8.5} = 6$ shown in Figure 5-17 (a), a microcrack can be seen arresting at a martensite packet. In Figure 5-17 (b), the microcrack path is tortuous with multiple deflections.

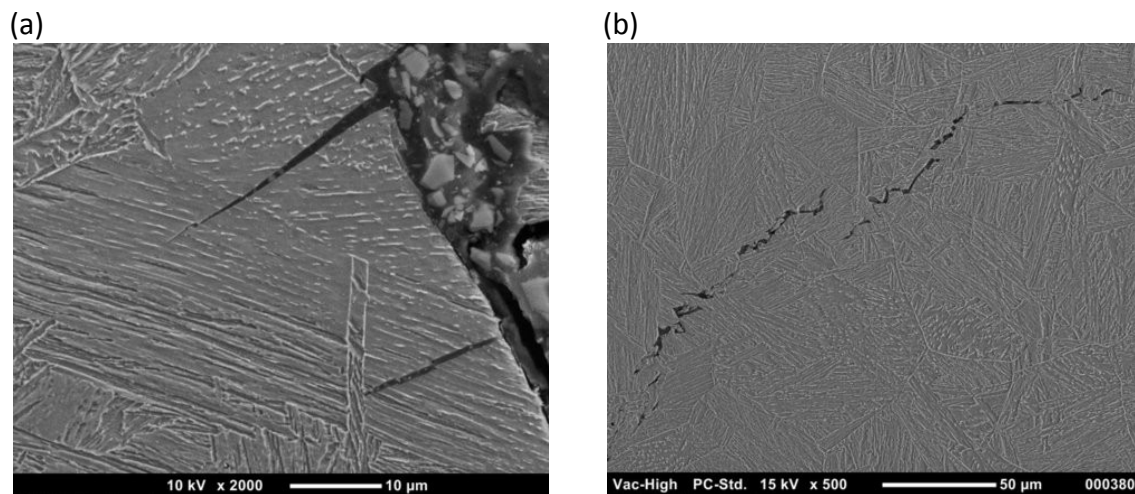


Figure 5-17 – Mounted fracture surface for X100-4 (a) GC HAZ $\Delta t_{8.5} = 6$ s (b) GC HAZ $\Delta t_{8.5} = 10$ s



The fine structure produced in X100-4 results from the higher hardenability with a suppression of the austenite transformation start and subsequently allows greater under-cooling of the austenite[219]. The prolonged bainite start with subsequent martensite transformation produced in X100-4 during austenite transformation gives a much wider operating window for welding procedures which yield acceptable properties. The increase in the prior austenite grains caused by the high peak temperature resulting from the welding heat flux increases the proeutectoid ferrite size as proposed by Umemoto *et al.* via the following relation[220]:

$$D_{\alpha}=5.7C_R^{-0.26}D_V^{0.46} \quad (4)$$

Equation 5-3

where C_R is cooling rate, D_V is the prior austenite grain size and D_{α} is the proeutectoid ferrite size. Toughness can be improved by increasing the concentration of high energy boundaries that a crack front encounters propagating through a material which require the path of the crack to deflect and thus absorb energy via stopping and re-starting[217]. Therefore finer pro-eutectoid ferrite which is favored by faster cooling rates and smaller austenite grains should enhance the toughness of the steel. Clearly from equation (4) an increase in cooling rate decreases the proeutectoid ferrite size; hence the drive towards lower energy welding procedures. Zhang and Knott [217] found that in studying the fracture toughness of bainite, martensite and mixtures of the two, that the finer microstructural features of the martensite yielded the best fracture toughness. In mixtures of bainite and martensite, the overall toughness was determined by the distribution of the phases.

Some of the scatter seen in the DBTT curves, particularly in the transition region, is likely due to the inhomogeneity developed in the thermal simulation. Analysis of the specimens could not detect any microstructural phase related discrepancy to account for the variation in hardness. As the samples were cut from the center of the specimen



where centerline segregation from the steel processing is known to occur, the variations may be the result of chemical segregation. In any case, sampling from this region with the inherent scatter produced yields a conservative evaluation which is deemed appropriate.

5.6 Conclusions

The continuous cooling transformation diagrams of three X100 line pipe steels in the GC-HAZ region of simulated P-GMAW have been created and show transformation products that range from martensite to granular bainite over a range of transformation start temperatures from 495 °C to 600 °C corresponding to Δt_{8-5} times of 1.2 to 50 seconds and heat inputs of approximately 0.3 to 15 kJmm⁻¹.

- Simulated thermal cycles with 1350 °C peak temperatures matched the single cycle GC-HAZ of the real weld most closely at $\Delta t_{8-5} = 6$ s and a simulated energy input of 1.9 kJ/mm⁻¹.
- The toughness of the materials were assessed by Charpy V notch for the base metal and CG-HAZ thermal cycles corresponding to Δt_{8-5} of 6 s and 10 s. It was found that the X100-4 steel with Ni, Mo and Cr additions had the best ETT at ~ -50 °C.
- The improved toughness of X100-4 was related to the refined bainite phase co-existing with fine lath martensite resulting from the increased hardenability and suppression of the austenite transformation start temperature.



5.7 Acknowledgements

This research was funded by CANMET-MTL and the Federal Interdepartmental Program for Energy Research and Development. The authors would like to thank Mr. M. Kerry for his machining expertise, Mr. R. Eagleson for mechanical testing, Mrs. C Bibby for TEM specimen preparation and analysis, and Ms. P. Liu for contributions to metallographic analysis and microhardness testing. The research is part of a larger consolidated program jointly funded by the Pipeline and Hazardous Materials Safety Administration of the U.S. Department of Transportation (DOT), and the Pipeline Research Council International, Inc. (PRCI). The views and conclusions in this paper are those of the authors and should not be interpreted as representing the official policies of any of these organizations.

The author (GG) also wishes to acknowledge CANMET-MTL management for providing the opportunity to work and have access to laboratory facilities during the course of this research and to NSERC and McGill University for funding grants.



6 CCT Diagrams of Weld Metal Applicable for Girth Welding of X100 line pipe

Graeme R Goodall¹, James Gianetto², John Bowker², Mathieu Brochu¹

¹McGill University, Mining and Materials Engineering, 3610 University St, Montreal, Quebec, H3A 2B2

²CANMET MTL, Ottawa, Ontario, K1A 0G1

6.1 Preface

The simulation of microstructures and properties that develop in weld metal used to overmatch high strength linepipe was studied using the techniques developed in the last two sections. Welds created using two different heat inputs were employed in manufacturing test material. A large single deposit was layered over a series of low energy multipass welds to evaluate the *in situ* properties. The continuous cooling transformation diagrams of five weld metal chemistries of varying carbon equivalents are reported. The properties developed in three of the chemistries were evaluated using full size Charpy bars thermally cycled at different cooling times.



6.2 Abstract

Continuous Cooling Transformation (CCT) diagrams for five weld metal chemistries applicable to mechanized pulsed Gas Metal Arc Weld (P-GMAW) of modern high strength pipe steel (SMYS>550 MPa) have been constructed. Welds at heat inputs of 1.5 kJmm⁻¹ and 0.5 kJmm⁻¹ have been created for simulation and analysis. Dilatometric analysis was performed on weld metal specimens cut from single pass 1.5 kJmm⁻¹ as deposited beads. A Gleeble 3800 thermomechanical simulator was used to generate synthetic welding cycles covering a range of heat inputs corresponding to $\Delta t_{8/5}$ cooling times from 1.9 to 50 seconds. The resulting microstructures were found to range from martensite to polygonal ferrite. Comparison of hardness values and microstructures between the as deposited 0.5 kJmm⁻¹ metal and the reheated weld metal from simulation are in excellent agreement.

Keywords:

CCT, Simulation, Weld Metal, Gleeble 3800, X100, Pipe Steel



6.3 Introduction

The design of welding consumables suitable for joining high strength steel is a challenge of increasing difficulty from both design criteria and mechanical compliance perspectives. The application of strain-based design to pipeline manufacture has changed both the criteria for strength overmatching and the fracture behavior of the ensuing weldment, specifically for gas pipelines in arctic regions [15, 93, 221]. Newer high strength steels are currently being developed for application in these harsh and unforgiving environments. While the design of the steel is critical, evaluating and understanding the transformation behavior of the weld metal integral to the weldment is fundamentally important.

The strength and toughness of welds is a function of their microstructure and this is dependent on the welding thermal history and weld metal chemical composition. In pipeline girth welding multiple passes are required to fill the joint. This results in both as deposited and reheated weld metal region, the proportion of which also greatly includes strength and toughness. Thermal simulation is an excellent method to evaluate the complexities of welding and produce samples that can be used to better characterize specific aspects of weld metal transformation behavior. A dilatometer can be used to measure the change in density caused by the transformation of iron between the two allotropic forms found at atmospheric pressure, austenite (γ) and ferrite (α) [188, 191, 222]. The most common measurement provided by dilatometry is a one dimensional representation of a volumetric change, i.e., the expansion or contraction along a fixed axis through the volume, as a function of thermally induced strain. Accurate translation of strain accumulated in the three dimensions to a linear measurement requires uniform strain accumulation in all three dimensions. This is most easily achieved via a homogeneous sample with a non isotropic grain structure prepared by careful melt preparation, controlled solidification and thermal aging as described by Yang and



Bhadeshia [191]. The generation of such a sample for as-deposited weld metal is virtually impossible as there are many influencing factors.

The chemical composition of a weld is different from that of the electrode due to the dilution and mixing effects from the base metal and the reactions of the electrode with the welding gas during deposition [7, 123]. The solidification of the liquid metal is initiated from the existing ferrite grains at the fusion line and grows epitaxially into the liquid metal. The columnar structure characteristic of gas metal arc (GMAW) welds results from a cellular solidification front of the δ ferrite arising from the high temperature gradient between the base metal and the liquid. Elemental segregation is possible between cells as solute is rejected by the solidifying δ -ferrite and this, combined with the moving heat source generated by the GMAW travel, results in a weld with inhomogeneous metallurgical properties [133]. However, studying the effect of imposed thermal cycles on as-deposited weld metal offers an excellent opportunity to evaluate the response of underlying weld beads to the thermal cycles generated in multi-pass welding.

Many authors and studies have advocated the benefits of reduced heat input during welding, citing the correlation of reduced heat input with a reduction in the microstructural coarseness for enhanced mechanical properties [69, 93, 223, 224]. Reducing the heat input of the weld also reduces the volume of metal which can be added as there is a finite heat flow and capacity. The resulting need for multiple weld passes to generate sufficient volume to fill the joint while maintaining a low heat input produces multiple thermal cycles within a weld and creates an inhomogeneous deposit consisting of layers with different microstructures and properties. In lower strength weld metals, particularly the C-Mn system, there is a regular microstructural evolution resulting from the reheating of the underlying weld metal to various peak temperatures [225]. In these welds, the newly deposited and solidified metal is clearly discernable



from the metal heated above the Ac_3 with subsequent grain coarsening or refining [224]. In the current drive towards manufacturing high strength steel weld metals capable of overmatching pipe steels with yield stresses in excess of 690 MPa, there has been a reduction in weld metal alloy content with the purpose of producing microstructures of fine acicular ferrite [114, 166, 226, 227]. A consequence of low heat input welding procedures with low alloy weld metals is a drastic reduction in the clarity of the zones resulting from the reheating of underlying beads. Evaluating the properties of these welds is very difficult as *in-situ* study is nearly impossible owing to the challenge of accurate data acquisition from very small physical regions. The same problem of accurate data acquisition applies to tests performed on multi-pass welds.

The welds generated for this study attempt to overcome part of this shortcoming by producing a weld with two distinct regions for study. The first is a multi-pass weld deposited with a nominal heat input of 0.5 kJmm^{-1} to generate a region characteristic of the P-GMAW process used for girth welds in joining pipe sections. A single pass weld at a higher 1.5 kJmm^{-1} nominal heat input was used to fill the remaining 50% of the joint. The single pass section could then be removed and thermally cycled to investigate what characteristic thermal cycles correspond to the low heat input multipass weld region.

The single pass region of the weld will be used to generate specimens for thermal simulation. The thermal simulation is designed to mimic P-GMAW welding thermal cycles and produce microstructures characteristic of low heat input multipass welds. The dilatometric analysis of the weld metal transformation as a function of temperature can then be compared to microstructures and properties of the as-deposited, reheated and simulated reheated weld metal.



6.4 Experimental Procedure

6.4.1 Weld and Specimen Preparation

Welds were made in flattened X100 pipe sections using five different metal-electrodes including a commercially available AWS 100s-G electrode, Bohler Welding union NiMo80. The compositions of the as-deposited weld metals are given in Table 6-1.

Table 6-1 –Composition of the as-deposited weld metal generated using different metal cored electrode chemistries

	WM1	WM2	NiMo80	MW3	WM4	Pipe
Wt %	C-Mn-Si-Mo	C-Mn-Si-Ni-Mo-Ti	C-Mn-Si-Ni-Mo-Ti	C-Mn-Si-Ni-Mo-Cr-Ti	C-Mn-Si-Ni-Mo-Cr-Ti	
C	0.084	0.064	0.100	0.087	0.093	0.061
Mn	1.6	1.5	1.4	1.5	1.6	1.78
Si	0.41	0.31	0.49	0.40	0.59	0.10
S	0.005	0.003	0.009	0.005	0.008	0.001
P	0.006	0.005	0.012	0.013	0.012	0.007
Ni	0.15	1.60	0.89	1.30	1.80	0.52
Cr	0.02	0.04	0.05	0.18	0.30	0.03
Mo	0.40	0.39	0.34	0.42	0.49	0.29
Cu	0.25	0.14	0.16	0.20	0.18	0.32
Al	0.008	0.005	0.007	0.005	0.005	0.032
Nb	0.009	0.007	0.008	0.008	0.008	0.030
V	0.004	0.004	0.005	0.005	0.006	0.004
Ti	0.008	0.015	0.029	0.028	0.022	0.008
B	<0.0005	<0.0005	<0.0005	<0.0005	<0.0005	<0.0005
O	0.044	0.042	0.045	0.040	0.032	0.001
N	0.0045	0.0047	0.0072	0.0051	0.0073	0.010
Fe	Bal.	Bal.	Bal.	Bal.	Bal.	Bal.

The welds were designed to generate two distinct zones each comprising roughly 50% of the joint and the same electrode was used for both zones. A low heat input multi-pass procedure was used to fill the first half of the joint and a 1.5 kJmm⁻¹ single pass nominal heat input bead was applied towards the cap. Mechanized pulsed gas metal arc welding (P-GMAW) was used with a robotic weld head to maintain uniform weld position and heat input throughout the procedure. The section of the pipe



containing the weldment was removed and specimens were prepared from the single bead section of the weldment for thermal simulation as shown in Figure 6-1.

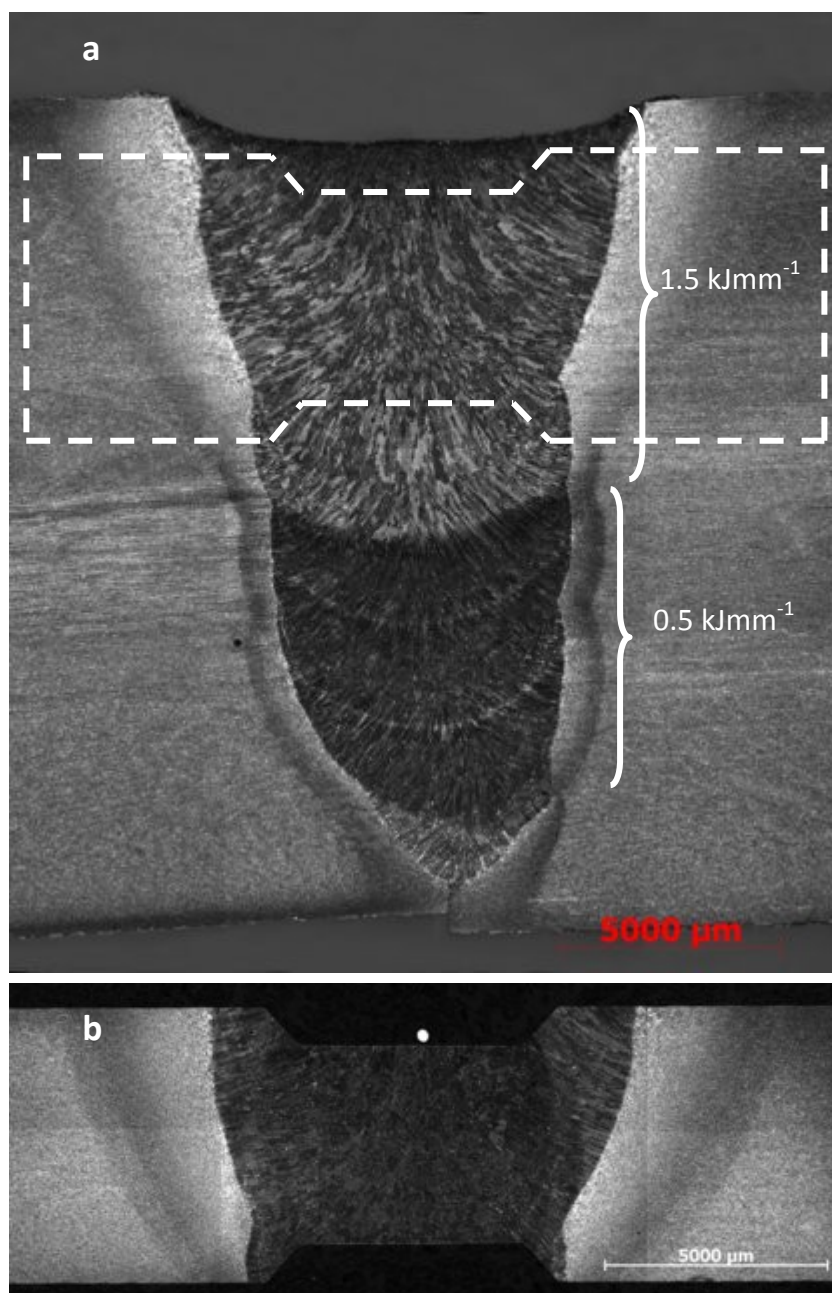


Figure 6-1 – Micrograph of the NiMo80 weld. (a) The complete weld showing the lower 0.5 KJ nominal energy input multi-pass region and upper 1.5 KJ single pass region with schematic of weld metal specimen orientation. (b) NiMo80 specimen after thermal cycling.



Specimens 6mm square and 75mm long were cut transverse to the weld length so that the single pass weld bead was located at mid length. The square bars were then rounded to a 5mm diameter at the mid-point over a 5mm length with a 45° chamfer. The resulting specimens yielded a rounded, axis symmetric zone of single pass deposited weld metal suitable for radial dilatometric analysis. The specimens were cut using computed numerical controlled electrical discharge machining (CNC – EDM) with a no-heat specification to ensure that there was no thermal cycle imposed on the samples during preparation. After every stage the newly cut forms were etched with a nital macro etchant for accurate positioning of the subsequent machining procedure.

6.4.2 Simulation

Thermal programs for a Gleeble™ 3800 thermo-mechanical simulator were designed using Rykalin [157] three dimensional cooling equations to simulate various GMAW heat input welding parameters using the following equation:

$$T - T_0 = \frac{q}{2\pi\lambda t} \exp\left(-\frac{r^2}{4kt}\right)$$

Equation 6-1

where T is the temperature, t is time, q is the heat input, λ is thermal conductivity, κ is thermal diffusivity, r is the radial distance from the weld center and T_0 is the initial temperature. The following relation was used to substitute for the radial distance r :

$$r = \sqrt{\frac{2q}{T_p c \rho \pi}}$$

Equation 6-2



where T_p is the peak temperature, c is the specific heat capacity, ρ is the density of the steel. Standard thermodynamic values for low carbon steel [228] and a 100 °C pre-heat were used in designing the cooling curves. All specimens were heated at 250 °C s⁻¹ to 1300 °C and held for one second. Different cooling curves were then imposed so that the controlled cooling time from 800 °C to 500 °C (Δt_{8-5}) increased from 3.5 to 50 seconds. Six controlled rates in all were studied to generate data for Δt_{8-5} cooling times of 3.5, 5, 7, 10, 20 and 50 seconds to keep the parameters relative to P-GMAW. As the Rykalin cooling deviates from the ASTM A1033 stipulation for linear cooling, the cooling rate measured at 700°C and the Δt_{8-5} cooling times are presented in Table 6-2.

Table 6-2 – Type of cooling curve, cooling rate at 700 °C and time to cool from 800 °C to 500 °C

Cooling Curve Type	Cooling Rate at 700 °C (°C s ⁻¹)	Δt_{8-5} (°C s ⁻¹)
Free cool	193.7	1.9
3D Rykalin	99.9	3.5
3D Rykalin	76.7	5.0
3D Rykalin	49.1	7.5
3D Rykalin	34.8	10.0
3D Rykalin	19.0	20.0
3D Rykalin	7.4	50.0

An uncontrolled free cool was also tested to ascertain the maximum cooling rate for the specimen geometry in the Gleeble system. Thermal control was maintained via a Type K thermocouple directly welded to the specimen at mid length of the reduced section. A linear variable differential transformer (LVDT) attached to quartz push-rods was placed across the reduced section of the specimen to measure the radial expansion and contraction of the specimen as a function of time and temperature. The grip spacing (free span) of the Gleeble copper jaws was set to 15mm with the adjustable jaw connected via a 4mm coupler to allow stress-free accommodation of the linear thermal expansion and contraction.



6.4.3 Microstructural Analysis

The full welds and the simulation weld metal specimens were analyzed using optical microscopy, scanning electron microscopy and micro hardness testing. The reduced section of the simulation specimens containing the weld metal was cut from the full bar, mounted in phenolic resin and ground to expose the transverse section as shown in Figure 6-1 (b). Full metallographic preparation to a final 1 μ m finish was completed with diamond suspensions and the specimens were etched with a 3% Nital solution with wetting agent for 15 seconds. Micro and macro-graphs were prepared for each sample using a Zeiss Axiovert 200M Microscope with motorized stage and Axiovision software. Microhardness of the samples was measured using a Clemex CMT micro-indenter at a 300 gram-force load. For full hardness surveys an x-y grid at 500 μ m spacing was superimposed over the entire reduced section of the specimen with a 50 μ m offset from all edges. Scanning electron microscopy of the samples was conducted with a JEOL JCM 5000 NeoScope.

6.4.4 Dilatometric Analysis

Data collected from the Gleeble system was plotted and analyzed using Origin software. Plots of relative linear expansion versus temperature were generated for all thermal cycles and the linear regions of the curve corresponding to the thermal contraction of the austenite and of the FCC transformation product (TP) were fit using a linear best fit equation. The lever rule was used to calculate the fraction of austenite transformed and the methodology is illustrated in Figure 6-2 [204].

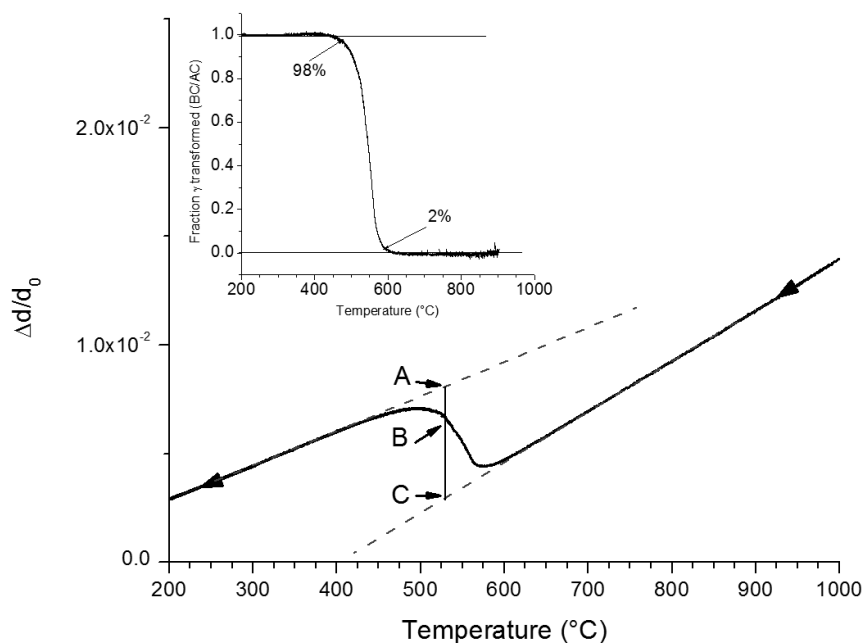


Figure 6-2— Illustration of the lever rule technique employed for calculating CCT transformation temperatures as the length of the BC line segment divided by AC. Start and finish temperatures are then calculated as 2% and 98% of the fraction transformed.

The fraction of austenite transformed is calculated as the quotient of the lines BC and AC where BC represents the difference between the dilation data and the FCC linear fit extrapolation, and AC is the difference between the FCC and TP linear fit equations, over the temperature range of interest. The onset and finish temperatures were calculated as the 2% and 98% values of the fraction transformed and intermediary transformations were detected using the first derivative of the fraction transformed. This is a modified method compiled from the work of Yang and Bhadeshia [191] to establish a reliable method for determining the martensite start temperature via strain offset and the general method proposed by de Andres *et al.* [188] for the calculation of transformation start temperatures by deviation from linearity in the FCC contraction.



The strain offset method yields an improved standard deviation in start temperatures, however, the transformation products resulting from the thermal cycles used here are not all the same. Therefore, the application of a strain offset, where the proposed offset is a function of a variable microstructure, was supplanted by a 2% offset in fraction transformed. This offset could be automatically calculated using best fit and regression analysis to yield more reliable data than could be acquired by manual detection of the point of deviation of linearity in the FCC contraction. To that end, all start and finish temperatures herein reported are those measured at 2 and 98% of the austenite transformation.

6.4.5 Mechanical Properties

A limited number of transverse specimens were thermally cycled in the Gleeble to generate re-heated weld metal Charpy v-notch (CVN) specimens for comparative toughness evaluation. Three specimens of WM2, NiMo80, and WM3 were tested in the as-welded (AW) condition and after thermal cycles with Δt_{8-5} cooling times of 5, 10 and 20 seconds. All of the specimens were notched in the middle of the weld metal from the root and were tested at -20 °C. Fractography of the broken surfaces was conducted with an SEM pre and post etching. Etching was conducted in two stages, the first with a solution of H₂O₂, HF and H₂O to remove $\approx 10 \mu\text{m}$ of surface deformation, and the second in 3% nital to reveal microstructural detail.

6.5 Results and Discussion

6.5.1 Thermal Simulation and CCT

Continuous cooling transformation diagrams compiled from dilatometric and microstructural data drawn at 2% and 98% of austenite transformation are presented in Figure 6-3 to Figure 6-7.



CCT Diagrams of Weld Metal Applicable for Girth Welding of X100 line pipe

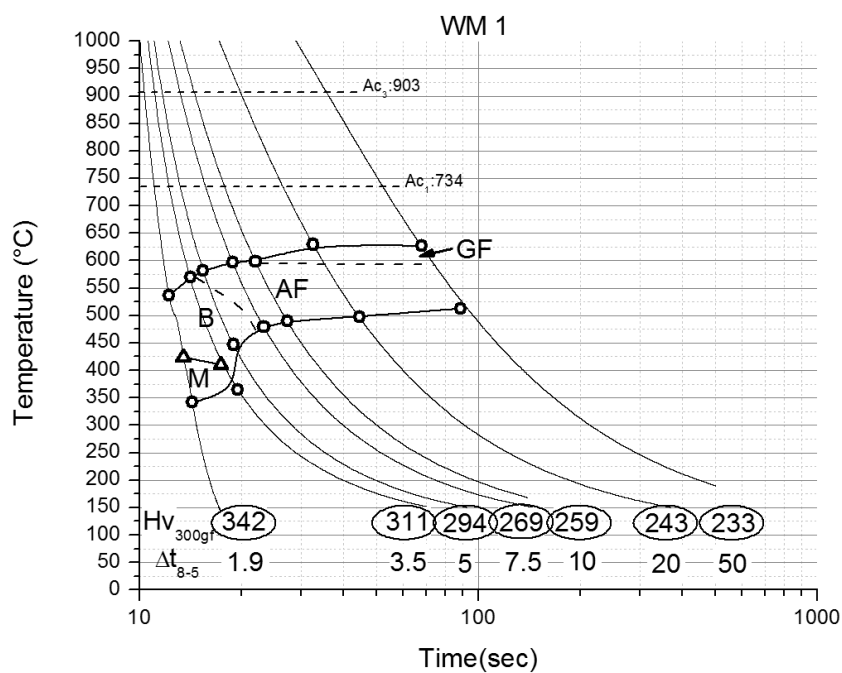


Figure 6-3 – CCT Diagram for WM 1 from 1300 °C

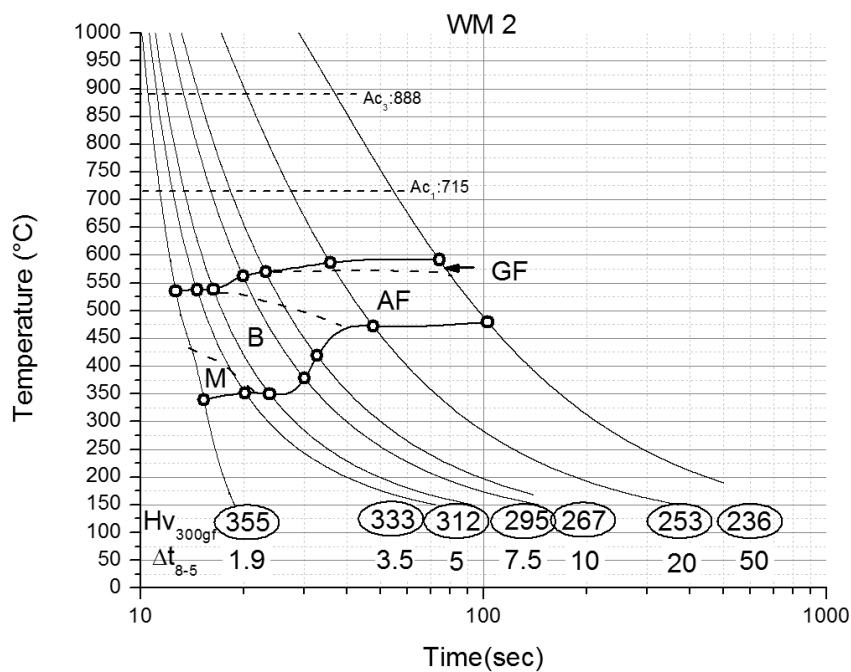


Figure 6-4 – CCT Diagram for WM 2 from 1300 °C



CCT Diagrams of Weld Metal Applicable for Girth Welding of X100 line pipe

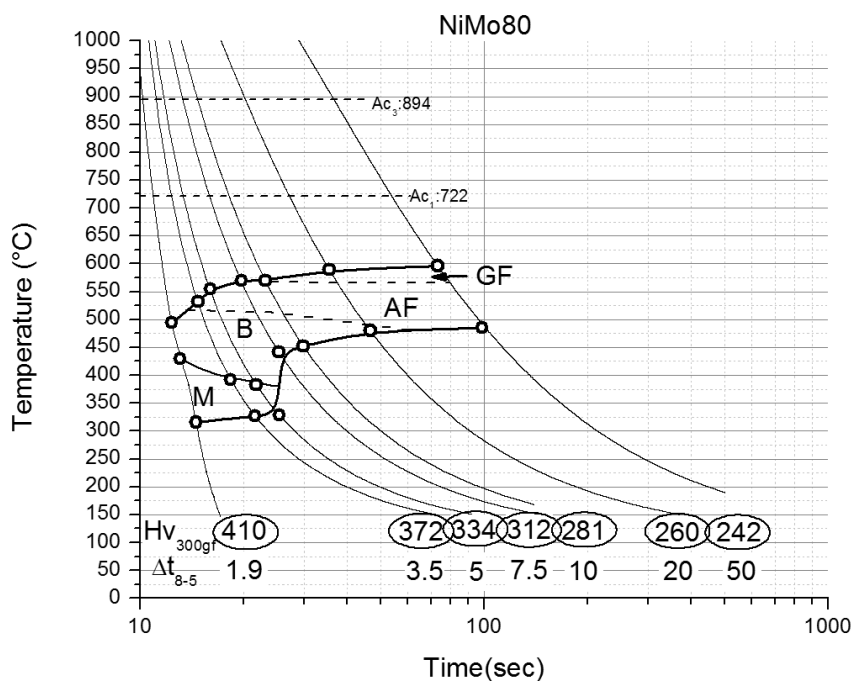


Figure 6-5 - CCT diagram for NiMo80 from 1300 °C

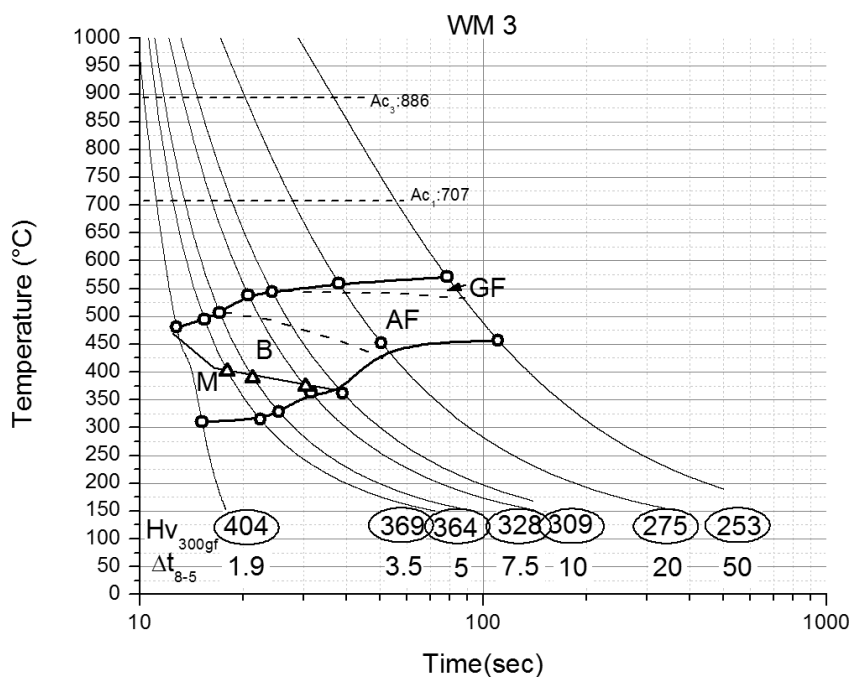


Figure 6-6 – CCT diagram for WM 3 from 1300 °C



CCT Diagrams of Weld Metal Applicable for Girth Welding of X100 line pipe

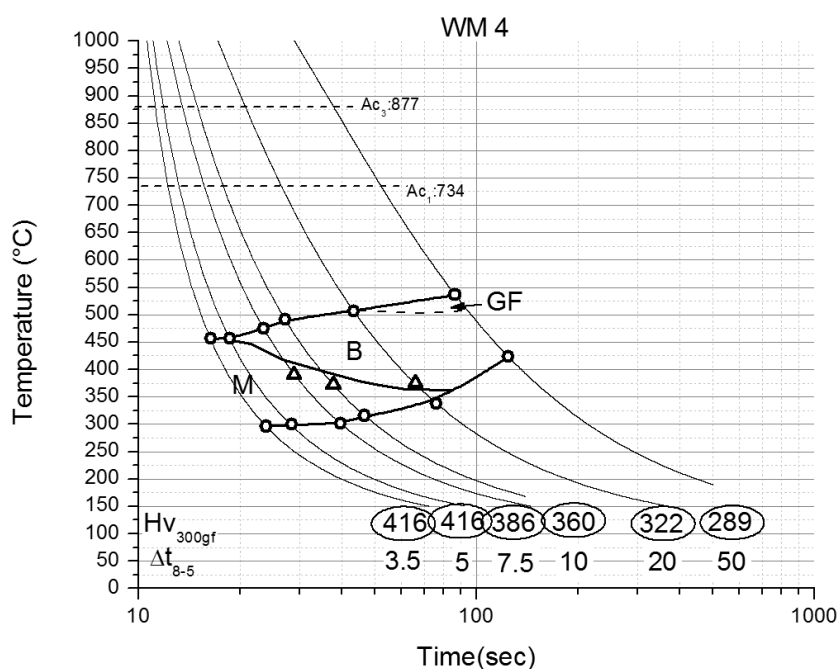


Figure 6-7 – CCT diagram for WM 4 from 1300 °C

The four weld metals, WM1, WM2, WM3 and WM4 have increasing alloy contents leading to higher carbon equivalents while NiMo80 is near the middle of the group. The carbon equivalents are given in Table 6-3 and have been calculated by the CE_{IW}, P_{cm} and CEN methods [22].

Table 6-3 – Calculated carbon equivalents for weld metal chemistries

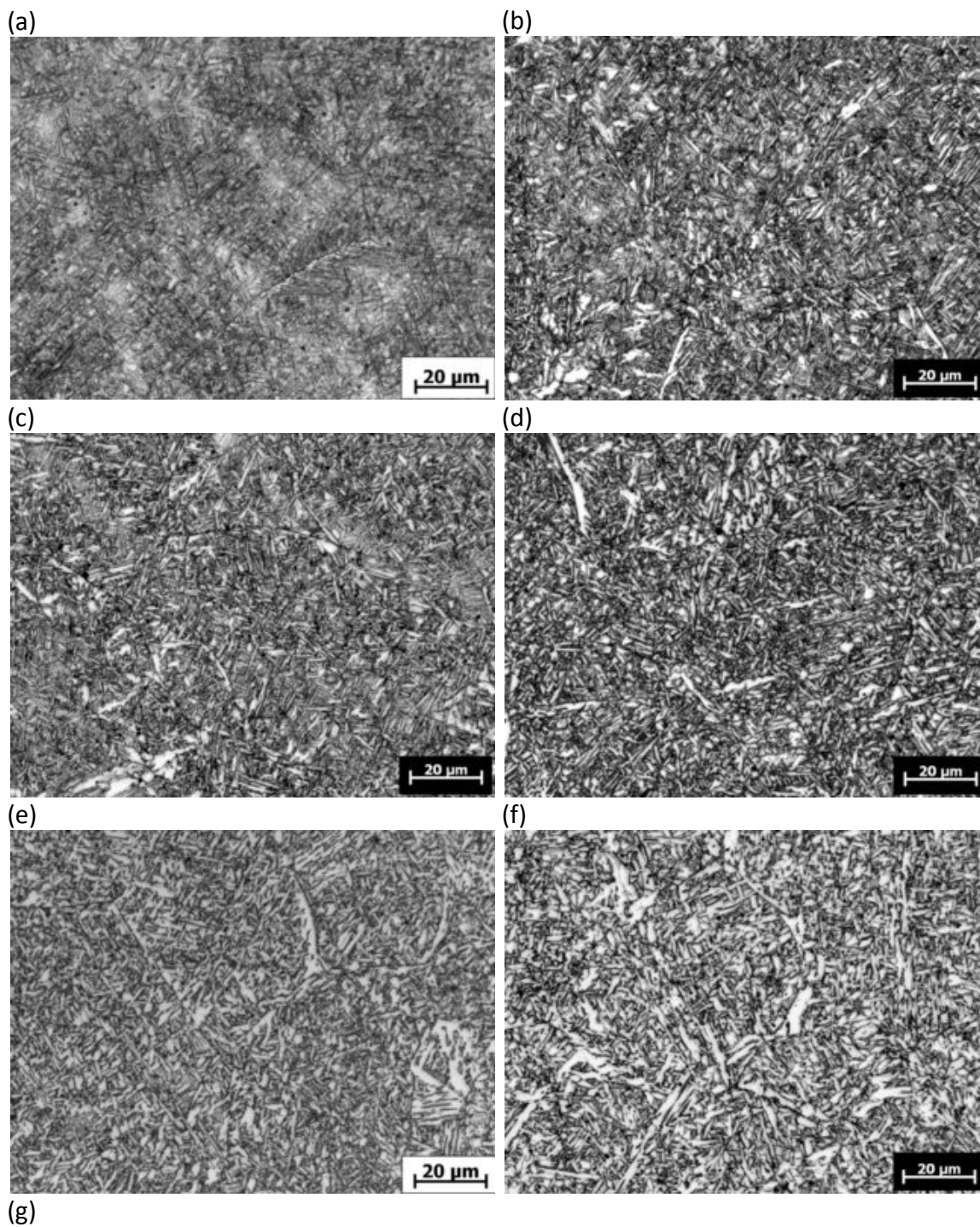
Alloy	Type	CE _{IW}	P _{cm}	CEN
WM1	C-Mn-Si-Mo	0.46	0.22	0.32
WM2	C-Mn-Si-Ni-Mo-Ti	0.52	0.21	0.31
NiMo80	C-Mn-Si-Ni-Mo-Ti	0.48	0.24	0.36
MW3	C-Mn-Si-Ni-Mo-Cr-Ti	0.56	0.25	0.37
WM4	C-Mn-Si-Ni-Mo-Cr-Ti	0.65	0.28	0.44



Figure 6-3 gives the CCT diagram for WM 1 with the lowest CE at 0.46. A pure martensite (M) sample was not achieved with the fastest cooling possible using the Gleeble ($\Delta t_{8-5} \approx 1.9$ s). This was supported by the hardness which was measured at 342 HV for the fastest cooling. The CCT diagram for WM 1 shows a progression from bainite (B) with some martensite to acicular ferrite (AF) and grain boundary ferrite (GF). The CCT diagram for WM 2 with a CE of 0.52 is given in Figure 6-4. There is a slight increase in the amount of bainite formed at the middle cooling rates and the initial hardness increased to 355 HV. NiMo80 has a CE of 0.48 which is less than WM 2 but shows a much more pronounced martensite region in the CCT given in Figure 6-5. This is most likely due to the higher carbon in the NiMo80 alloy. The NiMo80 microstructure shows a progression from martensite to bainite and acicular ferrite with grain boundary ferrite at the slowest cooling rates which fits with the model proposed by Farrar and Harrison [135]. A complete set of corresponding transformation microstructures for NiMo80 are presented in Figure 6-8(a)-(g) and show a bainitic and martensitic microstructure formed at $\Delta t_{8-5} = 1.9$ s with and the appearance of acicular ferrite at $\Delta t_{8-5} = 3.5$ s.



CCT Diagrams of Weld Metal Applicable for Girth Welding of X100 line pipe



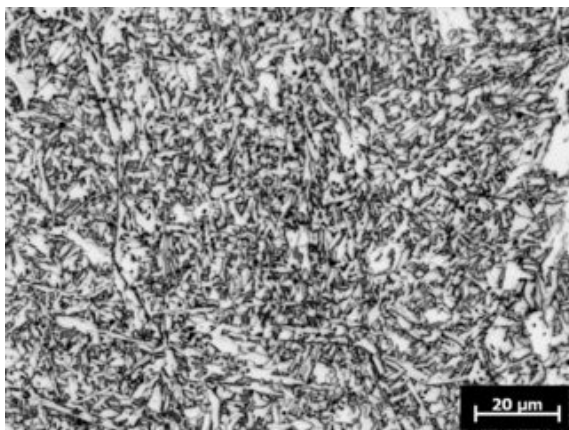


Figure 6-8 – NiMo80 Microstructures corresponding to $\Delta t_{8/5}$ cooling times of 2, 3.5, 5, 7.5, 10, 20 and 50 seconds. (a) Martensite and bainite. (b) Bainite and acicular ferrite. (c) Bainite and acicular ferrite. (d) Bainite and acicular ferrite. (e) Bainite and acicular ferrite. (f) Bainite and acicular ferrite with some grain boundary ferrite. (g) Acicular ferrite and grain boundary ferrite

The microstructure here has formed as a result of an imposed thermal cycle with a high peak temperature (1300 °C) well above the A_{c3} for the alloy. A rapid heating rate with an isothermal hold at peak allows for complete re-austenization of the alloy and the growth of the austenite grains [229-231]. The high inclusion content present in all welds is the supporting nucleation site for acicular ferrite, with the austenite grain boundary serving as a nucleation site for bainitic ferrite [137, 139, 141]. The Vickers hardness number measured for the NiMo80 subjected to a thermal cycle of $\Delta t_{8-5} = 1.9$ s is 409.9 ± 6.1 HV at 300 gram force load. The increase of alloy elements in WM 3 and WM 4, with corresponding increase in carbon equivalents to 0.56 and 0.65 respectively, leads to a suppression of the martensite and bainite start temperatures seen quite clearly in Figure 6-6 and Figure 6-7. WM 4 produces martensite and bainite over the cooling rates tested with ~10% grain boundary ferrite present at the slowest cooling rate. The high hardness of 416 HV at 3.5 and 5 s Δt_{8-5} cooling times is indicative of a martensitic matrix. The effect of increased alloy can be seen in Figure 6-9 where the transformation products for WM1 and WM4 at $\Delta t_{8-5} = 50$ s are presented. The microstructure of WM 4 is finer and has a hardness of 289 HV compared to 233 HV for WM1.

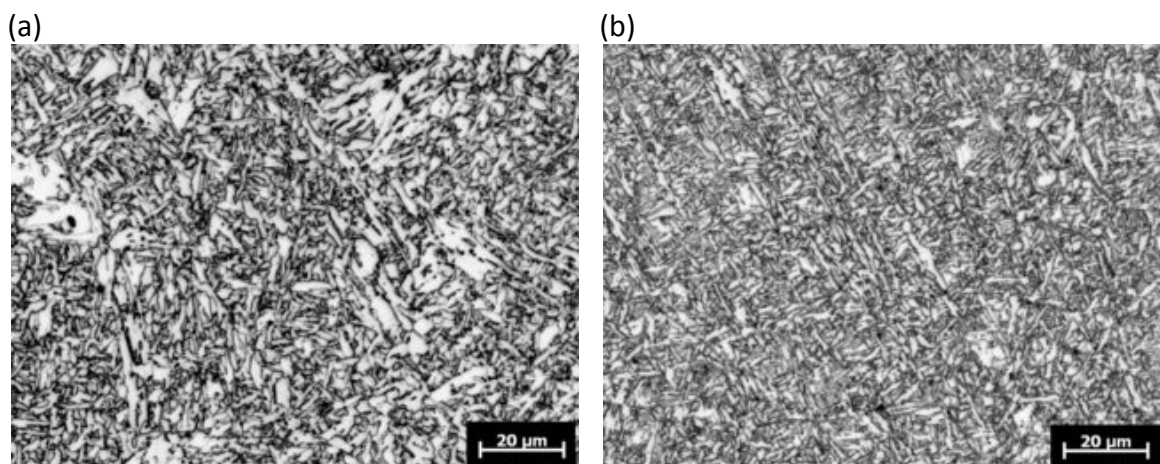


Figure 6-9- Microstructures formed after cooling at $\Delta t_{8/5} = 50s$. (a) WM1, $CE_{IW} = 0.46$ (b) WM4, $CE_{IW} = 0.65$

Utmost care was used in analyzing the microstructure and collecting hardness data for the samples. However, the stochastic nature of arc welding results in variations to both microstructure and composition which may not be obvious. In an attempt to measure the homogeneity of the weld metal thermal specimens (post thermal cycle), hardness maps were made to capture the whole reduced section containing the single pass weld deposit. Figure 6-10 shows the map for the NiMo80 specimen after a $\Delta t_{8/5}$ cooling time of 3.5 seconds.

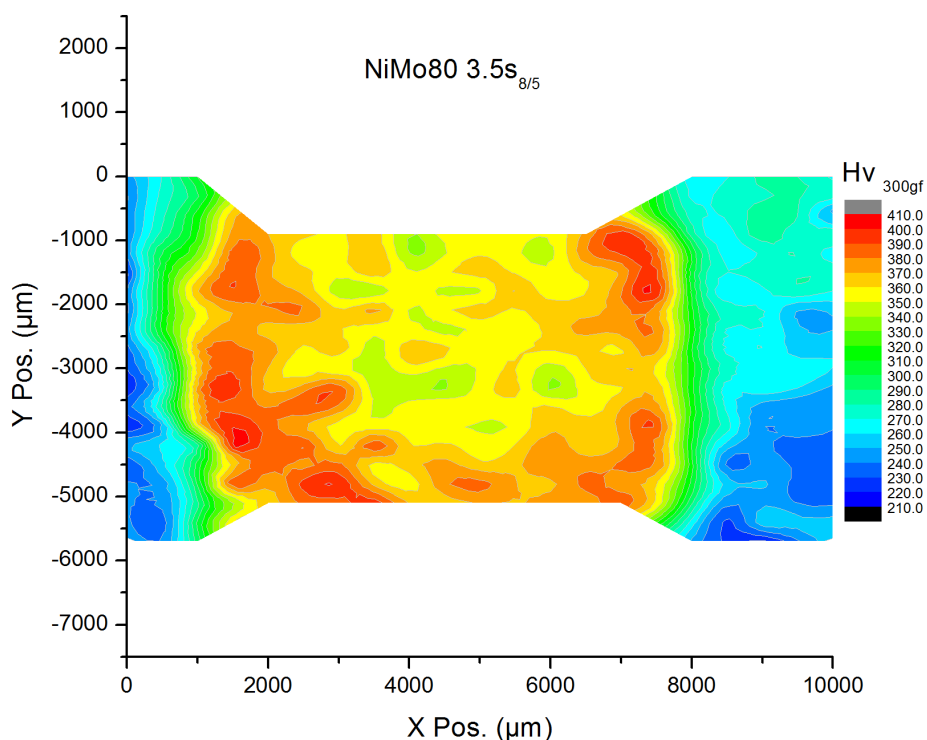


Figure 6-10 – Hardness map (in HV at 300 gf) for the NiMo80 specimen post thermal cycle showing a relatively homogeneous hardness profile through the center of the specimen.

The central region of the specimen has reasonably homogeneous hardness that varies from 340 HV to 370 HV. Interestingly, the region of the specimen located near the fusion boundary of the weld shows a marked increase in hardness. This is most probably a vestigial property from the high cooling rates experienced near the base metal. The sample shown is representative and the same homogeneity was found for all thermally simulated samples at all cooling rates.

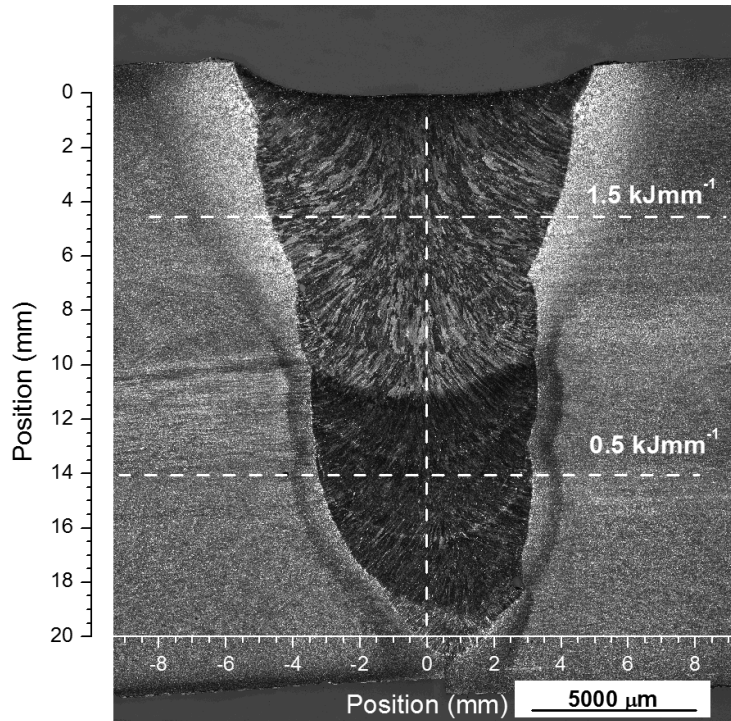
6.5.2 Weld analysis

The low heat multipass and high heat single pass regions of the welds were analyzed using microhardness traverses from base metal to base metal across the 1.5 kJmm⁻¹

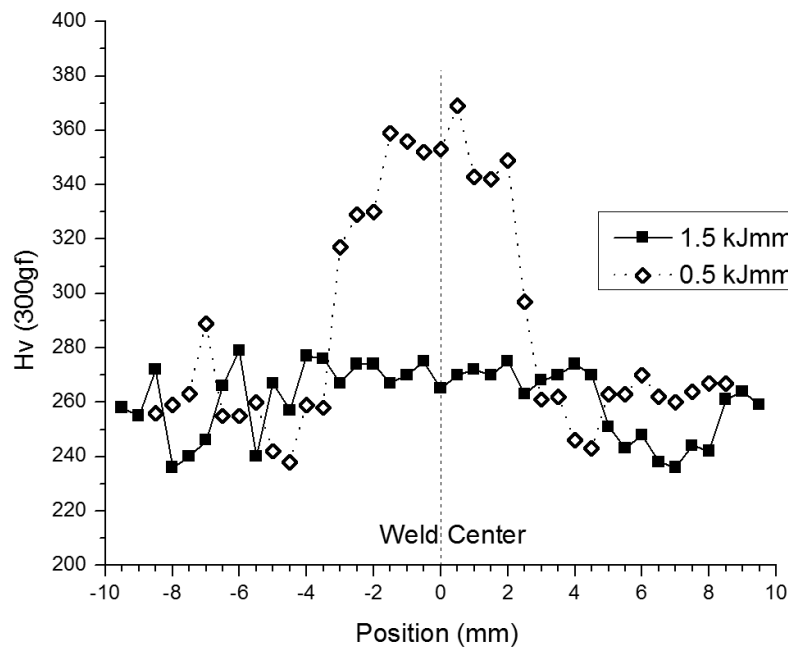


region and the 0.5 kJmm^{-1} region, and from the cap to the root as depicted in Figure 6-11(a) along with microstructural analysis. The high heat input beads were found to be significantly softer than the low heat input multi pass beads, but with less scatter. For NiMo80 the 1.5 kJmm^{-1} bead measured and average of $270 \pm 5.8 \text{ HV}$ while the 0.5 kJmm^{-1} multi pass weld region averaged $355 \pm 17.2 \text{ HV}$. The weld metal is in both cases harder than the heat affected zone (HAZ) region of the base metal included in the traverses, as shown in Figure 6-11(b). The results for all alloy compositions are presented in

Table 6-4, which shows that the high heat input region of the weld is softer than the low heat input region for all compositions and has significantly greater scatter in almost all cases.



(a)



(b)

Figure 6-11 – Microhardness surveys performed on the NiMo80 weld section. (a) Scale image showing the placement of the traverses through the 1.5 kJmm⁻¹ deposit, the 0.5 kJmm⁻¹ deposit and from the cap to the root. (b) Results of the cross weld traverses through the 1.5 kJmm⁻¹ and 0.5 kJmm⁻¹ deposits.



Table 6-4 – Average Vickers hardness numbers for the 1.5 and 0.5 kJmm⁻¹ weld regions

Weld Metal	Nominal	1.5 kJmm ⁻¹		0.5 kJmm ⁻¹	
		HV	Std. Dev	HV	Std. Dev
WM1	C-Mn-Si-Mo	248	4.5	290	13.9
WM2	C-Mn-Si-Ni-Mo-Ti	278	15.9	317	6.4
NiMo80	C-Mn-Si-Ni-Mo-Ti	270	5.8	355	17.2
WM3	C-Mn-Si-Ni-Mo-Cr-Ti	295	5.6	359	9.0
WM4	C-Mn-Si-Ni-Mo-Cr-Ti	335	8.1	366	2.1

The effect of the alloy content and increased carbon equivalent is demonstrated in Figure 6-12, where average hardness values of the 1.5 and 0.5 kJmm⁻¹ regions are plotted as a function of carbon equivalent. The linear best fit of the data yields the equations:

$$Hv_{1.5kJmm^{-1}} = 51.7 + 437CE_{IIW}$$

Equation 6-3

and

$$Hv_{0.5kJmm^{-1}} = 165 + 310CE_{IIW}$$

Equation 6-4

where HV is the Vickers hardness value at the specified nominal heat input and the CE_{IIW} is the carbon equivalent of the alloy. The least squares fits are 0.967 and 0.818 respectively.

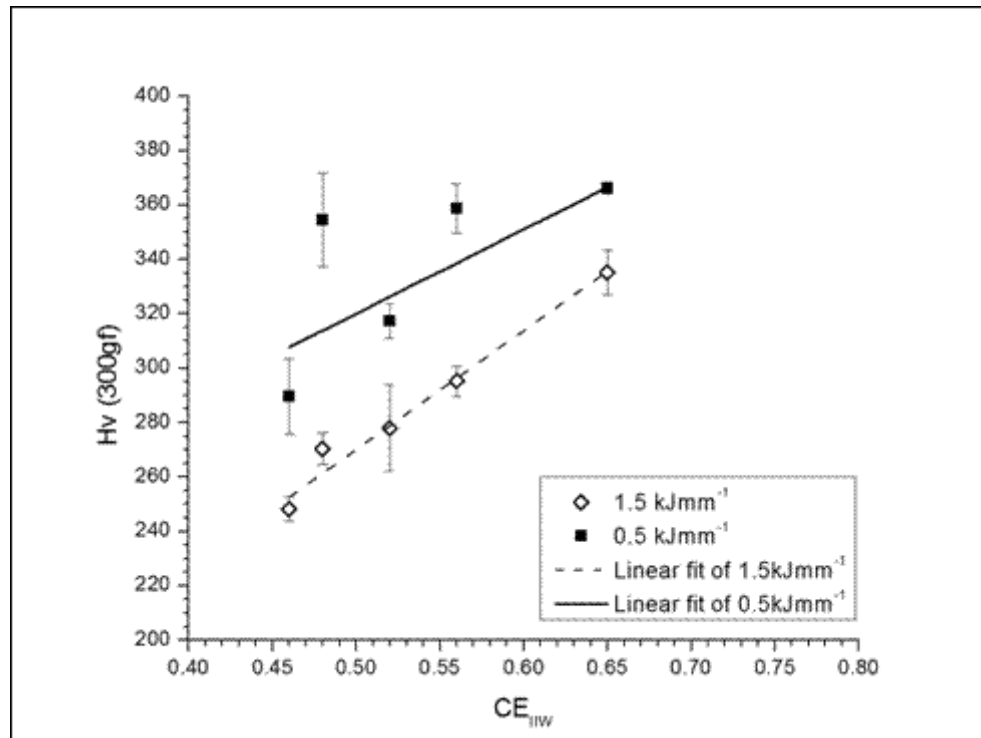


Figure 6-12 – Weld hardness as a function of carbon equivalent in the 1.5kJmm⁻¹ and 0.5 kJmm⁻¹ regions.

The rationale for using a single pass region for weld metal samples is illustrated in Figure 6-13 where hardness from the cap to the root is presented as a function of position. The upper portion of the deposit corresponding to the 1.5 kJmm⁻¹ single bead deposit has a much lower variability than the low heat input region where the effects of multiple deposits and ensuing imposed thermal cycles can be seen to give a cyclic hardness which would be entirely undesirable in a starting material for further study. The reasonable scatter in hardness of the 1.5 kJmm⁻¹ region shown in Figure 6-13 and the homogeneity of the sample post thermal cycle seen in Figure 6-10 ensure confident results when using the single pass region as a starting material.

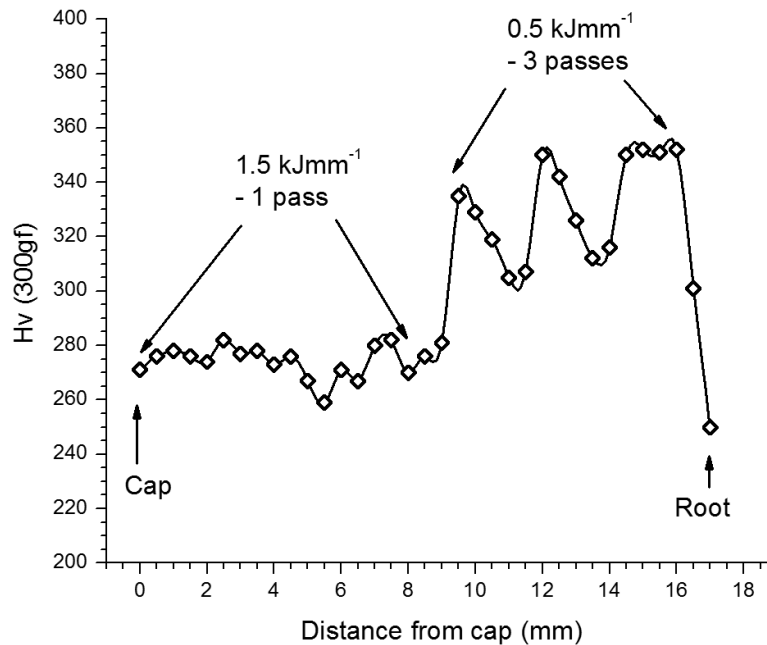


Figure 6-13 – Hardness survey for NiMo80 weld from the cap to the root section through both the 1.5 kJmm^{-1} and 0.5 kJmm^{-1} regions of the weld. The cyclic rise and fall of the hardness in the 0.5 kJmm^{-1} region corresponds to the multiple deposits of weld metal.

6.5.3 Simulation of as-deposited weld metal

The microstructures and hardnesses developed from the reheated weld metal simulations of the single pass 1.5 kJmm^{-1} bead were compared to microstructures formed in the 0.5 kJmm^{-1} multipass deposit for thermal cycles with comparable hardness values. Regions of the weld were found with microstructures that are directly comparable for constituent phases, coarseness and hardness. For WM 1 the single pass region of the weld showed a range of hardness from 304 – 276 HV which corresponds to simulated Δt_{8-5} cooling times of 4.2 – 6.8 s. The range for WM 2 is 324 – 311 HV



corresponding to Δt_{8-5} of 4.2 – 5.3s in the simulation of reheated weld metal. NiMo80 shows a range of 372 – 337 in the 0.5 kJmm^{-1} deposited weld metal with a corresponding simulated cooling range of 3.4 – 4.9 s. Figure 6-14 shows the microstructure developed for WM3 in the 0.5 kJmm^{-1} weld region and after a Gleeble thermal cycle of $\Delta t_{8-5} = 5\text{s}$.

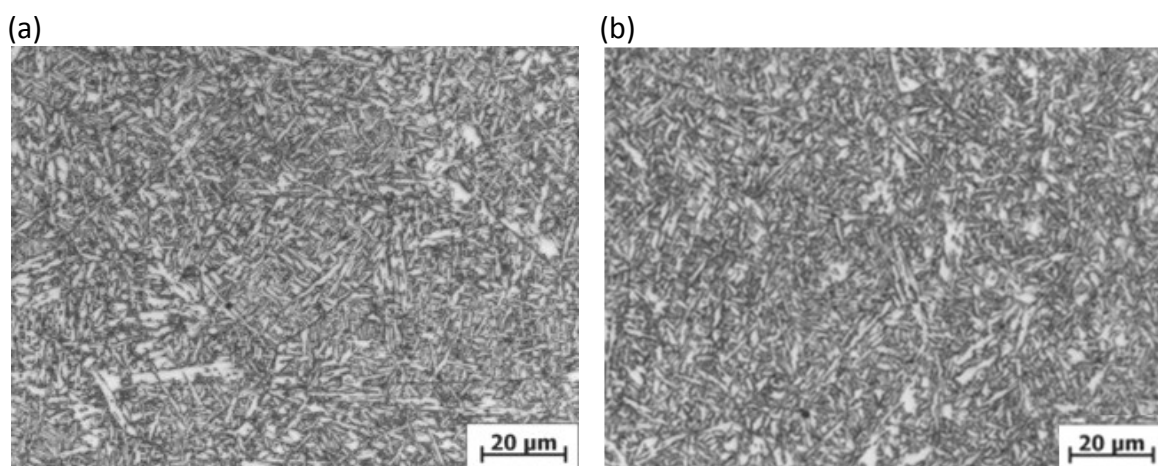


Figure 6-14 – Microstructures developed for WM3 (a) after a $\Delta t_{8/5} = 5\text{s}$ Gleeble thermal cycle (b) In the 0.5 kJmm^{-1} region of the weld

Both microstructures are composed of acicular ferrite and bainite with the only significant difference being the faint outline of the prior austenite grain boundaries visible in Figure 6-14 (a) resulting from the re-austenization of the sample during the thermal cycle. The hardness range for the as deposited 0.5 kJmm^{-1} region of WM 3 is 368 – 350 HV with the corresponding simulated reheat weld metal range of $\Delta t_{8-5} = 4.1 – 5.8$ s. The smallest range was found for WM 4 and is 368-362 HV in the as-deposited weld corresponding to simulation cooling times of 9.6 – 9.8 seconds. Thermal cycles with cooling times from 3.5 to 10s can therefore accurately reproduce both the hardness and the microstructure of the as-deposited weld metal for the 0.5 kJmm^{-1} regions.



6.5.4 Mechanical Properties

The CVN testing carried out at -20 °C revealed mixed failure of ductile and brittle for all three chemistries tested. The samples subjected to the longest simulated cooling cycles, $\Delta t_{8-5} = 20$ s, showed the highest absorbed energy at 141 ± 1 J, 164 ± 6 J, and 156 ± 6 J for WM2, NiMo80 and WM3 respectively. The data for all of the tests is summarized in Figure 6-15 where the trend of increasing toughness with cooling time is apparent for all three compositions.

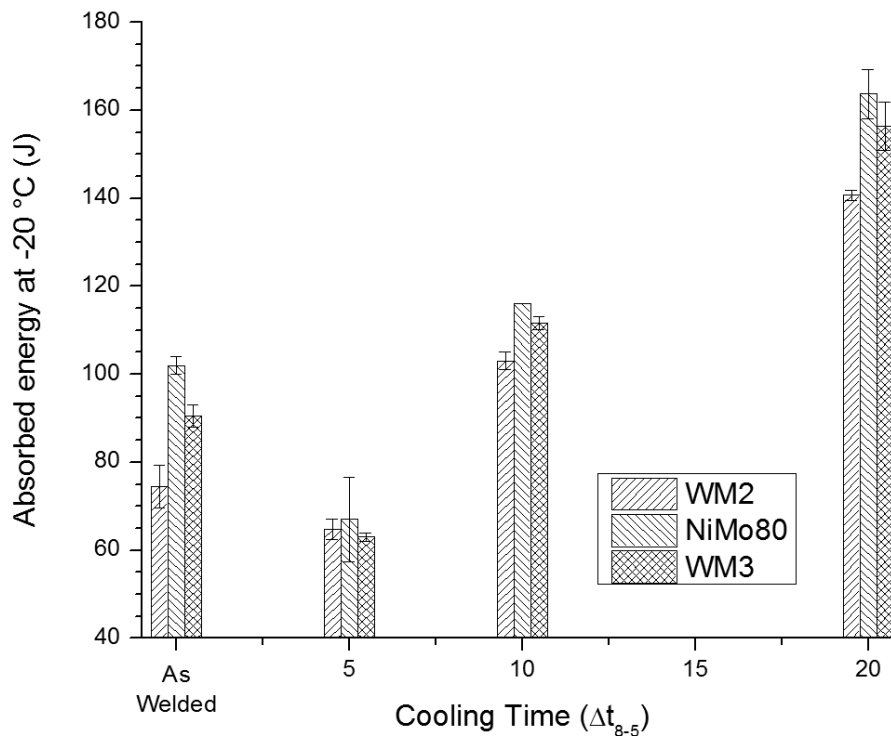


Figure 6-15 – Charpy V notch results for WM2, NiMo80 and WM3 tested at -20 °C for the as welded and at $\Delta t_{8/5}$ cooling times of 5, 10 and 20 seconds

The samples tested in the as-welded condition show absorbed energies in between the $\Delta t_{8-5} = 5$ and 10 s samples. While the failure of the (AW) specimens was mixed, there was a noticeable directionality of the fracture parallel to the columnar grains. Figure



Figure 6-1 (a) shows the AW microstructure and Figure 6-16 (a) presents a fractograph of the AW structure showing propagation along the columnar grains.

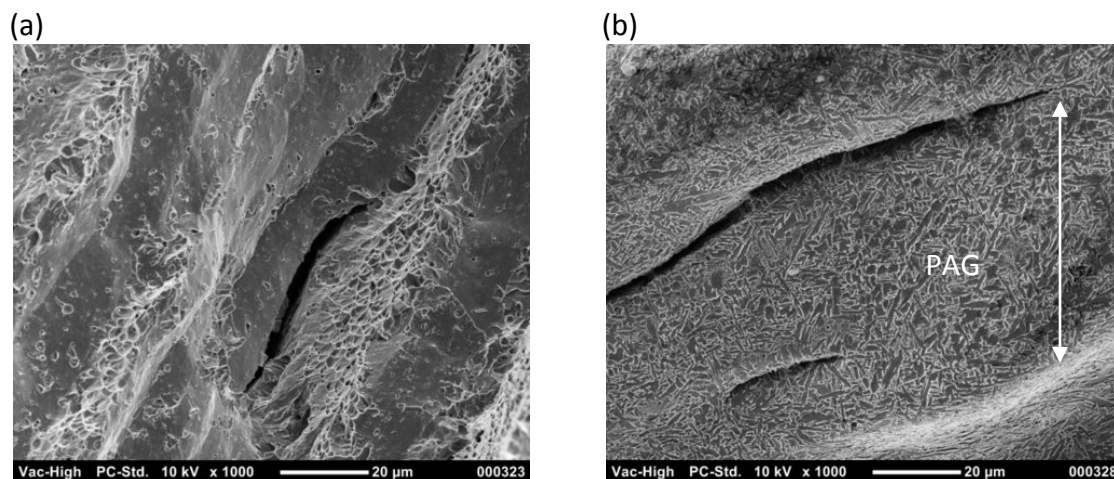


Figure 6-16 – Fractography of WM3 samples (a) unetched (b) etched

The etched fracture surface shown in Figure 6-16 (b) shows a secondary crack following the columnar PAG boundary and a short microcrack arrested at an acicular ferrite grain boundary. Comparison between the AW and re-heated microstructures is limited due to the variation between the underlying grain structure developed during cooling and that created by re-heating which is known to affect toughness [180, 226, 232, 233]. However, there is clearly a trend in Figure 6-15 showing improved toughness at cooling rates which yield acicular ferrite as seen in the CCT diagrams in Figure 6-4, Figure 6-5 and Figure 6-6. This improvement in toughness with reduction of bainite has been observed in weld metal where the deflection of the propagating crack through bainite is low [232].

6.6 Conclusions

Dilatometric analysis of 5 weld metals with compositions designed for use with mechanized GMAW pipe girth welds has generated CCT diagrams corresponding to



reheated weld metal regions at various heat input and cooling times. The transformation products range from martensite to acicular ferrite and bainite of varying coarseness with polygonal ferrite formed at longer cooling times.

- The use of a single high heat weld deposit as a starting material for subsequent thermal cycling applicable to the P-GMAW of X100 steel girth welds has been found to be an excellent option for weld metal thermal simulation.
- Accurate microstructures for a simulated 0.5 kJmm^{-1} weld are generated for the current compositions by thermal cycles with $\Delta t_{8/5}$ cooling rates of 3.5 to 10 seconds using a heating rate of $250 \text{ }^\circ\text{Cs}^{-1}$ to a peak temperature of $1300 \text{ }^\circ\text{C}$ with a hold time at peak of 1 second.
- The CCT diagrams and hardness regression equations give an operating window for a small range of chemistries applicable to X100 girth welds.
- The toughness of the reheated weld metal improves with increased cooling time due to the reduction in bainite constituent.

6.7 Acknowledgments

This research was funded by CANMET-MTL and the Federal Interdepartmental Program for Energy Research and Development. The authors would like to thank Mr. M. Kerry for his machining expertise, Mr. R. Eagleson for mechanical testing, and Ms. P. Liu for contributions to metallographic analysis and microhardness testing. The research is part of a larger consolidated program jointly funded by the Pipeline and Hazardous Materials Safety Administration of the U.S. Department of Transportation (DOT), and the Pipeline Research Council International, Inc. (PRCI). The views and conclusions in this paper are those of the authors and should not be interpreted as representing the official policies of any of these organizations.



CCT Diagrams of Weld Metal Applicable for Girth Welding of X100 line pipe

The author (G.G.) also wishes to acknowledge CANMET-MTL management for providing the opportunity to work and have access to laboratory facilities during the course of this research and to NSERC and McGill University for funding grants.



7 Thermal Simulation of HAZ regions in a modern High Strength Steel

Graeme R Goodall¹, James Gianetto², John Bowker², Mathieu Brochu¹

¹McGill University, Mining and Materials Engineering, 3610 University St, Montreal, Quebec, H3A 2B2

²CANMET MTL, Ottawa, Ontario, K1A 0G1

7.1 Selected discussion from chapter 4, 5 and 6

Welding high strength steel has been shown to affect both the HAZ and the weld metal of a weldment. In the GC HAZ, the high peak temperature allows grain growth which degrades properties relative to the base metal. This trend has also been reported for steels other than X100. In a 2008 publication *Shanmugam et al.* reported the microstructure and toughness of a the base, HAZ and weld metal of a 700 MPa steel [234]. The composition of the steel used is given as a range: Fe-(0.04-0.06)C-(0.035-0.05)Ti-(0.08-0.09)Nb-(0.3-0.4)Cr which can be compared directly to the to the X100 steels studied in Chapters 4 and 5. There are no parameters given for the welding process used, nor for the electrode composition. The appearance of the weld suggests an autogenous weld, however this is speculative as the welding details are omitted. *Shanmugam et al.* report that there is insignificant softening of the weld and HAZ as the hardness values measured in both regions are similar to the base metal [234]. In Chapter 4, the HAZ region of the X100-4 steel is shown at $\Delta t_{8/5}$ time of 6s. This cooling rate represents the HAZ developed for a low heat input P-GMAW girth weld, and the hardness of the HAZ is 325-350 HV which is significantly harder than the 270-300 HV of the base metal. However, the hardness of the HAZ can be decreased in the X100-4 steel



by increasing the heat input of the weld and lengthening the $\Delta t_{8/5}$ time. The CCT diagram given for X100-4 shows a range of hardness values in the HAZ from 357 – 256 HV and could best match the pipe steel at $\Delta t_{8/5}$ time of 25s. The supposition that *Shanmugam et al.* employed a high energy welding procedure is supported by the phases reported in the HAZ which are non-equiaxed ferrite, degenerated pearlite/upper bainite, and martensite–austenite constituent (M/A) in the order of increasing cooling rate and decreasing transformation temperature. There is no fracture or grain size data reported, however a study by *Kim et al.* on the toughness and fracture of the HAZ in ferritic/pearlitic and bainitic steels revealed that the fracture toughness can be improved in the ferritic/pearlitic steels by reducing the $\Delta t_{8/5}$ time [235].

The weld metal studied in Chapter 6 developed a range of hardness values and toughness as a function of $\Delta t_{8/5}$ cooling time. In a study by *Vega et al.* on the effects of multiple girth weld repairs on the microstructure and mechanical properties of an X52 pipe steel have been reported [236]. The toughness of the weldment was reported to be the lowest in the weld metal, which was added using a SMAW procedure and a heat input range of 1.2-1.5 kJmm⁻¹. The toughness values of the weld metal in Chapter 6 in the 1.5 kJmm⁻¹ as welded condition were ~ 75, 100 and 90 J for WM2, NiMo80 and WM3 tested at -20 °C respectively. These values can be compared to the HAZ toughness of X100-2, X100-4 and X100-5 for $\Delta t_{8/5}$ time of 6s tested at -20 °C of ~240, 245 and 150 J respectively. Clearly the toughness of the weld metal is significantly less than that of the X100 pipe steel HAZ, which is the same conclusion reached by *Vega et al.* in studying lower grade X52 pipe steel. The effect of different microstructures on the toughness in CVN samples of grade X70 and X90 pipe steel has been reported by *Wang et al* [237]. The authors found that improved strength and toughness were obtained in the X90 steel with acicular ferrite microstructure versus the X70 polygonal ferrite steel. The weld metals studied in Chapter 6 all yield mixed microstructures of martensite, bainite, and acicular ferrite at a $\Delta t_{8/5}$ time of 6s, depending on alloy composition. The toughness of



the weld metals improved with longer $\Delta t_{8/5}$ times which yield a greater proportion of acicular ferrite as per the *Wang et al.* findings.

7.2 Preface

The emerging dual torch welding technology has opened the door to new and previously unknown thermal cycles in the HAZ. In this manuscript, the transformation of a grade 550 linepipe was characterized and presented in a continuous cooling transformation diagram. The effects of intercritical and interrupted grain coarsened transformations that could arise from novel dual torch welding technology were evaluated through toughness testing of Charpy impact specimens. The fractographic analysis of the Charpy specimens post impact testing allows correlation of developed microstructure with HAZ properties.



7.3 Abstract

Thermal simulation of the heat affected zone (HAZ) resulting from single and dual torch mechanized P-GMAW has been achieved in an X80 line pipe. The continuous cooling of an X80 steel with initial acicular microstructure over Δt_{8-5} from 2 to 50 seconds results in mixed bainite and martensite microstructure at fast cooling times, bainite at intermediate cooling times and granular bainite with bainite at longer cooling times. These phases were confirmed through optical and electron microscopy. The resulting transformation temperatures have been assembled and presented as a continuous cooling transformation diagram. The toughness of the steel was examined with Charpy impact specimens for three simulated HAZ cooling cycles, grain coarsened (GC HAZ), intercritically reheated grain coarsened (ICR GC HAZ), and an interrupted intercritically reheated grain coarsened (NTR ICR GC HAZ). The NTR ICR GC HAZ is a novel heat affected zone that can result from dual torch welding at fast travel speed and close torch spacing. All of the thermally HAZ regions showed reduced toughness that was attributed to bainitic microstructure and large effective grain sizes.

Keywords

Dual torch, X80, Gleeble, HAZ, Bainite,



7.4 Introduction

Exploration of remote natural gas fields is currently underway in many regions of the globe. The majority of gas fields close to consumer markets have been established and expansion to meet global demand requires that new fields be tapped. One region with known gas deposits is the Arctic with access through Canada, Alaska and Siberia [15, 192]. In all of these countries, the main trunk gas lines are hundreds, if not thousands, of kilometers from proposed production sites. The arctic terrain is formidable and poses significant technological challenges in design and construction. From a design perspective, the cost efficiency of a pipeline project can be significantly improved by using less steel of a higher strength. Not only is less material required, but there are also fewer costs associated with transportation and fewer welding consumables are required to fill the joints of thinner walled pipe. Mechanization of the welding procedures can also realize significant savings and improve the consistency of the welds. Reducing the heat input of welds has been a strategy to improve mechanical performance in modern pipes, and the pulsed gas metal arc welding (P-GMAW) procedure has now been successfully married to the high efficiency welding procedures [69, 192]. The P-GMAW can be used as a single wire, tandem wire (two electrodes in the same nozzle feeding the same weld pool), dual torch (two torches fixed together each with one wire in separate weld pools) and dual tandem (two torches each with two wires at a fixed distance apart). The increase of efficiency afforded by mechanized procedure is impressive; for example, assume a pipe of approximately 1 meter diameter is welded with cellulosic stick at 0.025 m min^{-1} ($\sim 5 \text{ in min}^{-1}$), the circumference is clearly 3.14 meters and the time for one complete weld would be 126 minutes or just over 2 hours. A P-GMAW welding rig can operate at 1.2 meters per minute, reducing the weld time to 2.6 min per pass, an impressive reduction in time. Tandem processes can increase the travel speed further and dual processes halve the number of passes required to fill the joint.



The high efficiency of mechanized P-GMAW has many advantages for the producers of pipelines, but with any new process there are unknown variables that need to be addressed before confidence in that procedure can be assured. This is particularly true for dual torch procedures due to the potential for abnormal phase transformations. The allotropic transformation in steel between the face center cubic (FCC) austenite (γ) and the body centered cubic (BCC) ferrite (α) has been studied for well over one hundred years by metallurgists the world over and continues to produce new and exciting discoveries. Traditional welding processes or even the efficient P-GMAW procedures have always welded at a rate sufficiently slow to allow a complete transformation of the steel from the induced thermal cycle of each pass before the subsequent pass begins. With dual torch P-GMAW, the spacing between the electrodes allows for the possibility of interrupted cooling cycles resulting from the onset of the second thermal cycle before the completion of the first. This concept is illustrated in Figure 7-1 where the thermal cycle from the first pass is interrupted before the completion of the γ transformation and is re-heated into a region of incomplete α transformation.

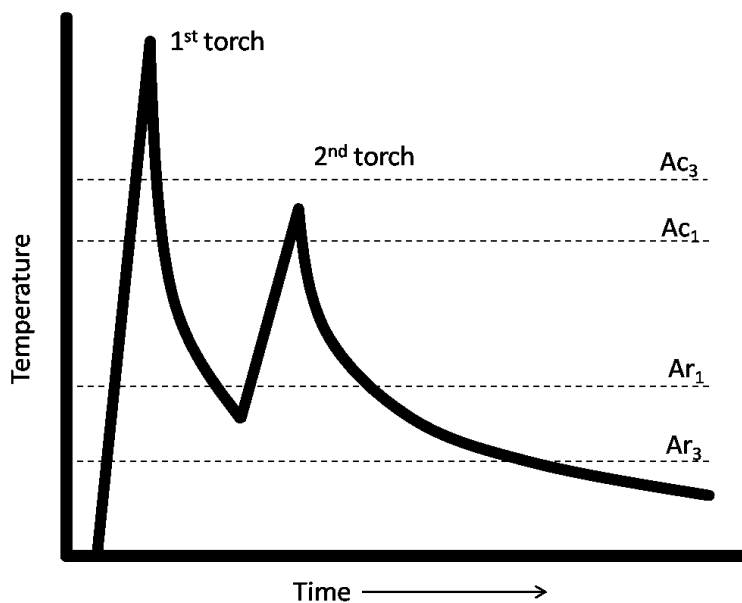


Figure 7-1 – Schematic of an interrupted thermal cycle from dual torch welding



While the incomplete $\alpha \rightarrow \gamma$ transformation resulting from heating to the dual phase ferrite- austenite region is not unusual, and produces a well known region of the heat affected zone (HAZ) known as the intercritically reheated (ICR) zone [167, 169, 170], the effect of an incomplete $\gamma \rightarrow \alpha$ has not been studied in relation to modern pipe steels. The grain coarsened heat affected zone (GC HAZ) is frequently the region of a weldment with the poorest mechanical performance and has been the subject of study by multiple researchers [52, 133, 238, 239].

The effect of simulated thermal cycles characteristic of P-GMAW processes has been investigated for a commercially produced X80 pipe steel. The GC HAZ along with variants of interrupted cooling cycles have been simulated and the transformation products studied via dilatometry, and microscopy and the mechanical properties evaluated for hardness and toughness.

7.5 Experimental Procedure

7.5.1 Materials

A modern pipe commercially produced via thermal mechanically controlled processing (TMCP) was selected for this work and has been identified as X80. The composition is given in Table 7-1 along with the carbon equivalents calculated using the following equations [22]:

$$CE_{IW} = C + \frac{Mn}{6} + \frac{Cu + Ni}{15} + \frac{Cr + Mo + V}{5}$$

Equation 7-1



$$P_{cm} = C + \frac{Si}{30} + \frac{Mn}{20} + \frac{Cu}{20} + \frac{Ni}{60} + \frac{Cr}{20} + \frac{Mo}{15} + \frac{V}{10} + 5B$$

Equation 7-2

where each element is in weight percent.

Table 7-1 – Composition of the pipe materials

	C	Mn	Si	Nb	Ti	N	Mo+Cr	Ni	CE _{IIW}	P _{cm}	B _s	M _s
X80	0.052	1.60	0.11	0.096	0.014	0.006	0.459	0.14	0.44	0.18	635	473

The specified mean yield stress for the pipe is 550 MPa. Samples were cut from the pipe at mid wall as 10 x 10 x 76 mm square cuboids with the long axis parallel to the pipe axis. Dilatometer specimens were prepared by rounding the center of the cuboid bars to a 6 mm diameter over a 6 mm length. The microstructure of the starting material consists of acicular ferrite as shown in Figure 7-2.

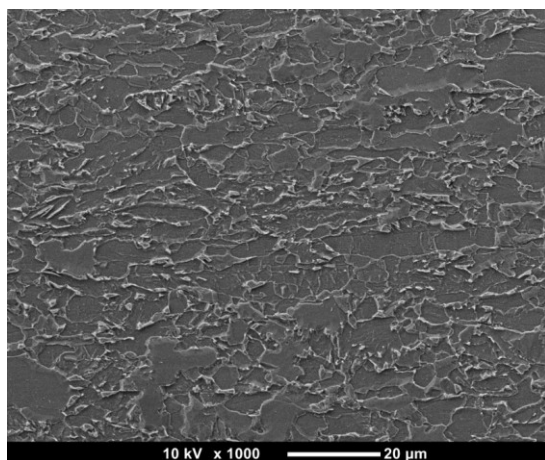


Figure 7-2 - Microstructure of X80 pipe

7.5.2 Simulation and testing

P-GMAW thermal cycles were simulated using a Gleeble 3800 thermo-mechanical simulator. Rykлайн 3D cooling curves were used for thermal simulation with a 100 °C pre



heat and the cooling rate is expressed as the cooling time from 800 °C to 500 °C (Δt_{8-5}). Thermal control was maintained via a Type K or Type R thermocouple welded directly to the specimen at mid-length using a jig supplied by the manufacturer. Samples for Charpy impact testing were notched post thermal cycling and reduced to standard dimensions (10 x 10 x 55 mm) before being assessed in a TINIUS OLSEN Model #64 impact tester at temperatures from -80 °C to 20 °C. Transformation start and finish temperatures were obtained by evaluating the volumetric expansion measured by a linear variable differential transformer (LVDT) attached to quartz push rods placed across the thermal center of the specimen during cycling. The deviations from linearity during thermal expansion or contraction owing to the density difference between α and γ were taken as the start and finish temperatures of transformation. The critical temperatures for thermal cycles employing interrupted or incomplete transformations were calculated by the lever rule from appropriate thermal cycles. The percentages of transformations (e.g. 10% A_{C_3}) refer to the temperature corresponding to that percentage of the total temperature between the A_{C_3} and A_{C_1} . Thermal cycles were designed to evaluate the effect of torch spacing on the same region of the HAZ, however the thermal mass of the Charpy specimens limited the maximum cooling rate to a Δt_{8-5} of 6s. To that end the following cycles were developed:

1. Heating at 500 °C s^{-1} to 1350 °C, holding for 1 second, cooling following a Rykalin 3D model with Δt_{8-5} = 6s to room temperature (GC-HAZ)
2. Heating at 500 °C s^{-1} to 1350 °C, holding for 1 second, cooling following a Rykalin 3D model with Δt_{8-5} = 6s to 150 °C, heating at 250 °C s^{-1} to 10% of the A_{C_3} , holding for 2 seconds, cooling following a Rykalin 3D model with Δt_{8-5} = 10s (ICR GC HAZ)
3. Heating at 500 °C s^{-1} to 1350 °C, holding for 1 second, cooling following a Rykalin 3D model with Δt_{8-5} = 6s to 50% of the measured A_{r_3} (interrupted transformation), heating at 250 °C s^{-1} to 10% of the A_{C_3} , holding for 2



seconds, cooling following a Rykalin 3D model with $\Delta t_{8-5} = 12s$ (NTR- ICR GC HAZ)

A series of dilatometer tests were also conducted to investigate the effect of prior austenite grain size on the transformation start temperature. Seven peak temperatures from 1100 °C to 1450 °C were selected and the heating rate of 500 °C^s⁻¹ was maintained to each peak followed by a hold at peak of 1 second. All samples were then cooled linearly to 1000 °C such that the total time above 1000 °C was 4 seconds regardless of peak temperature. Hardness measurements were conducted with a Clemex CMT microhardness indenter at 300 gram force load unless otherwise stated and values reported are the average of a minimum of 10 measurements

7.5.3 Microscopy

The microstructures developed from various thermal cycles were evaluated by light and scanning electron microscopy. Dilatometer specimens were sectioned transverse to the long axis approximately one millimeter from the control thermocouple. Charpy impact specimens cycled for microstructural analysis were sectioned both on the notch plane and transverse to the long axis one millimeter away from the control thermocouple. Both types of specimen were then mounted in phenolic resin and prepared for metallography using diamond grinding wheels to remove enough material to expose the junction of the control thermocouple. Polishing was achieved using diamond suspensions of increasing fineness to a 1 μm final polish. Light optical microscopy was performed on a Zeiss Axiovert 220 microscope and scanning electron microscopy was performed with a JEOL JCM 5000 NeoScope. Prior austenite grain sizes (PAG) were calculated by the linear intercept method from optical micrographs. Fracture analysis on Charpy impact bars was achieved by examining the broken surfaces and by immersing the specimens in a solution of 160 mL hydrogen peroxide (40%), 10 mL of hydrofluoric acid and 30 mL of distilled water for 1 minute to remove the fracture



surface roughness. The smoothed surfaces were then etched in 3% nital to reveal the grain structure of the fracture surface. Fracture samples were also mounted and ground to expose the notch plane after which they were micrographed pre and post etching to reveal micro-cracking and crack paths.

7.6 Results

7.6.1 CCT and Microstructure

The CCT diagram developed from a 1350 °C peak temperature is shown in Figure 7-3. The transformation start temperature increases gradually over the cooling rates tested from 514 °C at $\Delta t_{8-5} = 1.4$ to 625 °C at $\Delta t_{8-5} = 50$ s. For $\Delta t_{8-5} < 8$ s martensite forms with bainite at temperatures below 475 °C but does not constitute a single phase at any cooling rate tested. At prolonged cooling rates sufficient solute is partitioned from the transforming ferrite phase into the remaining austenite to form martensite – austenite (MA) islands in a matrix of coarse ferrite constituting granular bainite[130, 131].

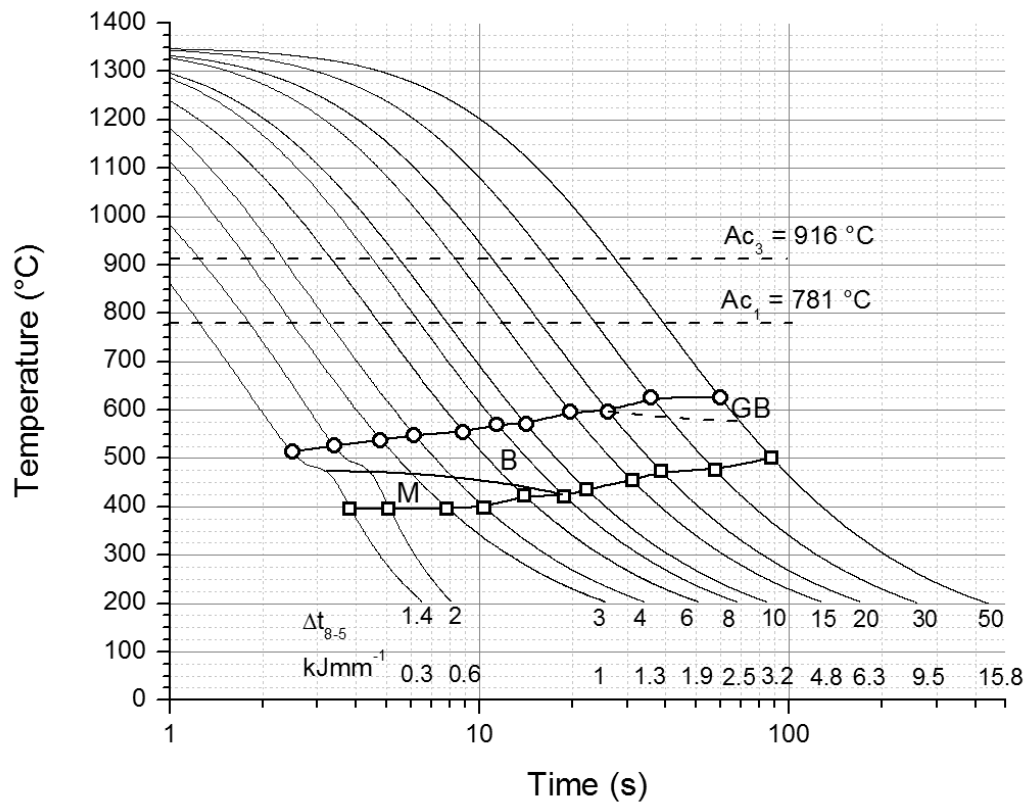


Figure 7-3 – CCT Diagram for X80 from 1350 °C

Microstructures of martensite, bainite and granular bainite are presented in Figure 7-4 (a)-(c) respectively. The bainitic sheaves originate at prior austenite grain boundaries and consist of fine laths of ferrite with aligned carbides between the laths. The MA islands formed at longer cooling times are equiaxed with a random distribution within the coarse ferrite.

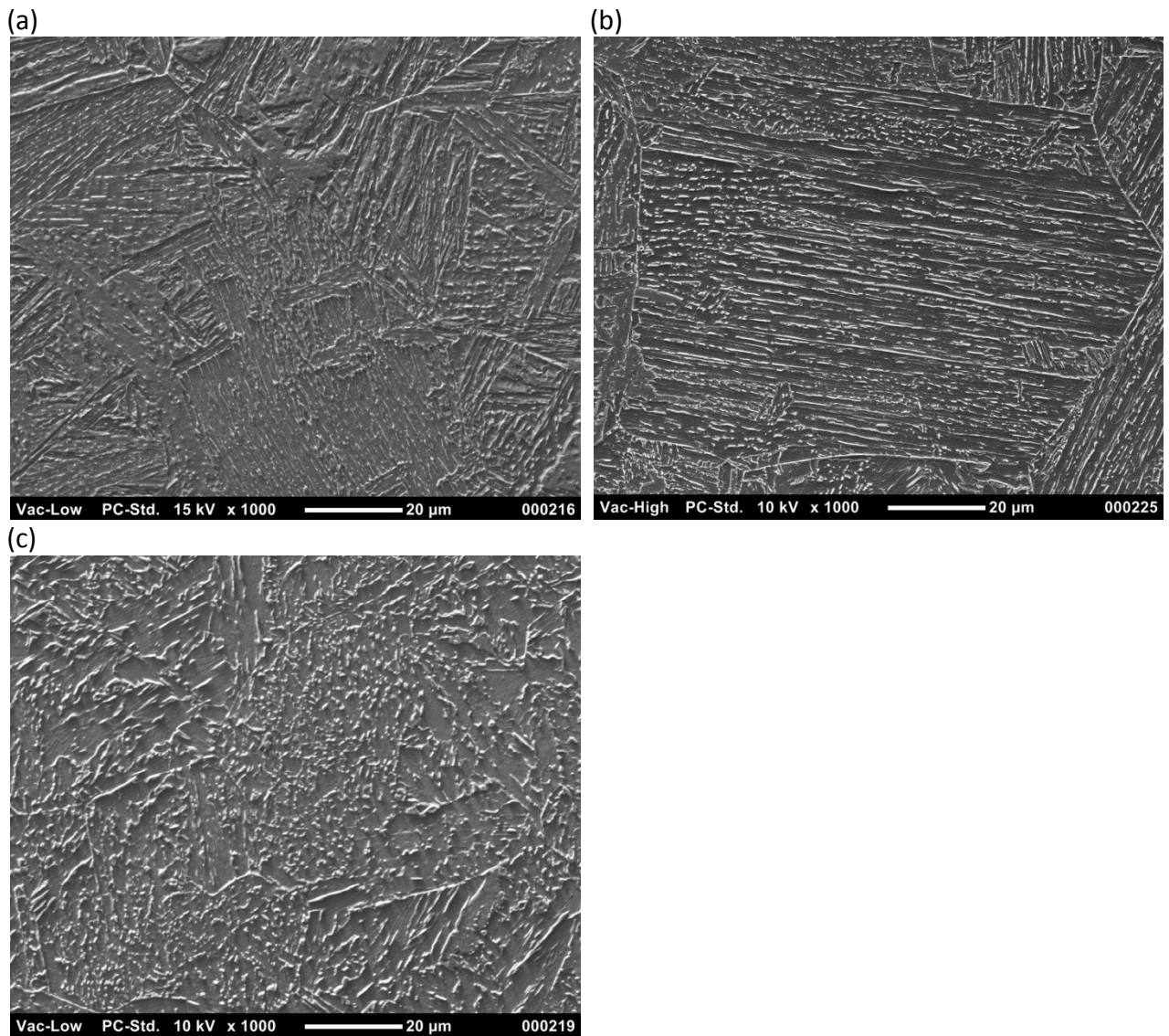


Figure 7-4 – Microstructures developed in X80 cooling from 1350 (a) bainite and martensite (b) bainite (c) granular bainite

7.6.2 *Prior austenite grain size*

The effect of peak temperature on the austenite grain size was examined by thermally cycling dilatometer specimens to different peak temperatures of 1100, 1200, 1300, 1350, 1400, 1425 and 1450 °C. The thermal cycles were designed so that the total time above 1000 °C was 4 seconds for each peak temperature including a hold of one



second at each respective peak temperature. The thermal profiles for the 7 specimens are shown in Figure 7-5 with the PAG as a function of peak temperature in the inset graph.

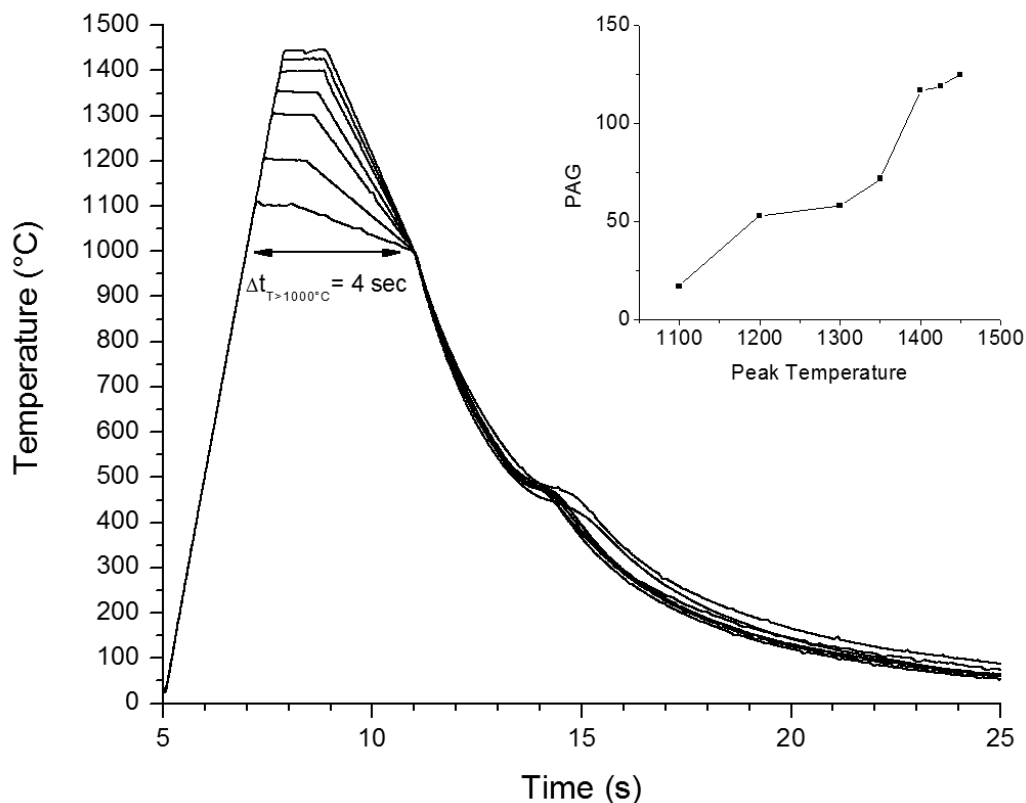


Figure 7-5 – Thermal cycles used to measure the prior austenite grain size and results (inset graph)

The PAG varied from $\sim 20 \mu\text{m}$ at 1100°C to $\sim 125 \mu\text{m}$ at 1450°C and corresponding micrographs are presented in Figure 7-6 (a) and (b) respectively. The dilatometric response of the steel was monitored during the thermal cycle and the start times as a function of peak temperature are given in Figure 7-7 along with the PAG. The variation of start temperature is from 552°C at a peak temperature of 1100°C to 474°C at a peak temperature of 1450°C . The specimens were free cooled (i.e., no heat was supplied via the Gleeble) from 1000°C and the Δt_{8-5} varies from 1.95 s to 1.73 s for 1100°C to 1450°C peaks respectively. From the CCT presented in Figure 7-3, there is an increase in the



start temperature of 10 °C for an increase of 0.6 s in the Δt_{8-5} from 1.4 to 2 s. The start measured for the 1350 °C PAG specimen is 516 °C at $\Delta t_{8-5} = 1.79$ s which would lie on the presented CCT diagram without deviation.

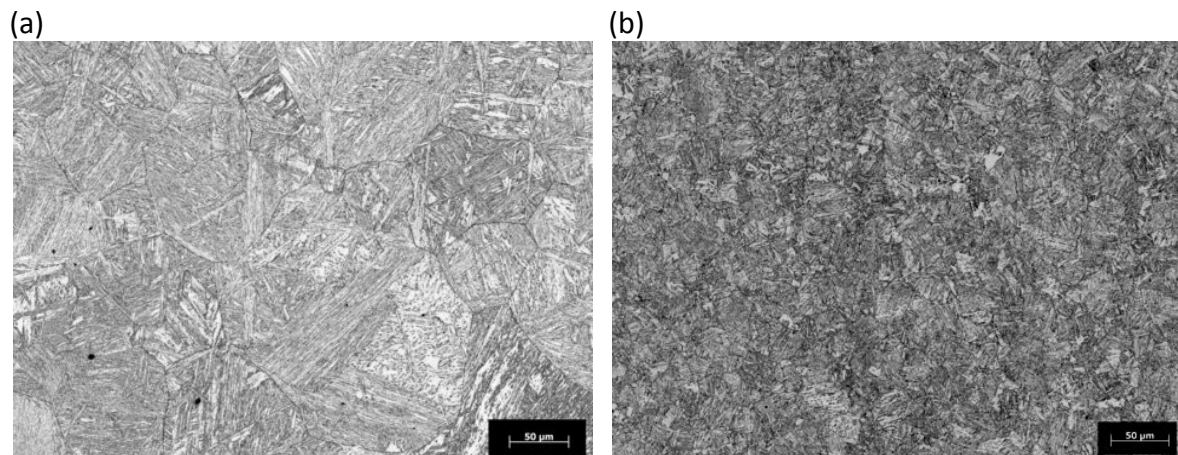


Figure 7-6 – Microstructure developed from (a) 1450 °C (b) 1100 °C

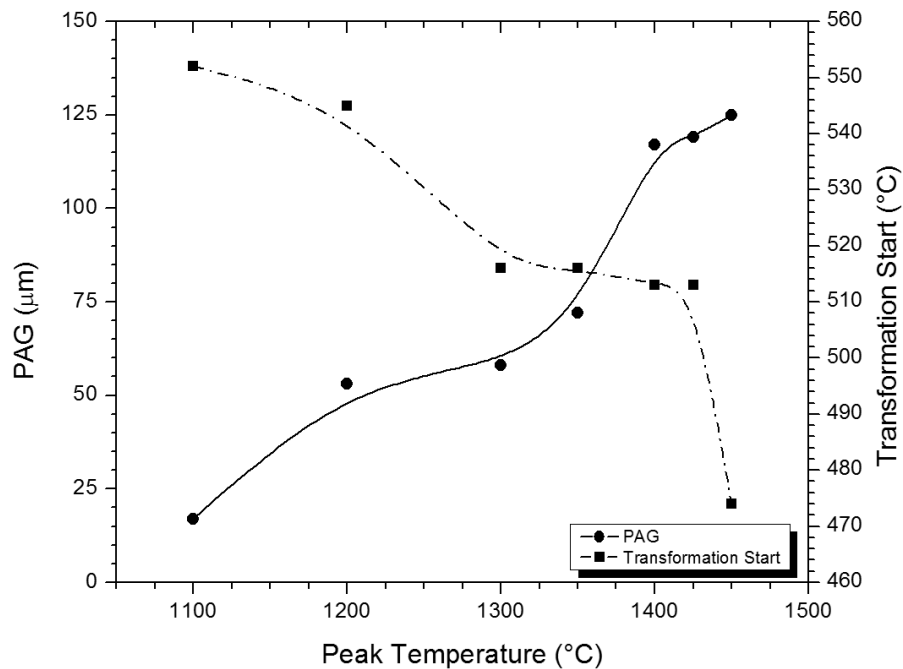


Figure 7-7– Correlation of prior austenite grain size (PAG) and transformation start temperature to peak temperature (moving average lines)



7.6.3 Thermal Simulation

The thermal cycle with dilatation data for the NTR- ICR GC HAZ program is presented in Figure 7-8 and shows the onset of the $\gamma \rightarrow \alpha$ transformation in the first cycle successfully interrupted by the imposition of the second thermal cycle. For the ICR GC HAZ cycle (not shown) the first thermal cycle is allowed to cool to 150 °C before the imposition of the second thermal cycle.

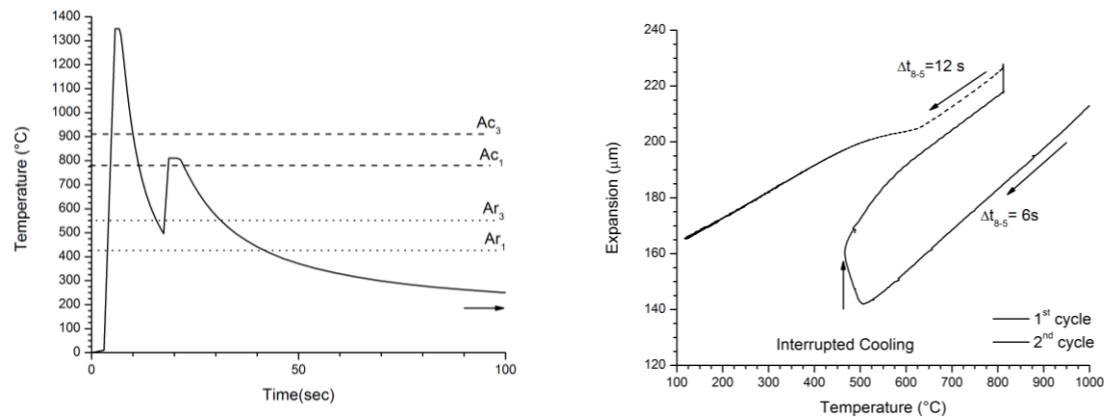


Figure 7-8 – Thermal cycle and dilatation response for NTR- ICR GC HAZ

The microstructures corresponding to the ICR GC HAZ and the NTR- ICR GC HAZ are presented in Figure 7-9 (a) and Figure 7-9 (b) respectively. The majority of both microstructures are composed of bainite. There is an increase in the coarseness of the bainite in the NTR- ICR GC HAZ and there is no delineation of the PAG as indicated in Figure 7-9 (a) for the microstructure of the completed ICR GC HAZ cycle. Hardness values were measured at random in the NTR and the ICR GC HAZ microstructures and at the PAG boundaries of the ICR GC HAZ samples. The PAG boundary of the ICR GC HAZ



sample is ~ 30 HV harder than the matrix, while the NTR GC HAZ specimen is ~10 HV harder than the ICR GC HAZ sample.

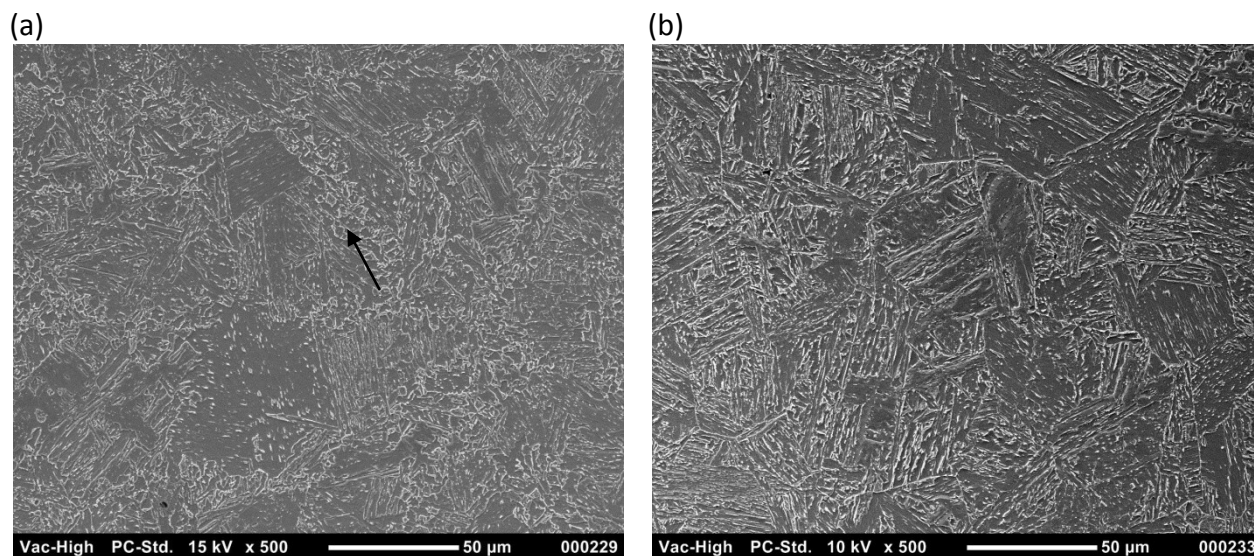


Figure 7-9 – Thermal simulation microstructures (a) ICR GC HAZ (arrow indicates decorated PAG boundary) (b) NTR-ICR GC HAZ

Table 7-2 – Hardness values for ICR GC HAZ and NRT ICR GC GC HAZ samples

Sample	Location	HV	Load (gf)
ICR GC HAZ	Random	248 ± 4	300
ICR GC HAZ	PAG boundary	279 ± 17	25
NTR ICR GC HAZ	Random	258 ± 8	300

The hardness data are presented in Table 7-2. Acicular ferrite is also present in the microstructure of the NTR- ICR GC HAZ. The measured start temperatures for the second $\gamma \rightarrow \alpha$ transformation of the ICR-GC- HAZ and the NTR- ICR GC HAZ are 718 °C and 615 °C respectively. The microstructure of the GC HAZ is the same as that presented in the CCT diagram (bainitic microstructure) in Figure 7-4 (b).



7.6.4 Toughness

Toughness of the X80 material was evaluated by Charpy impact for base metal, GC HAZ with $\Delta t_{8-5} = 6$ s, ICR GC HAZ, and NTR- ICR GC HAZ and is presented in Figure 7-10 (a) through (d) respectively. The energy transition temperature (ETT) was calculated as the temperature corresponding to the average of the upper and lower shelf energies [143, 218]. The upper shelf energy and the ETT as calculated from the graphs in Figure 7-10 are summarized in Table 7-3.

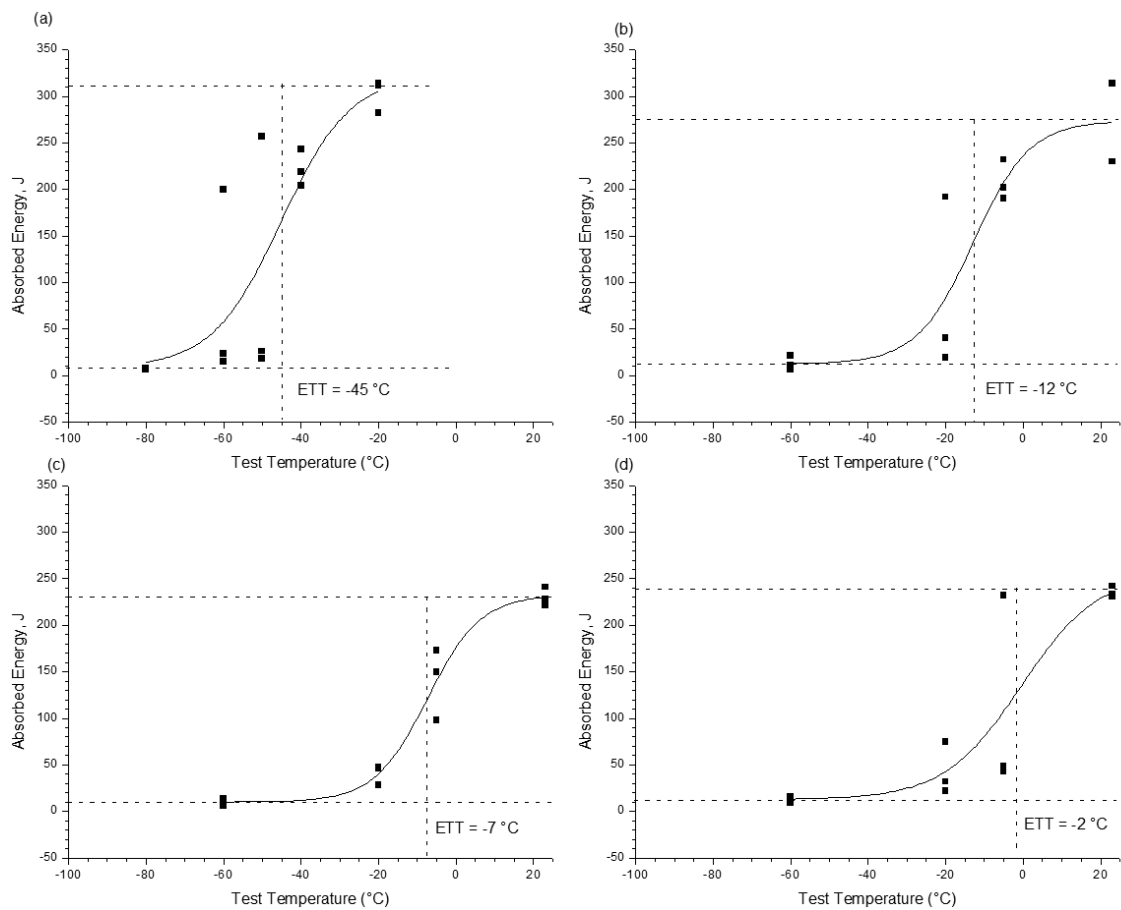


Figure 7-10 – Charpy impact energy versus test temperature for simulated X80 specimens (a) base metal (b) single cycle GC HAZ (c) ICR GC HAZ (d) NTR ICR GC HAZ



Table 7-3 - Charpy Impact Test Results

Specimen	Upper Shelf Energy (J)	ETT (°C)
Base Metal	303	-45
GC HAZ	273	-12
ICR-GC HAZ	232	-7
NTR ICR GC HAZ	256	-2

There is a dramatic reduction in both the upper shelf and the ETT with imposed thermal cycles. The GC HAZ specimen shows the highest upper shelf energy at 273 J and ETT of -12 °C. The ICR GC HAZ and NTR –ICR GC HAZ both have reduced upper shelf energies at 232 and 256 J respectively and the ETT for both thermal cycles are -7 °C and -2 °C respectively.

Figure 7-11 (a) through (d) show SEM fractographs for Charpy impact specimens broken at -60 °C. Cleavage facets of 50 to ~ 80 µm are found in all of the HAZ samples.

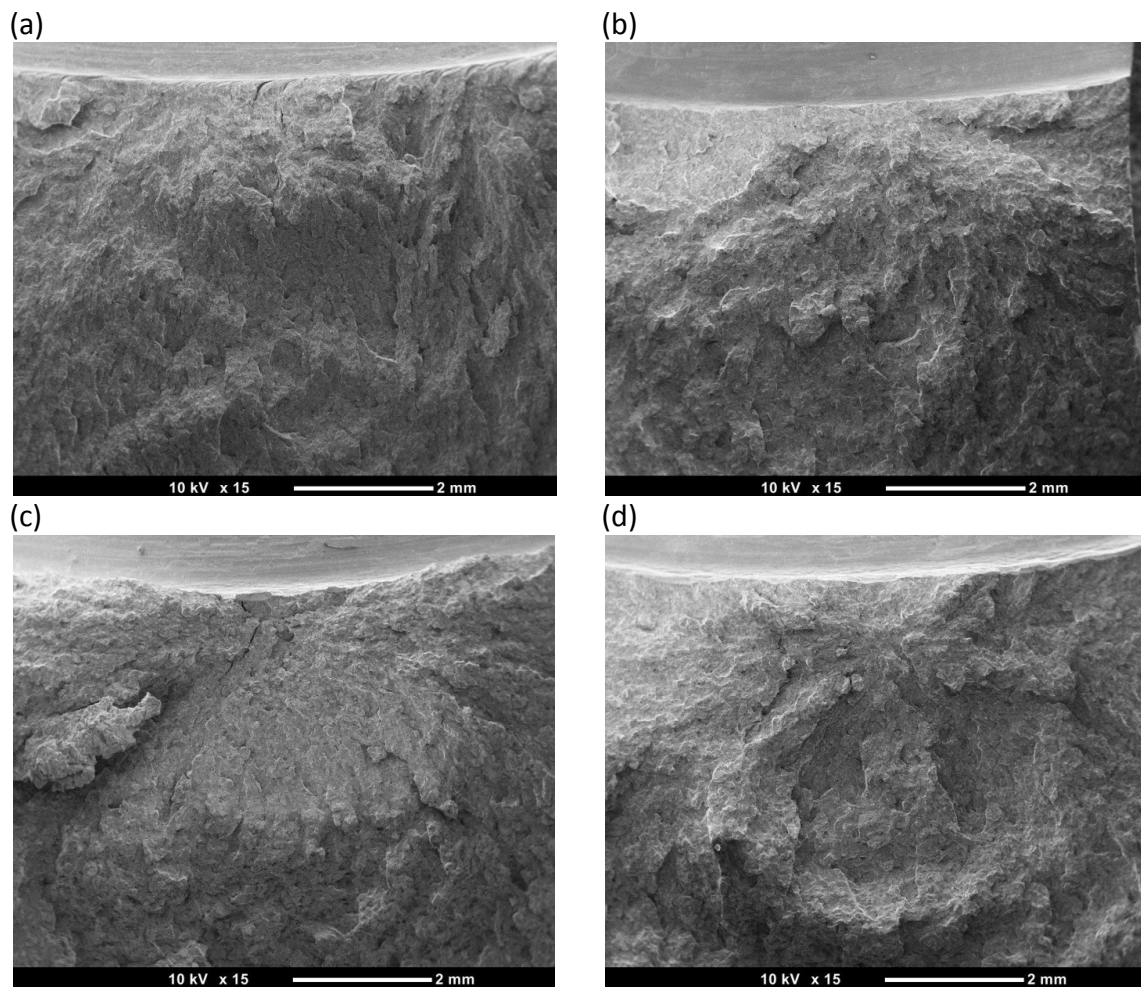


Figure 7-11 – Brittle fracture surfaces. (a) Base metal (b) GC-HAZ $\Delta t_{8-5} = 6s$ (c) ICR GC HAZ (d) NTR- ICR GC HAZ

The surfaces of samples that failed by cleavage were examined to establish the fracture initiation site. Transgranular fracture was seen in all HAZ specimens and no intergranular decohesion was observed. Multiple initiation sites were found in low temperature cleavage fracture specimens[215]. The pattern of major tear and radiating river lines was traced to the initiation site or sites. Large facets with low misorientations and MA particles were found to account for the triggering events as seen in Figure 7-12 (a) and (b) for a GC HAZ specimen.

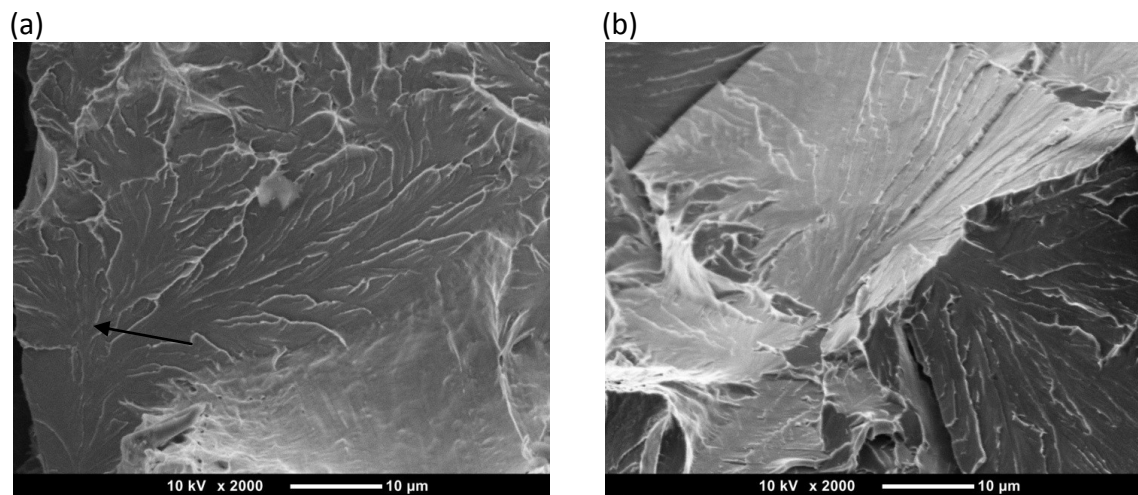


Figure 7-12 – Different types of cleavage triggering sites in a GC HAZ specimen (a) MA island (b) multiple facets with low misorientation

The etched cleavage facet of a GC HAZ sample is shown in Figure 7-13 (a) where the bainitic microstructure and PAG boundaries have been revealed. There is a secondary crack shown in Figure 7-13 (b) which can be seen to traverse both the PAG and the bainitic ferrite laths. The fracture front for the matching half of the same specimen mounted in resin is shown in Figure 7-13 (c) and secondary cracks in the bainitic structure are shown in Figure 7-13 (d).

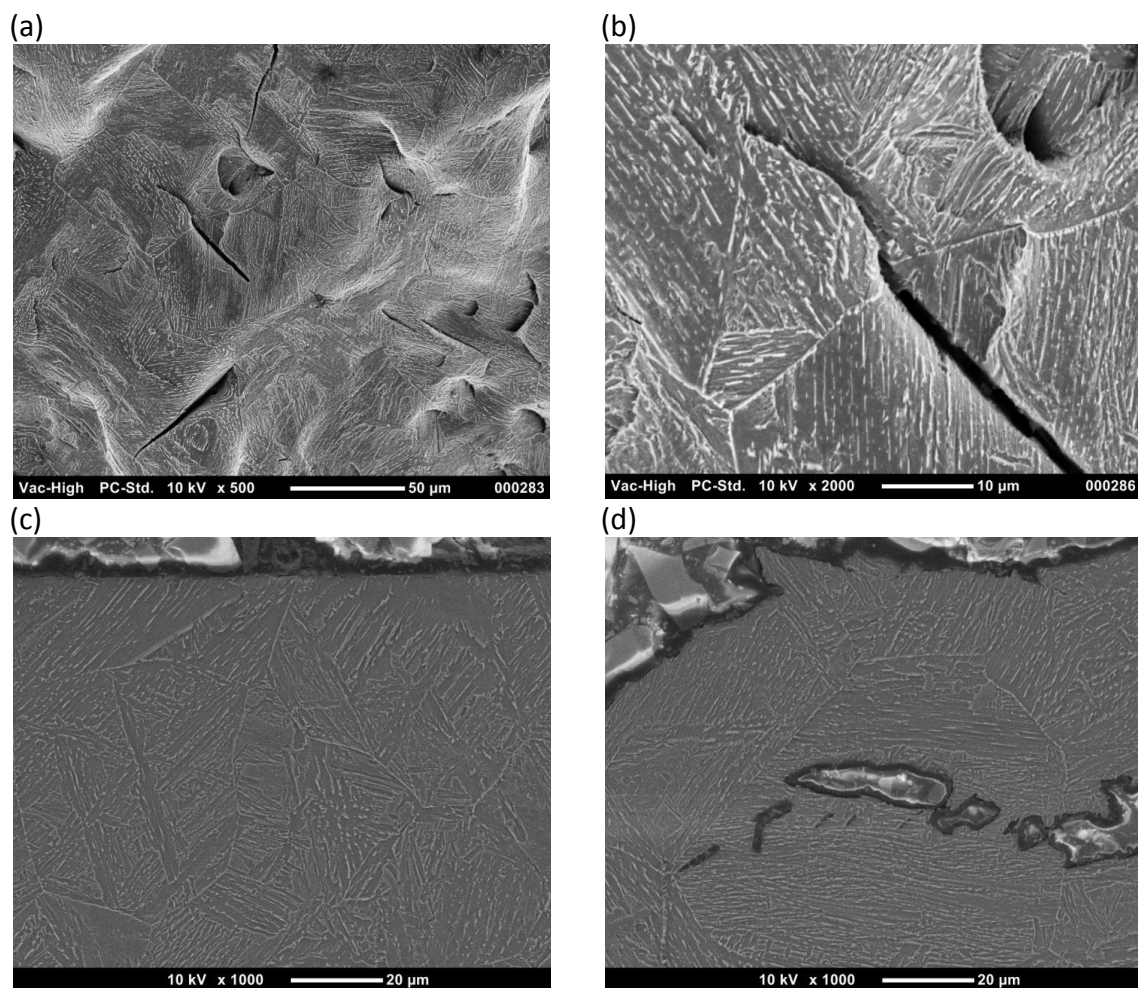


Figure 7-13 – SEM fractography (a) Etched cleavage facet (b) detail of micro-crack (c) crack front in the mounted GC HAZ sample (d) microcracking in the mounted sample

7.7 Discussion

The types of microstructures found in this steel are quite similar to those reported elsewhere for similar compositions and strengths [72, 143, 145, 218] and comprise primarily bainite, martensite and coarse bainite with MA islands referred to as granular bainite. The formation of bainite in the GC HAZ is facilitated by the rapid cooling rates employed to simulate low heat input welding parameters [207, 240-242]. The relatively high peak temperature experienced in the GC HAZ results in significant growth of the



austenite grains from reduced solute drag at grain boundaries and higher kinetic mobility [161, 200, 209]. While both acicular ferrite and bainite form by the same mechanism [243, 244], bainite nucleates at austenite grain boundaries while acicular ferrite nucleates intragranularly primarily on intermetallic inclusions [55, 193, 213, 245, 246]. The transformation start temperature is suppressed by a reduction in austenite grain size as can be seen in Figure 7-7. This phenomenon is attributed to the reduction in nucleation sites (austenite grain boundary area) required for nucleation [220]. The resulting under-cooling developed by suppressing the transformation start temperature favors displacive transformation products (bainite, martensite).

Numerous studies [148, 212, 213, 246, 247] have found that the same steel composition is capable of transforming to either bainite or acicular ferrite with the application of strain during cooling. In the present case, without strain, bainite has formed. However, the transformation of the microstructure to bainite from acicular ferrite is unfortunate as can be seen from the toughness data generated and presented in Figure 7-10 where the acicular base metal has superior upper shelf and ETT values. The ETT for all of the thermally cycled microstructures is close to, or above, -10°C which fails the toughness requirements for arctic applications. The poor lower shelf energy is a reflection of the large effective grain size in the HAZ region simulated here [248]. Zhang and Knott [217] found that cleavage fracture in bainitic and martensite microstructures was reduced by the fine distribution of microstructural features. The martensitic and mixed martensite- bainite microstructures exhibited improved fracture toughness compared to those comprised of pure bainite in their study.

The upper shelf energies for both the ICR GC HAZ and NRT ICR GC HAZ are quite close to that of the GC HAZ and all three are ~ 30 to 70 J less than the base metal. The rapid transition to brittle failure for the thermally cycled specimens is most probably due to microcracks forming at carbides within the bainite sheaves as reported by Zhang and



Knott [217] and is supported by the appearance of microcracks in the bainitic microstructures produced here as shown in Figure 7-13 (b) and (d). The resistance of bainite to crack propagation is known to be low [93, 165, 249] and frequently cracks traverse entire sheaves before encountering a high angle boundary of sufficient energy to cause deflection. In Figure 7-13 (b) a microcrack can be seen to traverse the bainitic sheaf of a cleaved facet with a deflection at the PAG. However, in Figure 7-13 (c) the cleavage front cleaves the entire PAG and bainite structure without deflecting. This behavior is seen throughout the HAZ samples and correlates to the cleavage facet sizes which are approximately that of the PAG. The detrimental effect of the ICR GC HAZ in creating local brittle zones (LBZs) is lessened here by the larger austenite grains formed in the $\alpha + \gamma$ region of the heat treatment. The localized increase in hardness from the PAG delineation with corresponding decrease in toughness is only ~ 30 HV which is unlikely to be sufficient to cause a significant reduction in toughness as reported elsewhere [151, 167, 169].

The slight increase in the upper shelf energy of the NTR-ICR-GC HAZ samples compared to the ICR GC HAZ (~ 20 J) is likely due to the absence of hard MA phase which delineates the prior austenite grain boundaries in the ICR GC HAZ and the introduction of the acicular ferrite phase. However the increased coarseness of the microstructure from prolonged cooling results in an increase in the ETT. The reaustenitization of mixtures of bainite α_b and austenite, and acicular ferrite α_a and austenite has been studied by Yang and Bhadeshia [250] for both isothermal and continuous transformations. They found that the reaustenitization of a $\alpha_b + \gamma$ mixture, first transformed isothermally at 460 °C, at 720 °C was detectable after 3 seconds and that a γ volume fraction increase of 0.05 occurred after 26 seconds. Thus, for the NTR ICR GC HAZ thermal cycle used here to represent close torch spacing in a dual torch setup, it is reasonable to assume that while some austenite will form during the second thermal cycle, the quantity will be minimal.



7.8 Conclusions

The transformation of an X80 pipe steel corresponding to different regions of the HAZ created by multi pass GMAW thermal cycles and the simulated effect of closely spaced mechanized dual torch P-GMAW has revealed the following:

- The continuous cooling of an X80 steel with initial acicular microstructure over Δt_{8-5} from 2 to 50 seconds results in mixed bainite and martensite microstructure at fast cooling times, bainite at intermediate cooling times and granular bainite with bainite at longer cooling times.
- The effect of peak temperature (with the total time above 1000 °C equal to 4s) on the prior austenite grain size is not monotonic, but plateaus over a 1200 °C to 1350 °C range
- The toughness of the steel is affected detrimentally in the GC HAZ and ICR GC HAZ regions equivalently with a reduction in the ETT to ~ -10 °C and the loss of ~ 70 J in the upper shelf impact energy
- The effect of interrupting the $\gamma \rightarrow \alpha$ transformation has no appreciable impact on improving the toughness of the ICR GC HAZ as the increase in upper shelf energy is offset by a reduction in the ETT

7.9 Acknowledgements

This research was funded by CANMET-MTL and the Federal Interdepartmental Program for Energy Research and Development. The authors would like to thank Mr. M. Kerry for his machining expertise, Mr. R. Eagleson for mechanical testing. The research is part of a larger consolidated program jointly funded by the Pipeline and Hazardous Materials Safety Administration of the U.S. Department of Transportation (DOT), and the Pipeline Research Council International, Inc. (PRCI). The views and conclusions in this paper are those of the authors and should not be interpreted as representing the official policies of any of these organizations.



Thermal Simulation of HAZ regions in a modern High Strength Steel

The author (G.G.) also wishes to acknowledge CANMET-MTL management for providing the opportunity to work and have access to laboratory facilities during the course of this research and to NSERC and McGill University for funding grants.



8 Comprehensive Conclusions

The safe construction of pipelines depends on a thorough understanding of the effect that welding high strength line pipe steel with modern mechanized P-GMAW technology has on the resulting microstructure and properties of both the line pipe and the weld metal. The effect of P-GMAW on modern high strength line pipe has been studied and the results are presented in this dissertation.

The initial research experiments were directed toward studying the transformations that occur in modern high strength line pipe as a result of girth welding using mechanized pulsed gas metal arc welding (P-GMAW) technology. These transformations have been explored and thermal cycles representative of P-GMAW processes were simulated with a Gleeble thermo-mechanical simulator. The changes exhibited by a grade 690 steel during cooling from two different peak temperatures were explored. It was demonstrated that there is a disparity between microstructural phases that form on cooling from a 1350 °C peak versus a 900 °C peak. The 1350 °C peak produced martensite, bainite and granular bainite over a Δt_{8-5} cooling range 1.3 to 50 seconds. The 900 °C peak produced martensite, bainite, polygonal ferrite, pearlite and martensite/austenite over a Δt_{8-5} cooling range of 1 to 9987 seconds. The suppression of reconstructive transformation products, also known as the hardenability, of the steel is increased when cooling from a higher peak temperature. Finally, in addition to increased hardenability, it was also shown that the thermal range over which both displacive and reconstructive transformations occur is narrower when cooling from a 1350 °C peak temperature.

The second research project was designed to expand the knowledge of line pipe transformations over a range of different steel compositions and to correlate the transformations to mechanical properties. The continuous cooling transformation



diagrams of three X100 (grade 690) line pipe steels in the grain coarsened heat affected zone were created through the dilatometric analysis of the transformations that occur in steel subjected to thermal simulation equivalent to that generated during P-GMAW. The transformation products identified by optical, scanning and electron microscopy vary from martensite, to bainite, to granular bainite over a range of transformation start temperatures from 495 °C to 600 °C corresponding to Δt_{8-5} times of 1.2 to 50 seconds and heat inputs of approximately 0.3 to 15 kJmm⁻¹. Simulated thermal cycles with 1350 °C peak temperatures matched the single cycle GC-HAZ of the real weld most closely at $\Delta t_{8-5} = 6$ s and a simulated energy input of 1.9 kJ/mm⁻¹. Toughness testing of the steel was achieved with Charpy impact tests on full size bars with thermal cycles from 1350 °C at Δt_{8-5} cooling times of 6 s and 10 s. It was found that the X100-4 steel with Ni, Mo and Cr additions had the best toughness properties for both simulated conditions. This improved toughness was related to the refined bainite phase co-existing with fine lath martensite resulting from the increased hardenability and suppression of the austenite transformation start temperature. The formation of a primarily bainitic microstructure, or a granular bainitic microstructure was found to be deleterious to toughness as cracks were shown to cleave entire grains.

The objective of the third set of experiments was to understand the effect of mechanized welding on the weld metal. The dilatometric analysis of five weld metals with compositions designed for use with mechanized GMAW pipe girth welds was achieved using samples thermally simulated to represent the reheated weld metal regions at various heat input and cooling times. The dilatometric data was correlated to microstructures observed through optical and scanning electron microscopes and compiled into separate CCT diagrams. The transformation products range from martensite to acicular ferrite and bainite of varying coarseness with polygonal ferrite formed at longer cooling times. This approach, used for the first time, to the best of the author's knowledge, created a weld consisting of two distinct regions which allows



direct comparison of thermal cycles and heat inputs in the same material. A single high heat weld deposit was used as a starting material for subsequent thermal cycling applicable to the P-GMAW of X100 steel girth welds. This method was found to be an excellent option for weld metal thermal simulation. Very close approximation of the 0.5 kJmm⁻¹ weld region was achieved using a 1.5 kJmm⁻¹ deposit subjected to thermal cycles with Δt_{8-5} cooling rates of 3.5 to 10 seconds depending on the chemistry. A heating rate of 250 °Cs⁻¹ to a peak temperature of 1300 °C with a hold time at peak of 1 second was used for all samples. The CCT diagrams and hardness regression equations generated give an operating window for a small range of chemistries applicable to X100 girth welds. The properties of three weld metal chemistries were assessed by Charpy impact toughness and show that an acicular ferrite microstructure formed at longer cooling times and had improved toughness.

The goal of the fourth research project was to expand the scientific understanding of transformations and properties to new and novel thermal cycles that have not previously been studied. The transformations characteristic of different positions in the HAZ of a GMAW weld in high strength X80 (grade 550) pipe steel and the effect of closely spaced mechanized dual torch P-GMAW were achieved through simulation using a Gleeble thermo–mechanical simulator. The continuous cooling of an X80 steel with initial acicular microstructure over Δt_{8-5} cooling times from 2 to 50 seconds resulted in mixed bainite and martensite microstructure at fast cooling rates, bainite at intermediate cooling rates and granular bainite with bainite at longer cooling times. This data was compiled into a CCT diagram. The effect of peak temperature (with the total time above 1000 °C equal to 4 s) on the prior austenite grain size is not monotonic, but plateaus over a 1200 °C to 1350 °C range. This is attributed to the high levels of Nb in this particular steel. The toughness of the steel is affected detrimentally in the GC HAZ and ICR GC HAZ regions equivalently with a reduction in the ETT to ~ -10 °C and the loss of ~70 J in the upper shelf impact energy. The application for the first time, to the best



of the author's knowledge, of an interrupted transformation that can occur from close torch spacing and fast travel speeds was achieved. No appreciable effect was found to improve the toughness of the ICR GC HAZ despite preventing the formation of MA at the prior austenite grain boundaries.

The transformation of line pipe steel in the grain coarsened, intercritically reheated grain coarsened and interrupted intercritically reheated grain coarsened heat affected zones is now characterized for a range of heat inputs that can arise during girth welding. The transformations that result from the reheating of weld metal during multi pass girth welding were characterized for five different compositions that span a range of weld metal chemistries. The mechanical properties that arise in these regions as a consequence of welding have been explored and characterized to enhance the scientific knowledge surrounding girth welding of modern high strength line pipe steels



9 Contributions to Original Knowledge

- 1) From the manuscript: Comparison of Base Metal and HAZ CCT diagrams for X100 pipe steel:
 - a) Continuous cooling transformation diagram of X100 (grade 690) steel applicable to a 900 °C peak temperature
 - b) Continuous cooling transformation diagram of X100 (grade 690) steel applicable to a 1350 °C peak temperature
 - c) Correlation of the effect of peak temperature on the transformations in X100 line pipe

- 2) From the manuscript: CCT diagrams and impact toughness applicable to the GC HAZ region generated in X100 line pipe
 - a) Continuous cooling transformation diagrams for two X100 (grade 690) steels applicable to a 1350 °C peak temperature and complimentary to the previously established 1350 °C diagram from the first manuscript.
 - b) Microstructure and property relationships for the GC HAZ detailing the range of heat inputs that result in deleterious toughness properties.
 - c) Identification of the initiation and brittle crack propagation mechanisms as they apply to the simulated GC HAZ of the X100 steels studied.

- 3) From the manuscript: CCT Diagrams of Weld Metal Applicable for Girth Welding of X100 line pipe



- a) Validation of a novel weld design to generate specimens for thermal simulation from P-GMAW processes
 - b) The continuous cooling transformation diagrams of five different weld metal compositions applicable to the re-heated zone generated by mechanized P-GMAW
 - c) Equations correlating the carbon equivalent (alloy content) of the weld metal and hardness generated in the re-heat regions
 - d) Microstructure property relationships for weld metal to facilitate the targeting of welding procedures and chemistry selection for appropriate toughness
- 4) From the manuscript: Thermal Simulation of HAZ regions in a modern High Strength Steel
- a) Continuous cooling transformation diagram for a modern high strength X80 (550 MPa) steel
 - b) Introduction of a novel thermal simulation of interrupted cooling as it relates to mechanized dual torch (P-GMAW) welding at close spacing and fast travel speed
 - c) Correlation of microstructure and properties in an X80 high strength steel for the grain coarsened, intercritically reheated grain coarsened, and interrupted intercritically reheated grain coarsened heat affected zone.



Appendix A – Experimental Techniques

The nature of a manuscript style thesis requires explanation of the experimental procedure used in each section. However, significantly more time during the thesis study period is often dedicated to devising and perfecting experimental procedures than can be included in a manuscript's experimental procedure. Therefore a more involved experimental procedure, including suggestions devised from experiments gone awry, is presented for the elucidation of future researchers.

Thermal Cycles

Measurement

Thermocouples imbedded into the walls of plates prepared for P-GMAW were used to acquire thermal cycles at various positions within the joint. Additionally, a thermocouple was plunged into the molten weld pool trailing the arc to measure the thermal profile of the solidifying weld metal. In general, the data from the imbedded welds was found to be noisy and it was very difficult predict the final position of the thermocouple in the HAZ due to slight variations in the amount of base metal melting. This problem is exacerbated by the oscillation of the electrode during P-GMAW. When thermocouples were exposed to the full arc, the junction in the thermocouple wire was lost, and an open circuit formed. The solidification of the weld metal would normally serve to re-form the junction, but without recording the time lag between the solidification of the pool and of the wire. In most cases, the temperatures recorded when the circuit closed, were significantly below the solidus of the steel. The thermocouples plunged into the molten pool could be properly shielded and were not exposed to the extreme energy of the arc, but rather the high temperature of the weld pool. Data that was gathered from thermocouples drilled into the joint walls that maintained a closed circuit throughout the experiment were then dissected from the weldment and the position of the thermocouple in relation to the fusion line was



measured. For ease of insertion and general experimental robustness, shielded thermocouples were used.

Analysis & Correlation

The measured thermal cycles were analyzed to extract the cooling rates at various intervals along with peak temperatures. The extracted data was then used to calculate various cooling curves using the Gleeble software. The measured and calculated curves were compared statistically using Origin to evaluate the best approximation of the real curve. Rykлайн 3D cooling curves were found to generate the closest approximation over the range of desirable cooling rates. A 100 °C pre heat and the cooling rate expressed as the cooling time from 800 °C to 500 °C (Δt_{8-5}) were used to generate a series of cooling curves.

Simulation Setup

Thermal control during simulation was maintained via a Type K or Type R thermocouple welded directly to the specimen at mid-length using a jig supplied by the manufacturer. Much practice was required to ensure high quality welds could be produced regularly. In general gap of ~ 1.5 mm with a total wire length of ~ 7 mm was found to produce the best results. For samples with multiple thermocouples, it was found that applying one half of the wires along the entire length of the specimen before welding the second wires behind the first prevented the jig from damaging the junctions during the impact process.

Heating rates in 10x 10 mm specimens were limited to 500 °Cs⁻¹ to minimize the amount of overshoot in achieving the desired peak temperature. Additionally, it was found to be very useful to reduce the proportional, and differential control values to 0.2 and 0.01. Sample programs for single and dual cycles programs are described below:



1. Heating at $500\text{ }^{\circ}\text{C}^{-1}$ to $1350\text{ }^{\circ}\text{C}$, holding for 1 second, cooling following a Rykalin 3D model with $\Delta t_{8-5} = 6\text{ s}$ to room temperature (GC-HAZ)
2. Heating at $500\text{ }^{\circ}\text{C}^{-1}$ to $1350\text{ }^{\circ}\text{C}$, holding for 1 second, cooling following a Rykalin 3D model with $\Delta t_{8-5} = 6\text{ s}$ to $150\text{ }^{\circ}\text{C}$, heating at $250\text{ }^{\circ}\text{C}^{-1}$ to 10% of the A_{c3} , holding for 2 seconds, cooling following a Rykalin 3D model with $\Delta t_{8-5} = 10\text{ s}$ (ICR GC HAZ)
3. Heating at $500\text{ }^{\circ}\text{C}^{-1}$ to $1350\text{ }^{\circ}\text{C}$, holding for 1 second, cooling following a Rykalin 3D model with $\Delta t_{8-5} = 6\text{ s}$ to 50% of the measured A_{r3} (interrupted transformation), heating at $250\text{ }^{\circ}\text{C}^{-1}$ to 10% of the A_{c3} , holding for 2 seconds, cooling following a Rykalin 3D model with $\Delta t_{8-5} = 12\text{ s}$ (NTR- ICR GC HAZ)

Specimens cut from the 5mm x5mm samples were heated at $250\text{ }^{\circ}\text{C}^{-1}$ to $1300\text{ }^{\circ}\text{C}$ and held for one second. It was found that the $500\text{ }^{\circ}\text{C}^{-1}$ heating rate resulted in fusion. In both cases, the 15mm grip spacing between the copper blocks was maintained for all specimens with a chiller temperature of $20\text{ }^{\circ}\text{C}$ to maintain equal thermal gradients in all specimens.

Analysis

Microscopy

The microstructures developed from various thermal cycles were evaluated by light and scanning electron microscopy. Dilatometer specimens were sectioned transverse to the long axis approximately one millimeter from the control thermocouple. Charpy impact specimens cycled for microstructural analysis were sectioned both on the notch plane and transverse to the long axis one millimeter away from the control thermocouple. Both types of specimen were then mounted in phenolic resin and prepared for metallography using diamond grinding wheels to remove enough material



to expose the junction of the control thermocouple. Polishing was achieved using diamond suspensions of increasing fineness to a 1 μm final polish. Light optical microscopy was performed on a Zeiss Axiovert 220 microscope and scanning electron microscopy was performed with a JEOL JCM 5000 NeoScope. Etching X100 steel is challenging due to the low carbon content of the steel. Various etchants were used to evaluate different microstructural features. A 3% nital etchant with a wetting agent proved to be excellent for revealing martensite and bainite features. Marshall's reagent and picric acid were used to reveal prior austenite grain boundaries, but were often no more successful than nital. Le Pera's etch, when used on sunny low humidity days, was found to be good for revealing MA. The best method for revealing prior austenite grain boundaries was to thermally cycle the specimen into the intercritical region and hold for 5s. Prior austenite grain sizes (PAG) were calculated by the linear intercept method from optical micrographs.

Selected specimens were prepared for TEM analysis to confirm the interpretation and classification of the microstructures identified optically and with SEM. Samples were cut with a precision saw using a general purpose diamond wafering blade. A slice of 500 μm thick was made. Discs were punched with a Gatan 3.0 mm diameter punch. The samples were reduced using silicon carbide 240, 320, 400, 600 and 1200 grit papers to reduce thickness of pieces equally on both sides. Approximately 40-50 μm thick samples were obtained. Samples were dimpled using 3 μm diamond paste and 4-6 μm CBN to a depth of approximately 30 μm and then fine dimpled using 1/4 μm diamond for about 1 minute. Ion milling was carried out using Gatan Duo-Mill with Liquid nitrogen cold stage to prevent heating of sample. TEM examination was carried out using a Philips CM20 FEG TEM equipped with a Schottky field emission gun that was operated at a voltage of 200 kV.

Charpy & Hardness



The Samples for Charpy impact testing were notched post thermal cycling and reduced to standard dimensions (10 x 10 x 55 mm) before being assessed in a TINIUS OLSEN Model #64 impact tester at temperatures from -120 °C to 22 °C. Fracture analysis on Charpy impact bars was achieved by examining the broken surfaces and by immersing the specimens in a solution of 160 mL hydrogen peroxide (40%), 10 mL of hydrofluoric acid and 30 mL of distilled water for 1 minute to remove the fracture surface roughness. The smoothed surfaces were then etched in 3% nital to reveal the grain structure of the fracture surface. Fracture samples were also mounted and ground to expose the notch plane where they were micrographed pre and post etching to reveal micro-cracking and crack paths. For full hardness surveys, an x-y grid at 500 μm spacing was superimposed over the entire reduced section of the specimen with a 50 μm offset from all edges. Vickers hardness numbers were calculated using a load of 300 g Clemex CMT microhardness indenter.

Dilatometry

Transformation start and finish temperatures were obtained by evaluating the volumetric expansion measured by a linear variable differential transformer (LVDT) attached to quartz push rods placed across the thermal center of the specimen during cycling. The specimens for dilatometric analysis were reduced at mid length to a cylinder of 6 mm diameter over 6 mm length. To assist in the examination of phases formed at extreme cooling rates, a few specimens were reduced to a 4 mm diameter over the 6 mm length. The deviations from linearity during thermal expansion or contraction owing to the density difference between α and γ were taken as the start and finish temperatures of transformation. The grip spacing (free span) of the Gleeble copper jaws was set to 15mm with the adjustable jaw connected via a 4mm coupler to allow stress-free accommodation of the linear thermal expansion and contraction. The resolution of the LVDT in the Gleeble system is given as 50 nm.



Data collected from the Gleeble system was plotted and analyzed using Origin software. Plots of relative linear expansion versus temperature were generated for all thermal cycles and the linear regions of the curve corresponding to the thermal contraction of the austenite and of the FCC transformation product (TP) were fit using a linear best fit equation. The lever rule was used to calculate the fraction of austenite transformed and the methodology is illustrated in Figure 6-2 [204]. The fraction of austenite transformed is calculated as the quotient of the lines BC and AC where BC represents the difference between the dilation data and the FCC linear fit extrapolation, and AC is the difference between the FCC and TP linear fit equations, over the temperature range of interest. The onset and finish temperatures were calculated as the 2% and 98% values of the fraction transformed and intermediary transformations were detected using the first derivative of the fraction transformed. This is a modified method compiled from the work of Yang and Bhadeshia [191] to establish a reliable method for determining the martensite start temperature via strain offset and the general method proposed by de Andres *et al.* [188] for the calculation of transformation start temperatures by deviation from linearity in the FCC contraction. The strain offset method yields an improved standard deviation in start temperatures, however, the transformation products resulting from the thermal cycles used here are not all the same. Therefore, the application of a strain offset, where the proposed offset is a function of a variable microstructure, was supplanted by a 2% offset in fraction transformed. This offset could be automatically calculated using best fit and regression analysis to yield more reliable data than could be acquired by manual detection of the point of deviation of linearity in the FCC contraction. Secondary transformations were plotted by analyzing the microstructure, ascertaining the phase distribution and correlating the percentage measured to the temperature of the percentage transformed.



10 References

- [1] L. Electric. (2010, Aug 24, 2010). *Tandem Mig*. Available: <http://content.lincolnelectric.com/pdfs/products/literature/nx240.pdf>
- [2] E. Tsuru, "Uoe Forming," in <http://www.freepatentsonline.com/6782921-0-large.jpg>, <http://www.freepatentsonline.com/6782921-0-large.jpg>, Ed., ed, 2002.
- [3] L. J. Cuddy, "Microstructures Developed During Thermomechanical Treatment of HSLA Steels," *Metallurgical Transactions a-Physical Metallurgy and Materials Science*, vol. 12, pp. 1313-1320, 1981.
- [4] D. Yapp and S. A. Blackman, "Recent Developments in High Productivity Pipeline Welding," *Journal of the Brazilian Society of Mechanical Sciences and Engineering*, vol. 26, pp. 89-97, 2004.
- [5] L. J. Cuddy and J. C. Raley, "Austenite Grain Coarsening in Microalloyed Steels," *Metallurgical Transactions a-Physical Metallurgy and Materials Science*, vol. 14, pp. 1989-1995, 1983.
- [6] H. Takechi, "Metallurgical Aspects on Interstitial-Free Sheet Steel from Industrial Viewpoints," *ISIJ International*, vol. 34, pp. 1-8, 1994.
- [7] J. F. Lancaster, *Metallurgy of Welding*, 6th ed. Norwich, NY: William Andrew Publishing, 1999.
- [8] A. J. Deardo, "Niobium in Modern Steels," *International Materials Reviews*, vol. 48, pp. 371-402, 2003.
- [9] L. Meyer, F. Heisterkamp, and W. Mueschenborn, in *Microalloying '75*, New York, 1975, pp. 153-167.
- [10] U. S. E. I. Administration, "Annual Energy Review 2008 (Aer)," D. o. Energy, Ed., ed, 2009.
- [11] T. P. Limited. (2010, August 22). *Mackenzie Gas Project*. Available: <http://www.transcanada.com/mackenzievalley.html>
- [12] A. P. Project. (2010, August 22, 2010). *Proect Description*. Available: http://www.thealaskapipelineproject.com/project_description
- [13] J. Hammond and J. M. Gray, "Development of International Standards for High Strength Linepipe," presented at the Rio pipeline conference and exposition, Rio de Janeiro, 2007.



References

- [14] A. P. Institute, "Api 5l Specification for Line Pipe, Rev 44," ed: API, 2010.
- [15] J. Zhou, D. Horsley, and B. Rothwell, "Application of Strain-Based Design for Pipelines in Permafrost Areas," presented at the IPC2006, Calgary, Alberta, Canada, 2006.
- [16] H.-G. Hillenbrand, C. Kalwa, and A. Liessem, "Technological Solutions for Ultra-High Strength Gas Pipelines," presented at the 1st International conference on super-high strength steels, Rome, Italy, 2005.
- [17] R. L. Brockenbrough and F. S. Merritt, *Structural Steel Designer's Handbook : Aisc, Aashto, Aisi, Astm, Arema, and Asce-07 Design Standards*, 4th ed. New York: McGraw-Hill, 2006.
- [18] W. D. Callister, *Materials Science and Engineering : An Introduction*, 7th ed. New York: John Wiley & Sons, 2007.
- [19] T. Takahashi and W. A. Bassett, "High-Pressure Polymorph of Iron," *Science*, vol. 145, pp. 483-486, July 31, 1964 1964.
- [20] Z. S. Basinski, W. Humerothery, and A. L. Sutton, "The Lattice Expansion of Iron," *Proceedings of the Royal Society of London Series a-Mathematical and Physical Sciences*, vol. 229, pp. 459-467, 1955.
- [21] M. A. Yescas-Gonzalez and H. K. D. H. Bhadeshia. (2007, Aug 17, 2010). Cast Irons. Available:
http://en.hzbsj.com.cn/newEbiz1/EbizPortalFG/portal/html/InfoContent.html?InfoPublish_InfoID=c373e9113da0962b8ffb1358c26ad8c0
- [22] N. Yurioka, "Physical Metallurgy of Steel Weldability," *Isij International*, vol. 41, pp. 566-570, 2001.
- [23] F. Grimpe, S. Meimeth, H. Meuser, E. Muthmann, A. Liessem, C. Stallybrass, and Tms, *The Development of High Strength Heavy Plate for the Pipe Industry Using Modern Experimental and Numerical Methods*, 2008.
- [24] N. Yurioka, H. Suzuki, S. Ohshita, and S. Saito, "Determination of Necessary Preheating Temperature in Steel Welding," *Welding Journal*, vol. 62, pp. S147-S153, 1983.
- [25] D. K. Bullens, *Steel and Its Heat Treatment*, Ed. 3, rev. ed. New York,: Wiley, 1927.
- [26] Duckwort.We and J. D. Baird, "Mild Steels," *Journal of the Iron and Steel Institute*, vol. 207, pp. 854-&, 1969.
- [27] R. A. Hadfield, *Metallurgy and Its Influence on Modern Progress, with a Survey of Education and Research*. London,: Chapman, 1925.



References

- [28] J. H. Woodhead and S. R. Keown, "The History of Microalloyed Steels," presented at the HSLA Steels: Metallurgy and Applications, Beijing, China, 1985.
- [29] E. O. Hall, "The Deformation and Ageing of Mild Steel .3. Discussion of Results," *Proceedings of the Physical Society of London Section B*, vol. 64, pp. 747-753, 1951.
- [30] N. J. Petch, "The Cleavage Strength of Polycrystals," *Journal of the Iron and Steel Institute*, vol. 174, pp. 25-28, 1953.
- [31] J. Heslop and N. J. Petch, "The Ductile-Brittle Transition in the Fracture of Alpha-Iron .2," *Philosophical Magazine*, vol. 3, pp. 1128-1136, 1958.
- [32] L. Meyer, C. Strabburger, and C. Schneider, "Effect and Present Application of the Microalloying Elements Nb, V, Ti, Zr and B in HSLA Steels," presented at the HSLA Steels: Metallurgy and Applications, Beijing, China, 1985.
- [33] K. J. Irvine, Pickerin.Fb, and T. Gladman, "Grain-Refined C-Mn Steels," *Journal of the Iron and Steel Institute*, vol. 205, pp. 161-&, 1967.
- [34] J. C. Cao, Q. Y. Liu, Q. L. Yong, and X. J. Sun, "Effect of Niobium on Isothermal Transformation of Austenite to Ferrite in HSLA Low-Carbon Steel," *Journal of Iron and Steel Research International*, vol. 14, pp. 51-55, May 2007.
- [35] M. Djahazi, X. L. He, J. J. Jonas, and W. P. Sun, "Nb(C, N) Precipitation and Austenite Recrystallization in Boron-Containing High-Strength Low-Alloy Steels," *Metallurgical Transactions a-Physical Metallurgy and Materials Science*, vol. 23, pp. 2111-2120, Aug 1992.
- [36] C. Feng, H. S. Fang, Y. K. Zheng, and B. Z. Bai, "Mn-Series Low-Carbon Air-Cooled Bainitic Steel Containing Niobium of 0. 02%," *Journal of Iron and Steel Research International*, vol. 17, pp. 53-58, 2010.
- [37] S. H. Park, S. Yue, and J. J. Jonas, "Continuous-Cooling-Precipitation Kinetics of Nb(Cn) in High-Strength Low-Alloy Steels," *Metallurgical Transactions a-Physical Metallurgy and Materials Science*, vol. 23, pp. 1641-1651, Jun 1992.
- [38] D. San Martin, F. G. Caballero, C. Capdevila, and C. G. de Andres, "Discussion on the Rate Controlling Process of Coarsening of Niobium Carbonitrides in a Niobium Microalloyed Steel," *Microalloying for New Steel Processes and Applications*, vol. 500-501, pp. 703-710, 2005.
- [39] D. San Martin, T. de Cock, A. Garcia-Junceda, F. G. Caballero, C. Capdevila, and C. G. de Andres, "Effect of Heating Rate on Reaustenitisation of Low Carbon Niobium Microalloyed Steel," *Materials Science and Technology*, vol. 24, pp. 266-272, Mar 2008.



References

- [40] S. Shanmugam, R. D. K. Misra, J. Hartmann, and S. G. Jansto, "Microstructure of High Strength Niobium-Containing Pipeline Steel," *Materials Science and Engineering a-Structural Materials Properties Microstructure and Processing*, vol. 441, pp. 215-229, Dec 2006.
- [41] D. Q. Bai, S. Yue, W. P. Sun, and J. J. Jonas, "Effect of Deformation Parameters on the No-Recrystallization Temperature in Nb-Bearing Steels," *Metallurgical Transactions a-Physical Metallurgy and Materials Science*, vol. 24, pp. 2151-2159, Oct 1993.
- [42] B. Campillo, J. L. Albarran, F. Estevez, D. Lopez, and L. Martinez, "Precipitation of Niobium Nitrides in a High Nitrogen HSLA Steel," *Scripta Metallurgica*, vol. 23, pp. 1363-1368, Aug 1989.
- [43] G. Glover, T. R. Thomson, and J. Williams, "Cold-Rolled HSLA Steels Containing Niobium and Vanadium," *Metals Forum*, vol. 1, pp. 35-44, 1978.
- [44] C. Roucoules, S. Yue, and J. J. Jonas, "Effect of Alloying Elements on Metadynamic Recrystallization in HSLA Steels," *Metallurgical and Materials Transactions a-Physical Metallurgy and Materials Science*, vol. 26, pp. 181-190, Jan 1995.
- [45] H. Tamehiro, M. Murata, R. Habu, and M. Nagumo, "Optimum Microalloying of Niobium and Boron in HSLA Steel for Thermomechanical Processing," *Transactions of the Iron and Steel Institute of Japan*, vol. 27, pp. 120-129, 1987.
- [46] I. Weiss and J. J. Jonas, "Dynamic Precipitation and Coarsening of Niobium Carbonitrides During the Hot Compression of HSLA Steels," *Metallurgical Transactions a-Physical Metallurgy and Materials Science*, vol. 11, pp. 403-410, 1980.
- [47] S. A. Bratus, A. M. Uzienko, L. B. Fainberg, and P. N. Smirnov, "Strain Ageing of Low-Carbon Sheet Steel," *Metallurgist*, vol. 19, pp. 598-600, 1975.
- [48] B. Dutta and C. M. Sellars, "Effect of Composition and Process Variables on Nb(C, N) Precipitation in Niobium Microalloyed Austenite," *Materials Science and Technology*, vol. 3, pp. 197-206, 1987.
- [49] K. A. Taylor, "Solubility Products for Titanium-Carbide, Vanadium-Carbide, and Niobium-Carbide in Ferrite," *Scripta Metallurgica Et Materialia*, vol. 32, pp. 7-12, Jan 1995.
- [50] M. Cohen and S. S. Hansen, "On the Fundamentals of HSLA Steels," presented at the HSLA Steels: metallurgy and applications, Beijing, China, 1985.
- [51] T. Gladman, "On Theory of Effect of Precipitate Particles on Grain Growth in Metals," *Proceedings Of The Royal Society Of London Series A-Mathematical And Physical Sciences*, vol. 294, p. 298, 1966.



References

- [52] D. P. Fairchild, N. V. Bangaru, J. Y. Koo, P. L. Harrison, and A. Ozekcin, "A Study Concerning Intercritical Haz Microstructure and Toughness in Hsla Steels," *Welding Journal*, vol. 70, pp. S321-S329, Dec 1991.
- [53] S. Hansen, J. B. Sande, and M. Cohen, "Niobium Carbonitride Precipitation and Austenite Recrystallization in Hot-Rolled Microalloyed Steels," *Metallurgical and Materials Transactions A*, vol. 11, pp. 387-402, 1980.
- [54] F. B. Pickering, "Transformation and Hardenability of Steels," presented at the Climax Molybdenum Company Symposium, Ann Arbor, 1967.
- [55] A. P. Coldren and J. L. Mihelich, "Acicular Ferrite HSLA Steels for Line Pipe," *Metal Science and Heat Treatment*, vol. 19, pp. 559-572, 1977.
- [56] M. R. Krishnadev and R. Ghosh, "Low-Temperature Mechanical-Behavior of an Acicular Ferrite HSLA (High Strength-Low Alloy) Line Pipe Steel," *Metallurgical Transactions a-Physical Metallurgy and Materials Science*, vol. 10, pp. 1941-1944, 1979.
- [57] Y. Smith, A. Coldren, and R. Cryderman, "High-Strength, Ductile Mn-Mo-Nb Steels with a Structure of Acicular Ferrite," *Metal Science and Heat Treatment*, vol. 18, pp. 59-65, 1976.
- [58] Y. Tomita, "Improved Lower Temperature Fracture Toughness of Ultrahigh Strength 4340 Steel through Modified Heat Treatment," *Metallurgical and Materials Transactions A*, vol. 18, pp. 1495-1501, 1987.
- [59] C. Ouchi, "Development of Steel Plates by Intensive Use of Tmcp and Direct Quenching Processes," *ISIJ International*, vol. 41, pp. 542-553, 2001.
- [60] J. Bauer, P. Fluss, E. Amoris, and V. Schwinn, "Microstructure and Properties of Thermomechanical Controlled Processing Steels for Linepipe Applications," *Ironmaking & Steelmaking*, vol. 32, pp. 325-330, Aug 2005.
- [61] A. Ghosh, R. Shukla, S. Das, and S. Chatterjee, "The Structure and Properties of a Thermo-Mechanically Processed Low Carbon High Strength Steel," *Steel Research International*, vol. 77, pp. 276-283, Apr 2006.
- [62] B. Hwang and C. G. Lee, "Influence of Thermomechanical Processing and Heat Treatments on Tensile and Charpy Impact Properties of B and Cu Bearing High-Strength Low-Alloy Steels," *Materials Science and Engineering a-Structural Materials Properties Microstructure and Processing*, vol. 527, pp. 4341-4346, 2010.
- [63] T. Siwecki. (2000) Improving the Properties of Steel by Optimisation of Tmcp Parameters. *Metal Forming*. 29-38. Available: <Go to ISI>://000165686000004
- [64] A. P. Institute, "Api 5l Specification for Line Pipe, Rev 44," ed: API, 200.
-



References

- [65] G. Demofonti, G. Mannucci, H.-G. Hillenbrand, and D. harris, "Suitability Evaluation of X100 Steel Pipes for High Pressure Gas Transprotation Pipelines by Full Scale Tests," presented at the 14th joint technical meeting on pipeline research EPRG - PRCI - APIA, Berlin, Germany, 2003.
- [66] A. Glover, D. Horsley, D. Dorling, and J. Takehara, "Construction and Installation of X100 Pipelines," presented at the International Pipeline Conference, Calgary, Canada, 2004.
- [67] G. Goodall, M. Brochu, J. A. Gianetto, and J. T. Bowker, "Weld HAZ Simulation in X100 Pipe Steel," presented at the Materials Science and Technology Conference, Pittsburgh, 2009.
- [68] H.-G. Hillenbrand, A. Liessem, K. Biermann, C. J. Heckmann, and V. Schwinn, "Development and Production of Linepipe Steels in Grade X100 and X120," presented at the Seminar of X120 grade high performance pipe steels, Beijing, China, 2005.
- [69] M. Hudson, "Welding of X100 Linepipe," Ph.D., School of industrial and manufacturing science, Cranfield, Bedfordshire, 2004.
- [70] G. Thewlis, "Weldability of X100 Linepipe," *Science and Technology of Welding and Joining*, vol. 5, pp. 365-377, 2000.
- [71] G. J. Goetz, "New X70-X80 Hsla Steels for Structural and Line Pipe Use," *Journal of Metals*, vol. 29, pp. 12-18, 1977.
- [72] S. Y. Han, S. Y. Shin, S. Lee, J. Bae, and K. Kim, "Effect of Cooling Conditions on Microstructures and Mechanical Properties in Api X80 Linepipe Steels," *Journal of the Korean Institute of Metals and Materials*, vol. 47, pp. 523-532, 2009.
- [73] S. Y. Shin, B. Hwang, S. Lee, N. J. Kim, and S. S. Ahn, "Correlation of Microstructure and Charpy Impact Properties in Api X70 and X80 Line-Pipe Steels," *Materials Science and Engineering: A*, vol. 458, pp. 281-289, 2007.
- [74] G. Demofonti, G. Mannucci, and Tms, *A Critical Revue of the Developed and Available Know How Devoted to a Safe Use of X100 Grade Steel in Large Diameter Pipelines*, 2008.
- [75] I. Takeuchi, J. Fujino, A. Yamamoto, and S. Okaguchi, "The Prospect of High-Grade Steel Pipe for Gas Pipelines," presented at the Pipe dreamer's conference, Yokohama, Japan, 2002.
- [76] S. Liu, "Critical Concerns of Welding High Strength Steel Pipelines: X-80 and Beyond " presented at the Pipe dreamer's conference, Yokohama, japan, 2002.
- [77] M. Okatsu, T. Hoshino, K. Amano, K. Ihara, T. Makino, and F. Kawabata, "Metallurgical and Mechanical Features of X100 Steel," presented at the Pipe Dreamer's Conference, Yokohama, Japan, 2002.



References

- [78] F. G. Caballero, C. Garcia-Mateo, J. Chao, M. J. Santofimia, C. Capdevila, C. G. de Andres, and Tms, *Ductility of Advanced Bainitic Steels*, 2008.
- [79] J. Chen, H. Bhadeshia, S. Hasler, H. Roelofs, U. Ulrau, and Tms, *Complete Calculation of Steel Microstructure for Strong Alloys*, 2008.
- [80] S. Curtze, V. T. Kuokkala, M. Hokka, P. Peura, P. Verleysen, and Tms, *Effects of Composition, Temperature and Strain Rate on the Mechanical Behavior of High-Alloyed Manganese Steels*, 2008.
- [81] A. Liessem, J. Schroder, M. Pant, M. Erdelen-Peppler, M. Liedtke, S. Hohler, C. Stallybrass, and Tms, *Manufacturing Challenges of High Strength Line Pipes*, 2008.
- [82] M. Militzer, S. Sarkar, K. Mukherjee, H. Azizi-Alizamini, W. J. Poole, and Tms, *Advanced Steels with Complex Ultra-Fine Grained Microstructures*, 2008.
- [83] L. Rancel, S. F. Medina, and Tms, *Influence of Microalloying Elements (Nb, V, Ti) on Bainitic High Strength Steels*, 2008.
- [84] C. P. Reip, J. Kempken, J. Schluter, and Tms, *Metallurgical Aspects of High-Strength Steel Grades and Their Processing through Csp (R) Technology*, 2008.
- [85] D. Fairchild, M. Macia, S. D. Papka, C. W. Petersen, J. H. Stevens, S. T. Barbas, N. Bangaru, J. Koo, and M. Luton, "High Strength Steels - Beyond X80," presented at the Pipe dreamer's conference, Yokohama, Japan, 2002.
- [86] M. C. Cesile, G. Porcu, A. Guindani, R. Venturini, and Tms, *Metallurgically Based Development of High Strength ($\sigma_y > 700$ Mpa) Thin Hot Strips by Arvedi Isp Technology*, 2008.
- [87] H. Makino, T. Inoue, S. Endo, T. Kubo, and T. Matsumoto, "Simulation Method for Crack Propagation and Arrest of Shear Fracture in Natural Gas Transmission Pipelines," presented at the Pipe dreamer's conference, Yokohama, Japan, 2002.
- [88] H. A. Ernst, D. N. Passarella, J. A. Villasante, R. Su, E. P. Lopez, and Tms, *Structural Integrity Analysis of Ultra High Strength Steel Tubes for Airbags*, 2008.
- [89] J. Y. Yoo, D. H. Seo, S. S. Ahn, K. B. Kang, and Tms, *Development of High Strength Linepipe Steel*, 2008.
- [90] G. Demofonti, G. Mannucci, D. Harris, and H. G. Hillenbrand, "Fracture Behaviour of X100 Gas Pipeline by Full Scale Tests," presented at the Pipe Dreamer's Conference, Yokohama, 2002.
- [91] R. M. Andrews, "Fracture Control in High Strength Steel Pipelines," presented at the Pipe Dreamer's Conference, Yokohama, Japan, 2002.



References

- [92] W. D. Callister, *Materials Science and Engineering : An Introduction*, 6th ed. New York, NY: John Wiley & Sons, 2003.
- [93] J. A. Gianetto, J. T. Bowker, R. Bouchard, D. Dorling, and D. Horsley, "Tensile and Toughness Properties of Pipeline Girth Welds," presented at the International Pipeline Conference, Calgary, Canada, 2006.
- [94] G. Knauf, "Eprg: Crack Arrest and Girth Weld Acceptance Criteria for High Pressure Gas Transmission Pipelines," presented at the Pipe dreamer's conference, Yokohama, Japan, 2002.
- [95] Y. Terada, M. Yamashita, T. Hara, H. Tamehiro, and N. Ayukawa, "Technical Report No 72. Development of Api X100 Uoe Line Pipe," *Nippon Steel* 72, January, 1997 1997.
- [96] F. Siciliano, D. G. Stalheim, J. M. Gray, and Asme, *Modern High Strength Steels for Oil and Gas Transmission Pipelines*, 2009.
- [97] L. E. Collins, D. Q. Bai, F. Hamad, X. D. Chen, and Isope, *High Strength Spiral Linepipe for Strain-Based Pipeline Designs*, 2007.
- [98] D. D. Kopeliovich, "Gas Metal Arc Welding," *metal_inert_gas_welding.jpg*, Ed., ed: http://www.substech.com/dokuwiki/doku.php?id=metal_inert_gas_welding_mig_gmaw, 2008.
- [99] H. B. Cary, *Modern Welding Technology*, 3rd ed. Englewood Cliffs, N.J.: Regents/Prentice Hall, 1994.
- [100] S. Kou, *Welding Metallurgy*. New York: Wiley, 1987.
- [101] A. I. Akulov and V. V. Spitsyn, "Rate of Formation and Transfer of a Drop of Electrode Metal in Co₂ Welding," *Welding Production*, vol. 15, pp. 7-8, 1968.
- [102] B. L. Ibatullin and V. F. Mukhin, "Conditions of the Spray Transfer of Electrode Metal in Co₂ Welding," *Automatic Welding Ussr*, vol. 33, pp. 21-23, 1980.
- [103] S. Liu and T. A. Siewert, "Metal Transfer in Gas Metal Arc-Welding - Droplet Rate," *Welding Journal*, vol. 68, pp. S52-S58, Feb 1989.
- [104] W. F. Ruehl and C. L. Collins, "Controlled Droplet Transfer in Gas Metal-Arc Welding," *Welding Journal*, vol. 49, pp. 95-8, 1970.
- [105] G. E. Cook and P. C. Levick, "Narrow Gap Welding with the Hot-Wire Gta Process," *Welding Journal*, vol. 64, pp. 27-31, 1985.
- [106] S. Ueguri, K. Hara, and H. Komura, "Study of Metal Transfer in Pulsed Gma Welding," *Welding Journal*, vol. 64, pp. S242-S250, 1985.



References

- [107] A. Joseph, D. Harwig, D. F. Farson, and R. Richardson, "Measurement and Calculation of Arc Power and Heat Transfer Efficiency in Pulsed Gas Metal Arc Welding," *Science and Technology of Welding and Joining*, vol. 8, pp. 400-406, Dec 2003.
- [108] Y. S. Kim and T. W. Eagar, "Metal Transfer in Pulsed Current Gas Metal Arc-Welding," *Welding Journal*, vol. 72, pp. S279-S287, Jul 1993.
- [109] H. S. Randhawa, P. K. Ghosh, and S. R. Gupta, "Some Basic Aspects of Geometrical Characteristics of Pulsed Current Vertical-up Gma Weld," *ISIJ International*, vol. 40, pp. 71-76, 2000.
- [110] P. K. Ghosh, S. R. Gupta, and H. S. Randhawa, "Characteristics of a Pulsed-Current, Vertical-up Gas Metal Arc Weld in Steel," *Metallurgical and Materials Transactions a-Physical Metallurgy and Materials Science*, vol. 31, pp. 2247-2259, Sep 2000.
- [111] K. L. Kenney, K. S. Miller, and H. B. Smartt, "Heat Transfer in Pulsed Gas Metal Arc Welding," presented at the Trends in Welding Research, Pine Mountain, Georgia, 1998.
- [112] D. V. Dorling and D. Taylor, "Developments in Tandem Pulsed Gas Metal Arc Welding for Grade 690 Pipelines," *Canadian Welding Association Journal*, pp. 8-10, 2005.
- [113] E. Lassaline, B. Zajaczkowski, and T. H. North, "Narrow Groove Twin-Wire Gmaw of High-Strength Steel," *Welding Journal*, vol. 68, pp. 53-58, Sep 1989.
- [114] S. R. Fiore, J. A. Gianetto, M. G. Hudson, S. Vaze, S. Khurana, J. T. Bowker, and D. V. Dorling, "Development of Optimized Weld Metal Chemistries for Pipeline Girth Welding of High Strength Line Pipe," *Ipc2008: Proceedings of the Asme International Pipeline Conference - 2008, Vol 3*, pp. 417-428, 2009.
- [115] J. Gianetto, J. T. Bowker, D. V. Dorling, and D. Horsley, "Analyzing Girth Welds," *Canadian Welding Association Journal*, pp. 31-36, 2007.
- [116] Y. Chen, Y. Y. Wang, and J. Gianetto, "Thermal and Microstructure Simulation of High Strength Pipeline Girth Welds," in *Proceedings of the Eighteenth*, H. W. Jin, et al., Eds., ed, 2008, pp. 33-39.
- [117] O. Grong and A. O. Kluken, "Miorstructure and Properties of Steel Weld Metals," in *Ferrous Alloy Weldments*. vol. 69 & 70, D. L. Olson and T. H. North, Eds., ed Brookfield: Trans Tech Publications Ltd, 1992, pp. 21-46.
- [118] H. K. D. H. Bhadeshia, "Simulation of Weld Metal Microstructure and Properties," *Computer Aided Innovation of New Materials li, Pts 1 and 2*, pp. 1729-1734, 1993.
- [119] D. Rojko and V. Gliha, "Simulations of Transformation Kinetics in a Multi-Pass Weld," *Materials and Manufacturing Processes*, vol. 20, pp. 833-849, 2005.



References

- [120] G. M. Evans, "The Effect of Micro-Alloying Elements in the C-Mn Steel Weld Metal," presented at the Trends in Welding Research, Gatlinburg, Tennessee, 1992.
- [121] G. M. Evans, "Effect of Manganese on the Microstructure and Properties of All-Weld-Metal Deposits," *Welding Journal*, vol. 59, pp. S67-S75, 1980.
- [122] G. M. Evans, "The Effect of Titanium in Manganese-Containing Sma Weld Deposits," *Welding Journal*, vol. 72, pp. S123-S133, Mar 1993.
- [123] K. E. Easterling, *Introduction to the Physical Metallurgy of Welding*, 2nd ed. Oxford [England] ; Boston: Butterworth-Heinemann, 1992.
- [124] D. Fairchild, M. Macia, N. Bangaru, J. Koo, A. Ozekcin, and H. Jin, "Welding Development for the World's Strongest Pipeline: X120," *Trends in Welding Research, Proceedings*, pp. 749-754, 2006.
- [125] T. Nakano, Y. Sugitani, K. Kanayama, and M. Ushio, "State of the Art Gmaw Wires for Pipeline Construction in Japan," presented at the Pipe Dreamer's Conference, Yokohama, Japan, 2002.
- [126] D. A. Porter and K. E. Easterling, *Phase Transformations in Metals and Alloys*, 2nd ed. Cheltenham, U.K.: Nelson Thornes, 2001.
- [127] S. David and J. Vitek, "Principles of Weld Solidification and Microstructures," presented at the International trends in welding science and technology, Gatlinburg, Tennessee, 1992.
- [128] H. W. Kerr, "Solidification and Grain Structure in Welds," presented at the International Trends in Welding science and Technology, Gatlinburg, Tennessee, 1993.
- [129] S. Liu, "Metallography of HSLA Steel Weldments," in *Ferrous Alloy Weldments*. vol. 69&70, D. L. Olson and T. H. North, Eds., ed: Trans Tech Publications, 1992, pp. 1-20.
- [130] G. Krauss and S. W. Thompson, "Ferritic Microstructures in Continuously Cooled Low-Carbon and Ultralow-Carbon Steels," *Isij International*, vol. 35, pp. 937-945, 1995.
- [131] G. Thewlis, "Materials Perspective - Classification and Quantification of Microstructures in Steels," *Materials Science and Technology*, vol. 20, pp. 143-160, Feb 2004.
- [132] E. A. Wilson, "The Gamma-Alpha-Transformation in Low-Carbon Irons," *Isij International*, vol. 34, pp. 615-630, 1994.
- [133] H. K. D. H. Bhadeshia and L.-E. Svensson, "Modelling the Evolution of Microstructure in Steel Weld Metals," in *Mathematical Modelling of Weld Phenomena*, H. Cerjak and K. E. Easterling, Eds., ed London: Institute of Materials, 1993, pp. 109-182.



References

- [134] S. S. Babu and H. Bhadeshia, "Transition from Bainite to Acicular Ferrite in Reheated Fe-Cr-C Weld Deposits," *Materials Science and Technology*, vol. 6, pp. 1005-1020, Oct 1990.
- [135] R. A. Farrar and P. L. Harrison, "Acicular Ferrite in Carbon Manganese Weld Metals - an Overview," *Journal of Materials Science*, vol. 22, pp. 3812-3820, Nov 1987.
- [136] C. Garcia-Mateo, J. Cornide, C. Capdevila, F. G. Caballero, C. G. de Andres, and Tms, *Acicular Ferrite Transformation under the Influence of V Precipitates*, 2008.
- [137] T. Yamada, H. Terasaki, and Y. Komizo, "Microscopic Observation of Inclusions Contributing to Formation of Acicular Ferrite in Steel Weld Metal," *Science and Technology of Welding and Joining*, vol. 13, pp. 118-125, Mar 2008.
- [138] J. R. Yang and H. K. D. H. Bhadeshia, "Orientation Relationships between Adjacent Plates of Acicular Ferrite in Steel Weld Deposits," *Materials Science and Technology*, vol. 5, pp. 93-97, Jan 1989.
- [139] J. R. Yang and H. K. D. H. Bhadeshia, "Acicular Ferrite Transformation in Alloy-Steel Weld Metals," *Journal of Materials Science*, vol. 26, pp. 839-845, Feb 1 1991.
- [140] H. Bhadeshia and J. Christian, "Bainite in Steels," *Metallurgical and Materials Transactions A*, vol. 21, pp. 767-797, 1990.
- [141] H. K. D. H. Bhadeshia, *Bainite in Steels : Transformations, Microstructure and Properties*, 2nd ed. London, UK: IOM Communications, 2001.
- [142] F. Fang, Q. L. Yong, C. F. Yang, and H. Su, "Microstructure and Precipitation Behavior in HAZ of V and Ti Microalloyed Steel," *Journal of Iron and Steel Research International*, vol. 16, pp. 68+, 2009.
- [143] S. Y. Han, S. Y. Shin, C. H. Seo, H. Lee, J. H. Bae, K. Kim, S. Lee, and N. J. Kim, "Effects of Mo, Cr, and V Additions on Tensile and Charpy Impact Properties of Api X80 Pipeline Steels," *Metallurgical and Materials Transactions a-Physical Metallurgy and Materials Science*, vol. 40A, pp. 1851-1862, 2009.
- [144] A. Mark, M. Westphal, D. Boyd, J. McDermid, and D. Embury, "Microstructural Design of Multiphase Advanced High Strength Steels," *Canadian Metallurgical Quarterly*, vol. 48, pp. 237-245, 2009.
- [145] J. Niu, L. H. Qi, Y. L. Liu, L. Ma, Y. R. Feng, and J. X. Zhang, "Tempering Microstructure and Mechanical Properties of Pipeline Steel X80," *Transactions of Nonferrous Metals Society of China*, vol. 19, pp. S573-S578, 2009.
- [146] W. H. Sun, G. D. Wang, J. M. Zhang, and D. X. Xia, "Microstructure Transformation Behaviour of 610 Mpa HSLA Steel Plate for 150 000 M(3) Oil Storage Tank Construction," *Journal of Iron and Steel Research International*, vol. 17, pp. 48-52, 2010.



References

- [147] F. Y. Xu, Y. W. Wang, B. Z. Bai, and H. S. Fang, "Cct Curves of Low-Carbon Mn-Si Steels and Development of Water-Cooled Bainitic Steels," *Journal of Iron and Steel Research International*, vol. 17, pp. 46-50, 2010.
- [148] S. B. Yin, X. J. Sun, Q. Y. Liu, and Z. B. Zhang, "Influence of Deformation on Transformation of Low-Carbon and High Nb-Containing Steel During Continuous Cooling," *Journal of Iron and Steel Research International*, vol. 17, pp. 43-47, 2010.
- [149] Y. Q. Zhang, H. Q. Zhang, J. F. Li, and W. M. Liu, "Effect of Heat Input on Microstructure and Toughness of Coarse Grain Heat Affected Zone in Nb Microalloyed HSLA Steels," *Journal of Iron and Steel Research International*, vol. 16, pp. 73-80, 2009.
- [150] M. X. Zhang and P. M. Kelly, "Accurate Orientation Relationship between Ferrite and Austenite in Low Carbon Martensite and Granular Bainite," *Scripta Materialia*, vol. 47, pp. 749-755, 2002.
- [151] E. Bayraktar and D. Kaplan, "Mechanical and Metallurgical Investigation of Martensite-Austenite Constituents in Simulated Welding Conditions," *Journal of Materials Processing Technology*, vol. 153-54, pp. 87-92, Nov 10 2004.
- [152] A. Lambert, J. Drillet, A. F. Gourgues, T. Sturel, and A. Pineau, "Microstructure of Martensite - Austenite Constituents in Heat Affected Zones of High Strength Low Alloy Steel Welds in Relation to Toughness Properties," *Science and Technology of Welding and Joining*, vol. 5, pp. 168-173, 2000.
- [153] M. F. Ashby and K. E. Easterling, "A 1st Report on Diagrams for Grain-Growth in Welds," *Acta Metallurgica*, vol. 30, pp. 1969-1978, 1982.
- [154] M. I. Onsoien, M. M'Hamdi, and A. Mo, "A Cct Diagram for an Offshore Pipeline Steel of X70 Type," *Welding Journal*, vol. 88, pp. 1S-6S, Jan 2009.
- [155] H. K. D. H. Bhadeshia, L. E. Svensson, and B. Gretoft, "A Model for the Development of Microstructure in Low-Alloy Steel (Fe-Mn-Si-C) Weld Deposits," *Acta Metallurgica*, vol. 33, pp. 1271-1283, 1985.
- [156] C. D. Lundin and G. Zhou, "A Comparison of Published HAZ Thermal Simulation Methods Used to Derive Weld HAZ Thermal Cycles," *Acta Metallurgica Sinica*, vol. 13, pp. 223-232, February, 2000 2000.
- [157] N. N. Rykalin and A. V. Nikolaev, "Welding Arc Heat Flow," *Welding in the World, Le Soudage Dans Le Monde*, vol. 9, pp. 112-133, 1971.
- [158] K. Poorhaydari, B. M. Patchett, and D. G. Ivey, "Estimation of Cooling Rate in the Welding of Plates with Intermediate Thickness," *Welding Journal*, vol. 84, pp. 149S-155S, Oct 2005.



References

- [159] J. C. Ion, K. E. Easterling, and M. F. Ashby, "A 2nd Report on Diagrams of Microstructure and Hardness for Heat-Affected Zones in Welds," *Acta Metallurgica*, vol. 32, pp. 1949-8, 1984.
- [160] W. B. Li, K. E. Easterling, and M. F. Ashby, "Laser Transformation Hardening of Steel .2. Hypereutectoid Steels," *Acta Metallurgica*, vol. 34, pp. 1533-1543, Aug 1986.
- [161] M. Shome, "Effect of Heat-Input on Austenite Grain Size in the Heat-Affected Zone of HSLA-100 Steel," *Materials Science and Engineering a-Structural Materials Properties Microstructure and Processing*, vol. 445, pp. 454-460, Feb 2007.
- [162] I. Andersen and Ø. Grong, "Analytical Modelling of Grain Growth in Metals and Alloys in the Presence of Growing and Dissolving Precipitates--I. Normal Grain Growth," *Acta Metallurgica Et Materialia*, vol. 43, pp. 2673-2688, 1995.
- [163] I. Andersen, Ø. Grong, and N. Ryum, "Analytical Modelling of Grain Growth in Metals and Alloys in the Presence of Growing and Dissolving Precipitates--II. Abnormal Grain Growth," *Acta Metallurgica Et Materialia*, vol. 43, pp. 2689-2700, 1995.
- [164] K. Poorhaydari, B. M. Patchett, and D. G. Ivey, "Transformation Twins in the Weld HAZ of a Low-Carbon High-Strength Microalloyed Steel," *Materials Science and Engineering a-Structural Materials Properties Microstructure and Processing*, vol. 435, pp. 371-382, Nov 2006.
- [165] J. A. Gianetto, J. E. M. Braid, J. T. Bowker, and W. R. Tyson, "Heat-Affected Zone Toughness of a Tmcp Steel Designed for Low-Temperature Applications," *Journal of Offshore Mechanics and Arctic Engineering*, vol. 119, pp. 134-144, May 1997.
- [166] M. R. Krishnadev, W. L. Zhang, V. Vaidya, A. Gendron, J. T. Bowker, and R. Rene, "Extra Low Carbon Welding Consumables for HSLA 80 and HSLA 100 Steels and Improving HAZ Toughness at High Heat Inputs," *Metal Welding and Applications*, pp. 55-70, 1999.
- [167] C. L. Davis and J. E. King, "Effect of Cooling Rate on Intercritically Reheated Microstructure and Toughness in High-Strength Low-Alloy Steel," *Materials Science and Technology*, vol. 9, pp. 8-15, Jan 1993.
- [168] A. H. Cottrell, *Theory of Crystal Dislocations*. New York: Gordon and Breach, 1965.
- [169] C. L. Davis and J. E. King, "Cleavage Initiation in the Intercritically Reheated Coarse-Grained Heat-Affected Zone .1. Fractographic Evidence," *Metallurgical and Materials Transactions a-Physical Metallurgy and Materials Science*, vol. 25, pp. 563-573, Mar 1994.
- [170] C. L. Davis and J. E. King, "Cleavage Initiation in the Intercritically Reheated Coarse-Grained Heat Affected Zone .2. Failure Criteria and Statistical Effects," *Metallurgical and*



References

- Materials Transactions a-Physical Metallurgy and Materials Science*, vol. 27, pp. 3019-3029, Oct 1996.
- [171] Y. Adonyi, "Heat-Affected Zone Characterization by Physical Simulations - an Overview on the Use of the Gleeble Discusses the Advantages and Disadvantages of Thermomechanical Simulation," *Welding Journal*, vol. 85, pp. 42-47, Oct 2006.
- [172] C. Feng, H. S. Fang, B. Z. Bai, and Y. K. Zheng, "Phase Transformation and Strength-Toughness of a F-Gba/B-G Diphas Steel Containing 0.02%Nb," *Acta Metallurgica Sinica*, vol. 46, pp. 473-478, 2010.
- [173] M. R. Krishnadev, W. L. Zhang, J. T. Bowker, V. Vaidya, A. Gendron, and R. Rene, "High Heat Input Weldability through Alloying and Welding Practice in Modern HSLA Steels," *International Symposium on Steel for Fabricated Structures*, pp. 67-74, 1999.
- [174] J. C. Lippold, E. F. Nippes, and W. F. Savage, "Investigation of Hot Cracking in 5083-O Aluminum-Alloy Weldments," *Welding Journal*, vol. 56, pp. S171-S178, 1977.
- [175] W. F. Savage, E. P. Nippes, and M. C. Mushala, "Copper-Contamination Cracking in Weld Heat-Affected Zone," *Welding Journal*, vol. 57, pp. S145-S152, 1978.
- [176] J. T. Bowker, J. A. Gianetto, and M. W. Letts, "The Structure of Real Weld and Simulated Heat-Affected Zones for a Range of Offshore Structural Grade Steels," *Journal of Metals*, vol. 36, pp. 102-102, 1984.
- [177] D. W. Walsh, M. J. Cieslak, and W. F. Savage, "Temperature-Measurements in Resistance-Heated Specimens - Longitudinal Gradients," *Welding Journal*, vol. 65, pp. S184-S192, Jul 1986.
- [178] G. A. Knorovsky, C. V. Robino, R. C. Dykuizen, and D. O. MacCallum, "Dilatometry in the Gleeble: What Did You Really Measure?," presented at the Trends in Welding Reserach, Pine Mountain, Georga, 1998.
- [179] M. Toyoda, M. Mochizuki, S. Matsushima, Z. Zhang, O. Gundersen, and C. Thaulow, "Behavior of Phase Trasnformation and Thermal Stress During Welding Heat Cycles," 2002.
- [180] D. Rojko and V. Gliha, "The Influence of Simulated Thermal Cycle on the Formation of Microstructures of Multi-Pass Weld Metal," *Metalurgija*, vol. 44, pp. 19-24, Jan-Mar 2005.
- [181] A. L. Christenson, E. C. Nelson, and C. E. Jackson, "A High Speed Dilatometer and the Transformation of Six Steels in Cooling," *Transactions of the American Institute of Mining Engineers*, vol. 162, pp. 606-626, 1945.



References

- [182] P. L. Harrison and R. A. Farrar, "Application of Continuous Cooling Transformation Diagrams for Welding of Steels," *International Materials Reviews*, vol. 34, pp. 35-51, 1989.
- [183] J.-C. Zhao and M. R. Notis, "Continuous Cooling Transformation Kinetics Versus Isothermal Transformation Kinetics of Steels: A Phenomenological Rationalization of Experimental Observations," *Materials Science and Engineering: R: Reports*, vol. 15, pp. 135-207, 1995.
- [184] M. Atkins, *Atlas of Continuous Cooling Transformation Diagrams for Engineering Steels*, Rev. U.S. ed. Metals Park, Ohio: American Society for Metals, 1980.
- [185] T. Kasugai and M. Fujita, *Atlas of Cct Diagrams for Welding (I)*. Ibaraki, Japan: NRIM, 1999.
- [186] T. A. Kop, J. Sietsma, and S. Van der Zwaag, "Dilatometric Analysis of Phase Transformations in Hypo-Eutectoid Steels," *Journal of Materials Science*, vol. 36, pp. 519-526, Jan 2001.
- [187] T. A. Kop, J. Sietsma, and S. VanderZwaag, "The Transformation Kinetics of Construction Steels; a Combined Dilatometric and Dta Approach," *Euromat 97 - Proceedings of the 5th European Conference on Advanced Materials and Processes and Applications: Materials, Functionality & Design, Vol 1*, pp. 537-540, 1997.
- [188] C. G. de Andres, F. G. Caballero, C. Capdevila, and L. F. Alvarez, "Application of Dilatometric Analysis to the Study of Solid-Solid Phase Transformations in Steels," *Materials Characterization*, vol. 48, pp. 101-111, Feb 2002.
- [189] T. A. Kop, J. Sietsma, and S. van der Zwaag, "Ferrous Phase Transformation Kinetics: A Combined Dilatometric-Calorimetric Approach," *Accelerated Cooling/Direct Quenching of Steels, Conference Proceedings from Materials Solution '97*, pp. 159-165, 1997.
- [190] J. Z. Zhao, C. Mesplont, and B. C. De Cooman, "Model for Extracting Phase Transformation Kinetics from Dilatometry Measurements for Multistep Transformations," *Materials Science and Technology*, vol. 18, pp. 1115-1120, 2002.
- [191] H. S. Yang and H. K. D. H. Bhadeshia, "Uncertainties in Dilatometric Determination of Martensite Start Temperature," *Materials Science and Technology*, vol. 23, pp. 556-560, May 2007.
- [192] M. W. Hukle, D. B. Lillig, B. D. Newbury, J. Dwyer, and A. M. Horn, "Development and Qualification of Pipeline Welding Procedures for Strain Based Design," in *International Conference on Offshore Mechanics and Arctic Engineering (OMAE)*, San Diego, California, USA, 2007, pp. 217-223.



References

- [193] S. Imai, "General Properties of Tmcp Steels," in *12th International Offshore and Polar Engineering Conference*, Kitakyushu, Japan, 2002, pp. 392-396.
- [194] Y. C. Liu, F. X. Zhu, Y. M. Li, and G. D. Wang, "Effect of Tmcp Parameters on the Microstructure and Properties of an Nb-Ti Microalloyed Steel," *Isij International*, vol. 45, pp. 851-857, 2005.
- [195] W. Steven and A. G. Haynes, "The Temperature of Formation of Martensite and Bainite in Low-Alloy Steels," *Journal of Iron and Steel Research International*, 1956.
- [196] F. G. Caballero, C. Capdevila, and C. G. De Andres, "An Attempt to Establish the Variables That Most Directly Influence the Austenite Formation Process in Steels," *Isij International*, vol. 43, pp. 726-735, 2003.
- [197] C. Capdevila, F. G. Caballero, and C. G. de Andres, "Austenite Grain Size Effects on Isothermal Allotriomorphic Ferrite Formation in 0.37c-1.45mn-0.11v Microalloyed Steel," *Materials Transactions*, vol. 44, pp. 1087-1095, Jun 2003.
- [198] T. De Cock, C. Capdevila, J. P. Ferrer, F. G. Caballero, J. A. Jimenez, and C. G. de Andres, "Recrystallisation and Dilatometric Behaviour of Low Carbon and Ultralow Carbon Steels," *Materials Science and Technology*, vol. 24, pp. 832-837, Jul 2008.
- [199] D. San Martin, F. G. Caballero, C. Capdevila, and C. Garcia-de-Andres, "Study and Modelling of the Influence of Second Phase Particles on the Austenite Grain Growth in a Niobium Microalloyed Steel," *Revista De Metalurgia*, vol. 42, pp. 128-137, Mar-Apr 2006.
- [200] M. Shome, D. S. Sarma, O. P. Gupta, and O. N. Mohanty, "Precipitate Dissolution and Grain Growth in the Heat Affected Zone of HSLA-100 Steel," *Isij International*, vol. 43, pp. 1431-1437, 2003.
- [201] T. A. Kop, J. Sietsma, and S. van der Zwaag, "Anisotropic Dilatation Behaviour During Transformation of Hot Rolled Steels Showing Banded Structure," *Materials Science and Technology*, vol. 17, pp. 1569-1574, Dec 2001.
- [202] A. B. Cota, P. J. Modenesi, R. Barbosa, and D. B. Santos, "Determination of Cct Diagrams by Thermal Analysis of an HSLA Bainitic Steel Submitted to Thermomechanical Treatment," *Scripta Materialia*, vol. 40, pp. 165-169, 1998.
- [203] J. Trzaska and L. A. Dobrzanski, "Modelling of Cct Diagrams for Engineering and Constructional Steels," *Journal of Materials Processing Technology*, vol. 192-193, pp. 504-510, 2007.
- [204] A. International, "Astm A1033-10 Standard Practice for Quantitative Measurement and Reporting of Hypoeutectoid Carbon and Low-Alloy Steel Phase Transformations," ed. 100 Barr Harbor Drive, PO Box C700, West Conshohocken, PA 19428-2959, United States.: ASTM International, 2010, p. 14.



References

- [205] H. S. Yang and H. K. D. H. Bhadeshia, "Austenite Grain Size and the Martensite-Start Temperature," *Scripta Materialia*, vol. 60, pp. 493-495, Apr 2009.
- [206] A. Garcia-Junceda, C. Capdevila, F. G. Caballero, and C. G. de Andres, "Dependence of Martensite Start Temperature on Fine Austenite Grain Size," *Scripta Materialia*, vol. 58, pp. 134-137, Jan 2008.
- [207] M. Shome, O. P. Gupta, and O. N. Mohanty, "Effect of Simulated Thermal Cycles on the Microstructure of the Heat-Affected Zone in HSLA-80 and HSLA-100 Steel Plates," *Metallurgical and Materials Transactions A*, vol. 35A, pp. 985-996, Mar 2004.
- [208] G. Q. Li, J. F. Wang, D. Z. Wen, A. D. Xiao, and J. Fu, "Low Cost HSLA-Steel Produced by Bof-Csp Process: A Primary Study on Ti Microalloyed Pipe Line Steel," *Journal of Iron and Steel Research International*, vol. 16, pp. 466-473, May 2009.
- [209] M. Shome, O. P. Gupta, and O. N. Mohanty, "A Modified Analytical Approach for Modelling Grain Growth in the Coarse Grain HAZ of HSLA Steels," *Scripta Materialia*, vol. 50, pp. 1007-1010, Apr 2004.
- [210] R. A. Farrar and Z. Y. Zhang, "Experimental-Verification of the Continuous-Cooling Transformation Diagram Produced by the Dilatometry Metallography Method," *Journal of Materials Science Letters*, vol. 12, pp. 1606-1611, Oct 15 1993.
- [211] S. Zajac, V. Schwinn, and K. H. Tacke, "Characterisation and Quantification of Complex Bainitic Microstructures in High and Ultra-High Strength Linepipe Steels," in *Microalloying for New Steel Processes and Applications*. vol. 500-501, ed, 2005, pp. 387-394.
- [212] C. H. Lee, H. K. D. H. Bhadeshia, and H. C. Lee, "Effect of Plastic Deformation on the Formation of Acicular Ferrite," *Materials Science and Engineering A*, vol. 360, pp. 249-257, 2003.
- [213] Z. H. Tang and W. Stumpf, "The Role of Molybdenum Additions and Prior Deformation on Acicular Ferrite Formation in Microalloyed Nb-Ti Low-Carbon Line-Pipe Steels," *Materials Characterization*, vol. 59, pp. 717-728, Jun 2008.
- [214] F. T. Han, B. Hwang, D. W. Suh, Z. C. Wang, D. L. Lee, and S. J. Kim, "Effect of Molybdenum and Chromium on Hardenability of Low-Carbon Boron-Added Steels," *Metals and Materials International*, vol. 14, pp. 667-672, Dec 2008.
- [215] D. Rittel, B. Tanguy, A. Pineau, and T. Thomas, "Impact Fracture of a Ferritic Steel in the Lower Shelf Regime," *International Journal of Fracture*, vol. 117, pp. 101-112, Sep 2002.
- [216] B. Tanguy, J. Besson, R. Piques, and A. Pineau, "Ductile to Brittle Transition of an A508 Steel Characterized by Charpy Impact Test: Part I: Experimental Results," *Engineering Fracture Mechanics*, vol. 72, pp. 49-72, 2005.



References

- [217] X. Z. Zhang and J. F. Knott, "Cleavage Fracture in Bainitic and Martensitic Microstructures," *Acta Materialia*, vol. 47, pp. 3483-3495, Sep 1999.
- [218] S. Y. Han, S. Y. Shin, S. Lee, N. J. Kim, J. H. Bae, and K. Kim, "Effects of Cooling Conditions on Tensile and Charpy Impact Properties of Api X80 Linepipe Steels," *Metallurgical and Materials Transactions a-Physical Metallurgy and Materials Science*, vol. 41A, pp. 329-340, 2010.
- [219] F. G. Caballero, M. K. Miller, C. Garcia-Mateo, C. Capdevila, and C. de Andres, "Phase Transformation Theory: A Powerful Tool for the Design of Advanced Steels," *Jom*, vol. 60, pp. 16-21, Dec 2008.
- [220] M. Umemoto, H. G. Zing, and I. Tamura, "Effect of Cooling Rate on Grain-Size of Ferrite in a Carbon-Steel," *Materials Science and Technology*, vol. 3, pp. 249-255, Apr 1987.
- [221] B. D. Newbury, M. W. Hukle, M. D. Crawford, and D. B. Lillig, "Welding Engineering for High Strain Pipelines," *Proceedings of the Seventeenth (2007) International Offshore and Polar Engineering Conference, Vol 1- 4, Proceedings*, pp. 2996-3000, 2007.
- [222] D. A. Porter and K. E. Easterling, *Phase Transformations in Metals and Alloys*, 2nd ed. Cheltenham, U.K.: Nelson Thornes, 2001.
- [223] R. W. Fonda and G. Spanos, "Microstructural Evolution in Ultra-Low-Carbon Steel Weldments - Part I: Controlled Thermal Cycling and Continuous Cooling Transformation Diagram of the Weld Metal," *Metallurgical and Materials Transactions a-Physical Metallurgy and Materials Science*, vol. 31, pp. 2145-2153, Sep 2000.
- [224] J. A. Gianetto, N. J. Smith, J. T. Mcgrath, and J. T. Bowker, "Effect of Composition and Energy Input on Structure and Properties of High-Strength Weld Metals," *Welding Journal*, vol. 71, pp. S407-S419, Nov 1992.
- [225] D. L. Olson and T. H. North, *Ferrous Alloy Weldments*. Switzerland ; Brookfield, VT: Trans Tech Pub., 1992.
- [226] E. Keehan, J. Zachrisson, and L. Karlsson, "Influence of Cooling Rate on Microstructure and Properties of High Strength Steel Weld Metal," *Science and Technology of Welding and Joining*, vol. 15, pp. 233-238, Apr 2010.
- [227] Y. Komizo, H. Terasaki, and T. Yamada, "Morphological Development for Acicular Ferrite in High Strength Pipeline Steel Weld Metal," *Ipc2008: Proceedings of the Asme International Pipeline Conference - 2008, Vol 3*, pp. 483-487, 2009.
- [228] W. D. Callister, *Materials Science and Engineering : An Introduction*, 7th ed. New York: John Wiley & Sons, 2007.



References

- [229] F. G. Caballero, C. Capdevila, and C. G. De Andres, "Modelling of Kinetics of Austenite Formation in Steels with Different Initial Microstructures," *Isij International*, vol. 41, pp. 1093-1102, 2001.
- [230] C. Capdevila, F. G. Caballero, and C. G. de Andres, "Proposition of Two Parameters for a Good Characterisation of the Austenitising Condition of Microalloyed Steels," *Thermec'2003, Pts 1-5*, vol. 426-4, pp. 1611-1616, 2003.
- [231] S. Chatterjee, H. S. Wang, J. R. Yang, and H. K. D. H. Bhadeshia, "Mechanical Stabilisation of Austenite," *Materials Science and Technology*, vol. 22, pp. 641-644, Jun 2006.
- [232] J. R. Yang, C. Y. Huang, C. F. Huang, and J. N. Aoh, "Influence of Acicular Ferrite and Bainite Microstructures on Toughness for an Ultra-Low-Carbon Alloy Steel Weld Metal," *Journal of Materials Science Letters*, vol. 12, pp. 1290-1293, 1993.
- [233] J. R. Yang, C. C. Yang, and C. Y. Huang, "The Coexistence of Acicular Ferrite and Bainite in an Alloy-Steel Weld Metal," *Journal of Materials Science Letters*, vol. 11, pp. 1145-1146, 1992.
- [234] S. Shanmugam, N. K. Ramiseti, R. D. K. Misra, J. Hartmann, and S. G. Jansto, "Microstructure and High Strength-Toughness Combination of a New 700 mpa Nb-Microalloyed Pipeline Steel," *Materials Science and Engineering: A*, vol. 478, pp. 26-37, 2008.
- [235] J. H. Kim, Y. J. Oh, I. S. Hwang, D. J. Kim, and J. T. Kim, "Fracture Behavior of Heat-Affected Zone in Low Alloy Steels," *Journal of Nuclear Materials*, vol. 299, pp. 132-139, 2001.
- [236] O. E. Vega, J. M. Hallen, A. Villagomez, and A. Contreras, "Effect of Multiple Repairs in Girth Welds of Pipelines on the Mechanical Properties," *Materials Characterization*, vol. 59, pp. 1498-1507, 2008.
- [237] W. Wang, Y. Shan, and K. Yang, "Study of High Strength Pipeline Steels with Different Microstructures," *Materials Science and Engineering: A*, vol. 502, pp. 38-44, 2009.
- [238] H. Furuya, S. Aihara, and K. Morita, "A New Proposal of HAZ Toughness Evaluation Method - Part 1: HAZ Toughness of Structural Steel in Multilayer and Single-Layer Weld Joints," *Welding Journal*, vol. 86, pp. 1S-8S, Jan 2007.
- [239] T. W. Park and C. Y. Kang, "The Effects of Pwht on the Toughness of Weld HAZ in Cu-Containing HSLA-100 Steel," *ISIJ International*, vol. 40, pp. S49-S53, 2000.
- [240] J. A. Gianetto, J. E. M. Braid, J. T. Bowker, and W. R. Tyson, "Heat-Affected Zone Toughness of a Tmcp Steel Designed for Low-Temperature Applications," *Journal of Offshore Mechanics and Arctic Engineering-Transactions of the Asme*, vol. 119, pp. 134-144, May 1997.



References

- [241] G. Spanos, R. W. Fonda, R. A. Vandermeer, and A. Matuszeski, "Microstructural Changes in HSLA-100 Steel Thermally Cycled to Simulate the Heat-Affected Zone During Welding," *Metallurgical and Materials Transactions a-Physical Metallurgy and Materials Science*, vol. 26, pp. 3277-3293, Dec 1995.
- [242] W. H. Sun, G. D. Wang, J. M. Zhang, D. X. Xia, and H. Sun, "Microstructure Characterization of High-Heat-Input Welding Joint of HSLA Steel Plate for Oil Storage Construction," *Journal of Materials Science & Technology*, vol. 25, pp. 857-860, 2009.
- [243] S. S. Babu and H. Bhadeshia, "Mechanism of the Transition from Bainite to Acicular Ferrite," *Materials Transactions Jim*, vol. 32, pp. 679-688, Aug 1991.
- [244] J. R. Yang and H. Bhadeshia, "Acicular Ferrite Transformation in Alloy-Steel Weld Metals," *Journal of Materials Science*, vol. 26, pp. 839-845, Feb 1991.
- [245] C. G. de Andres, C. Capdevila, D. San Martin, and F. G. Caballero, "Effect of the Microalloying Elements on Nucleation of Allotriomorphic Ferrite in Medium Carbon-Manganese Steels," *Journal of Materials Science Letters*, vol. 20, pp. 1135-1137, 2001.
- [246] F. Xiao, B. Liao, D. Ren, Y. Shan, and K. Yang, "Acicular Ferritic Microstructure of a Low-Carbon Mn-Mo-Nb Microalloyed Pipeline Steel," *Materials Characterization*, vol. 54, pp. 305-314, 2005.
- [247] M.-C. Zhao, K. Yang, F.-R. Xiao, and Y.-Y. Shan, "Continuous Cooling Transformation of Undeformed and Deformed Low Carbon Pipeline Steels," *Materials Science and Engineering A*, vol. 355, pp. 126-136, 2003.
- [248] N. Okumura, "Cleavage Fracture of Low-Carbon Ferritic Steels with Fine-Grain Size," *Metal Science*, vol. 17, pp. 581-589, 1983.
- [249] G. Huppi, "Reheat Zone Microstructural Development and Toughness in Selected HSLA Steel Weld Metals," Ph.D., Metallurgical Engineering, Colorado School of Mines - Center for Welding Research, Golden, 1986.
- [250] J. R. Yang and H. Bhadeshia, "Reaustenitization Experiments on Some High-Strength Steel Weld Deposits," *Materials Science and Engineering a-Structural Materials Properties Microstructure and Processing*, vol. 118, pp. 155-170, Oct 1989.